

EXPERIMENTAL MEASUREMENTS OF HYPERSONIC INSTABILITIES OVER OGIVE-CYLINDERS AT MACH 6

THESIS

J. Luke Hill, Second Lieutenant, USAF

AFIT-ENY-MS-20-M-265

DEPARTMENT OF THE AIR FORCE
AIR UNIVERSITY

AIR FORCE INSTITUTE OF TECHNOLOGY

Wright-Patterson Air Force Base, Ohio

DISTRIBUTION STATEMENT A
APPROVED FOR PUBLIC RELEASE; DISTRIBUTION UNLIMITED.

The views expressed in this document are those of the author and do not reflect the official policy or position of the United States Air Force, the United States Department of Defense or the United States Government. This material is declared a work of the U.S. Government and is not subject to copyright protection in the United States.

AFIT-ENY-MS-20-M-265

EXPERIMENTAL MEASUREMENTS OF HYPERSONIC INSTABILITIES OVER OGIVE-CYLINDERS AT MACH 6

THESIS

Presented to the Faculty

Department of Aeronautics and Astronautics

Graduate School of Engineering and Management

Air Force Institute of Technology

Air University

Air Education and Training Command

in Partial Fulfillment of the Requirements for the

Degree of Master's Degree of Science

J. Luke Hill, B.S.

Second Lieutenant, USAF

March 2020

DISTRIBUTION STATEMENT A
APPROVED FOR PUBLIC RELEASE; DISTRIBUTION UNLIMITED.

AFIT-ENY-MS-20-M-265

Abstract

Hypersonic boundary layer transition experiments were performed in the Air Force Research Laboratory (AFRL) Mach 6 Ludwieg Tube over a meter long ogive-cylinder model with interchangeable nose tip angles and bluntnesses. Measurements of instabilities were captured via focused laser differential interferometry (FLDI), surface mounted pressure sensors, and high speed Schlieren imagery at nominal unit Reynolds numbers ranging from $3.89 * 10^6\, m^{-1}$ to $1.36 * 10^7\, m^{-1}$. These experiments were conducted in an attempt to replicate and increase the community's understanding of observations made in the Purdue University Boeing/AFOSR Mach 6 Quiet Tunnel (BAM6QT) over a similar geometry where apparent entropy layer instabilities were measured using hot-wire anemometers and surface mounted pressure sensors. The measured apparent entropy layer instabilities appeared to dominate transition over the body of the geometry and have spurred interest in the hypersonic transition community on the implications of such findings for other geometries such as blunt cones. This current study attempts to isolate the effects of increasing tip angle and spherical bluntness on instabilities measured downstream over the cylindrical body of an ogive-cylinder. Results indicate that shallow, sharp ogive tips develop clear modal instabilities downstream with apparent second Mack mode "rope-like" structures in Schlieren images and an unknown, low frequency band hypothesized to be an entropy layer instability that manifests as elongated, flat structures in Schlieren visualization. These modal instabilities exhibit non-linear interactions with themselves and the lower frequency entropy layer instability. This interaction is determined to dominate the transition to turbulence and the instability structures are observed interacting with one another in the Schlieren images. As tip angle of the sharp ogives is increased,

there is an initial delay in the presence of modal instabilities over the model and then a rapid emergence and nonlinear breakdown to turbulence of the instabilities. FLDI was capable of measuring frequency content of the modal instabilities within the boundary layer and also what appears to be the entropy layer instability outside the boundary layer for the sharp tip variants. When spherical bluntness is added to the sharp ogives, a significant delay in transition occurs and no clear modal instabilities are observed. This delay in transition continues further with increased bluntness with no reversal phenomenon observed. Some of the blunted tips also exhibit nonlinear interactions during their breakdown to turbulence with no modal instabilities present in the frequency spectra. Despite the relative success of FLDI in measuring instabilities over the sharp tip ogives, the FLDI setup struggled to measure many of the other instabilities that the pressure sensors and Schlieren images captured over the other geometries. It is determined that the FLDI focal point separation distance was too narrow compared to the wavelength and orientation of the instabilities over the ogive-cylinder. Recommendations to the experimental hypersonic instability community regarding the sensitivity of the FLDI focal points to the wavelength of the expected instabilities are provided.

Acknowledgements

Experiments are useless without computations. - Steve Schneider

Computations are useless without experiments. - Graham Candler [1]

This work would not have been accomplished without the amazing support of the researchers at AFRL, AFIT, and across the hypersonic research community who have mentored and guided me along this journey. Special thanks goes out to my advisor, Lt Col Jeffrey Komives, and my co-advisor, Dr. Mark Reeder, for allowing me to crowd their offices almost daily to talk over ideas and complications I faced throughout this study. Dr. Matt Borg's leadership and assistance in this project was perhaps the most valuable. I can honestly say that everything I know about operating a hypersonic tunnel is due to Dr. Borg's mentorship. To Dr. Joe Jewell, I thank you for leaving behind a legacy of excellence at the tunnel and for facilitating the research that I was able to perform. You have a tremendously busy schedule and yet you made time for me and I appreciate that. Speaking of Purdue faculty, I cannot thank Dr. Steve Schneider enough for his contributions and comments regarding this work. Dr. Schneider is a legend in this line of research and his team's efforts over the past three decades are what inspired my own work and I appreciate the conversations we have shared over the past year. I also must thank my research partner, Second Lieutenant Ryan Oddo, who worked tireless with me in the tunnel to get both of our projects completed on time and with whom I have shared many a 2am phone call discussing the intricacies of our unique problem sets. First Lieutenant Braeden Sheets was a tremendous help during this study and his expertise with the operation of the tunnel facility was crucial to us meeting the tight deadlines. I must also thank Elizabeth

[1] *Exchange between these two legends of hypersonic research at the conclusion of Dr. Candler's talk at the 2020 AIAA SciTech session honoring the legacy of Dr. Schneider*

Benitez who's assistance on this project was critical in getting FLDI up and working. Elizabeth is doing amazing work in experimental hypersonic testing and diagnostics and I appreciate her assistance on this project. I want to thank Dr. Daniel Chin for his involvement in getting the complicated video and image processing techniques fleshed out. I thank the AFIT model shop who's professionalism, timeliness, and attention to detail made the manufacturing of the most critical components in this project an effortless ordeal.

Most of all, I thank the love of my life who stood by me throughout this challenging and rewarding experience. Thank you.

J. Luke Hill

Table of Contents

Page

Abstract 1

Acknowledgements 3

List of Figures 8

List of Tables 21

I. Introduction 1

II. Review of Literature 3

2.1 Brief History of Boundary Layer Instability Research 4
2.2 Hypersonic Regime Characteristics 11
2.2.1 Thin Shock Layers 11
2.2.2 Entropy Layers 12
2.2.3 High Viscous Interactions 15
2.2.4 High Temperatures 16
2.2.5 Low-Density Flow 17
2.3 Laminar to Turbulent Boundary Layer Transition 18
2.4 Hypersonic Instability Mechanisms 22
2.4.1 The Mack Modes 25
2.4.2 Hypersonic Blunt Cone Transition Reversal Phenomenon 31
2.4.3 Modern Hypersonic Blunt Cone Transition and Instability Research 37
2.4.4 Nonlinear Interactions and Breakdown to Turbulence 43
2.5 Purdue Cone-Ogive-Cylinder Entropy Layer Experiment 50
2.5.1 Flared Cone Model 50
2.5.2 Cone-Ogive-Cylinder Model 52
2.5.3 Numerical Predictions 53
2.5.4 Experimental Results - Surface Measurements 56
2.5.5 Experimental Results - Off-Surface Measurements 57

III. Methodology 64

3.1 AFRL Mach 6 Ludwieg Tube Facility 65
3.1.1 Tunnel Components 66
3.1.2 Tunnel Flow Conditions 71
3.2 Seven Degree Half Angle Sharp Cone 83
3.2.1 Geometry 83
3.2.2 Run Conditions 86

Page

3.3 Ogive-Cylinder Model . . . 86
3.3.1 Overall Design . . . 87
3.3.2 Nose Tip Design . . . 90
3.3.3 Run Conditions . . . 101
3.4 Diagnostics . . . 104
3.4.1 Surface Mounted Pressure Sensors . . . 105
3.4.2 Focused Laser Differential Interferometry . . . 109
3.4.3 High Speed Schlieren . . . 117

IV. Results and Analysis . . . 128

4.1 Seven Degree Half Angle Cone . . . 128
4.1.1 Schlieren visualization resolves the boundary layer and second mode instabilities . . . 129
4.1.2 FLDI and Schlieren measure the same second mode instabilities . . . 132
4.1.3 Spatial to temporal frequency analysis of Schlieren reveals more instability features . . . 136
4.2 Ogive-Cylinder Model . . . 139
4.2.1 Schlieren results . . . 139
4.2.2 FLDI results . . . 168
4.2.3 Surface pressure sensor results . . . 178

V. Conclusion . . . 213

5.1 Key Findings . . . 214
5.1.1 The sharp ogive tips exhibit strong modal instabilities with nonlinear effects and breakdown . . . 214
5.1.2 A possible entropy layer instability is observed . . . 215
5.1.3 The blunted ogive tips exhibit non-modal transition with nonlinear effects . . . 216
5.1.4 An apparent transition reversal is observed over the blunted ogives . . . 216
5.1.5 A new curvature Reynolds number allows for characterization of the ogive-cylinder transition trends . . . 217
5.2 Recommendations and Future Work . . . 217
5.2.1 Expanded FLDI capabilities and characterization . . . 217
5.2.2 Angle of attack improvements . . . 218
5.2.3 Transition characterization studies . . . 218
5.2.4 Continue to test the geometry . . . 219

Appendix A. Run Conditions . . . 220

Page

Appendix B. FLDI Components 223

Appendix C. Nose Geometry Equations 224

Bibliography 225

List of Figures

Figure		Page
1	X-15 Boundary Layer Transition Location During Wind Tunnel Testing vs During Flight Testing [1]	7
2	Stetson's Iconic 7° Cone in AEDC Tunnel B [2]	9
3	Streamline Entropy Gradient (Adapted from [3])	13
4	Shock Curvature with Increasing Freestram Mach Number	14
5	Entropy Layer Swallowing Effect (Adapted from [4])	15
6	Merged Shock Layer	17
7	Mechanisms of Boundary Layer Transition (adapted from [5])	19
8	Boundary Layer Transition Process Over a Flat Plate (adapted from [6])	21
9	Eiegenvalue structure across boundary layer at freestream Mach 10 [7]	26
10	2D Mack mode temporal amplification rate vs Mach number [7]	27
11	General acoustic pressure-fluctuation structure of Mack modes ($U(y)$ is the mean flow profile and $p(y)$is the pressure disturbance profile) [8]	27
12	First and second mode maximum spatial amplification rates [9]	29
13	Second Mode Diagram [10]	30
14	Supersonic Mode Diagram [10]	30
15	Second Mack Mode (a) Schlieren Visualization (b) Pressure Time Series (c) Pressure Power Spectral Densities [11]	32

Figure Page

16 Stetson nosetip bluntness effect on frustrum transition at Mach 5.9 (a) blunt cone transition location normalized by sharp cone transition location (b) blunt cone transition Reynolds number normalized by sharp cone transition Reynolds number [12] 35

17 Marineau et al. Log(PSD) of Cones at $Re/m \approx 17 * 10^6/m$ (a) $R_n = Sharp$ (b) $R_n = 5mm$ (c) $R_n = 9.5mm$ (d) $R_n = 12.7mm$ (e) $R_n = 25.4mm$ (f) $R_n = 50.8mm$ [13] 39

18 Jewell's reinterpretation of Stetson's diagram (a) Transition Location (b) Transition Reynolds Number (c) Transition Reynolds Number vs Nose Radius Reynolds Number [14, 12] 40

19 Computed second mode N-factor for Stetson's conditions [14] 41

20 Kennedy's enhanced Schlieren image (a) 0.508mm nosetip radius (b) 1.524mm nosetip radius (c) 2.54mm nosetip radius (d) 5.08mm nosetip radius [15] 42

21 Kennedy's Short Time Series Fourier Transform at $Re/m = 18.27 * 10^6$ (a) 2.54mm nosetip radius (b) 5.08mm nosetip radius [15] 42

22 Power spectra over Stetson et al.'s 7 degree half angle cone showing second mode and higher frequency nonlinear interaction band [16, 17] 43

23 Various forms of nonlinear frequency interactions (adapted from [18]) 45

24 Bicoherence over Kimmel and Kendall's cone at (a) station 36 (laminar boundary layer with instabilities) (b) station 37 (onset of boundary layer transition) [17] 48

25 Flared cone model (a) body contour profile (b) disassembled photo [19] 51

26 Flared cone model (a) computed N factor results for first (35 and 81 kHz) and second mode (higher frequencies) (b) experimental results showing only second mode [19] 52

Figure Page

27 Cone-ogive-cylinder model (a) sketch (b) tip contour profiles (c) disassembled photo [19] 54

28 Cone-ogive-cylinder predicted N factor for the 25 degree tip [19] 55

29 Surface power spectral density results (a) 30 degree tip results (b) 25 degree tip results [19] 56

30 Instability frequency independent of Reynolds number [19] 58

31 Instability frequency dependent on tip angle [19] 59

32 Instability pressure RMS amplitude vs axial location on the 30 deg tip model [19] 60

33 Mean flow solution normalized density contours over the 30 deg tip model [19] 60

34 Hot wire anemometer results over the 34 degree tip model (a) power spectral densities (c) signal coherence with surface mounted sensor [19] 61

35 Locations of maximum entropy layer instability magnitude above the model [19] 61

36 Hot wire measurements showing spectral broadening indicative of transition most likely caused by entropy layer instability [19] 62

37 Perspective render of the AFRL Ludwieg tube [20] 65

38 (a) Compressors (b) Vacuum Pumps [21] 67

39 AFRL Mach 6 Ludwieg tube driver tube [21] 68

40 AFRL Mach 6 Ludwieg tube test section [21] 70

41 AFRL Mach 6 Ludwieg tube vacuum tanks [21] 71

42 AFRL Mach 6 Ludwieg tube fast-action valve plug [21] 72

43 Initial design CFD results (a) Nozzle Mach number contours (b) steady exit Mach number profile (c) unsteady exit Mach number profile [20] 73

Figure Page

44 Mach number vs time at the nozzle exit [21] 74

45 Experimental pitot probe results 815mm downstream from nozzle exit (a) Mach contours (b) horizontal pitot rake results [21] 76

46 Initial pitot pressure fluctuations [20] 77

47 Pitot rake pressure fluctuations [21] 77

48 Tunnel stagnation pressure traces (a) actual psia trace (b) normalized pressure trace 79

49 Nominal driver tube pressure vs unit Reynolds number for both quasi-steady periods 82

50 Oddo's seven degree half angle sharp cone mounted in the AFRL Mach 6 Ludwieg tube [22] 83

51 Roughness distribution of Oddo's seven degree half angle sharp cone [22] 84

52 Diagram of Oddo's seven degree half angle sharp cone [22] 85

53 Rendering of Hill's ogive-cylinder model 87

54 Photo of cylindrical body with mounting adapter attached 88

55 Slice view with dimensions of the ogive-cylinder model 88

56 Sensor wires running out the back end of the model 89

57 Tip renders (a) 14 degree sharp (b) 28 degree sharp (c) 14 degree 1/4R blunted (d) 28 degree 1/4R blunted (e) 14 degree 1/2R blunted (f) 28 degree 1/2R blunted (g) 56 degree sharp (h) fully blunted 90

58 Shock curvature and entropy layer for (a) constant curvature ogive tip (b) non-constant curvature blunted ogive tip 93

59 Sharp ogive tips (a) 14 degree (b) 28 degree (c) 56 degree 94

60 Tangent ogive diagram 95

Figure Page

61 14, 28, and 56 degree sharp ogive tip contours 96

62 Blunted ogive tips (a) 14 degree ogives (sharp, 1/4R, 1/2R) (b) 28 degree ogives (sharp, 1/4R, 1/2R) (c) fully spherically blunted tip 97

63 Spherically blunted tangent ogive diagram 98

64 Blunted Tip Contours (sharp, 1/4R, 1/2R) (a) 14 degree ogives (b) 28 degree ogives 99

65 Unused 3/4R blunted ogive tips (a) 14 degree ogive (b) 28 degree ogive 100

66 Unused conical tips (a) 7 degree (b) 14 degree (c) 28 degree 100

67 (a) Rendering of model mounted on the test section sting (b) picture of the assembled model and sensors on the test section sting 102

68 Laser zeroing technique (a) laser sting mount (b) nozzle exit mirror (c) overall setup 104

69 Digital protractor angle of attack measurements (a) at the sting mount (b) at mid-length on the model 105

70 Kulite XCE-062-15A diagram [23] 106

71 Kulite XCE-062-15A power spectral density noise levels 107

72 PCB 132B38 diagram [24] 108

73 PCB signal background noise (a) prior to solution (b) after solution 109

74 Hypothetical hypersonic use case for FLDI [25] 110

75 Example LDI diagram 111

76 Example FLDI diagram 112

77 Current FLDI setup diagram 113

78 FLDI setup rails (a) emitting rail and optics (b) receiving rail and optics 114

Figure Page

79 Beam profile of the FLDI beams (a) 2D view the focal point (b) 3D view at the focal point (c) 2D view 3/4in forward (d) 2D view 3/4in rearward 115

80 FLDI pre-run noise compared to first and second quasi-steady period signals from example run 116

81 Schlieren setup diagram 118

82 Schlieren setup (a) emitting side (b) receiving side 120

83 Oddo Schlieren imaging window 121

84 Ogive-cylinder Schlieren imaging window diagram 121

85 Ogive-cylinder Schlieren imaging window with screws used for pixel scaling 122

86 Spatial frequency estimate used to determine most prominent wavelength 123

87 Cross-correlation between frames used to estimate wave propagation speed 124

88 Iterate across rows of x-pixels and frames to build time accurate average frequency content 125

89 Resulting outputs of the spatial to temporal frequency analysis 126

90 Example output of traditional temporal FFT using same data set 126

91 Schlieren images of boundary layer over Oddo's cone at nominal 300psia driver tube pressure(a) raw frame (b) background subtracted frame (c) average of 1000 background subtracted frames 129

92 Second mode instabilities over cone (a) $P_{DT} = 100psia$ (b) $P_{DT} = 150psia$ (c) $P_{DT} = 200psia$ (d) $P_{DT} = 250psia$ (e) $P_{DT} = 300psia$ 131

93 FLDI and Schlieren viewing window diagram 132

Figure Page

94 PSD comparison between FLDI and Schlieren (a) $P_{DT} = 150psia$ (b) $P_{DT} = 200psia$ (y-axis uses arbitrary units) 134

95 Traditional FFT PSD results from Schlieren vs height above cone normalized by boundary layer height (a) $P_{DT} = 150psia$ (b) $P_{DT} = 200psia$ 135

96 FLDI measurements with increasing driver tube pressure (the 100psia case shows a non-physical electrical noise peak) 136

97 Spatial to temporal frequency PSD over Oddo's cone vs normalized height above model (a) $P_{DT} = 100psia$ (b) $P_{DT} = 150psia$ (c) $P_{DT} = 200psia$ (d) $P_{DT} = 250psia$ (e) $P_{DT} = 300psia$ 137

98 Schlieren images of boundary layer over the ogive-cylinder (a) raw frame (b) background subtracted frame (c) average of 1000 background subtracted frames 140

99 Average boundary layer height Schlieren images at $P_{DT} = 125psia$ (a) 14 degree sharp ogive (b) 28 degree sharp ogive (c) 56 degree sharp ogive 142

100 Schlieren image of modal instabilities forming and breaking down within the upper and lower boundary layers over the body of the 14 degree sharp ogive-cylinder at $P_{DT} = 100psia$ 143

101 Boundary layer instabilities for the 14 degree sharp ogive tip (a) $P_{DT} = 75psia$ (b) $P_{DT} = 100psia$ (c) $P_{DT} = 125psia$ (d) $P_{DT} = 150psia$ 144

102 Boundary layer instabilities for the 28 degree sharp ogive tip (a) $P_{DT} = 75psia$ (b) $P_{DT} = 100psia$ (c) $P_{DT} = 125psia$ (d) $P_{DT} = 150psia$ 145

103 Schlieren above the 56 degree sharp ogive tip (a) $P_{DT} = 75psia$ (b) $P_{DT} = 150psia$ (c) $P_{DT} = 250psia$ 146

104 Instabilities observed over 1/4R blunted ogives (a) 14 degree ogive with 1/4R bluntness at $P_{DT} = 200psia$ (b) 28 degree ogive with 1/4R bluntness at $P_{DT} = 250psia$ 147

Figure Page

105 Schlieren over 1/2R blunted ogives and the fully blunted tip (a) 14 degree ogive with 1/2R bluntness at $P_{DT} = 250psia$ (b) 28 degree ogive with 1/2R bluntness at $P_{DT} = 250psia$ (c) fully spherically blunted tip at $P_{DT} = 200psia$ 148

106 PSD of Schlieren over the 14 degree sharp ogive (a) $P_{DT} = 75psia$ (b) $P_{DT} = 100psia$ (c) $P_{DT} = 125psia$ (d) $P_{DT} = 150psia$ 149

107 PSD of Schlieren over the 28 degree sharp ogive (a) $P_{DT} = 75psia$ (b) $P_{DT} = 100psia$ (c) $P_{DT} = 125psia$ (d) $P_{DT} = 150psia$ 150

108 PSD of Schlieren over the 56 degree sharp ogive (a) $P_{DT} = 100psia$ (b) $P_{DT} = 125psia$ (c) $P_{DT} = 150psia$ (d) $P_{DT} = 200psia$ (e) $P_{DT} = 250psia$ 151

109 PSD of Schlieren over the blunted ogives (a) 14 degree ogive with 1/4R bluntness at $P_{DT} = 200psia$ (b) 14 degree ogive with 1/2R bluntness at $P_{DT} = 250psia$ (c) 28 degree ogive with 1/4R bluntness at $P_{DT} = 250psia$ (d) 28 degree ogive with 1/2R bluntness at $P_{DT} = 250psia$ (e) fully spherically blunted tip at $P_{DT} = 200psia$ 152

110 Spatial to temporal PSD of Schlieren over the 14 degree sharp ogive (a) $P_{DT} = 75psia$ (b) $P_{DT} = 100psia$ (c) $P_{DT} = 125psia$ (d) $P_{DT} = 150psia$ 154

111 Wave structure observed in Schlieren and the corresponding spatial to temporal PSD for the 14 degree ogive-cylinder at $P_{DT} = 125psia$ (a) low frequency elongated, flat structure (b) high frequency rope-like structure (c) low frequency PSD (d) high frequency PSD 155

112 Wave structure observed in Schlieren and the corresponding spatial to temporal PSD for the 28 degree ogive-cylinder at $P_{DT} = 100psia$ (a) instability structure (b) instability PSD 156

113 Spatial to temporal PSD of Schlieren over the 28 degree sharp ogive (a) $P_{DT} = 75psia$ (b) $P_{DT} = 100psia$ (c) $P_{DT} = 125psia$ (d) $P_{DT} = 150psia$ 157

Figure Page

114 Elongated wave exhibiting nonlinear interaction and breakdown over the 28 degree sharp ogive at $P_{DT} = 100psia$ (a) $t = 0\mu s$ (b) $t = 17.9\mu s$ (c) $t = 35.7\mu s$ (d) $t = 53.7\mu s$ (e) $t = 71.4\mu s$ (f) $t = 89.3\mu s$ 158

115 Spatial to temporal PSD of Schlieren over the 56 degree sharp ogive (a) $P_{DT} = 100psia$ (b) $P_{DT} = 125psia$ (c) $P_{DT} = 150psia$ (d) $P_{DT} = 200psia$ (e) $P_{DT} = 250psia$ 160

116 Normalized spatial to temporal PSD of Schlieren over the 14 degree sharp ogive for entire frame height at (a) $P_{DT} = 75psia$ (b) $P_{DT} = 100psia$ (c) $P_{DT} = 125psia$ (d) $P_{DT} = 150psia$ 161

117 Normalized spatial to temporal PSD of Schlieren over the 28 degree sharp ogive for entire frame height at (a) $P_{DT} = 75psia$ (b) $P_{DT} = 100psia$ (c) $P_{DT} = 125psia$ (d) $P_{DT} = 150psia$ 162

118 Normalized spatial to temporal PSD of Schlieren over the 56 degree sharp ogive for entire frame height at (a) $P_{DT} = 100psia$ (b) $P_{DT} = 125psia$ (c) $P_{DT} = 150psia$ (d) $P_{DT} = 200psia$ (e) $P_{DT} = 250psia$ 163

119 Normalized spatial to temporal PSD of Schlieren over the bluinted ogives for entire frame height (a) 14 degree ogive with 1/4R at $P_{DT} = 200psia$ (b) 14 degree ogive with 1/2R at $P_{DT} = 250psia$ (c) 28 degree ogive with 1/4R at $P_{DT} = 200psia$ (d) 28 degree ogive with 1/2R at $P_{DT} = 250psia$ (e) fully spherically blunted tip at $P_{DT} = 200psia$ 165

120 Schlieren images and spatial to temporal frequency analysis of entropy layer instability above the 28 degree ogive with 1/2R bluntness at $P_{DT} = 250psia$ (a) frame 1 at $t = 0\mu s$ (b) frame 2 at $t = 8.9\mu s$ (c) frame 3 at $t = 17.9\mu s$ (d) spatial to temporal FFT PSD of all shown frames 166

121 Schlieren images and spatial to temporal frequency analysis of entropy layer instability above the 56 degree sharp ogive at $P_{DT} = 200psia$ (a) frame 1 at $t = 0\mu s$ (b) frame 2 at $t = 8.9\mu s$ (c) frame 3 at $t = 17.9\mu s$ (d) spatial to temporal FFT PSD of all shown frames 167

Figure Page

122 FLDI and Schlieren viewing window diagram for the ogive-cylinder 168

123 FLDI PSD vs normalized height above the 14 degree ogive model at the PCB3 location and $P_{DT} = 100psia$ (a) and (b) first quasi-steady period peak frequencies vs height (c) and (d) second quasi-steady period peak frequencies vs height 169

124 FLDI PSD vs normalized height above the 14 degree ogive model at the PCB4 location and $P_{DT} = 100psia$ (a) and (b) first quasi-steady period peak frequencies vs height (c) and (d) second quasi-steady period peak frequencies vs height 171

125 Shift in FLDI PSD peak frequency between $P_{DT} = 75$ and $P_{DT} = 100$ for the 14 degree sharp ogive 172

126 FLDI PSD vs normalized height above the 28 degree ogive model at the PCB3 location and $P_{DT} = 125psia$ (a) first quasi-steady period peak frequencies vs height (b) second quasi-steady period peak frequencies vs height 173

127 FLDI PSD vs normalized height above the 28 degree ogive model at the PCB4 location and $P_{DT} = 125psia$ (a) and (b) first quasi-steady period peak frequencies vs height (c) and (d) second quasi-steady period peak frequencies vs height 174

128 FLDI PSD at 4mm above PCB3 for the 56 degree sharp ogive, 14 degree and 28 degree ogives with 1/4R and 1/2R bluntness, and the fully blunted tip at $P_{DT} = 125psia$ and $P_{DT} = 200psia$ 175

129 Comparison of instability waves in the boundary layer relative to the FLDI focal points (a) Oddo's cone second mode instability (b) 14 degree sharp ogive second mode instability (c) 28 degree sharp ogive low frequency instability 176

130 Examples of FLDI traces (y-axis) vs time (x-axis) (a) Oddo's cone (b) 14 degree sharp ogive (c) 28 degree sharp ogive 178

Figure Page

131 PSDs at each run condition for the Kulites down the length of the 14 degree sharp ogive sampled during second quasi-steady periods (a) $P_{DT} = 75psia$ (b) $P_{DT} = 100psia$ (c) $P_{DT} = 125psia$ (d) $P_{DT} = 150psia$ (note: the ≈75kHz spike is electrical noise) 180

132 PSDs of each Kulite sensor at various driver tube pressures over the 14 degree sharp ogive sampled during second quasi-steady period (a) Kulite 2 (b) Kulite 3 (c) Kulite 4 (d) Kulite 5 (e) Kulite 6 (note: the ≈75kHz spike is electrical noise) 181

133 PSDs at each run condition for the Kulites down the length of the 28 degree sharp ogive sampled during second quasi-steady periods (a) $P_{DT} = 75psia$ (b) $P_{DT} = 100psia$ (c) $P_{DT} = 125psia$ (d) $P_{DT} = 150psia$ (note: the ≈65-75kHz spike is electrical noise) 182

134 PSDs of each Kulite sensor at various driver tube pressures over the 28 degree sharp ogive sampled during second quasi-steady periods (a) Kulite 2 (b) Kulite 3 (c) Kulite 4 (d) Kulite 5 (e) Kulite 6 (note: the ≈75kHz spike is electrical noise) 184

135 PSDs at each run condition for the Kulites down the length of the 56 degree sharp ogive sampled during second quasi-steady periods (a) $P_{DT} = 75psia$ (b) $P_{DT} = 100psia$ (c) $P_{DT} = 125psia$ (d) $P_{DT} = 150psia$ (e) $P_{DT} = 200psia$ (f) $P_{DT} = 250psia$ (note: the ≈65-75kHz spike is electrical noise) 185

136 PSDs of each Kulite sensor at various driver tube pressures over the 56 degree sharp ogive sampled during second quasi-steady periods (a) Kulite 2 (b) Kulite 3 (c) Kulite 4 (d) Kulite 5 (e) Kulite 6 (note: the ≈65-75kHz spike is electrical noise) 186

137 PSDs at each run condition for the PCBs down the length of the 14 degree sharp ogive of second quasi-steady periods (a) $P_{DT} = 75psia$ (a) $P_{DT} = 100psia$ (a) $P_{DT} = 125psia$ (a) $P_{DT} = 150psia$ (note: the ≈150kHz spike and other higher frequency spikes are electrical noise) 187

Figure Page

138 PSDs of each PCB sensor at various driver tube pressures over the 14 degree sharp ogive sampled during second quasi-steady periods (a) PCB 1 (b) PCB 2 (c) PCB 3 (d) PCB 4 (e) PCB 5 (f) PCB 6 (note: the ≈150kHz spike and other higher frequency spikes are electrical noise) 189

139 Bicoherence of the PCB traces for the 14 degree sharp ogive at a driver tube pressure of 100psia (a) PCB2 (b) PCB3 (c) PCB4 (d) PCB5 (note: the ≈150kHz spike and other higher frequency spikes are electrical noise) 190

140 PSDs of each PCB sensor at various driver tube pressures over the 28 degree sharp ogive sampled during second quasi-steady periods (a) PCB 1 (b) PCB 2 (c) PCB 3 (d) PCB 4 (e) PCB 5 (f) PCB 6 191

141 Bicoherence of the PCB traces for the 28 degree sharp ogive at a driver tube pressure of 100psia (a) PCB3 (b) PCB4 (c) PCB5 (d) PCB6 192

142 PSDs of each PCB sensor at various driver tube pressures over the 56 degree sharp ogive sampled during second quasi-steady periods (a) PCB 1 (b) PCB 2 (c) PCB 3 (d) PCB 4 (e) PCB 5 (f) PCB 6 194

143 PCB PSD vs driver tube pressure over the 14 degree 1/4R blunted ogive sampled during second quasi-steady periods (a) PCB 1 (b) PCB 2 (c) PCB 3 (d) PCB 4 (e) PCB 5 (f) PCB 6 195

144 PCB PSD vs driver tube pressure over the 14 degree 1/2R blunted ogive sampled during second quasi-steady periods (a) PCB 1 (b) PCB 2 (c) PCB 3 (d) PCB 4 (e) PCB 5 (f) PCB 6 196

145 PCB PSD vs driver tube pressure over the 28 degree 1/4R blunted ogive sampled during second quasi-steady periods (a) PCB 1 (b) PCB 2 (c) PCB 3 (d) PCB 4 (e) PCB 5 (f) PCB 6 198

146 Bicoherence of the PCB traces for run 83 (a) PCB4 (b) PCB5 (c) PCB6 199

Figure Page

147 PCB PSD vs driver tube pressure over the 28 degree 1/2R blunted ogive sampled during second quasi-steady periods (a) PCB 1 (b) PCB 2 (c) PCB 3 (d) PCB 4 (e) PCB 5 (f) PCB 6 200

148 PCB PSD vs driver tube pressure over the spherically blunted tip sampled during second quasi-steady periods (a) PCB 1 (b) PCB 2 (c) PCB 3 (d) PCB 4 (e) PCB 5 (f) PCB 6 201

149 Example of transition onset and turbulence in the frequency domain 202

150 14, 28, and 56 degree sharp ogives transition Reynolds number vs freestream unit Reynolds number 203

151 Example of apparent transition reversal observed in the frequency spectra 203

152 Transition Reynolds number vs freestream unit Reynolds number for the (a) 14 degree ogive variants (b) 28 degree ogive variants 204

153 Example of earlier onset of transition over the 28 degree ogive curvature than the 14 degree ogive curvature variant for the same tip bluntness of 1/4 base radius 205

154 Transition Reynolds numbers of the blunted 14 and 28 degree ogives 206

155 Transition Reynolds numbers for all ogive-cylinder variants tested 207

156 Transition Reynolds numbers versus nose radius Reynolds number for all ogive-cylinder variants tested 208

157 Transition Reynolds numbers versus ogive radius Reynolds number for all ogive-cylinder variants tested 209

158 Generic diagram of curvature for a given curve 210

159 Curvature Reynolds number versus transition Reynolds number 212

160 14 degree sharp ogive nose example contours 224

List of Tables

Table		Page
1	Comparison of predicted and experimental second Mack mode instabilities over the flared cone [19]	53
2	Cone-ogive-cylinder predicted N factor table for the various tips [19]	55
3	30 degree tip experimental results compared to predicted frequencies [19]	57
4	Nominal Run Conditions	82
5	Schlieren setup components	118
6	Oddo Schlieren imaging specs	119
7	Ogive-cylinder Schlieren imaging specs	121
8	Boundary layer heights determined from Schlieren for Oddo's cone at various driver tube pressures	130
9	Estimated wavelengths and wave propagation speeds over Oddo's cone	138
10	Boundary layer heights determined from Schlieren	141
11	Run conditions part 1	220
12	Run conditions part 2	221
13	Run conditions part 3	222
14	FLDI components list	223
15	Nose Geometry Equations	224

EXPERIMENTAL MEASUREMENTS OF HYPERSONIC INSTABILITIES OVER OGIVE-CYLINDERS AT MACH 6

I. Introduction

The field of hypersonic boundary layer instabilities and transition is one of the most enigmatic and complexing topics in fluid mechanics that is currently challenging the hypersonic research community. Without a firm understanding of the underlying mechanisms that drive boundary layer transition, hypersonic system designers are left ill-equipped to make engineering level decisions for their systems. The desire to understand the underlying mechanisms that cause boundary layer instabilities to form, amplify, and breakdown into turbulence have pushed the aerospace community to pioneer new experimental and computational methods. The current high tempo pace of the hypersonic research field has led to many new innovations and a growing interest in understanding the flow phenomena that dominate the regime.

One such flow phenomena that has plagued the hypersonic instability and transition community for the last half century is the blunt cone transition reversal phenomenon. When cones are placed at zero angle of attack in hypersonic flows and their nosetip is progressively blunted, a delay in transition is observed that scales with the amount of bluntness. This behavior holds true to a certain critical bluntness at which point the delay in transition is halted and the transition location on the cone rapidly moves forward as more bluntness is added. This reversal in transition is not well understood by the instability research community and has left many researchers speculating what could be the primary cause of the behavior. A possible explanation to this phenomenon is the presence of an entropy layer instability that is introduced

by adding bluntness to the tip of hypersonic geometries.

Recent research with a meter long cone-ogive-cylinder geometry with variable nose tip angles in the Purdue Mach 6 quiet tunnel uncovered the presence of a possible entropy layer instability in the region above the boundary layer over the body of the geometry. These instabilities were measured above the surface of the model using hot-wire anemometers and were traced to being the primary cause for transition over the model [19]. While this ogive-cylinder geometry is not the traditional conical geometry that is often used in fundamental hypersonic instability research, it does possess unique qualities that make it an interesting geometry for further work.

To address the need for further understanding of instabilities over ogive-cylinder geometries and how they relate to other geometries (such as blunt cones), this study uses a new ogive-cylinder model to perform a series of hypersonic instability and transition experiments. The ultimate goal of this study is to expand the hypersonic research community's understanding of the flow phenomena surrounding the ogive-cylinder geometry and the effect of nose geometry on the measured instabilities. Both surface and off surface measurements are collected using Schlieren imaging, focused laser differential interferometry (FLDI), and pressure sensors a meter long ogive-cylinder geometry in the Air Force Research Laboratory Mach 6 Ludwieg tube in an effort to obtain this goal.

II. Review of Literature

Across the high speed aerodynamics community there is a research effort to explore and quantify the fundamental phenomena leading to hypersonic boundary layer instabilities and transition. This literature review will provide insight into the history behind boundary layer instability research and the developments made to explore the hypersonic transition regime. In particular, the deviation of stability theory and experimental data on the prediction of lengthwise transition location for hypersonic vehicles with various nose bluntness will be explored.

While there is a vast amount of literature relating to this field of study, the complex nature of the underlying phenomena means that a carefully constructed compilation of previous work is necessary. Section 2.1 begins the review with a brief historical overview of the progression of boundary layer instability research over the past century, setting the context for this research. The sections that follow this historical overview provide more in-depth technical reviews of the various aspects of boundary layer transition research and hypersonics. Section 2.2 begins these technical reviews by delving into the six unique characteristics that distinguish hypersonic flight from the other flight regimes. Section 2.3 follows by explaining the processes by which a laminar boundary layer develops instabilities and transitions to turbulence. With the basics of the hypersonic regime and boundary layer transition established, Section 2.4 combines the two subjects by looking into the instability modes and mechanisms that are dominant in hypersonic boundary layers and cause disturbances to propagate and break down into turbulence. Finally, combining all of the theory and technical breakdown of hypersonic instability mechanisms, Section 2.5 provides an in-depth look at the experiments conducted at Purdue's Mach 6 Quiet Tunnel and how these experiments influenced this author's choice of experiments for this current study.

2.1 Brief History of Boundary Layer Instability Research

The desire to understand and quantify the transition of a boundary layer from lamiunar to turbulent has inspired aerodynamicists for well over a century. The advent of modern boundary layer transition research is often attributed to the works of Lord Rayleigh and Osbourne Reynolds. Rayleigh produced a series papers in the late 1800s and early 1900s providing the first notable analytical results indicating the presence of inviscid flow instabilities. One of the most important findings of Rayleigh was his criterion for inviscid instability which states that a point of inflection must exist in a flow profile for it to be inviscidly unstable [26]. Alongside Rayleigh's works, the research of Reynolds provided some of the earliest characterizations of flow instability. His 1895 paper proposed the use of the now famous Reynolds number relating inertial to viscous effects as a primary factor in determining transition location for various flow geometries [27].

While Rayleigh's and Reynolds's derivations and findings greatly increased the community's understanding of inviscid and viscous instability effects, the assumptions they utilized limited the scope of application and so little progress was made towards understanding the whole story of why transition occurs. The independent works of Taylor in 1915 and Prandtl in 1921 further demonstrated the destabilizing effects of viscosity on otherwise stable flow and helped to fill in much of what Reynolds and Rayleigh derived, but still no experimental data supporting the theory was existent [28, 29].

With reasonable evidence pointing towards the presence of inviscid and viscous instability effects, the field of boundary layer instability analysis began to pick up momentum. In the 1930s, Tollmien and Schlichting published a series of findings in which they were able to analytically derive the structure of low speed boundary layer instabilities. These unstable structures are commonly referred to as Tollmien-

Schlichting (TS) waves. An in depth discussion of the structure of TS waves will be provided in Section 2.3. Tollmien and Schlichting's works are attributed with being one of the earliest applications of stability theory for transition prediction and were groundbreaking for their time [30, 31, 32, 33, 34, 35].

Despite the apparent successes of Tollmien and Schlichting, many experimentalists disputed their claims for the next decade as the instrumentation and experimental techniques of the time were incapable of measuring these predicted TS waves. The drastic need for accurate transition prediction and verification methods become evident in the late 1930s as World War II began and aircraft began pushing the limits of aerodynamic design. The research by Germany's Schubauer and Skramstad's research team in the early 1940s is a prime example of how valuable the prediction of transition was considered. Schubauer and Skramstad's research during the war is the first documented case of experimental measurements of sinusoidal velocity fluctuations in a boundary layer, but due to wartime restrictions, their findings were not published until 1947 [7]. They took these measurements using hot-wire anemometers on the surface of a flat plate in a low-noise tunnel and successfully demonstrated that the data matched the predicted structure and frequency of TS waves. Schubauer and Skramstad were able to achieve tunnel turbulence levels below 0.1 percent, establishing the importance of proper characterization of tunnel noise/disturbance conditions for instability experiments [36].

With Schubauer and Skramstad's experimental verification of Tollmien and Schlichting's theory, the concept of coupling boundary layer stability theory with experimental verification quickly grew in popularity. This expanded use of stability theory proved important moving into the mid-1900s as flight began to reach transonic and supersonic speeds. Mack's publication of the Boundary Layer Linear Stability Theory AGARD Report in 1984 proved to be a significant shift forward in the transition prediction

community as a unified method was developed for predicting compressible subsonic and supersonic regime boundary layer instabilities. While Mack's contributions to the boundary layer stability community from the 1960s through the 1980s were already being implemented into the research field by the time of his AGARD report, this publication compiled all of the notable research findings in boundary layer stability theory that were completed prior and established the standards for how the different methodologies were interconnected. As a result, Mack defined the basis for modern incompressible, compressible, inviscid, viscous, and three-dimensional linear stability theories [7]. Mack's work also established/legitimized many of the methods that are still used today to quantify instability characteristics and growth such as the e^N method and N-factors which were developed in detail in Jaffe, Okamura, and Smith's report in 1970 [37]. Mack's report forms the basis of what is known as Linear Stability Theory (LST) and is discussed in further depth in Section 2.4.1.

Another notable result summarized in Mack's report was his discovery of higher order, two-dimensional instability modes that are present during supersonic and hypersonic flight. These higher order instability modes are now referred to as the "Mack modes." The exact nature of these modes are explained in depth in Section 2.4.1, but the reader should note that there are a variety of modes that are strongly dependent on Mach number and flow conditions to determine which is most dominant. The second Mack mode is of prime importance in hypersonic flows over conical bodies around Mach six which matches the conditions used in experiments of this thesis. More specifics on the nature and structure of the Mack modes and other hypersonic instabilities are explored in Section 2.4. For further information and specific details on the nature of the research at the time, the reader is encouraged to read Section 1.1 of Mack's report which provides his perspective and historical background on boundary layer transition research that led up to his LST paper [7].

With the foundation laid by Mack and the Cold War space race in full swing, the 1980s saw a surge in research related to understanding the intricacies of boundary layer transition in hypersonic flight. Launch and re-entry velocities during space missions can easily reach Mach numbers exceeding 10 to 25 [38]. The first instance of a recorded hypersonic flight was in 1949 when the United States tested a modified V-2 rocket's upper stage and reached Mach 6.7 before burning up during re-entry [39]. The programs of the 1950s and 1960s that led to the landing on the moon, such as the X-15 hypersonic plane program, all worked to further the fields understanding of hypersonic flight, but little progress was made in understanding the specific phenomena that drove boundary layer transition at these velocities. As an example, Figure 1 demonstrates this lack of transition prediction capability for the X-15 [1].

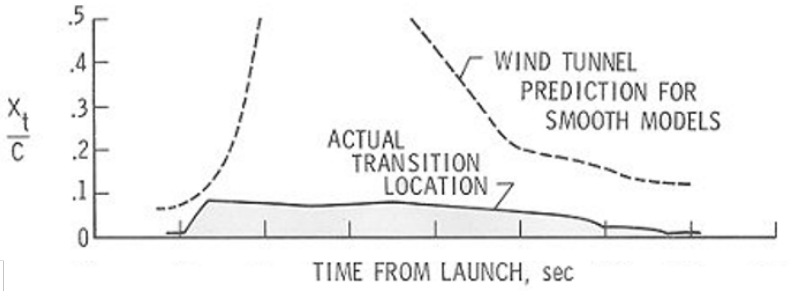


Figure 1. X-15 Boundary Layer Transition Location During Wind Tunnel Testing vs During Flight Testing [1]

To overcome unreliable transition prediction, thermal protection systems (TPS), structural components, and control systems were often overdesigned to handle the "worst case scenario" loads of transitional/fully-turbulent flows over a majority of the vehicles. The challenging flight environment and trajectory profiles of hypersonic vehicles leads to their designs incorporating highly coupled flight systems. The importance of transition prediction on overall system design is made most evident in the Defense Science Board's National Aerospace Plane (NASP) Review of 1988:

Estimates [of transition] range from 20% to 80% along the body ... The estimate made for the point of transition can affect the design vehicle gross take off weight by a factor of two or more. [40]

This method of over designing hypersonic systems to ensure mission success worked well for the early space programs, but as more complicated and ambitious systems such as the shuttle program and NASP emerged in 1980s, a need for a better understanding of hypersonic transition was needed to allow for system optimization. This need led to the works documented by Kendall, Demetriades, and Stetson from the 1970s through the 1990s [41, 42, 43]. All three researchers were experimentalists performing research in parallel to Mack and other analytical researchers to design, perform, and analytically validate experiments at hypersonic velocities with the specific intent of furthering the community's understanding of hypersonic boundary layer instabilities and transition mechanisms. Kendall's 1975 publication was the first paper to experimentally verify the presence of the second Mack mode in hypersonic boundary layers and that these disturbances were the most dominant instability [41]. Demetriades's publication in 1978 confirmed the findings of Kendall, but his research in the early 1970s established many of the standards for performing hypersonic stability research using slender cones that were used by the community moving forward [42, 43].

Stetson built on Demetriades's stability experiment methods to become the most prominent researcher in the field of hypersonic boundary layer transition over conical bodies in the 1970s through the 1990s. Stetson's reports are still considered the standard for hypersonic transition research [44, 45, 46]. In particular, Stetson's research into nosetip bluntness effects on conical hypersonic bodies revealed many intricacies of hypersonic boundary layer instability phenomena and left many questions for the community to answer that are still being actively investigated. One of the most prominent results from Stetson's research was his finding of the nosetip bluntness in-

stability reversal phenomenon. In short, his research revealed that blunting the nose of a conical body delays second mode instability effects and effectively increases the transition Reynolds number, but at some critical nose bluntness this effect reverses and transition moves back upstream [12, 47, 48]. To this day, the exact reasons for why this behavior occurs is still unknown and thus is one of the primary factors driving the research in this thesis [49]. A photograph of Stetson's iconic work in the Arnold Engineering Development Center's (AEDC) Tunnel B is shown in Figure 2 where many of his findings were made. More specifics on this transition reversal phenomenon and the effect of nose bluntness on transition will be discussed in Section 2.4.2.

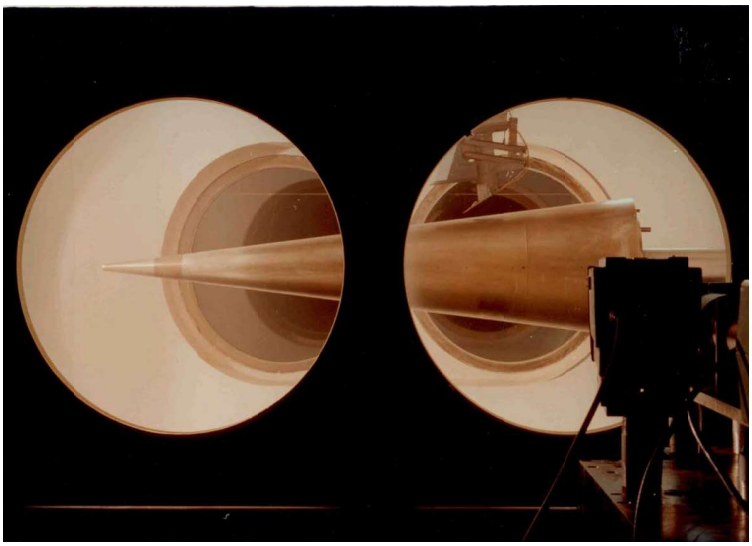


Figure 2. Stetson's Iconic 7° Cone in AEDC Tunnel B [2]

While the 1990s saw great progress in hypersonic instability research, the transition community as a whole saw a large jump forward in analytical methods with introduction of the parabolized stability equations (PSE) that were summarized in a review article by Herbert in 1997. With a similar basis to that of Mack's LST method, PSE introduces a more flexible approach to stability theory that allows it

to be used alongside direct numerical simulation solutions to resolve highly accurate linear and non-linear instability predictions [50].

After PSE's introduction, the field of instability research for hypersonic applications saw a reduction of interest directly tied to the end of the Cold War and a decreasing national interest in hypersonics. By the official conclusion of the US shuttle program in 2011, the hypersonic instability community in the US was reduced to an even more intimate number of research facilities and university laboratories. Only recently has the US hypersonic program seen a resurgence in growth and thus the problems surrounding hypersonic boundary layer instabilities and transition are back at the forefront of research efforts. The recent development of the input-output stability analysis at the University of Minnesota is proving that there are new methods for instability prediction that have direct applications for the complex, often non-linear, and coupled interactions of hypersonic boundary layer instabilities [51].

Beyond the introduction of input-output numerical instability capabilities, recent developments in wind tunnel research of hypersonic boundary layer instabilities have proven promising as well. The development of high frequency surface mounted pressure transducers are now capable of accurately capturing the high frequencies associated with hypersonic instabilities. An expansion of non-intrusive techniques has also occurred in recent years such as the advent of modern focused laser differential interferometry (FLDI) and high speed cameras capable of capturing hypersonic flow features. These techniques are offering new ways for the experimental community to work alongside the computational/analytical community to verify and observe predicted transition and instability behaviors. Details on modern techniques utilized in this study will be provided in Chapter III.

It is obvious that the rich history of hypersonic instability and transition research is still relevant to progressing the field today. With a brief qualitative understanding

of the history behind this field now covered, a more technical deep dive into the various aspects of hypersonic instabilities is now required. The following sections provide insight into the intricacies of hypersonic flight and transition phenomena.

2.2 Hypersonic Regime Characteristics

In order to move forward with the technical discussion, a more refined understanding of what exactly being "hypersonic" means. The hypersonic flight regime is often nebulous to those not intimately familiar with the regime's defining traits. Commonly simplified to Mach five or greater speeds, the hypersonic regime is actually defined by a variety of unique aerodynamics characteristics that distinguish it from the subsonic and supersonic regimes and not simply defined by a Mach threshold. In general, five primary characteristics of hypersonic flight are typically used to characterize the hypersonic regime: 1) thin shock layers, 2) high viscous interactions, 3) high temperatures, 4) low densities, 5) entropy layers. The following subsections will provide details to each of these unique characteristics. Particular attention will be made in the Section 2.2.2 where entropy layers are discussed since these are most relevant to the research performed for this thesis.

2.2.1 Thin Shock Layers.

As a body flies through the atmosphere at a speed faster than the speed of sound, a shock forms at the leading edge of the body. For a given wedge body deflection angle, the shock angle of the flow over the body decreases as the Mach number increases. It should also be noted that the three-dimensional nature of conical bodies allows for shallower shock angles than wedges at equivalent half angle and Mach number. This differenc in shock angle is caused by the conical body having a "three-dimensional relieving effect" that allows the pressure of the shock layer to be relieved behind the

shock more efficiently [38].

Continuing to follow the principles of oblique shock theory, as Mach number continues to increase for a given deflection angle and the shock angle becomes shallower, the density increase across the shock also increases. This means that at hypersonic velocities, a higher mass flow can pass through a smaller region after the shock than in lower velocity cases. The flowfield between the shock and the body is known as the shock layer. In hypersonic flight, the principles of oblique shock theory means that the shock layer is very thin [38].

As a result of the thin shock layers in hypersonic flows, a variety of complex interactions occur. One such interaction is between the shock and the thick, viscous boundary layer on the body. This viscous interaction with the shock is most prevalent in lower Reynolds number scenarios, but as the Reynolds number increases, the thin shock actually allows for simplified models such as Newtonian theory to be used to compute flow calculations around the body [52, 53]. A discussion of the viscous effects associated with hypersonic flows will be discussed in Section 2.2.3.

2.2.2 Entropy Layers.

The second prominent feature of hypersonic flows is the presence of an entropy layer and is of particular interest for this study. The entropy layer is most prominent for blunted bodies in hypersonic flows, but can also be present if a sharp body creates a warped shock. In short, as a streamline crosses a shock in a supersonic or hypersonic flow, the process of crossing the shock is irreversible. This irreversibility is non-isentropic and means that the shock serves as a source of entropy generation for a given streamline. The increase of a given streamline's entropy level past the shock is proportional to the strength and obliqueness of the shock being passed through [3]. Given a blunted cone geometry in supersonic flow with uniform entropy distribution, a

bow shock forms at some standoff distance from the tip of the cone. Figure 3 depicts a blunt cone in high Mach flow. Streamline a crosses the shock and stagnates on the nosetip of the body. This stagnation streamline encounters a strong, near-normal shock which causes the entropy increase across the shock to be highest of the incoming flow. On the other hand, streamlines b and c approach the bow shock with increasing distance away from the leading edge and thus encounter weaker, more oblique shocks with decreasing entropy increase across the shock. Since the streamlines each see a slightly weaker shock further away from the nosetip, a gradient in entropy develops behind the shock. This region of entropy gradient is known as the entropy layer [52].

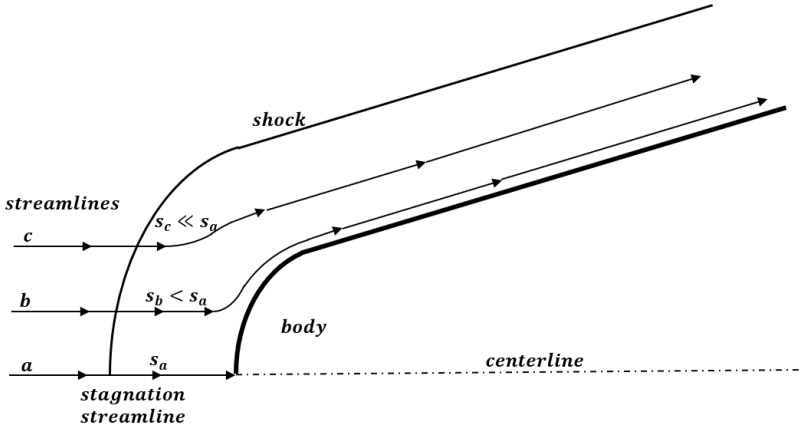


Figure 3. Streamline Entropy Gradient (Adapted from [3])

For hypersonic bodies with blunt nosetips, the bow shocks that form are no longer uniform in curvature like those formed under lower supersonic conditions. Instead, hypersonic bow shocks "bend" with downstream distance to create a warped shock with increased curvature. The higher the Mach number, the more accentuated this effect becomes and the closer the curvature of the shock follows the bodyline of the vehicle [3]. This shock warping versus Mach number effect is demonstrated in Figure 4. The highly warped shocks of higher Mach numbers amplify the effects of the entropy layer phenomenon and creates regions of very high entropy gradient in the

entropy layer.

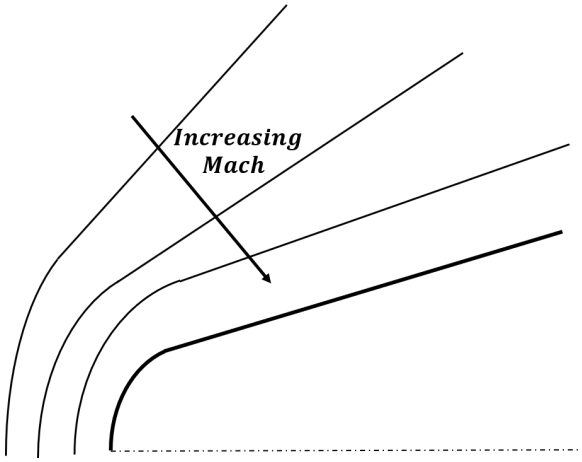


Figure 4. Shock Curvature with Increasing Freestram Mach Number

Bow shocks reach a point in their curvature where the shock is approximately linear far away from the nosetip portion of the shock structure. The entropy layer is bounded by the streamline that crosses the shock at the beginning of this linear region. Figure 5 depicts this entropy layer edge streamline. The region below this entropy edge streamline has positive entropy gradient while the region above this streamline has approximately zero entropy gradient. As the entropy layer convects downstream, the growing boundary layer along the body eventually overtakes the entropy edge streamline. The distance from the body leading edge at which this occurs is known as the entropy layer swallowing length and is depicted in Figure 5 as x_{sw} [12].

The exact effects of the entropy layer have long evaded the aerodynamics community, but a few phenomena have been analytically derived and experimentally observed. Via Crocco's theorem, $v \times \omega = \nabla H_0 - T\nabla S$, where v is the flow velocity vector, ω is vorticity, H_0 is stagnation enthalpy, T is flow temperature, and S is entropy, it is understood that the presence of an entropy gradient results in the vorticity within the entropy layer that is proportional in strength to that of the entropy gradi-

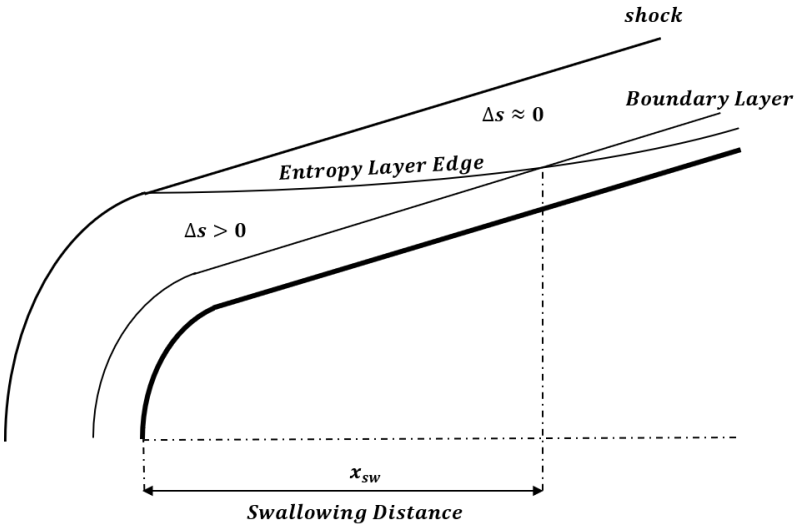


Figure 5. Entropy Layer Swallowing Effect (Adapted from [4])

ent [54]. This vorticity has been shown analytically to modulate the density gradient within the boundary layer and resultingly dampen the effects of second mode instability growth on blunt cones [55]. Experiments have verified this instability damping effect of entropy layers on blunt geometries [47, 49]. More specifics of this second mode damping effect of the entropy layer are explored in Section 2.4.

2.2.3 High Viscous Interactions.

In the same way that a large entropy gradient is formed in hypersonic flows due to the high Mach numbers, near body effects due to viscosity are amplified under hypersonic conditions. As high velocity, hypersonic flows are decelerated near the vehicle body, the large kinetic energy of the flow is largely converted through friction to internal energy via a process known as viscous dissipation. This increase in internal energy manifests itself as a increased skew in the boundary layer temperature profile which can affect flow stability and behavior [52].

Hypersonic boundary layer characteristics tend to be dominated by this increased temperature profile. This influence of temperature on the boundary layer is made

evident by an increased boundary layer thickness than in lower velocity flows. This thicker boundary layer effect may seem counter intuitive, but two primary factors driven by temperature drive the phenomenon. First, viscosity coefficient for a gas increases with temperature, thus causing the boundary layer to grow faster than at lower temperatures. Second, since a boundary layer maintains constant pressure, p through its thickness, an increase in temperature, T results in a drop in density, ρ via $\rho = p/RT$ where R is the specific gas constant. To maintain mass flow through the boundary layer with this reduced density means that the boundary layer must be larger. Combining the viscous coefficient and density effects results in the boundary layer in hypersonic flows being thicker than in lower Mach conditions [52].

As a result of viscous dissipation increasing the boundary layer thickness, viscous effects begin to influence the inviscid flow outside the boundary layer by creating a larger "effective body shape." This interaction of the boundary layer on the inviscid flow contours in turn results in invsicd flow affecting downstream boundary layer characteristics. This back-and-forth relationship between the boundary layer and the outer inviscid flow is known as viscous interaction. The viscous interaction effect has impact on surface pressure distributions, skin friction, and heat transfer which results in a dramatic influence on hypersonic vehicle lift, drag, stability, and thermal loading.

Another viscous interaction can occur if the shock layer lies close enough to the vehicle body while the boundary layer grows enough to create a "merged shock layer" as is shown in Figure 6 In this scenario, the conventional boundary layer analysis is no longer valid and the shock layer must be treated as fully viscous.

2.2.4 High Temperatures.

Directly related to the viscous interactions in hypersonics flow is the presence of high temperature gas effects. As Section 2.2.3 discussed, the dissipation of kinetic

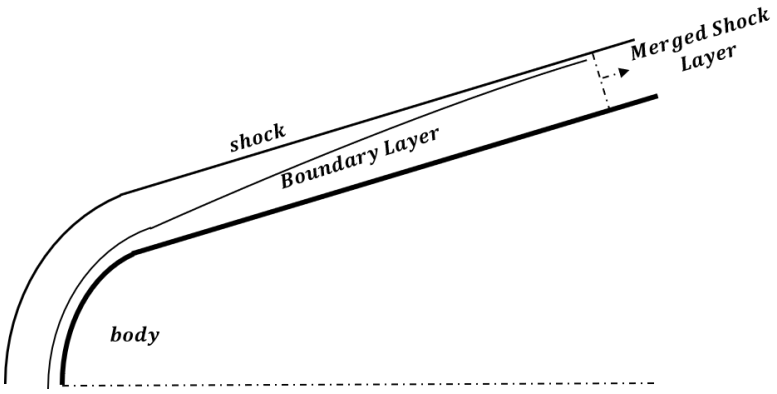


Figure 6. Merged Shock Layer

energy in the boundary layer re-routes the energy into internal modes and leads to much higher temperature profiles. With high enough Mach number, this excitation of internal energies is able to excite vibrational and rotational energy modes and can lead to dissociation and ionization of the gas [52].

2.2.5 Low-Density Flow.

The final primary defining characteristic of hypersonic flight is the presence of low density freestream flow. While low density flow effects are not of direct impact to this current study, it is still worth noting that they do have a significant effect for hypersonic systems at high altitudes. It should also be noted that this defining characteristic is not directly a result of hypersonic flow phenomena (such as near body viscous dissipation causing lower boundary layer densities), but is primarily driven by the environment/altitudes at which hypersonic vehicles must fly. At the velocities hypersonic vehicles cruise at, low altitude densities would cause viscous dissipation to overheat the surface of the vehicles. To prevent overheating of the surface, hypersonic vehicles often are designed to fly at tens of thousands to hundreds of thousands of feet above sea level while at cruise conditions. At these altitudes, assumptions of continuum flow break down and a variety of atypical physical effects begin to occur

near the body of the vehicle.

2.3 Laminar to Turbulent Boundary Layer Transition

With the basics of hypersonic flow established, it is now essential to examine the nature of how boundary layer flows transition from laminar to turbulent. Boundary layer transition is a complex and often multi-faceted process that is affected by many aspects including flight conditions and body geometry. Despite this complexity, there are some basic principles of boundary layer transition that hold true for nearly all flow conditions. This section looks to provide the reader with a foundation of how boundary layer transition occurs so that the next sections on hypersonic instabilities can be built up.

While Rayleigh and and Reynolds established the foundations of flow instabilities and transition behaviors during the late 1800s and early 1900s, the intricacies of boundary layer transition still remain an area of active research. Despite transition having many areas that are not well understood, there are a few key principles of the transition process that hold true regardless of the flow type.

Oftentimes, the process of a boundary layer transition is visualized using Morkovin's diagram seen in Figure 7. This diagram provides the various paths that boundary layers can transition. While this is useful for those familiar with all the different aspects and intricacies of boundary layer transition, perhaps a simpler and more easily understood description of this process is to simply view the boundary layer as a system that responds to inputs by outputting a response. Based on the concepts developed by Candler's Input-Output Analysis team at University of Minnesota, this way of treating the flow as a system considers any given laminar flow (boundary layer flow or otherwise) to be a system that can 1) be subject to environmental disturbances, 2) receive these disturbances as inputs, 3) process those inputs as a system response,

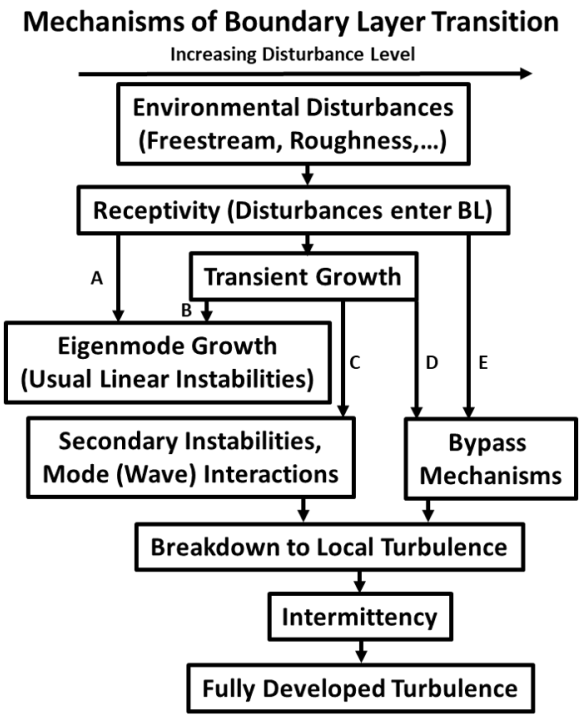


Figure 7. Mechanisms of Boundary Layer Transition (adapted from [5])

and then 4) output a response. With this model established, the process of transition can now be analyzed in further detail.

To begin the transition process, there must be some sort of *disturbance input* into the flow system. These disturbance inputs can come in many forms that vary in magnitude and impact. Natural environmental disturbances are always present in real fluid flows due to the fact that real systems always have imperfections. These natural disturbances are often created through minute freestream noise, small surface roughness features, or even random molecular interactions. Larger disturbances such as large surface disturbances and injected mass flow can also be present given the characteristics of the flow/vehicle. If a disturbance is large enough, it can allow for a "bypass" of the traditional transition mechanisms and will cause transition to immediately occur. It should be noted that flow disturbances don't necessarily have to originate within the boundary layer itself which leads into the concept of disturbance

reception.

Once a disturbance is generated outside the boundary layer, the process known as *disturbance receptivity* determines whether or not the disturbance makes its way into the boundary layer. Receptivity in itself is an entire area of active research, but there are a few key aspects of receptivity that the author should be aware of. Disturbance receptivity is very dependent on the type of disturbance present, the boundary layer profile, and flow conditions. If a boundary layer presents unfavorable conditions for a given disturbance form or frequency, that disturbance will not enter into the boundary layer or will be damped through the boundary layer shear layer before entering. If a boundary layer presents favorable conditions for a given disturbance form or frequency, that disturbance will be allowed into the boundary layer to be processed by the boundary layer system. It should be noted that in every flow there are a large variety of disturbances present, but only those disturbances that are viable for the boundary layer will be received and can be observed within it. This concept of a boundary layer being "tuned" to specific instabilities is key in the field of hypersonic instability and transition research and will be described in more depth in Section 2.4.

Once a boundary layer receives a disturbance, the process of *system disturbance response* determines whether the disturbance will temporally and/or spatially amplify or damp. There are many avenues by which the system can respond to the presence of a disturbance. Those disturbances which are considered stable within the boundary layer will often damp out and have a negligible effect on transition. It is the unstable boundary layer disturbances which maintain or amplify their amplitude that have a primary influence on transition location. Each flight regime and body geometry has a specific set of boundary layer instabilities that dominate the transition process.

Once the boundary layer system processes the instability mechanisms, the final step of the transition process is the *system disturbance response*. If the system allows

for an instability to propagate and grow, there becomes a point at which the instability causes the flow to lose its stability and break down into turbulence. It should be noted however, that transition is often not as simple as a single position in the flow at which turbulent flow begins. Often, the process of laminar to turbulent transition due to environmental or small disturbances is unsteady and complex. Due to this complexity, transition is often referred to as a region instead of a position. In the transition region, intermittent turbulent spotting is often present before the flow breaks down to a fully turbulent flow front.

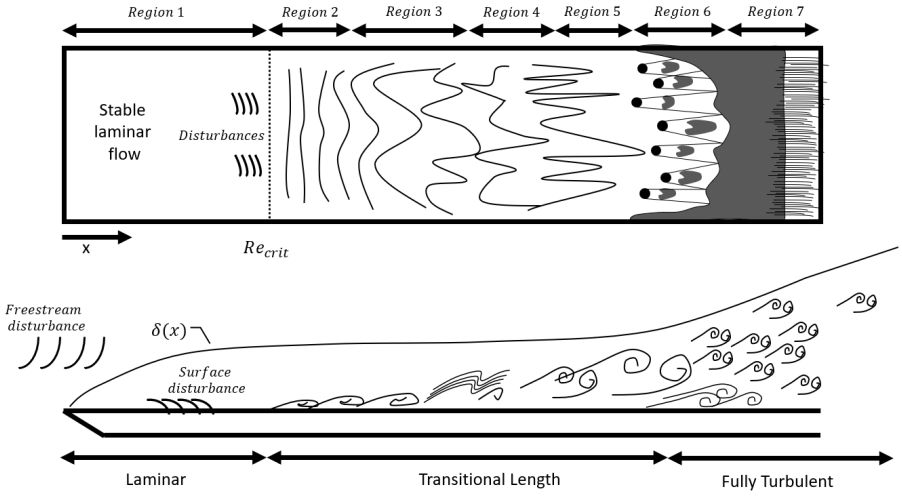


Figure 8. Boundary Layer Transition Process Over a Flat Plate (adapted from [6])

As visualized in Figure 8, perhaps the best example of the laminar to turbulent transition process is by White where he describes the transition to turbulence of a laminar boundary layer over a flat plate. He breaks down the transition process into seven distinct steps:

1. Stable laminar flow near the leading edge
2. Small disturbances turn into 2D Tollmien-Schlichting waves.
3. Breakdown of TS waves into unstable 3D waves and hairpin eddies

4. Vortex breakdown at regions of high localized shear

5. Cascading vortex into fully 3D fluctuations

6. Formation of turbulent spots at locally intense fluctuations

7. Coalescence of spots into fully turbulent flow

This simple transition example by White demonstrates natural transition due to the amplification of Tollmein-Schlichting waves. While very specific, this example demonstrates all of the key concepts of the transition process. One of the key take-aways from this example is that despite there being a stable laminar flow present over the flat plate, infinitesimally small disturbances are still present that lead to the formation of the Tollmein-Schlichting instability waves. It should also be emphasized that the transition does not occur at a single point, but is instead a process that occurs over a distance. Within this transition length, the original instability loses its semi-stable two-dimensional structure and breaks down into unstable and complex three-dimensional structures that eventually form into turbulence.

2.4 Hypersonic Instability Mechanisms

With the basics of the hypersonic flight regime and boundary layer transition covered, it is now appropriate to marry the two concepts and focus on the instability mechanisms specific to hypersonic flows that often cause transition to occur. It should be noted that even though hypersonic flows are inherently complex flow systems, the same concepts as described in Section 2.3 still apply. To further reinforce this point, there are many instability modes that are present in lower Mach flows that are still present in different hypersonic flight conditions. A discussion of a few of these various instability mechanisms is appropriate to move forward.

While the theory behind Tollmein-Schlichting waves is over 100 year old and was proven to exist shortly after World War II in very low velocity flows over a flat plate, this instability is still present and relevant over hypersonic vehicles. In particular, Stetson makes direct mention of the likely presence of TS waves near the tip of blunted hypersonic conical bodies. The low relative Mach numbers before the sonic line behind the near-normal section of the bow shock in front of the vehicle allows for the presence of modes typically found in lower Mach flows [46]. TS waves are unstable two dimensional waves that arise in boundary layers typically due to natural disturbance propagation. They propagate downstream and will either amplify or damp streamwise depending on flow and boundary conditions [30, 31, 32, 33, 34, 35]. One influencing factor on the amplification of TS waves is the presence of pressure gradients in the flow. It was shown by Schubauer and Skramstad that the presence of a negative pressure gradient damped TS wave amplification and that the opposite holds for positive pressure gradients [36].

Another common low Mach instability that is relevant for hypersonic flows is the Kelvin-Helmholtz instability. The Kelvin-Helmholtz instability is an inviscid instability that occurs in the interference plane between two fluids flowing at different velocities in the same direction. Chandrasekhar's derives the Kelvin-Helmholtz instability equations in detail and the key takeaway to note for this instability is that it will always be present in some regards when a flow has differences in downstream velocity with respect to the normal direction to the flow [56].

Another class of instabilities that are found in hypersonic flight and lower Mach regimes are centrifugal instabilities. Centrifugal instabilities are closely tied to the Raleigh criterion for inviscid instability which states that any inviscid flow profile with an inflection point will inherently be unstable [57]. Since the Raleigh criterion was originally derived for incompressble flows, for hypersonic flows where compressibility

is important, a compressible flow equivalent of the Raleigh criterion was developed by Mack using the generalized inflection point [7]. From the principles explained in these criterion, centrifugal instabilities form when there is concavity in the wall profile along the boundary layer. Perhaps the most prominent centrifugal instability is the Görtler instability that is often found in curved scramjet inlets. The Görtler instability forms vortex-like three dimensional disturbances in the boundary layer that progress downstream and can lead to turbulent breakdown.

Crossflow instabilities are closely related to centrifugal instabilities. Crossflow instabilities are inviscid phenomena that are present when the downstream flow profile of the boundary layer is warped by a crossflow component that is normal to the tangential component. This warping introduces a profile inflection point which can create vortices similar in principle to Görtler vortices, but inherently different in structure. These instabilities are often found over axisymmetric bodies at non-zero angles of attack.

While this list of instability mechanisms is by no means the most comprehensive available, it does shed light on the fact that there are many instability mechanisms present in hypersonic flows, each competing for dominance over the transition phenomenon. The reader is encouraged to read the writings of Stetson, Fedorov, Schneider, Mack, and other similar authors to build a stronger understanding of all the intricacies surrounding the different boundary layer instabilities and how they behave in hypersonic flows. With this foundation built, it is now appropriate to delve into two specific hypersonic instability modes that are uniquely dominant over hypersonic conical bodies at Mach number surrounding Mach 6.

2.4.1 The Mack Modes.

From the 1940s into the 1960s, a great deal of analytical and numerical work towards describing complex flow instabilities was completed, but little consideration was made towards understanding the possibility of a flow instability having multiple solutions or modes [7]. The Lees-Lin proof of 1946 is one of the first efforts to describe the dependence of instability structure on Mach numbers for $\bar{M}^2 < 1$, where $\bar{M}$ is the local Mach number of the mean flow in the direction of the instability waves relative to the phase velocity of the waves. The Lees and Reshotko paper of 1962 describes the possibility of non-unique instability modes for $\bar{M}^2 > 1$, but it was not until Mack's works of the 1960s that a thorough investigation of multi-mode instabilities was made [7, 58, 59].

Mack's publication of Linear Stability Theory in the 1980s was the most comprehensive compilation of multi-mode instabilities. Commonly referred to as the "Mack modes," these instabilities are most prominent in supersonic and hypersonic flows and are derived as the most amplified pressure-fluctuation eigenfunctions when the flow system is linearized through LST. These amplified eigenfunction modes behave physically as trapped acoustic ray pressure-fluctuations within the boundary layer [8]. The mode number corresponds to the number of peaks in the pressure-fluctuation structure or the number of pressure-fluctuation inflection points minus one. This can best be visualized in Figure 9 where the pressure-fluctuation eigenfunctions of the first six modes of the 2D noninflectional neutral waves are visualized.

Under Mack's terminology, the first Mack mode is structurally identical to high speed Tollmien-Schlichting waves and is relatively unique in behavior among the Mack modes [8]. For relatively low Mach numbers below Mach 2, the first mode is often the most prevalent mode and the other modes are largely neglected [8]. For incompressible flows, the first mode is most unstable as a two-dimensional wave. For

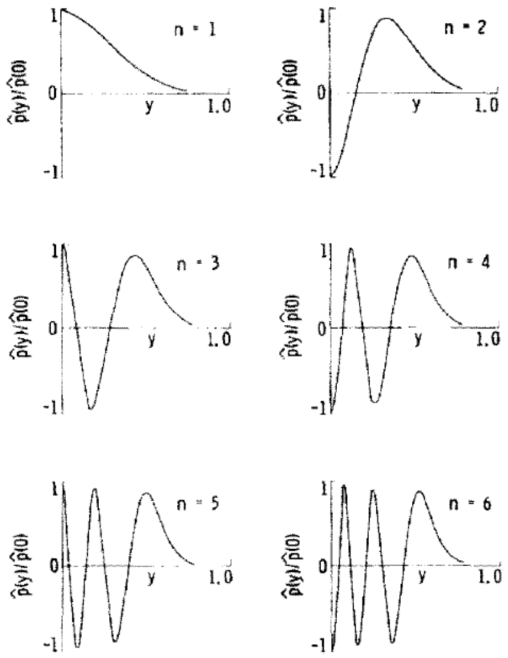


Figure 9. Eiegenvalue structure across boundary layer at freestream Mach 10 [7]

supersonic and hypersonic velocities, the first mode becomes most amplified when the waves are oblique [9]. As Mach number increases above Mach 2.2, the higher modes become more prominent. It is at these higher Mach numbers that the dominance of the second Mack mode becomes evident.

Figure 10 demonstrates the overpowering high temporal amplification rate of the second Mack mode for high Mach numbers. Mack notes in his works that the second Mack mode's prominence across a large number of Mach numbers is largely what distinguishes this class of instabilities from lower Mach number instabilities. Not only does the first/primary mode of this instability family quickly become overcome by the secondary mode, but as Mach numbers increase even higher modes become relevant [7].

The second, third, and higher Mach modes exist due to the presence of a sonic line relative to the disturbance phase velocity within the boundary layer that allows the

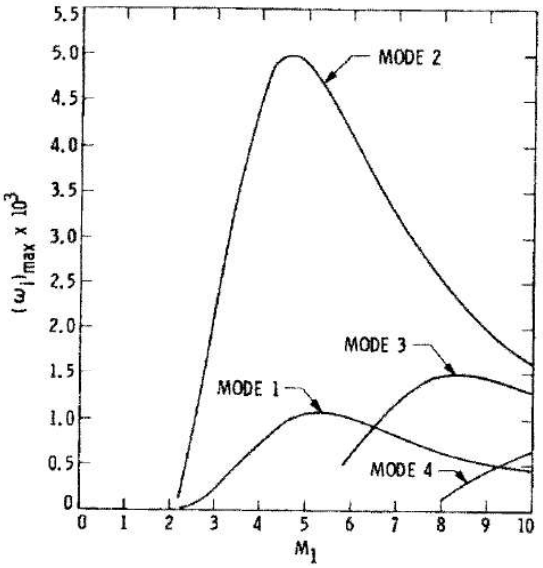


Figure 10. 2D Mack mode temporal amplification rate vs Mach number [7]

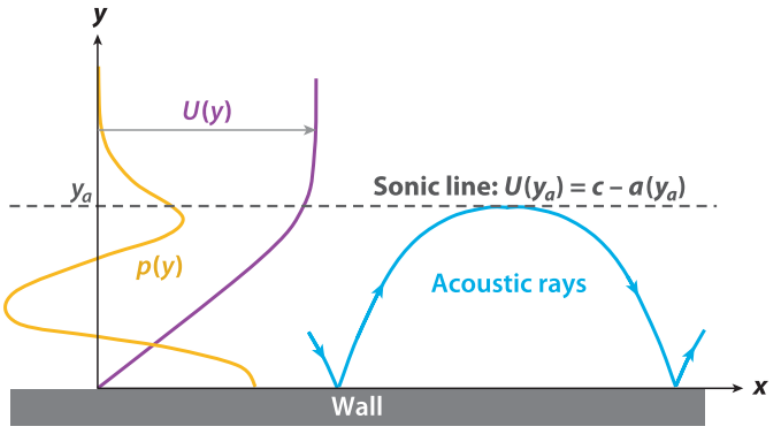


Figure 11. General acoustic pressure-fluctuation structure of Mack modes ($U(y)$ is the mean flow profile and $p(y)$is the pressure disturbance profile) [8]

boundary layer to behave as an acoustic wave-guide [8]. A generalized visualization of the acoustic ray nature of these instabilities can be observed in Figure 11. These higher modes are inviscid acoustic waves [8]. A result of this boundary layer waveguide

behavior is that the disturbance waves become "tuned" to the boundary layer. As the boundary layer grows, the disturbances amplify at increasing rates and drop in frequency in direct correlation to the thickness of the boundary layer. The instability will continue to amplify until an optimal tuning is achieved (maximum amplification rate) at which point the boundary layer will either develop nonlinearities, become unstable, and transition, or the instability will begin to attenuate and dissipate before transition occurs [9]. It should be noted that the presence of a highly amplified Mack mode instability in a hypersonic boundary layer does not necessarily mean the flow is turbulent or going to transition because the system can have oscillatory features and still remain laminar.

Unlike the first Mack mode, the higher modes are most unstable as two-dimensional waves. The second Mack mode in particular is exclusively most unstable as a two-dimensional wave as demonstrated in Figure 12 where ϕ is the disturbance wave angle relative to the downstream flow [9]. Also, at lower supersonic Mach numbers where the first mode is dominant, the flow is typically only able to support one instability mode (the first mode) in the boundary layer. For hypersonic boundary layers, multiple modes can be present at one time which allows to complex interactions and coupling not seen in lower Mach regimes [9]. Despite the capability of hypersonic flows to support multiple instability modes, it is expected for nearly all geometries, especially cones at zero angle of attack, that the second Mack mode is most dominant and most often is the cause of natural transition to turbulence [9].

The physical behavior of the Mack modes has been shown both analytically and experimentally to have the largest disturbance amplitudes in hypersonic boundary layers near the outer edge of the boundary layer [9, 10]. For increasing Mach numbers, the location where the gradient of the product of density and vorticity is zero, also known as the generalized inflection point, moves upward in the boundary layer. Major

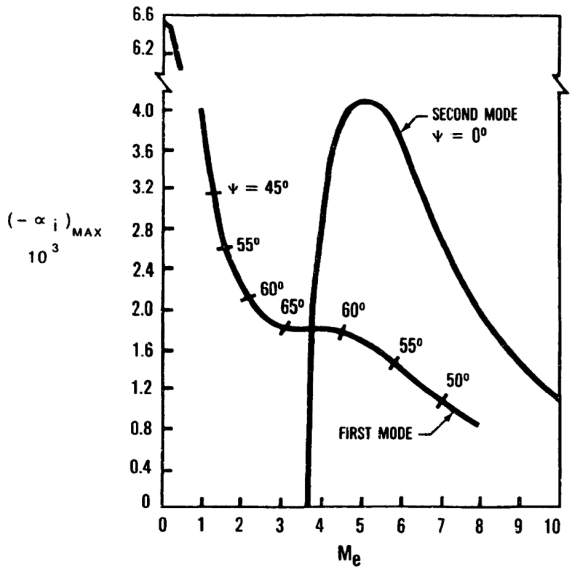


Figure 12. First and second mode maximum spatial amplification rates [9]

boundary layer disturbance in a hypersonic boundary layer occur near the generalized inflection point, thus the max disturbance amplitudes are high in the boundary layer [9]. Figure 13 visualizes the physical structure of the second Mack mode. It should be noted the importance of the relative sonic line in the behavior of the second Mack mode. Below the sonic line, the disturbance progesses downstream at a supesonic velocity and behaves in an acoustic manner. Above the sonic line, the disturbance progresses downstream subsonically and forms "rope-like" structures along the critical layer where the local mean flow velocity and the disturbance propagation speed are equivalent. Due to the subsonic nature of the overall disturbance velocity, this form of the second Mack mode instability is referred to as the subsonic variant and is the most common form of this instability [10].

Along with the subsonic variant of the second Mack mode, there is also a supersonic variant (visualized in Figure 14) that is often referred to as the supersonic mode. If the phase speed of the disturbance is supersonic with respect to the mean flow, a second sonic line is formed above the rope-like structure. This second sonic

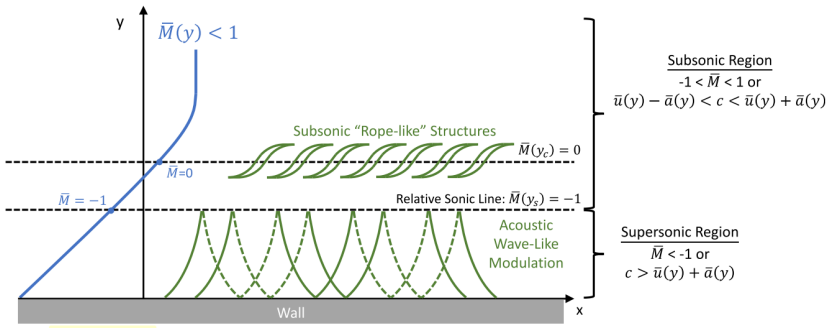


Figure 13. Second Mode Diagram [10]

line causes Mach waves to form above it that decay upstream at relative supersonic speeds [10]. While the presence of the supersonic mode has been well known since Mack's works in the 1980s, there is still a great deal of work being completed to understand its effects on transition. It has been shown that the supersonic mode takes away energy from the trapped acoustic wave boundary layer instabilities found in the traditional subsonic second mode instability and dissipates this energy into the flow via the decaying Mach waves [60]. It has also been shown that the presence of a cold wall tends to excite the supersonic mode [61].

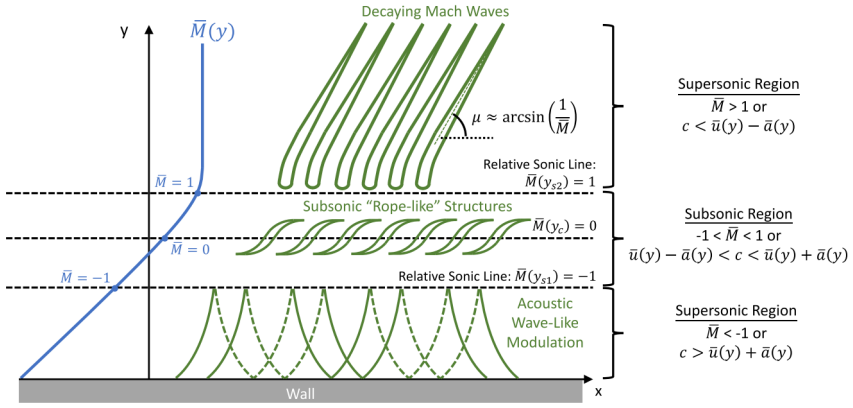


Figure 14. Supersonic Mode Diagram [10]

Besides exciting the supersonic mode, it has also been shown that for a given second mode instability frequency in a hypersonic boundary layer, the presence of

a cold wall boundary condition destabilizes the second mode instability and allows for faster amplification of the disturbance [7, 9]. It has been shown numerically that this faster amplification of the second mode instability will lead to lower transition Reynolds numbers, but very few experiments have produced consistent and repeatable results corroborating these numerical findings.

Experimentally, the Mack modes can be identified through a variety of techniques. The second Mack mode in particular produces strong features that can be easily recognized in wind tunnel testing. When high speed Schlieren visualization is used in the boundary layer region of bodies in hypersonic wind tunnel testing, the presence of second mode instabilities can be identified via the rope-like structures that form at the boundary layer edge as seen in Figure 15 (a). Along with Schlieren imaging, high speed surface mounted pressure sensors are often utilized in tandem to provide point-accurate pressure fluctuation data. Figures 15 (b) and (c) show an example of the pressure time series and pressure power spectral densities respectively for the run visualized in Schlieren in Figure 15 (a). By using techniques like these together, it is possible to track the development and behavior of the Mack mode instabilities with high spatial and temporal accuracy.

2.4.2 Hypersonic Blunt Cone Transition Reversal Phenomenon.

It is readily recognized that the second Mack mode is typically the most dominant boundary layer instability over slim hypersonic bodies. In particular, sharp conical bodies at Mach 6 and zero angle of attack have been shown to consistently produce, amplify, and transition due to the second Mack mode instability [9]. Despite this strong understanding of the second mode effects on sharp cones, blunt conical bodies pose a much more challenging and less understood instability and transition behavior. It has been shown that for low levels of nosetip bluntness, increasing the amount of

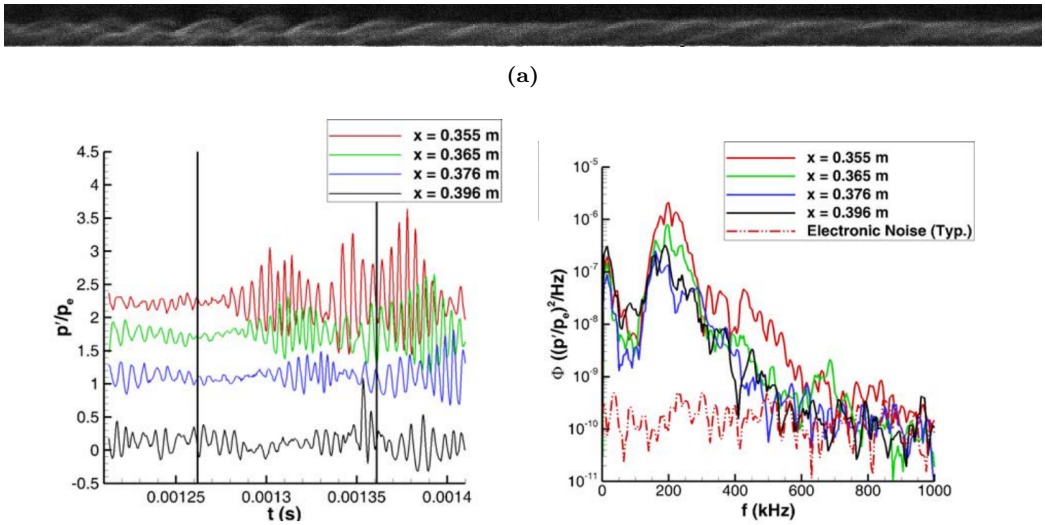


Figure 15. Second Mack Mode (a) Schlieren Visualization (b) Pressure Time Series (c) Pressure Power Spectral Densities [11]

bluntness causes a delay in transition with a corresponding increase in transition Reynolds number relative to the sharp tip case. This trend continues as bluntness is increased until a critical nosetip bluntness is reached at which point further increase of the nosetip bluntness results in a rapid drop in transition Reynolds number. As further bluntness is added, the transition point will move towards the tip and can surpass the original transition point of the sharp tip case [12]. This behavior of transition delay and sudden amplification due to nosetip bluntness is known as the hypersonic blunt cone transition reversal phenomenon and has been one of the most challenging problems in hypersonic instability research for the past fifty years.

Some of the first documented cases of hypersonic boundary layer transition reversal on conical bodies being greatly influenced by nosetip bluntness were made in the midst of the space race in the late 1950s. The NACA reports of Evvard, Diaconis, and Jack are some of the first documented cases of transition reversal affecting hypersonic blunt bodies [62, 63, 64, 65]. Many in the transition research field at the time believed wall cooling could be a significant reason for the behaviors observed in

experiments, but it was Stetson and Rushton in the late 1960s who began to postulate about bluntness itself having an effect on the boundary layer stability [66].

Perhaps the most well documented series of experiments on nosetip bluntness effects on hypersonic cones can be found in Stetson's works from the 1970 and 1980s. While there was a great deal of research into hypersonic blunt cone transition effects leading up this point, much of the research was scattered and not collected in an organized manner. Stetson's papers during this time period worked to compile the current understanding of the field and presented the effects of blunt cone transition reversal in an organized and systematic manner. Figure 16 is the most iconic diagram produced from Stetson's findings and provides insight into the behavior of this transition phenomenon. At first, Stetson's diagram can appear overwhelming, but a breakdown of the various components and terms helps shed light on the various intricacies present.

Both the upper and lower portions of Figure 16 use an x-axis that is the blunt tip frustrum transition location, x_{T_B}, normalized by entropy layer swallowing distance, x_{sw}. Stetson and other researchers of his time believed that the behaviors associated with bluntness transition reversal were closely tied to the entropy layer generated with increasing bluntness. The entropy layer swallowing distance was found to provide a consistent and repeatable normalization scaling factor that showed consistent transition trends and thus is used by Stetson and others to display this phenomenon's behavior. As for the y-axes of the two plots, Figure 16 (a) uses a y-axis that corresponds to the blunt tip frustrum transition location, x_{T_B}, normalized by the sharp tip frustrum transition location, x_{T_S}. Figure 16 (b) uses a left hand y-axis that is the blunt tip boundary layer edge transition Reynolds number, $(Re_{x_T})_B$, normalized by the sharp tip boundary layer edge transition Reynolds number, $(Re_{x_T})_S$. The right hand y-axis in the lower portion of the figure is the sharp tip freestream edge

unit Reynolds number, $(Re/FT)_{e_S}$, normalized by the blunt tip freestream edge unit Reynolds number, $(Re/FT)_{e_B}$.

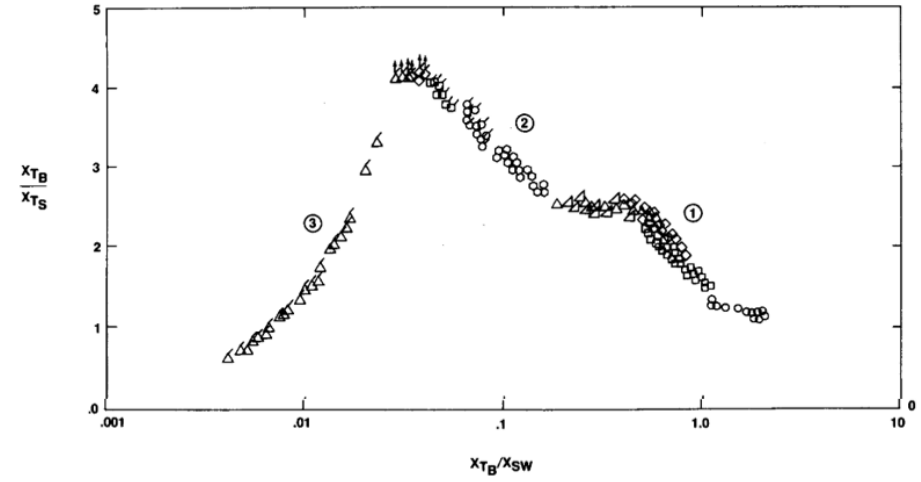
Data is plotted in both the upper and lower portion of the figure of the transition data for various models with increasing nosetip bluntness, represented as nose radius over base radius, R_N/R_B. In the lower figure, the freestream edge unit Reynolds number ratio is also plotted as a solid line. It was found that a relationship between the transition point and Reynolds number ratios could be established using the following equation,

$$\frac{x_{t_B}}{x_{T_S}} = \frac{(Re_{x_T})_B}{(Re_{x_T})_S} * \frac{(Re/FT)_{e_S}}{(Re/FT)_{e_B}} \tag{1}$$

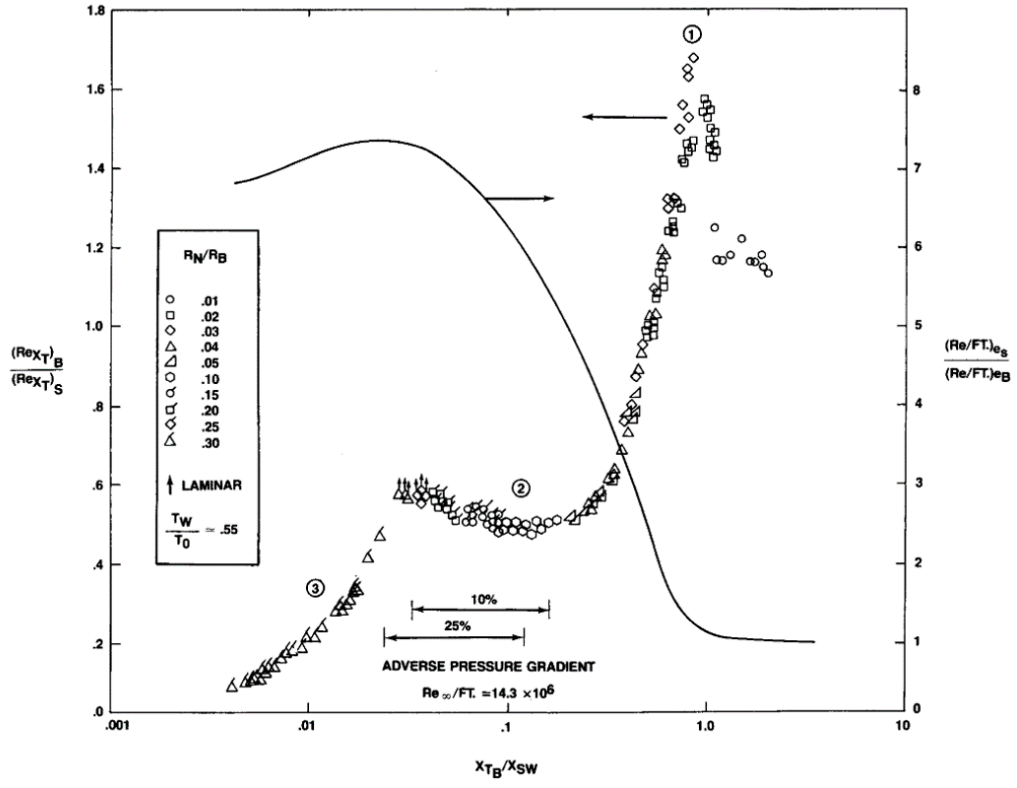
Utilizing this relationship and delving into Stetson's data, three regions of interest become evident.

Region 1 ($X_T/X_{SW} \approx 1.0$).

The first region identified occurs for the smallest amounts of bluntness when the transition location is nearly the same as the entropy swallowing distance. This region is marked by a small rearward displacement in transition location relative to the sharp case as is seen in the upper portion of the figure. The reason for this rearward displacement is revealed in the lower portion of this figure where it can be seen that the edge unit Reynolds number is negligibly reduced, but the transition Reynolds number increases. This shows that the edge unit Reynolds number reduction for the small nosetip bluntness cases is not enough to overcome the increase in transition Reynolds number.



(a)



(b)

Figure 16. Stetson nosetip bluntness effect on frustrum transition at Mach 5.9 (a) blunt cone transition location normalized by sharp cone transition location (b) blunt cone transition Reynolds number normalized by sharp cone transition Reynolds number [12]

Region 2 ($X_T/X_{SW} \approx 0.10$).

As the nosetip bluntness increases, the second region of interest becomes evident for bluntness ratios ranging from $R_N/R_B = 0.04$ to 0.25 where $X_T/X_{SW} \approx 0.01$. This region is marked by a fairly consistent delaying in transition location, as observed in the upper portion of the figure, but also has a significant drop in transition Reynolds number, as indicated in the lower portion of the figure. Stetson notes that this counter-intuitive behavior is most likely due to a "shifting of dominant roles of transition parameters." He also notes that, despite the transition Reynolds number dropping rapidly in this region, there is also a significant reduction of edge unit Reynolds number which overwhelms the transition Reynolds drop.

The leftmost boundary of Region 2 is denoted by the point of maximum transition delay ($\frac{x_{T_B}}{x_{T_S}} > 4.2$). It can be noted that, despite the consistent delay in transition, the transition Reynolds number dips down below the original transition Reynolds number for the sharp case for the majority the region. This behavior was not understood by Stetson and is still a point of contention within the transition community.

Region 3 ($X_T/X_{SW} < 0.03$).

The final region that can be observed from Stetson's data is marked by a rapid forward progression of transition on the frustrum as is observed in the upper portion of the figure. This behavior was observed for nose bluntness ratios around $R_N/R_B = 0.30$ where $X_T/X_{SW} < 0.03$. Despite the fact that as X_T/XSW became smaller, the favorable pressure gradient became stronger (which should be a stabilizing effect), the transition Reynolds numbers continued to drop so much that transition neared the tip of the model itself.

Stetson notes that this region has four unique qualities that make it stand out when compared to the previous to regions and suggest that other effects are dominating

the transition behavior.

1. The transition location for this region was unpredictable and could vary from fully turbulent to fully laminar between runs.

2. While the other regions showed symmetric transition behavior around the circumference of the model, this region would display asymmetric transition at zero angles of attack with some cases having one side fully turbulent with the other side being fully laminar.

3. The transition region was long with some cases never showing fully turbulent flow along the model.

4. The transition point on the frustrum was very sensitive to roughness on the nosetip.

In the end, it was determined that the observations being made by Stetson were indicating that blunt cone transition phenomena were being dominated by a multitude of competing factors. These factors included entropy layer effects, surface roughness, pressure gradient, and more, but no clear dominant factor appeared to produce consistent transition behavior or could explain the rapid and often inconsistent transition reversal behavior as bluntness is increased.

2.4.3 Modern Hypersonic Blunt Cone Transition and Instability Research.

Despite the great amount of effort put forth by Stetson, Kimmel, and others in the hypersonic instability/transition research community up through the 1990s to better understand bluntness effects on transition, there is still a great deal of recent and ongoing work to better understand this phenomenon. To properly expand upon

and explain all of the research articles and papers that have been published over the past two decades regarding this research area would be overwhelming, but a few nominal examples from recent years exemplify the current state of research and recent advancements in experimental and computational work.

Marineau et al. in 2014 performed an intensive study of blunt cone transition effects at Mach 10 through a variety of experiments and accompanying computational analysis on a variety of blunt cone configurations. The findings of Marineau's study closely aligned with those of Stetson's work nearly thirty years prior. The modern equipment and post-processing techniques available in this work did allow some new observations. One such modern technique that compliments and adds to the findings of Stetson is the use of power spectral densities plotted against length of the cone with various nose bluntnesses as observed in Figure 17. This visualization technique shows the clear delay and eventual decimation of the second Mack mode. The drop in frequency of the second mode as the tip is slightly blunted is directly related to the thicker downstream boundary layer where the instability forms. The highest bluntness cases show a clear non-modal transition behavior with no second mode frequencies. It was concluded that the higher bluntness cases were being dominated by instabilities not tied to the traditional Mack modes such as transient growth and entropy layer instabilities, thus further confirming Stetson's suspicions three decades earlier [13].

In 2016, Jewell and Kimmel also revisited the Mach 6 blunt cone experiments of Stetson where they revisualized Stetson's results and produced complimentary results. Their work utilized the STABL computational fluid dynamics code package where they performed mean flow solutions and PSE-Chem stability analysis for 11 different nose tip bluntnesses. They recreated Stetson's transition reversal chart, seen in Figure 18, by using converged DNS solutions of the flow to provide accurate

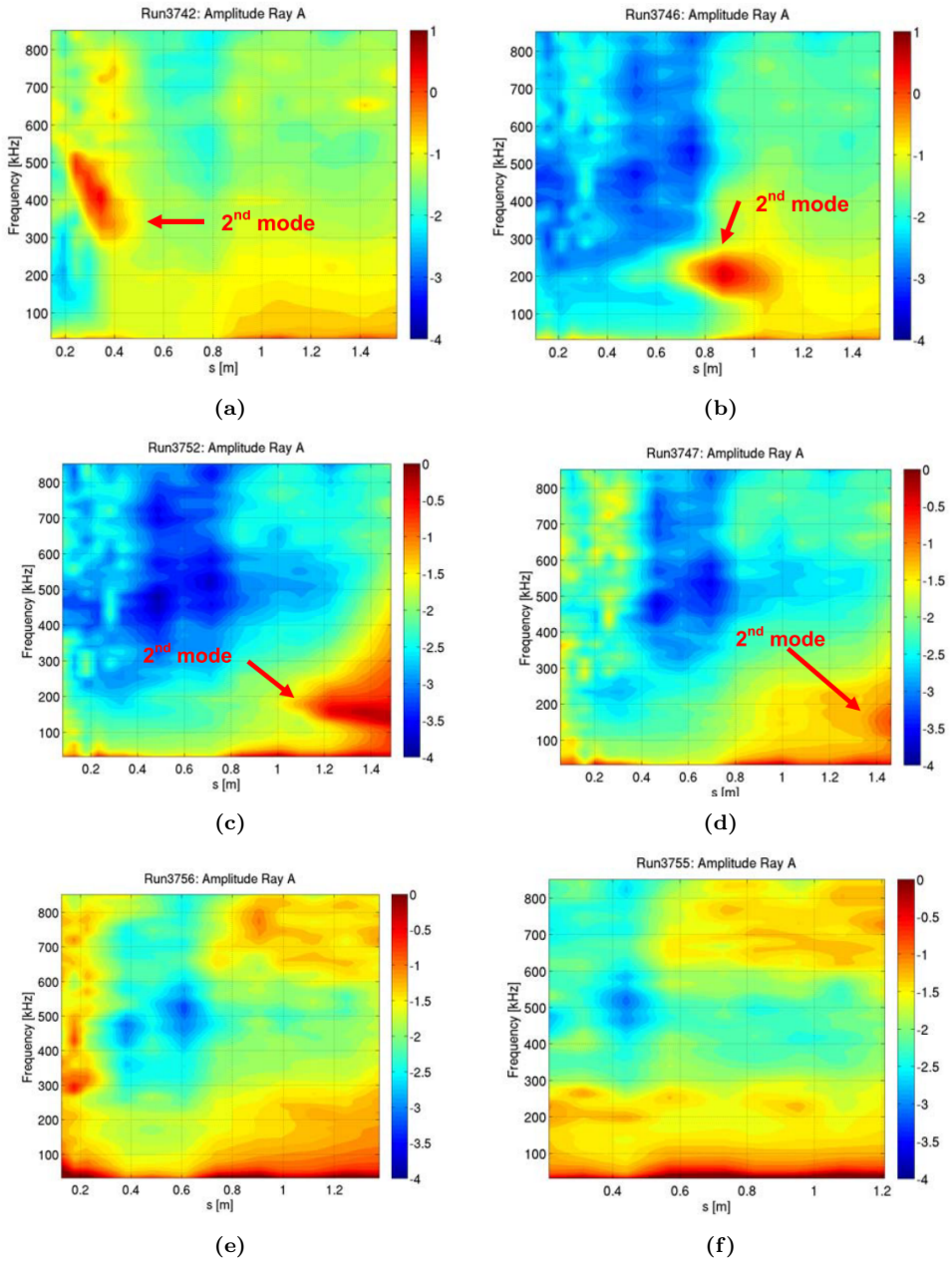


Figure 17. Marineau et al. Log(PSD) of Cones at $Re/m \approx 17 * 10^6/m$ **(a)** $R_n = Sharp$ **(b)** $R_n = 5mm$ **(c)** $R_n = 9.5mm$ **(d)** $R_n = 12.7mm$ **(e)** $R_n = 25.4mm$ **(f)** $R_n = 50.8mm$ **[13]**

entropy layer estimates [67]. Jewell and Kimmel also utilized a trend first visualized in Marineau et al.'s previously mentioned paperwhere Reynolds number based on transition location is plotted against Reynolds number based on nose radius. Using Stetson's data, Figure 18 shows the clear trend of transition reversal in a clear manner

that is easier to visualize when compared to Stetson's original diagrams [14].

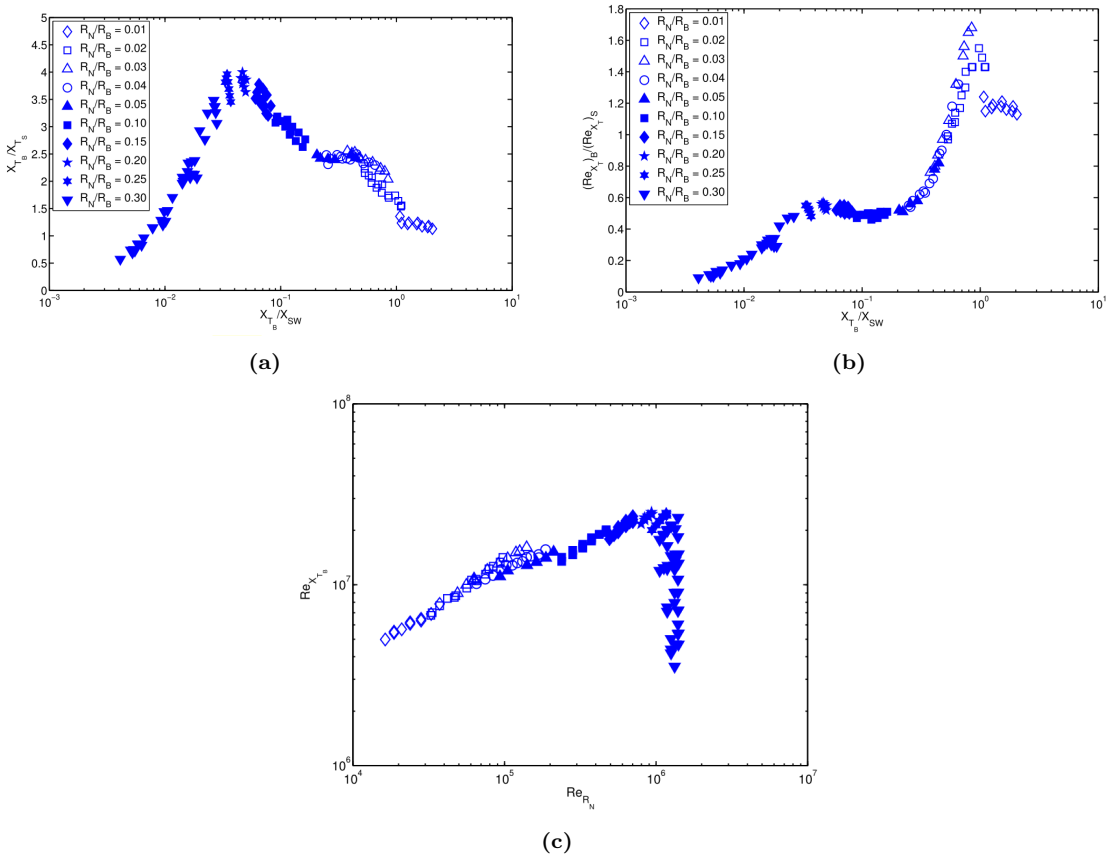


Figure 18. Jewell's reinterpretation of Stetson's diagram (a) Transition Location (b) Transition Reynolds Number (c) Transition Reynolds Number vs Nose Radius Reynolds Number [14, 12]

Along with re-visualizing Stetson's results, Jewell and Kimmel's STABL results were able to return predicted N-factors for the second Mack mode as seen in Figure 19. It can be easily observed that as the nose radius increases, the predicted N-Factor quickly drops to levels below 1. Known experimental cases have shown that transtional N-factors for similar geometries are around 5.5 [68]. With these experimental results in mind, it is immediately evident that the cases where transition occurs for higher tip bluntness are in a regime where the second Mack mode is below a level where transition is expected to occur. Jewell and Kimmell note that there is strong evidence that the noise characteristics of the tunnel in which an experiment

is conducted can greatly effect the N-factor at which transition occurs [69]. This is most likely tied to a mismatch between the strongest frequencies in the freestream noise and the unstable frequencies that are supported by the boundary layer. Despite this possible source of error, Jewell and Kimmel inevitably agreed with Steton's and Marineau et al.'s conclusions that transient growth and entropy layer instabilities are most likely dominating the high bluntness cases [14].

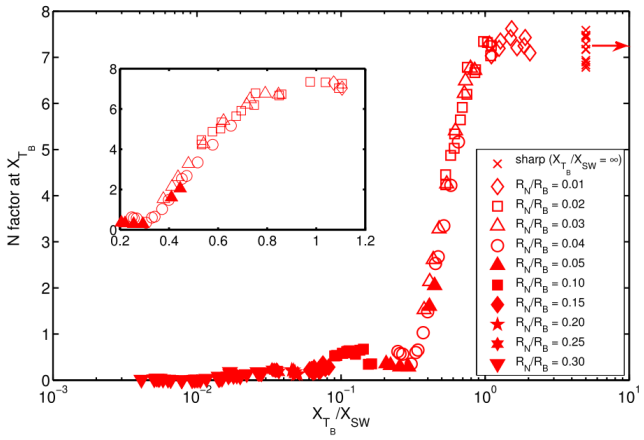
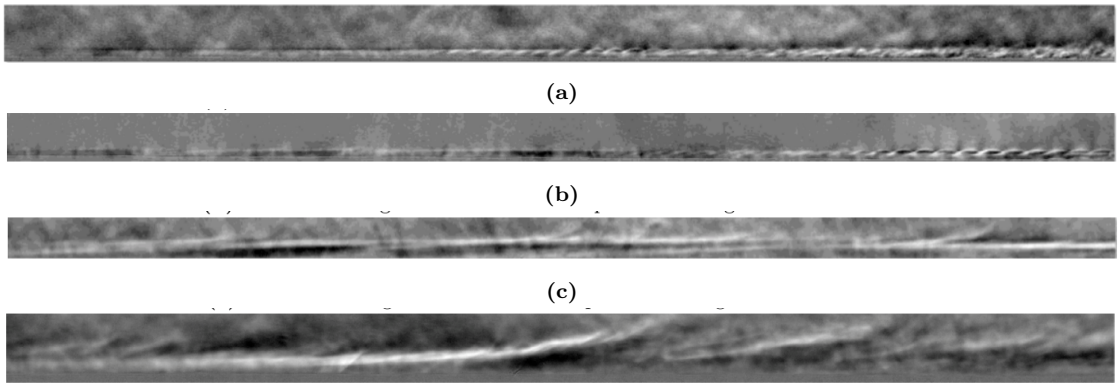


Figure 19. Computed second mode N-factor for Stetson's conditions [14]

Beyond revisiting Stetson's work, there are many examples of recent works that produce unique results regarding blunt cone transition behavior. High speed Schlieren and PCB pressure sensor measurements of instabilities over various bluntness cones in the Air Force Research Lab Mach 6 Ludwieg tube reported by Kennedy et al is an excellent example of modern experimental techniques used to further develop blunt cone transition research. Shown in Figure 20, the Schlieren results from this study depict a clear alteration of the second mode wavepacket structure as nosetip bluntness is increased. As bluntness increases, the traditional "rope-like" structure of the second mode is elongated into "whisps" that extend well above the boundary layer. These whisp structures match findings from other researchers including those of Grossir et al. in 2014 [70]. These Schlieren results, coupled with the PCB pressure

sensor results in Figure 21 tell a story of nonmodal instabilities dominating the higher bluntness cases and further suggest the presence of other effects starting to dominate transition behavior as bluntness is increased[15].



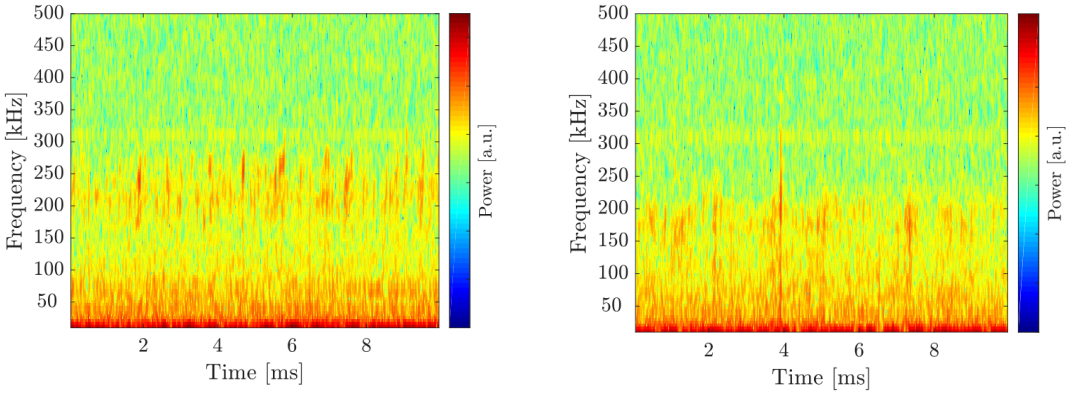
(a)

(b)

(c)

(d)

Figure 20. Kennedy's enhanced Schlieren image (a) 0.508mm nosetip radius (b) 1.524mm nosetip radius (c) 2.54mm nosetip radius (d) 5.08mm nosetip radius [15]



(a) **(b)**

Figure 21. Kennedy's Short Time Series Fourier Transform at $Re/m = 18.27 * 10^6$ (a) 2.54mm nosetip radius (b) 5.08mm nosetip radius [15]

Perhaps the most comprehensive paper on the current state of research into bluntness effects on hypersonic flow instabilities and transition is Paredes et al.'s publication in the Journal of Spacecraft and Rockets in 2019. This article provides an overview of the NATO Science and Technology Organization (STO) Applied Vehicle Technology (ATV)-240 group who's primary goal was to better explain blunt cone

transition reversal. They found that increased nose bluntness resulted in higher transient amplification near the nose region. They also found that roughness near the nose became much more significant on instability/transition characteristics as bluntness increased. These transient growth and roughness effects are postulated to interact with one another with the roughness elements possibly seeding the boundary layer near the tip with small perturbations that are transiently amplified for blunter tips. Despite the significant findings of this study however, the authors note that there is still a great deal of work that could be done to understand nonmodal growth of traveling disturbances within the entropy layer and their effect on transition reversal [71].

2.4.4 Nonlinear Interactions and Breakdown to Turbulence.

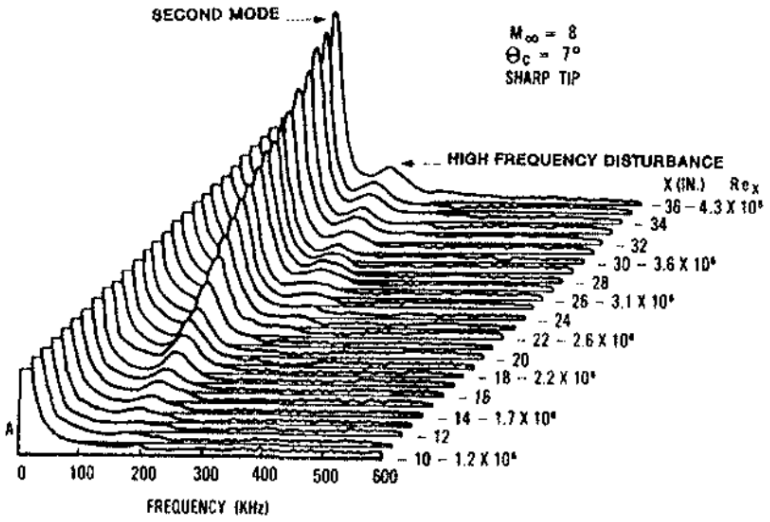


Figure 22. Power spectra over Stetson et al.'s 7 degree half angle cone showing second mode and higher frequency nonlinear interaction band [16, 17]

As was alluded to in Section 2.3, the process of a boundary layer instability breaking down to turbulence often involves the presence of nonlinear interactions. For hypersonic flows, nonlinear interactions often dominate the breakdown of the boundary layer to turbulence and have been shown to create complex transition mechanisms

and instability coupling. Traditional boundary layer instability prediction techniques such as Linear Stability Theory (LST) and the Parabolized Stability Equations (PSE) have a distinct inability to capture nonlinear interactions within the boundary layer. The discrepancy between linear prediction methods and experimentally observed nonlinear interactions are perhaps best exemplified in the findings of Stetson, Donaldson, and Siler in 1983 over a sharp, 7 degree half angle cone at Mach 8. As is shown in Figure 22, hot-wire anemometer measurements in the boundary layer over the geometry indicated the presence of a strong second mode disturbance with a 80-120kHz frequency band [16]. This observed second mode frequency band agreed well with Mack's LST predictions for the same geometry and run conditions, but the experimental data also showed the presence of a higher frequency band at approximately twice the frequency of the second mode band. This higher frequency band did not match the stability predictions of Mack's LST for second of third mode instabilities and thus were determined to most likely be nonlinear interactions [72, 73].

When nonlinear interactions occur within a boundary layer, signal traces from a sensor placed within the boundary can exhibit signs that point to nonlinear effects. These nonlinear interactions of frequencies within in a given signal can take many forms as is shown in Figure 23. Given a signal with a base amplitude and frequency response of X, the presence of other frequencies, Y, that nonlinearly react with the base signal will provide differing compound signal effects [18]. For hypersonic boundary layers, the phase and amplitude of various frequencies within the boundary layer often become coupled and interact with one another in a nonlinear fashion. While clean signal traces such as those shown in Figure 23 show that nonlinear effects can be recognized at a glance, in reality experimental data is often much noisier and the nonlinear effects are not as easy to identify.

With the recognition that nonlinear effects appear to dominate many cases of

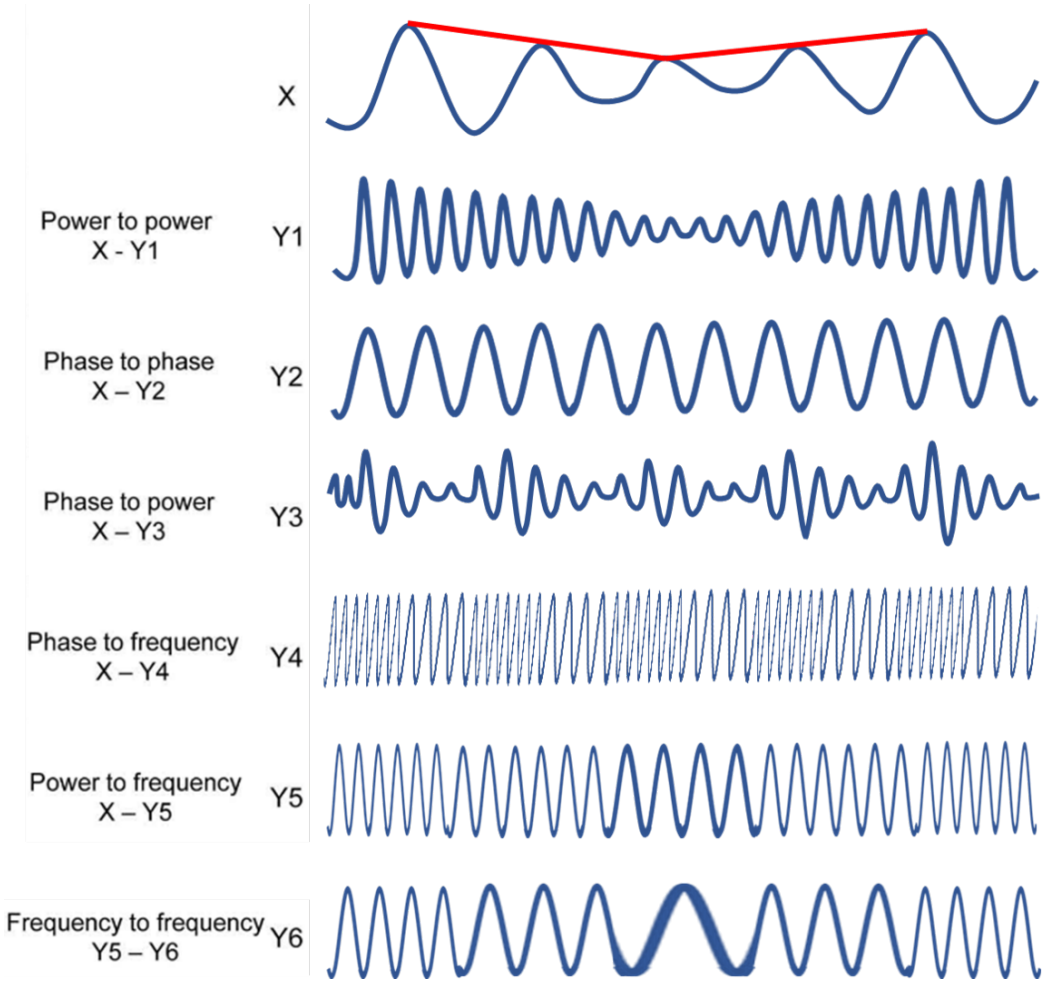


Figure 23. Various forms of nonlinear frequency interactions (adapted from [18])

hypersonic boundary layer transition and that these effects are often buried in complex data sets, the hypersonic boundary layer instability and transition community began looking for techniques to capture and characterize the influence of nonlinear interactions during experiments. One of most prominent techniques used by the hypersonic instability research community that originated in fields such as biomedicine and plasma physics is bicoherence analysis. First used in hypersonic boundary layer analysis by Kimmel and Kendall in 1991, bicoherence provides a measure of nonlinear interactions within a signal while taking into account phase and amplitude effects [17].

Kimmel and Kendall provide excellent insight into the use of bicoherence to analyze hypersonic signals, so a summary of their description of the technique is provided now. Bicoherence arises as a normalization of a signal's bispectra which is analogous to traditional power spectra analysis. While a signal's power spectra is a first-order spectrum with units of mean square signal per Hertz, $|S^2|/Hz$, the bispectrum is a second-order spectrum with units of mean cube signal per Hertz squared, $|S^3|/Hz^2$. While the power spectrum is the Fourier tranform of the autocorrelation of a signal, the bicoherence is the two-dimensional Fourier transform of the second order autocorrelation of a signal

$$R_{xxx}(\tau_k, \tau_l) = E[x(t)x(t+\tau_k)x(t+\tau_l)] \tag{2}$$

where τ is time delay at two different lag values k and l, $x(t)$ is a fluctuating wave form, and E[ffl] is an expected or average value. From this second order autocorrelation, the bispectrum, $B(\omega_k, \omega_l)$ can be written in terms of the Fourier components as

$$B(\omega_k, \omega_l) = \lim_{t\to\infty} \frac{1}{t} E[X(\omega_k)X(\omega_l)X^*(\omega_m)] \tag{3}$$

where ω is the circular frequency, t is the measurement time, X is the Fourier coefficient, and ω_m is the sum of the frequency content for two separate wave frequencies (i.e. $\omega_m = \omega_k + \omega_l$). The asterisk denotes a complex conjugate.

Normalizing the bispectrum, B, by the expected mean squared Fourier coefficients for the two frequencies multiplied with one another, $E[|X(\omega_k)X(\omega_l)|^2]$, and the summed frequencies, $E[|X(\omega_m)|^2]$, results in the bicoherence being obtained as follows

$$b^2(\omega_k, \omega_l) = \frac{|B(\omega_k, \omega_l)|^2}{E[|X(\omega_k)X(\omega_l)|^2]E[|X(\omega_m)|^2]} \tag{4}$$

The bicoherence is bounded in value from zero (completely independent waves) and one (fully coupled waves). While this description of bicoherence is useful in theory, in reality a discretized Fourier transform is used for experimental data sets and thus a discretized form of bicoherence is needed. The expected values are estimated by obtaining ensemble averages over a number of records, M. The resulting discrete bicoherence is

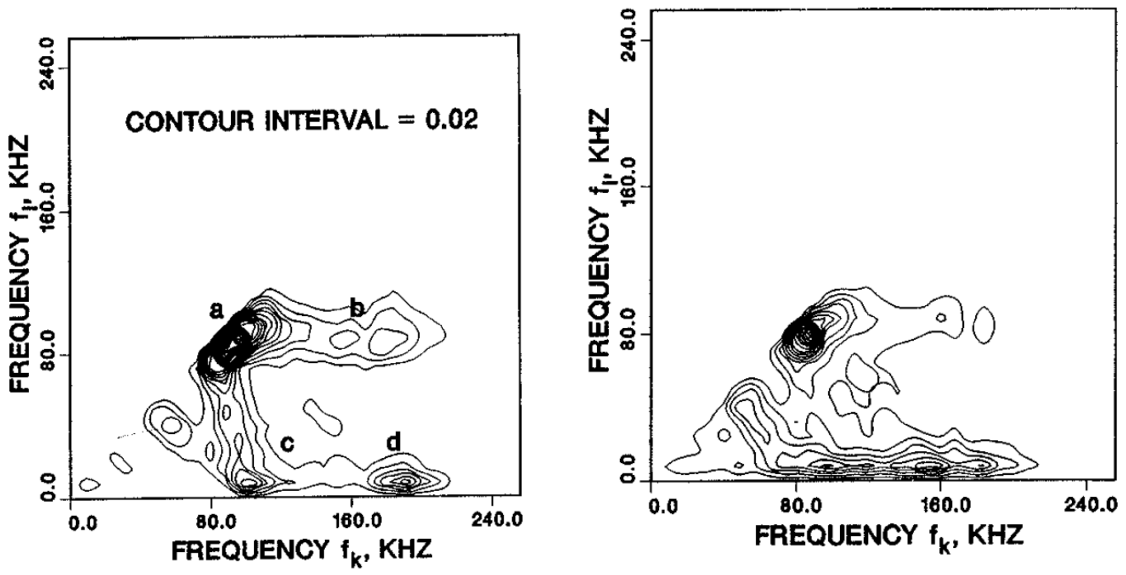
$$b^2_{k,l} = \frac{|\frac{1}{M}\sum_{i=1}^{M} X_k^{(i)} X_l^{(i)} X_m^{*(i)}|^2}{[\frac{1}{M}\sum_{i=1}^{M} |X_k^{(i)} X_l^{(i)}|^2][\frac{1}{M}\sum_{i=1}^{M} |X_m^{(i)}|^2]} \tag{5}$$

The true usefulness of this bicoherence is its ability to preserve phase information where the power spectrum typically destroys phase information. This is made evident by taking the numerator of equation 5 and placing it into exponential form as

$$B_{k,l} = \frac{1}{M}\sum_{i=1}^{M} |X_k^{(i)}||X_l^{(i)}||X_m^{(i)}| exp[-j(\theta_k^{(i)} + \theta_l^{(i)} - \theta_m^{(i)})] \tag{6}$$

where θ is the phase angle of the Fourier coefficient, X. If the waves at ω_k, ω_l, and ω_m are independent and randomly excited, then their phases will also be random, independent, and uniformly distributed from $[0, 2\pi]$. This uniform distribution of phase angle means that the values of $\theta_k^{(i)} + \theta_l^{(i)} - \theta_m^{(i)}$ in the exponent will average to zero, thus providing little to no bicoherence value return. If one of the fluctuations in the signal is affected by nonlinear interactions between two waves, their phases and amplitudes will be dependent and non-uniformly distributed, thus resulting in a non-zero bicoherence average [17].

From Kimmel and Kendall's study, it was found that the bicoherence methods described proved useful in determining two nonlinear interactions within the hypersonic



(a) (b)

Figure 24. Bicoherence over Kimmel and Kendall's cone at (a) station 36 (laminar boundary layer with instabilities) (b) station 37 (onset of boundary layer transition) [17]

boundary layer. The two primary nonlinear interactions observed were harmonics and phase-locking. Harmonic interactions occur when a given frequency interacts with itself to produce sub-harmonic oscillations. Harmonic interactions appear in the bicoherence as a strong interaction of a given frequency with itself and are denoted as peak *a* in Figure 24 (a). In the power spectra, harmonic interactions are often revealed as higher frequency peaks at multiples of the primary frequency and were determined by Kimmel and Kendall to be the most likely reason for the second, high frequency peak in Figure 22. Phase-locked interactions on the other hand are the result of two different frequencies interacting with one another due to similar phase velocities. Phase-locked interactions appear as peaks in bicoherence between a high frequency and a low frequency and is denoted as peak *c* in Figure 24 (a). In the power spectra, phase-locked interactions are not as easy to identify since they do not produce harmonic frequency peaks like harmonic interactions, but if their presence leads to the amplification of the lower frequency, then a low frequency peak may be observed.

Harmonics and phase-locked interactions are not entirely independent. As Figure 24 (a) shows, once a sub-harmonic peak forms at a higher frequency, this new peak can itself interact with the original primary peak (peak b) and the lower frequency content (peak d). Bicoherence was found to not only be useful for characterizing nonlinear interactions as the instabilities amplified, but was also found to be useful in describing the breakdown of the boundary layer to turbulence due to the nonlinear interactions. Figure 24 (b) shows that at a further downstream location where transition onset was determined to begin, it is observed that the harmonic interaction bicoherence amplitude reduces and the low frequency phase-locked interactions broaden. This broadening of the bicoherence domain and reduction in overall bicoherence amplitude was determined to be a strong indication of nonlinear breakdown to turbulence [17].

More recent developments in measuring and characterizing nonlinear interactions include a study performed by Zhu et al. in 2016 over a flared, sharp cone at Mach 6. Similar to the findings of Stetson, Kimmel, and Kendall, Zhu et al. found that their geometry exhibited strong harmonic interactions of the second Mack mode and phase coupling with the phase coupling appearing to dominate transition. Through the use of particle image velocimetry, it was determined that the nonlinear interactions of second mode packets with lower frequencies resulted in vortical and dilatational waves developing in conjunction with the second mode waves. The presence of vorticity and dilatation was determined to be a nonlinear energy transfer mechanism for energy to be moved from the second Mack mode into the lower frequency band. The findings from their study further imply that nonlinear interactions are a primary factor of boundary layer breakdown and suggest that vorticity and dilatation effects can accelerate phase-locked interactions [74].

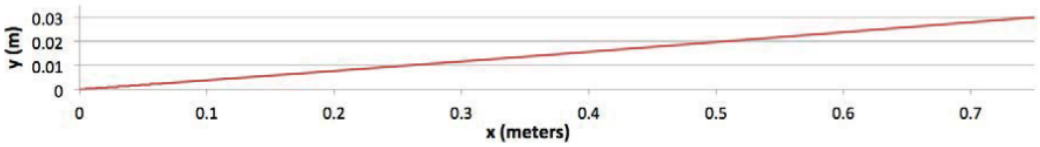
2.5 Purdue Cone-Ogive-Cylinder Entropy Layer Experiment

In an attempt to better understand the intricacies associated with entropy layer instabilities that are most likely plaguing the blunt cone transition reversal phenomenon, a series of experiments were carried out from 2011-2015 in the Purdue Mach 6 Quiet Tunnel (BAM6QT) facility. The BAM6QT shares many geometric and run time qualities with the AFRL Mach 6 Ludwieg Tube, but produces a significantly "quieter" freestream due to reduced freestream noise emanating from the nozzle walls. These experiments entailed the use of a 1 meter long cone-ogive-cylinder model with variable nose tip geometries to generate and measure entropy layer instabilities and transition effects. A hotwire anemometer was used to measure high frequency flow oscillations at various downstream positions and heights above the model while surface mounted pressure transducers were used to track instabilities at the model surface [19].

2.5.1 Flared Cone Model.

The original intentions of these experiments were to demonstrate first Mack mode effects on blunt cone transition. In an attempt to achieve this effect, a sharp tipped, flared cone design, pictured in Figure 25, was created. The model was designed using optimization techniques alongside STABL analysis by Lindsay Kirk at NASA-Johnson Space Center for first mode amplification under the BAM6QT run conditions [75].

Despite the attempt to optimize first mode amplification in the design of the flared cone model, it was later discovered that the optimization process failed to properly stipulate that the second Mack mode instabilities had to be amplified at a lower rate than the first mode. As a result, it was found through numerical analysis as shown in Figure 26 (a), and experimental results as shown in Figure 26 (b), that the first mode failed to be present or dominate in the boundary layer over the model. The



(a)

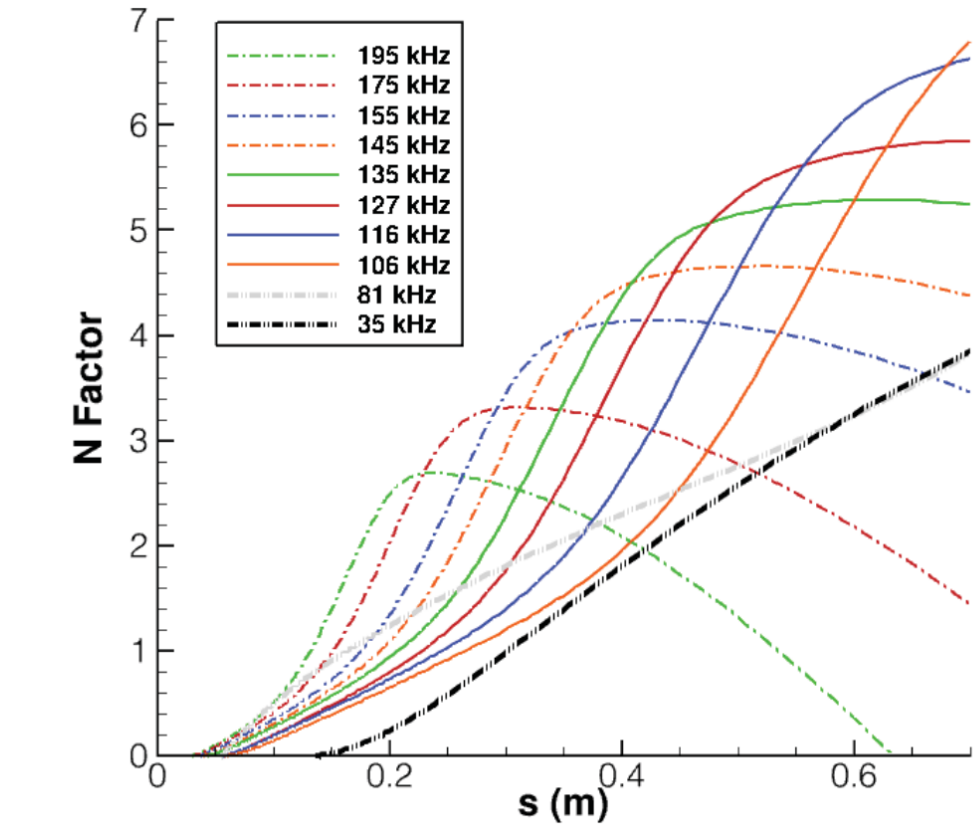


(b)

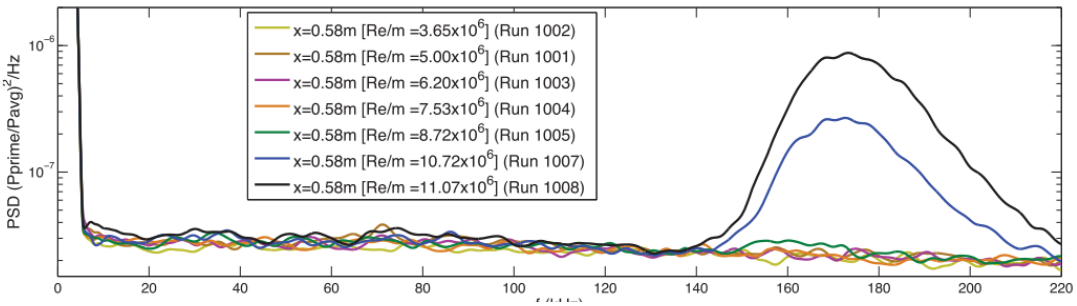
Figure 25. Flared cone model (a) body contour profile (b) disassembled photo [19]

use of a flare on the cone was intended to maintain a relatively constant thickness boundary layer, thus allowing a greater distance for the first mode N factors to grow than a non-flared cone setup. Unfortunately, the flared geometry also greatly affected the second mode, and thus caused the flow to be dominated by second mode effects, washing out any first mode factors [19].

Despite the unfortunate lack of first mode excitation, there was a successful agreement between predicted and measured second mode instabilities over the flared cone. Table 1 demonstrates this strong agreement between the STABL predictions and the experimental measurements. There is a clear drop in frequency in frequency of the instability as the boundary layer grows downstream and the RMS of the signal grows as the instability amplifies just as the N factor predicts. These effects, while not the desired intent of this experiment, were still considered positive due to the strong agreement between the theory and the experimental data in regards to the second mode [19].



(a)



(b)

Figure 26. Flared cone model (a) computed N factor results for first (35 and 81 kHz) and second mode (higher frequencies) (b) experimental results showing only second mode [19]

2.5.2 Cone-Ogive-Cylinder Model.

Due to the complications exciting and measuring the first mode over the flared cone model, the research team moved on to a cone-ogive-cylinder model in an attempt to correct the original issues faced. The basic premise of the design was to vary the

Table 1. Comparison of predicted and experimental second Mack mode instabilities over the flared cone [19]

	Frequency (kHz)		Magnitude	
x (m)	Predicted	Measured	Predicted N factor	Measured RMS
0.5m	195	190	8.4	0.064
0.58m	175	170	9.8	0.082
0.68m	153	153	10.6	0.109

conical tip angle of the model to determine the effects on instabilities downstream. The long cylindrical body was designed with the intent to provide the maximum distance for any first mode instabilities generated in the tip region to be amplified downstream. The sharp, conical tip section was blended into the cylindrical body of the geometry via an ogive curve fit described in Zucrow and Hoffman's Gas Dynamics book from 1985 [76]. This method for designing the nose tip of this geometry as it will be addressed in Chapter 4 of this report during the description of this author's model [19].

After iterating on the general cone-ogive-cylinder design, the research team inevitably selected a design with eight interchangeable nosetip angles, pictured in Figure 27. Surface mounted Kulite XCQ-062-15A high frequency pressure transducers were placed down the length of the geometry and a hot wire anemometer was used above the model to measure flow instabilities [19].

2.5.3 Numerical Predictions.

Initial stability analysis performed using PSE-Chem in the STABL software package showed promising first mode N factor results. Figure 28 (a) shows one such result that indicates the first mode frequencies to be on the order of and even dominate

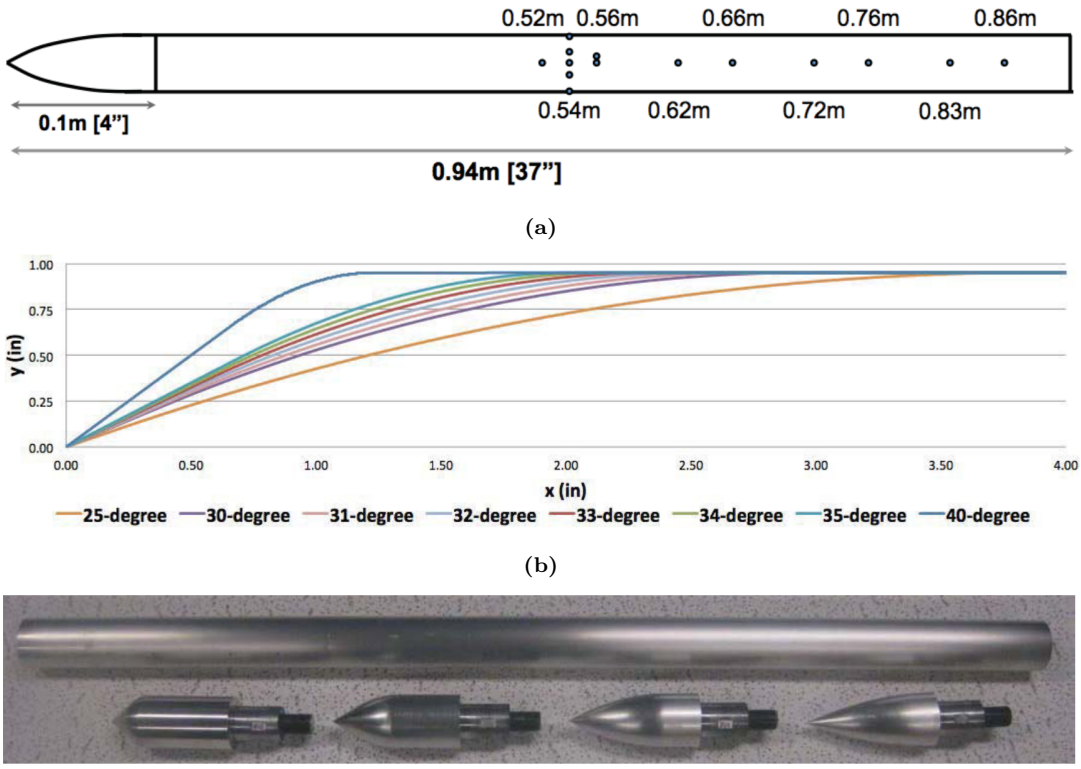


Figure 27. Cone-ogive-cylinder model (a) sketch (b) tip contour profiles (c) disassembled photo [19]

over second mode frequencies. After performing the same predictive analysis for the various nose tips, Table 2 was generated and showed promising implications of a first mode instabilitiy to be present on the geometry. It was found during this analysis that the cylinder diameter had little effect on the predicted instability characteristics. Another model was considered that would have had a flared portion over the cylinder to allow for a relatively constant boundary layer height, but it was found that this had a greater effect on amplifying the second mode instead of the first mode. This result aligned with the results found over the flared cone and thus this flared cylinder model was not made for the experiments [19].

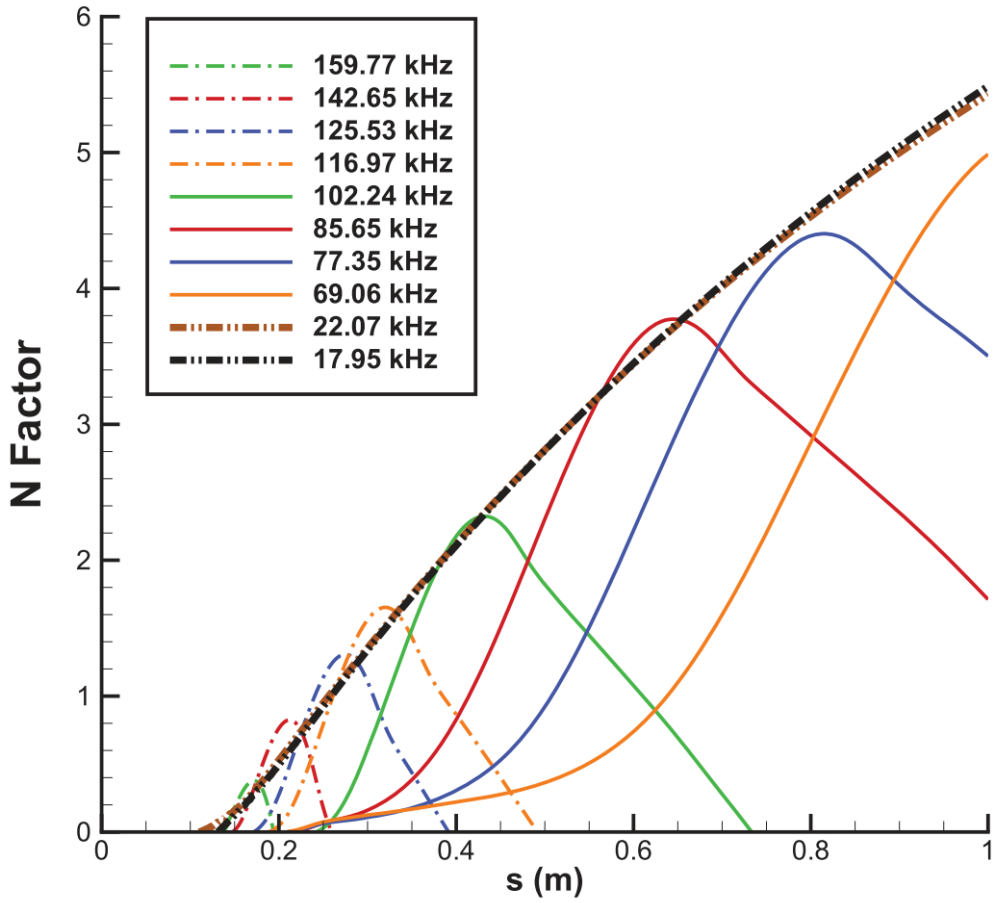


Figure 28. Cone-ogive-cylinder predicted N factor for the 25 degree tip [19]

Table 2. Cone-ogive-cylinder predicted N factor table for the various tips [19]

Leading-Edge Cone Half-Angle (degrees)	1st Mode N Factor	2nd Mode N Factor
20	0.05	3
25	2.0	2.1
30	1.9	1.3
35	1.6	0.7
45	0.7	0.3

2.5.4 Experimental Results - Surface Measurements.

With the numerical predictions made, the research team proceeded to perform experimental studies of the cone-ogive-cylinder model with the various nose tip angles. Power spectra of surface measurements from some of the first tests on this model, pictured in Figure 29 and tabulated in Table 3, revealed an apparent 20-40 kHz broadband disturbance that matched neither first or second Mack mode predictions and appeared to be much more prevalent on the higher nose angle model [19].

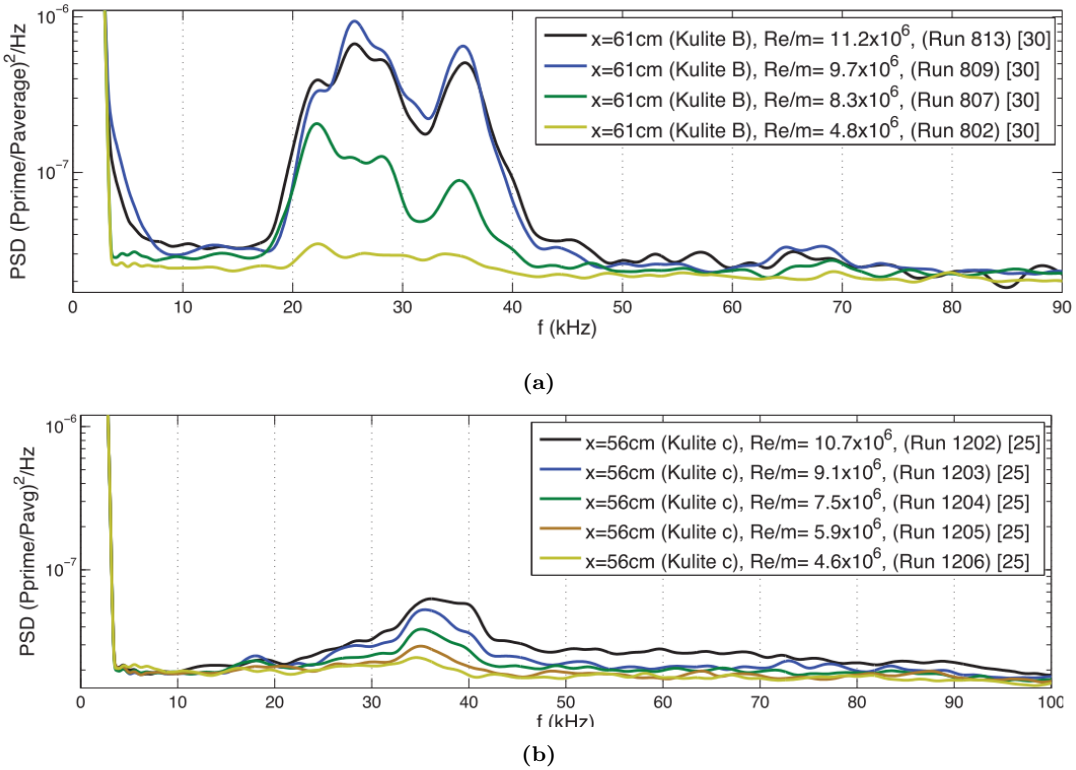


Figure 29. Surface power spectral density results (a) 30 degree tip results (b) 25 degree tip results [19]

With this broadband disturbance feature appearing in the power spectra for the surface measurements, the research team performed a series of verification techniques to ensure what was showing up was not a modal instability. The research team was able to show that the 20-40 kHz response was not affected by model vibrations and was not affected boundary layer disruptions (1-4mm "trip-strips" placed around the

Table 3. 30 degree tip experimental results compared to predicted frequencies [19]

P_0 (psia)	First-Mode (kHz)	Second-Mode (kHz)	Disturbance Range (kHz)
160	17	85	20-40
80	10	43	20-40

model). It was shown that the instability maintained constant frequency for a given tip angle regardless of freestream unit Reynolds number and length based Reynolds number as shown in Figure 30. It was also shown that the instability was present for almost all of the nose angles, but that the frequency varied with the tip angle as shown in Figure 31 [19].

It was observed during the surface measurement analysis, that the instability structure appears to amplify to a certain point along the model length, dampen for a short segment, and then rapidly re-amplify. This effect can be observed from 0.71m to 0.91m in the power spectral results of Figure 30 and is emphasized in Figure 32 where the pressure RMS over the instability frequencies are depicted [19].

With the evidence of the instability not being dependent on the boundary layer, it was hypothesized that the instability was being generated in the entropy layer and there were little to no modal instabilities present in the measurements. The damping and re-amplification effect of instability was attributed to most likely being an entropy layer swallowing process effect. Figure 33 shows a mean flow solution for the 30 degree tip case and indicates that the swallowing length occurs at approximately 0.75 meters down the length of the cylinder where the damping of the instability occurs [19].

2.5.5 Experimental Results - Off-Surface Measurements.

With the instability measured on the surface being identified as most likely an entropy layer instability, the research team conducted off-surface measurements using

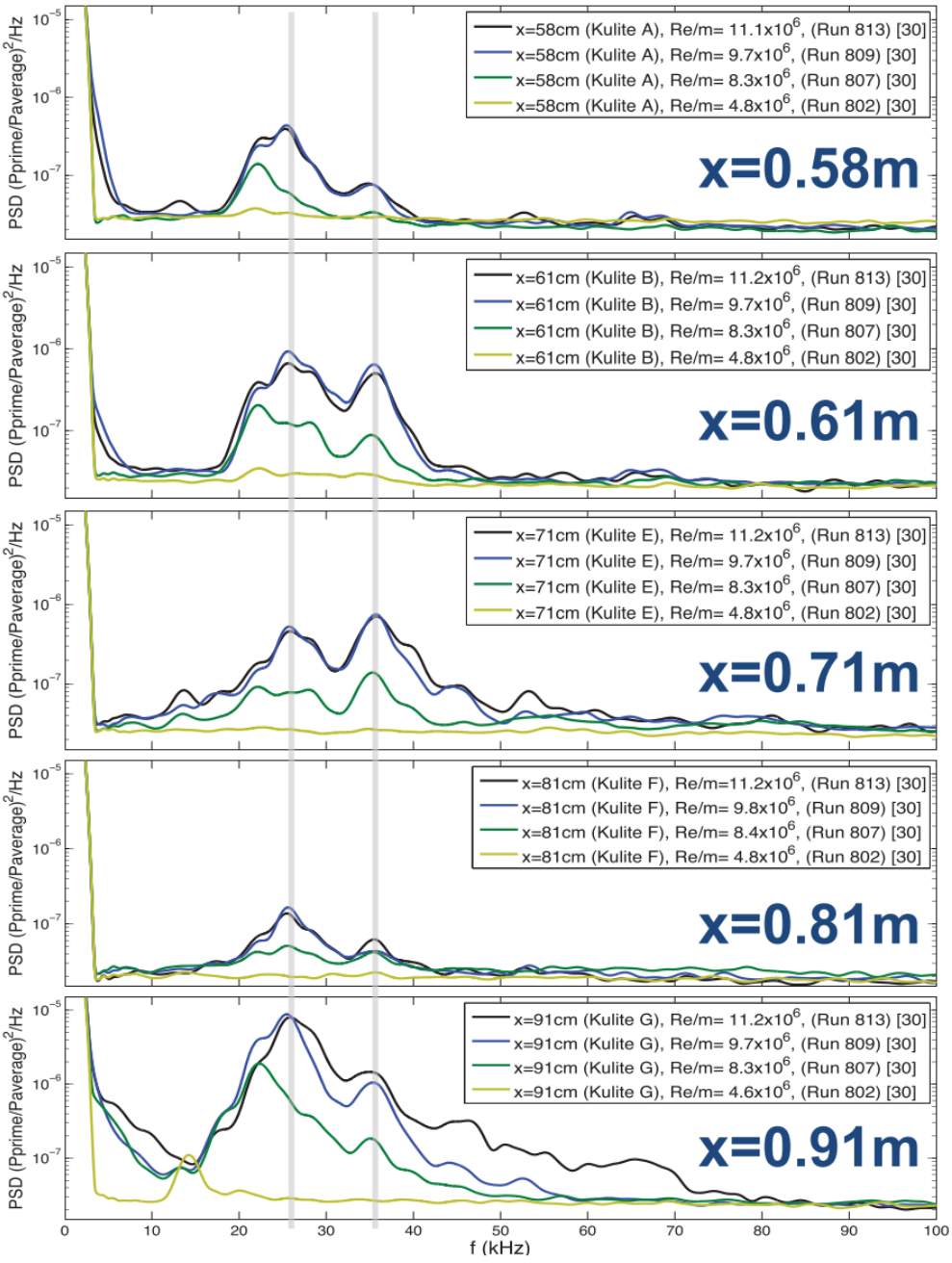


Figure 30. Instability frequency independent of Reynolds number [19]

a hot wire anemometer to characterize the structure and behavior of the instability above the model. It was found that the anemometer was capable of detecting and measuring disturbances outside and within the boundary layer as shown in Figure 34

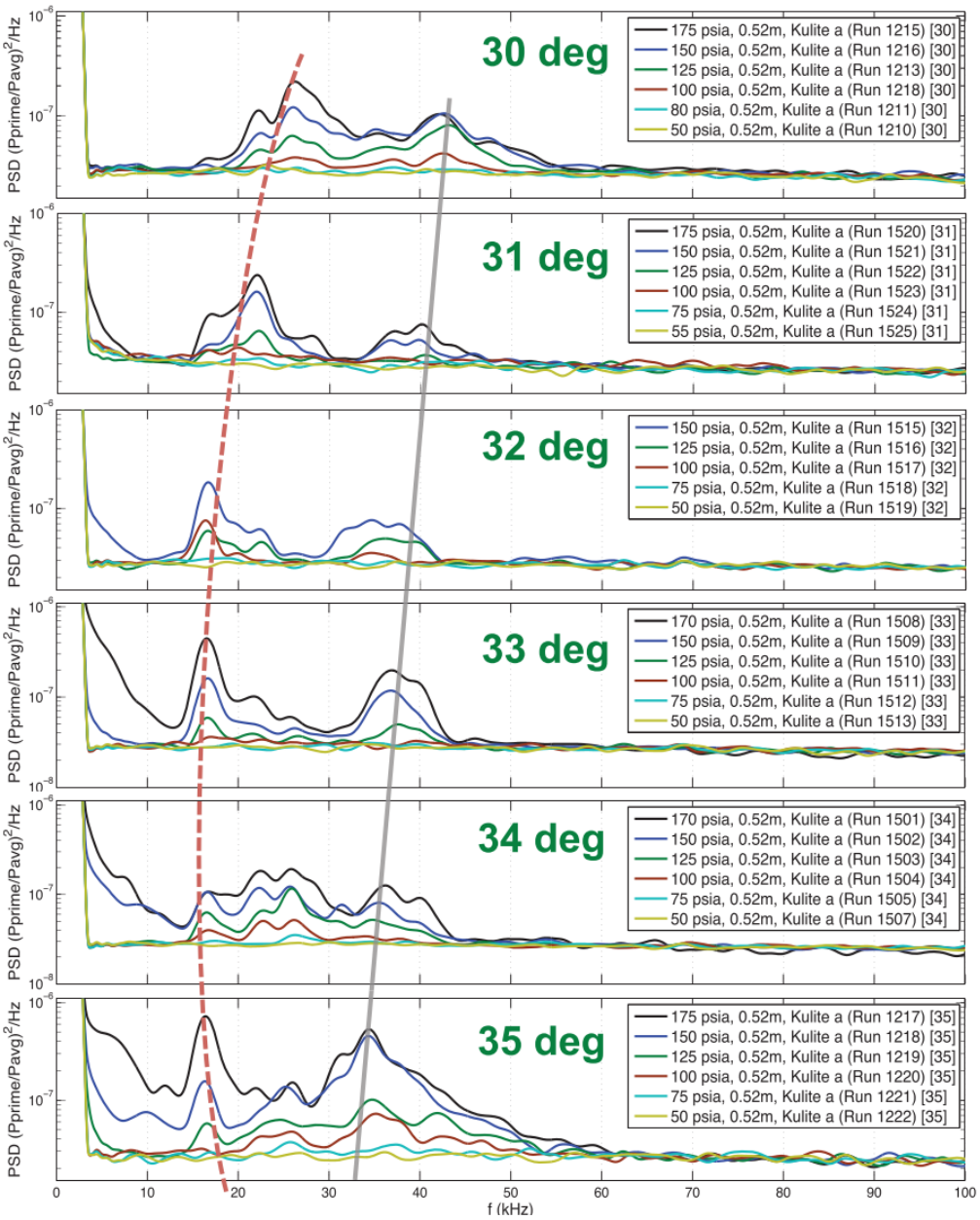


Figure 31. Instability frequency dependent on tip angle [19]

(a). Cross correlation and coherence analysis show that the instabilities picked up by the hot wire most likely are the same instabilities measured by the surface mounted sensors as shown in 34 (b) [19].

By taking hot wire measurements at various axial locations and heights above

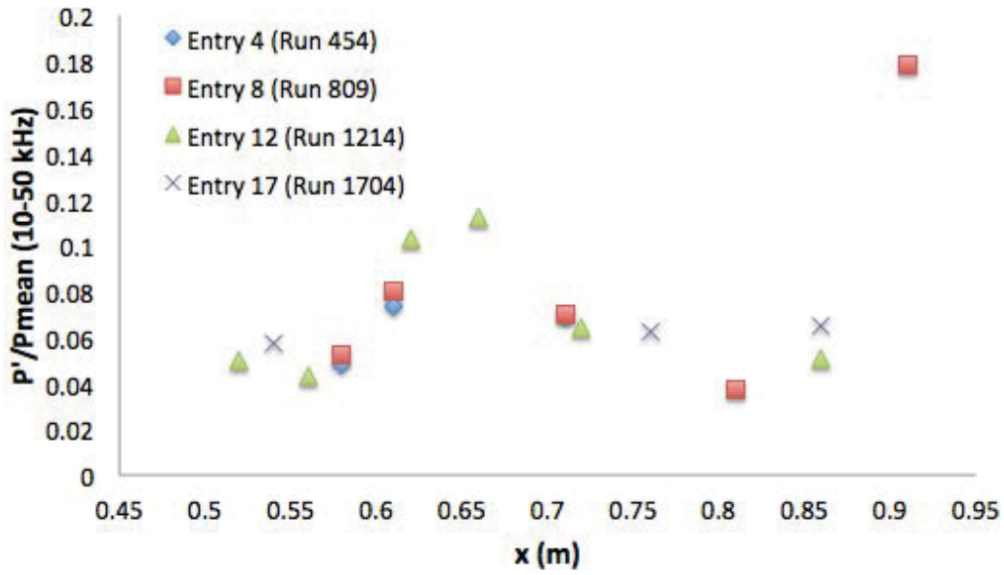


Figure 32. Instability pressure RMS amplitude vs axial location on the 30 deg tip model [19]

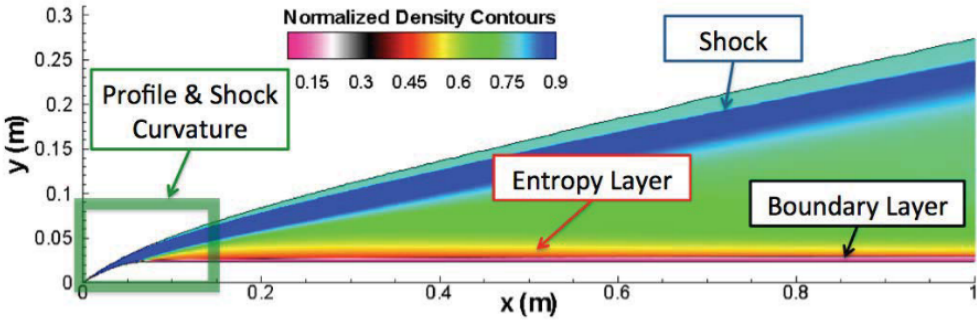
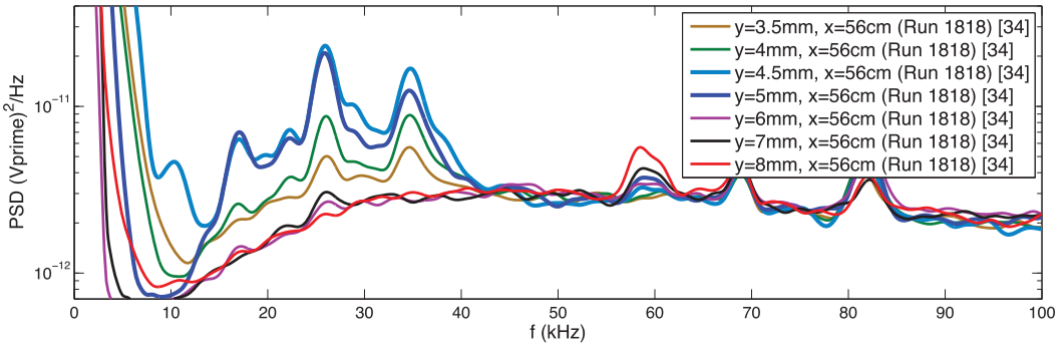
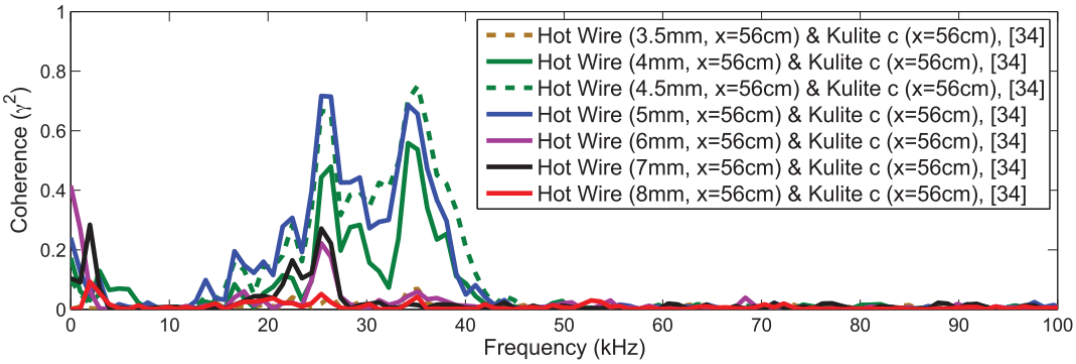


Figure 33. Mean flow solution normalized density contours over the 30 deg tip model [19]

the model, the position of maximum measured entropy layer instability magnitude was created in Figure 35. From this result, it is clear that the tip angle has a direct influence on the measured instability and that the instability appears to originate outside of the boundary layer and is eventually swallowed. Unfortunately, no hot wire measurements could be taken any further rearward where the surface measurements showed the damping and rapid re-amplification of the instability [19].



(a)



(b)

Figure 34. Hot wire anemometer results over the 34 degree tip model (a) power spectral densities (c) signal coherence with surface mounted sensor [19]

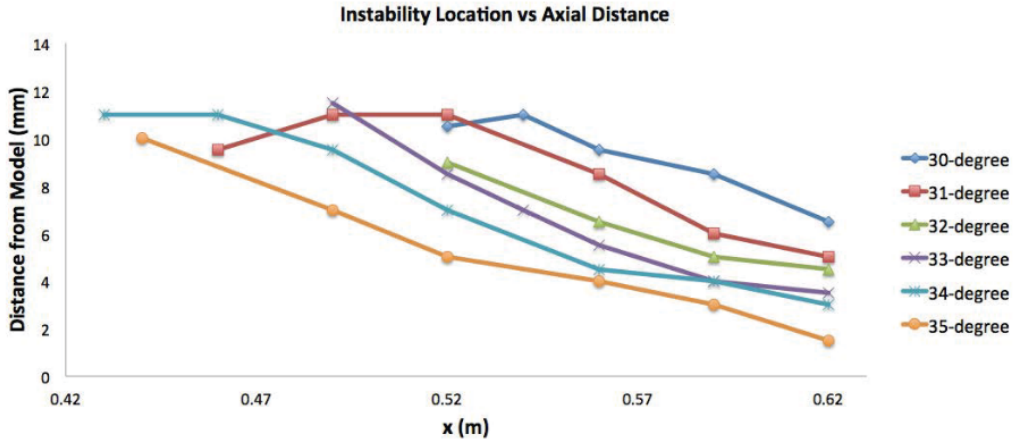


Figure 35. Locations of maximum entropy layer instability magnitude above the model [19]

For the 35 degree tip model, transition was detected by both the surface and hot wire measurements starting at approximately 0.62 meters down the length of the body as shown in Figure 36. The hot wire measurements imply that the spectral broadening detected by the hot wire was most likely centered around the instability frequencies and thus most likely caused by the instabilities themselves [19].

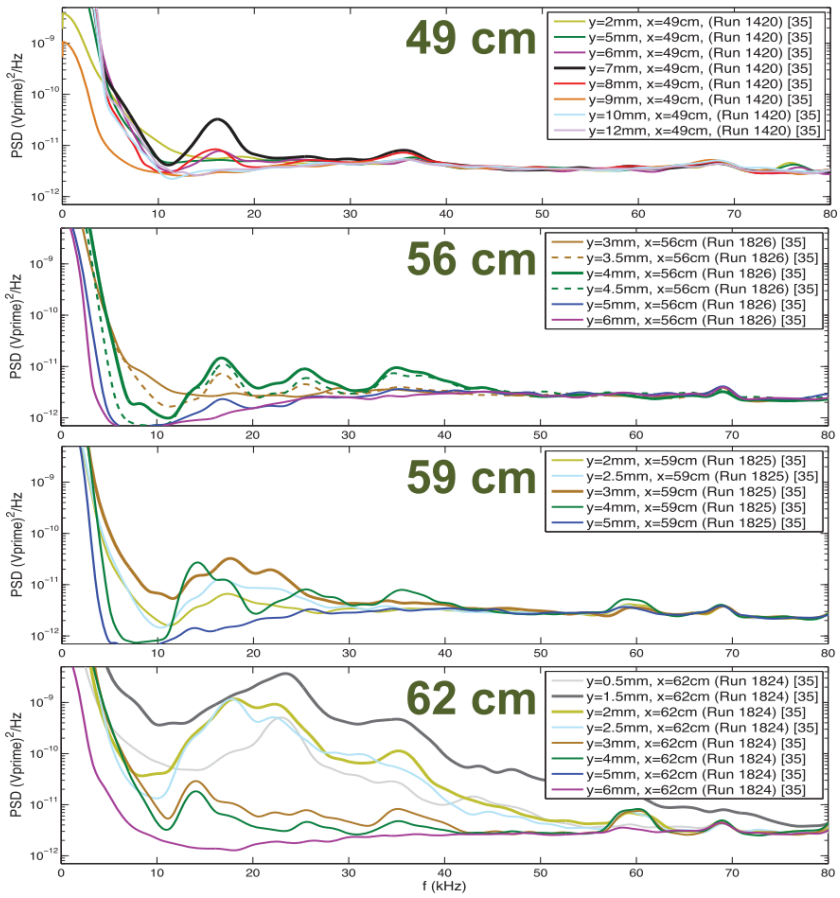


Figure 36. Hot wire measurements showing spectral broadening indicative of transition most likely caused by entropy layer instability [19]

In the end, the results imply that a cone-ogive-cylinder model such as the one used in these studies is capable of creating measurable entropy layer instabilities that can lead to transition on the cylindrical body of the model. While the intended purpose of creating, amplifying, and measuring first mode instabilities was not achieved in his

study, the coincidence of finding instabilities most likely created and amplified by the entropy was a significant and unique finding that leaves much more work to be done to explain the instability's behavior.

III. Methodology

The initial task given to this author was to perform research into the fundamental physics behind the blunt cone transition reversal phenomenon. Upon a review of the literature leading up to the current state of the research community, it was determined by this author that the entropy layer instability results produced by researchers at Purdue over a long cone-ogive-cylinder geometry were worth pursuing further [19]. The Purdue research team's findings are one of the most detailed instances of hypersonic entropy layer instability being measured over a relevant geometry and leaves plenty of room for further investigation.

A new ogive-cylinder model with exchangeable nose geometries was designed and ran in a series of experiments in the Air Force Research Lab's Mach 6 Ludwieg tube facility. This new model's tips were designed using a new geometry profile technique and has a slightly larger cylinder radius than Purdue's original model. Two different models of surface mounted, high frequency pressure sensors were used along the centerline of the cylindrical body of the model. Along with surface mounted pressure transducers, the novel, non-intrusive off-surface disturbance measurement technique known as a focused laser differential interferometry (FLDI) was used in an attempt to measure dominant frequencies and identify the accompanying instabilities inside and outside the boundary layer. Lastly, high speed Schlieren was used to capture images of the boundary layer instabilities and flow features such as the boundary layer thickness.

Validating cases for the various techniques used in this study were performed for a well characterized geometry. A seven degree half angle sharp cone described in detail in a thesis by Second Lieutenant Ryan Oddo was used in the same AFRL Mach 6 Ludwieg tube facility as validating cases for the measurement techniques used in this study [22]. Spectral analysis techniques including power spectral densities,

spatial to temporal fast Fourier transforms, and bicoherences were used to process the experiment data sets.

3.1 AFRL Mach 6 Ludwieg Tube Facility

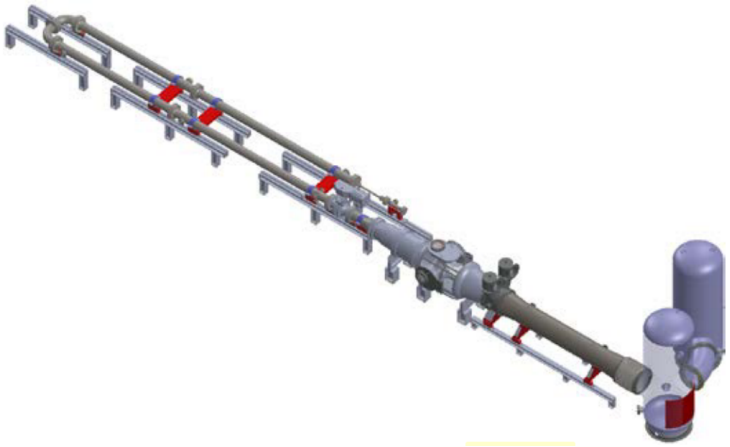


Figure 37. Perspective render of the AFRL Ludwieg tube [20]

All of the experiments in this study were carried out in the Air Force Research Lab (AFRL) Mach 6 Ludwieg tube facility at Wright-Patterson Air Force Base in Dayton, Ohio. This facility was designed and built under the supervision of Dr. Roger Kimmel of the AFRL Aerospace Systems Directorate. This low-enthalpy tunnel operates on dry air and is configured with a 30 inch exit diameter nozzle that is capable of delivering two, 100ms periods of steady Mach 6 flow at a variety of Reynolds numbers. The tunnel has a freestream unit Reynolds number range of $2.28 * 10^6/m$ to $3.01 * 10^7/m$ for driver tube pressures of 50psia and 580psia respectively. The tunnel has operation turnaround times of 5 and 12 minutes for the lower and upper limit driver tube pressures. The majority of this turnaround time is dominated by the driver tube pressurization and test section vacuuming.

Figure 37 depicts a rendering of the full tunnel length including the stagnation chamber, test section, and vacuum chamber. The mission of the tunnel is *to provide*

hands-on access for engineers to conduct basic research in fluid dynamics, instrumentation development and related disciplines [20]. Currently, the tunnel is under the direct supervision and operation of Dr. Matthew Borg who coordinates and leads both academic and applied research efforts in the facility. A state-of-the art tunnel control room was completed in 2019 which allows for the complete operation of the facility without the operator having to leave the control room between runs.

3.1.1 Tunnel Components.

The basic premise behind the Ludwieg tube has been described many times (such as by Friehmelt et al. [77]). In short, a Ludwieg tube consists of a high pressure driver tube that is isolated from a low pressure section by either a valve or diaphragm. A test section is place between these two chambers with a converging-diverging nozzle that accelerates the flow to speeds determined by the pressure ratio and nozzle geometry. Upon the release of the valve/diaphragm, the high pressure flow is quickly accelerated through the nozzle into the vacuum, providing high Mach number flow through the test section. Once the the driver tube pressure reaches a low enough pressure, the valve is then closed and the driver tube is re-pressurized. The Ludiweg tube tunnel thus allows for quick turnaround testing and easily repeatable results [20].

The AFRL Ludwieg tube design closely follows the basic premise behind the generic Ludwieg tube design. The AFRL facility was designed with the specific intent of providing researchers with fast turn-around operation capabilities with high amounts of flexibility. The current operation design point is Mach 6, but the tunnel also has nozzles capable of Mach 4 and Mach 8 flow that the tunnel is capable of accommodating. The tunnel is currently actuated using a fast piston valve, but also has the capability of supporting a burst diaphragm and ball valve. The driver tube, diffuser, and vacuum tanks all contain access ports for maintenance and modification

purposes. The test section contains three access ports with the main port using an autoclave door for swift access. The following subsections provide a more in-depth breakdown of the various components making up the facility.

Compressors and Vacuum Pumps.

In order to provide redundancy, the tunnel is powered by two compressors, see Figure 38 (a), and two vacuum pumps, see Figure 38 (b). The compressors are Sauer 580 psi, 50 SCFM models, operating and 27 HP each. The vacuum pumps are Leybold 444 CFM models, operating at 25 HP each. With these compressors and vacuum pumps, the tunnel is capable of pressurizing the stagnation chamber to 220 psi (a typical operation pressure) in five minutes and to 580 psi (the upper pressure limit) in 12 minutes [20].



(a) **(b)**

Figure 38. (a) Compressors (b) Vacuum Pumps [21]

In order to heat the stagnation chamber air to the operating temperature of 500K, a commercial Sylvania 18kW resistance heater is used. An accumulator tank was not needed in this design due to bypass system design. The compressors run continuously during operation until the desired operator defined set pressure is achieved at which point a bypass valve opens and allows the excess compressed air to be vented off. This allows for the stagnation chamber to be quickly charged in back-to-back runs

without having to start and stop the compressors [20].

Driver Tube.



Figure 39. AFRL Mach 6 Ludwieg tube driver tube [21]

The driver tube for the tunnel, shown in Figure 39, is a 9.75 inch inner diamter 304 stainless steel pipe that consists of two parallel 35ft sections connected by a 180 degree bend. This design, known as a "reflexed driver tube," was chosen due to space constraints to keep the entire tunnel enclosed inside the facility. Unsteady CFD simulations was used to confirm that the use of a bend in the driver tube would not produce undesirable shock reflections in the tunnel. The total internal length of the driver tube is 82ft which provides approximately two, 100ms periods of steay flow. During the run, the air used in the two steady periods originates from only the first 30ft of the driver tube and thus is not contaminated by secondary flow due to the bend. The driver tube is also freely mounted on a rail system that allows for the entire assembly rear of the nozzle to be rolled back for maintenance and also provides relief for thermal expansion of the system. Lastly, the driver tube is wrapped in blanket

resistance heaters and insulating wrap to maintain the stagnation temperature of 500K. This method of heating the entire length of the driver tube minimizes effects due to convection and non-uniform heating requirements [20].

Nozzle.

The nozzle of the tunnel is composed of three sections which consist of a 316 stainless steel throat and two 6061-T6 aluminum downstream sectios. The nozzle was originally designed using the method of characteristics, but viscous CFD simulations were later used to finalize the final contour. Boundary layer growth effects from the viscous CFD resulted in the nozzle wall area ratio being increased by 23% from the initial inviscid results by decreasing the throat diameter. The final Mach 6 nozzle design resulted in a 3.71in throat diameter and a 30in exit diameter. Upstream of the nozzle throat is a 10in diamater straight lead-in that is followed by the contraction section. Overall, the nozzle assembly measures 117 inches long [20].

Test Section.

The tunnel test section is a 50in diameter, carbon steel chamber and is shown in Figure 40. Three access ports provide both maintenance and optical access to the test section. Two of the ports are positioned opposite each other on the sides of the tunnel and the final port is located on the top of the tunnel. Each port can hold windows up to 12in in diameter. A variety of windows can be used in any of these ports that allow for Schlieren, FLDI, infrared, and other imaging/optical techniques to be used. The nearside of the test section uses pneumatic driven autoclave door to provide quick access to the test section. On both sides of the test section, Thor labs optical tables are used to provide vibrationally dampened optical mounting surfaces [20].



Figure 40. AFRL Mach 6 Ludwieg tube test section [21]

Diffuser and Vacuum Tanks.

Downstream of the test section is a 44in diameter capture cone that funnels the flow into the diffuser. The diffuser is a 127in long, 29.5in diameter straight pipe with a 6 degree convergin inlet and a 4 degree diverging cone exit. A safety vent is located between the test section and the diffuser to ensure the test section is not over-pressurized. The diffuser then dumps into a double receiver vacuum tank as shown in Figure 41. The vacuum tank consists of two, 2000 gallon chamber connexted via an elbow joint. During the operation of the tunnel, the vacuum tanks and the test section are pulled down to near-vacuum conditions before the valve is actuated to allow for the flow to begin [20].

Valve.

The tunnel uses a fast action plug valve to initiate runs as shown in Figure 42. The tunnel is also capable of using a ball valve or diaphragms for capability redun-



Figure 41. AFRL Mach 6 Ludwieg tube vacuum tanks [21]

dancy. The fast valve uses an aluminum plug that is held in position before a run by the pressure of the driver tube. When a run command is given to the tunnel, vacuum is rapidly pulled behind the plug, causing it to be slammed back and allow the pressurized air from the driver tube to be flowed into the nozzle. A nylon cushion is position behind the plug to prevent metal-on-metal contact [21].

3.1.2 Tunnel Flow Conditions.

While the tunnel has been in operation for a number of years, there is still a good deal of characterization that needs to be completed of the flow quality. Despite this

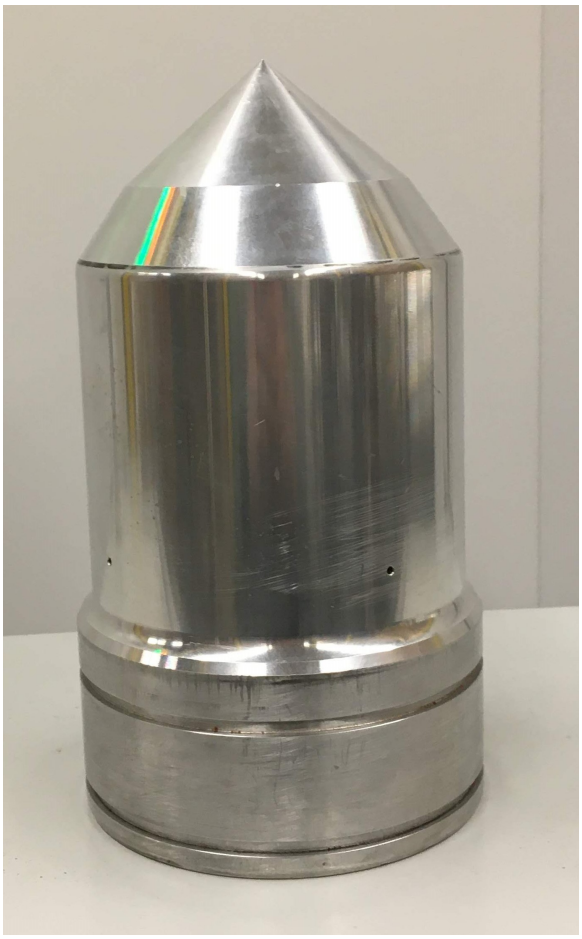


Figure 42. AFRL Mach 6 Ludwieg tube fast-action valve plug [21]

lack of available characterization details, there are still plenty of computational and experimental data available to provide a basic understanding of the flow conditions in the tunnel. As will be shown in this subsection, it should be noted that this tunnel is not a "quiet tunnel" by any meaning of the term, but the flow is consistent and repeatable between runs.

Mach Profile.

Initial CFD simulations of the nozzle showed promising Mach number contours as observed in Figure 43 (a). While the nozzle exit area is 30in, viscous CFD results

showed a boundary layer thickness of approximately 6cm at the exit of the nozzle, effectively decreasing the core flow exit diameter to approximately 25.3in. Both steady and unsteady CFD simulations, shown in Figure 43 (b) and (c) respectively, were run of the tunnel operation and showed core flow exit Mach numbers of approximately Mach 6.1 [20].

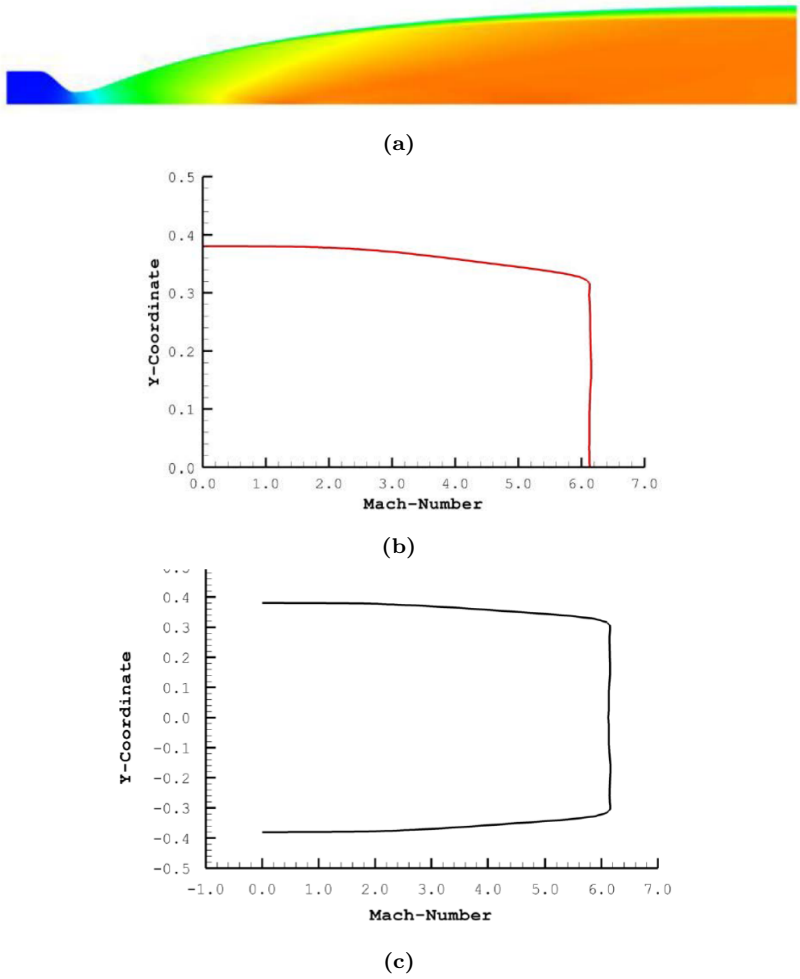


Figure 43. Initial design CFD results (a) Nozzle Mach number contours (b) steady exit Mach number profile (c) unsteady exit Mach number profile [20]

An initial pitot probe verification study was conducted by Kimmel et al. to determine the Mach number variation across the run time of the tunnel. Four pitot probes were positioned at the nozzle exit and used a variety of mounting techniques to determine if there were dependencies on the pitot configuration. Depicted in Figure

44, the results from this study show a Mach number of approximately Mach 6.0 at the nozzle exit with a standard deviation of 2.3%. It is believed that the high standard deviation was due to pressure transducer complications and is a conservative estimate of the tunnel noise at the nozzle exit [20].

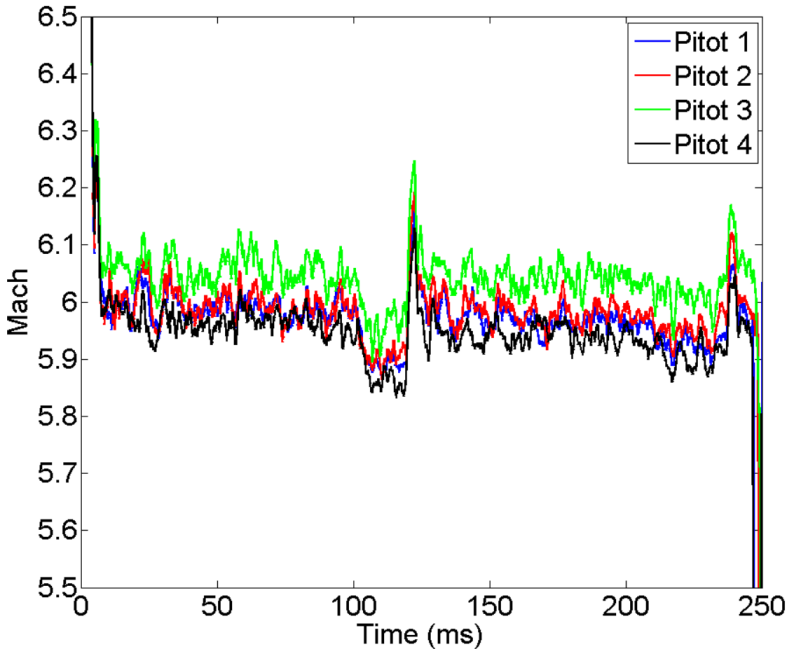


Figure 44. Mach number vs time at the nozzle exit [21]

In an attempt to verify the Mach profile across the test section further downstream from the nozzle exit, a series of pitot rake surveys were executed by the AFRL team with the assistance of AFIT partners and reported by Second Lieutenant David LaBuda in 2019. The team completed the study by using a 30 inch wide pitot probe rake 815mm downstream of the nozzle exit and rotated the sting over a period of 52 runs to produce the results found in Figure 45. This downstream location was chosen due to it being the most downstream mounting position currently capable in the tunnel. From these results it was found that the Mach numbers at the outer edge of the core flow were up to an entire Mach number higher than the core flow. It was also determined from these measurements that the core flow of Mach 6.14 was

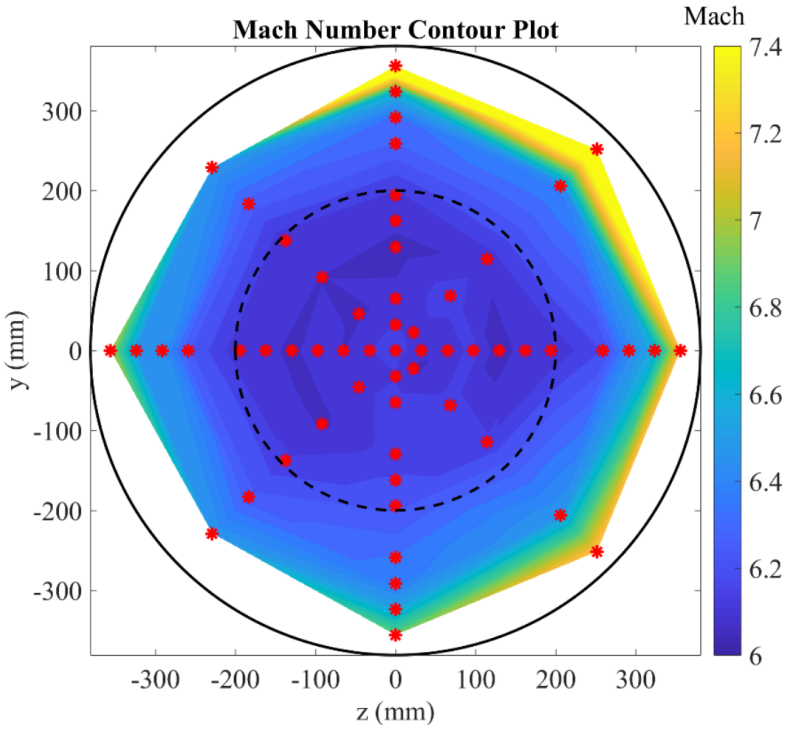
approximately 400mm (15.7in) in diameter at this downstream position (denoted by the dashed circle in the figure) [21].

From these experimental findings, it is determined that the core flow of the tunnel can be considered to be approximately Mach 6.0 to 6.14 all the way out to the rearmost mounting position within the test section. It is also determined that the core flow may not extend out to the full 25.3in diameter as predicted in the CFD results. With this information, it determined that any models placed within the test section can be considered to be in core flow if they lie within the 15.7in diameter core flow found by LaBuda [21]. No further pitot rake tests have been completed at other axial positions within the tunnel to provide more extensive conclusions, but there are plans to conduct more tests in the near future.

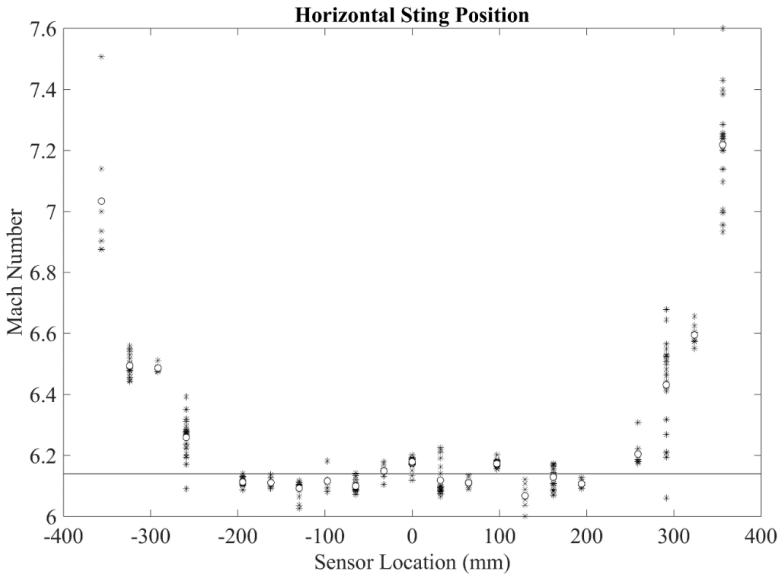
Noise Characteristics.

As previously mentioned, this tunnel is not considered a "quiet tunnel," but there are some experimental results that provide insight into the noise characteristics of the tunnel. Kimmel et al.'s initial report on the tunnel performance used a pitot probe at the nozzle exit to determine the percent RMS fluctuation for the various valve types that the tunnel supports. The results from this study, shown in Figure 46, indicate that the fast valve produced approximately 3% RMS noise. This study did not use the fast valve at stagnation pressures below 300 psia, but the noise level did not change much between the cases that were run [20].

LaBuda performed a similar analysis to Kimmel et al. at the rearmost axial mounting position in the test section of 815mm. Using the same pitot rake configuration that created his Mach contours, Figure 47 shows the results from the noise study reported by LaBuda. From these results it was determined that the core flow at the rearmost axial position maintains a noise level below 2% RMS. Outside the core flow,



(a)



(b)

Figure 45. Experimental pitot probe results 815mm downstream from nozzle exit (a) Mach contours (b) horizontal pitot rake results [21]

the noise levels quickly rise with noise exceeding 10% RMS outside a 300mm radius [21].

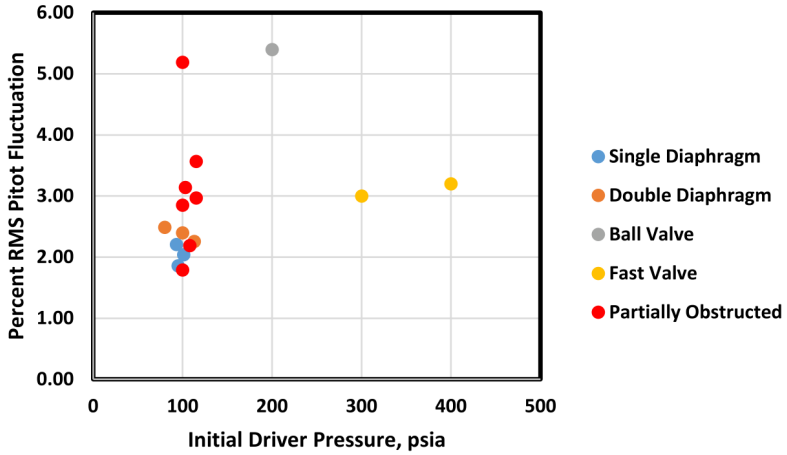


Figure 46. Initial pitot pressure fluctuations [20]

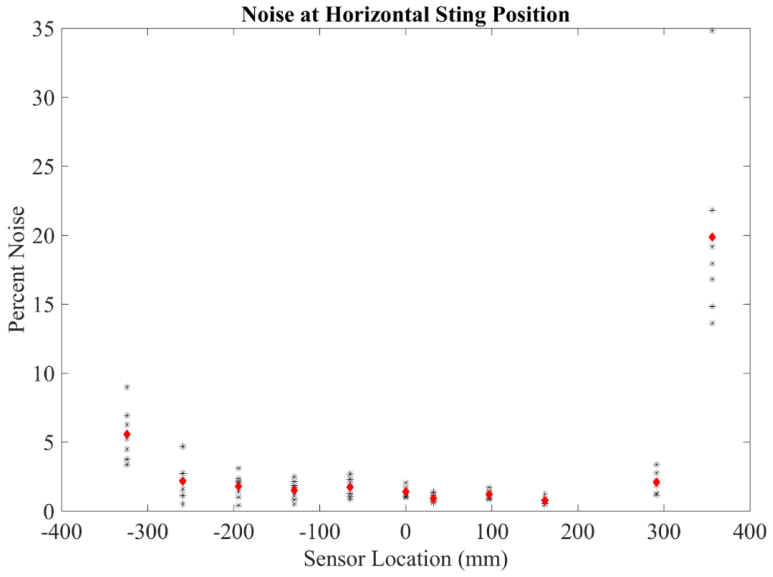


Figure 47. Pitot rake pressure fluctuations [21]

Nominal Run Conditions.

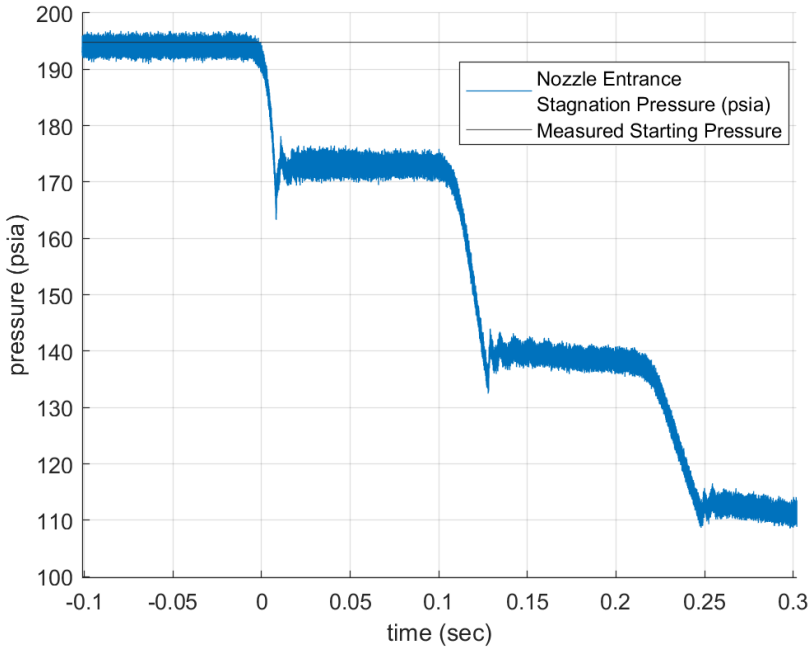
The driver tube stagnation conditions for a given run are completely user defined prior to charging the driver tube. The stagnation temperature is technically variable, but in order to prevent liquefaction of the air during the Mach 6 expansion, the stagnation temperature is held constant at 505K for every run.

As for the stagnation pressure during a run, it is consistently observed that there are losses during the startup of the nozzle and in-between the two, 100ms quasi-steady flow periods when the reflected shock within the driver tube reaches the nozzle throat. Using a pressure probe located prior to the nozzle converging section entrance, the stagnation pressure during each run is tracked. Figure 48 shows an example case of the pressure trace during a run with a set point stagnation pressure of 200 psia. Figure 48 (a) shows the actual pressure trace measurements during the run while Figure 48 (b) shows the trace normalized by the initial measured set pressure.

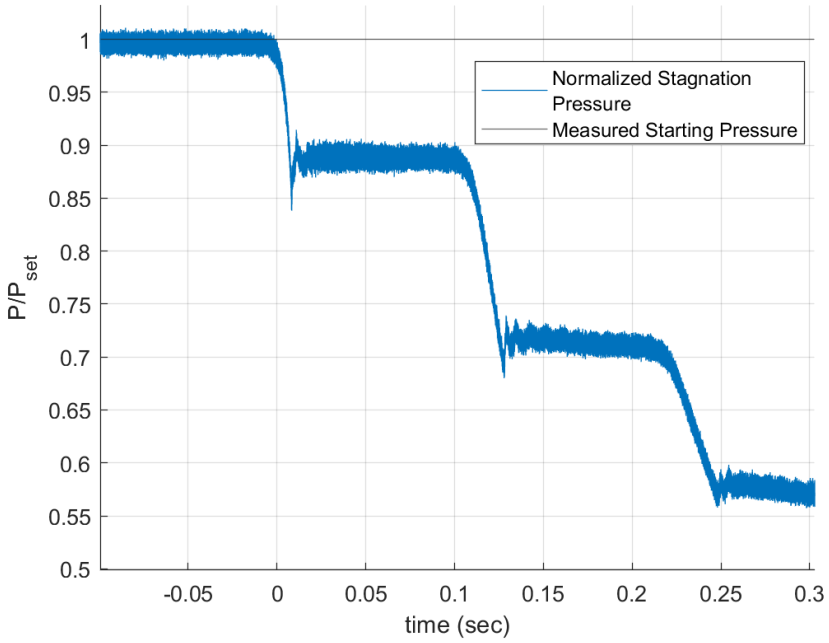
From Figure 48, a few features of the tunnel's stagnation pressure qualities can be observed. First, it can be observed that, while the set pressure for the run was 200psia, the actual initial driver tube pressure drifts down below this set pressure. This is believed to be due to a small leak in the driver tube section near the plug. As a result, every run in the tunnel exhibits a driver tube pressure drift prior to the run beginning. It is believed that the leak is between the driver tube and another component with a back-pressure of 150psia. As a result, runs with a set point driver tube pressure below 150psia will drift upwards, while runs with a set point driver tube pressure above 150psia drift downwards. This drifting effect is consistently observed, but has little effect on the overall run conditions since the drift is typically only a few psia from the set point.

It can also be observed from Figure 48 that the stagnation pressure of the tunnel experiences an approximate 10% loss during startup for the first 100ms period and then drops to approximately 30% loss after the shock impingement for the second 100ms period. These 10% and 30% stagnation pressure drops are consistent regardless of set pressure within the tunnel and are unavoidable due to the nature of physical losses in the system during startup and shock impingement.

Using the known driver tube parameters for each run and assuming a 10% and



(a)



(b)

Figure 48. Tunnel stagnation pressure traces (a) actual psia trace (b) normalized pressure trace

30% stagnation pressure loss for the two quasi-steady 100ms periods, the nominal run conditions for each period can be determined. Assuming isentropic expansion through the nozzle, a series of calculations can be made with the end goal being to determine the unit Reynolds number of each run. The unit Reynolds number is a common parameter used in wind tunnel testing as it is a dimensional variant of the common non-dimensional Reynolds number that allows for any length scale to be applied. It can be considered to be a freestream parameter than is given non-dimensionality when a length scale is applied. The calculation of the freestream unit Reynolds number per length (Re_∞/L) is shown in Equation 7.

$$\frac{Re_\infty}{L} = \frac{\rho_\infty \, U_\infty}{\mu_\infty} \tag{7}$$

where ρ_∞ is the freestream density (kg/m^3), U_∞ is the freestream velocity (m/s), and μ_∞ is the freestream dynamic viscosity ($kg/m * s$). Each of these parameters used to define the freestream unit Reynolds number is not inherently known for each run, so the isentropic expansion of a calorically perfect gas ($\gamma = 1.4$) is assumed for the following calculations:

$$T_0 = T_{DT} \left(\frac{P_0}{P_{DT}} \right)^{\frac{\gamma-1}{\gamma}} \tag{8}$$

where T_0 is the stagnation temperature after the expansion (K), T_{DT} is the driver tube temperature (held at $505K$ for all runs in this facility), P_0 is the stagnation pressure after the expansion (N/m^2), P_{DT} is the driver tube pressure (N/m^2), and γ is the ratio of specific heat (assumed constant for air at $\gamma = 1.4$. Note that for now the ratio of P_0/P_{DT} can be assumed to be 0.9 and 0.7 for the first and second quasi-steady periods respectively. In reality, two pressure sensors for each run measure the actual driver tube and stagnation pressures and can be applied using this same method, but

for providing a nominal set of run condtions, the typical 0.9 and 0.7 ratios will be used. Moving forward and assuming an ideal gas:

$$\rho_0 = \frac{P_0}{RT_0} \tag{9}$$

where ρ_0 is the stagnation density (kg/m^3) and R is the specific gas constant for air ($287.06J/(kg * K)$). Continuing with the assumption of isentropic expansion and calorically perfect gas:

$$T_\infty = T_0 \left(1 + \frac{\gamma - 1}{2} M_\infty^2\right)^{-1} \tag{10}$$

where T_∞ is the freestream static temperature of the flow in the test section (K) and M_∞ is the freestream Mach number ($M_\infty = 6.1$). Along with freestream static temperature, the freestream density can be estimated:

$$\rho_\infty = \rho_0 \left(1 + \frac{\gamma - 1}{2} M_\infty^2\right)^{\frac{-1}{\gamma - 1}} \tag{11}$$

where ρ_∞ is the freestream density (kg/m^3). Finally, freestream dynamic viscosity is found by following the model used by Mack in his 1984 AGARD report for freestream temperatures above $110.4K$ [7]. It should be noted that the freestream temperatures for all the runs conducted in this study were well below the $110.4K$ threshold for this viscosity calculation, but it has been justified previously that this model is sufficient to characterize such flows [78]. The model appears as follows:

$$\mu_\infty * 10^5 = 1.458 \frac{T_\infty^{\left(\frac{3}{2}\right)}}{T_\infty + 110.4} \tag{12}$$

where μ_∞ is the freestream dynamic viscosity ($kg/(m * s)$).

Using each of these equations in conjunction with one another and assuming the typcial 10% and 30% stagnation pressure losses for the two quasi-steady periods, the

nominal run conditions for each driver tube pressure used in this study are tabulated as shown in Table 4. Note that these are estimated nominal run conditions and that the actual run conditions were slightly different run to run. Figure 49 shows the true freestream unit Reynolds numbers achieved for each nominal run condition used in this study, but the reader can see Appendix A for a full list of all the actual flow conditions for each run used in this study.

Table 4. Nominal Run Conditions

P_{DT} $(psia)$	T_{DT} (K)	Quasi-Steady Period	M_∞	P_0 $(psia)$	T_0 (K)	u_∞ (m/s)	T_∞ (K)	ρ_∞ (kg/m^3)	μ_∞ $(kg/m*s)$	Re_∞/L $(1/m)$
75	505	1	6.1	67.5	490	932	58	0.0160	$3.83*10^{-6}$	$3.89*10^{6}$
75	505	2	6.1	52.5	456	899	54	0.0134	$3.52*10^{-6}$	$3.41*10^{6}$
100	505	1	6.1	90	490	932	58	0.0213	$3.83*10^{-6}$	$5.19*10^{6}$
100	505	2	6.1	70	456	899	54	0.0178	$3.52*10^{-6}$	$4.54*10^{6}$
125	505	1	6.1	112.5	490	932	58	0.0266	$3.83*10^{-6}$	$6.48*10^{6}$
125	505	2	6.1	87.5	456	899	54	0.0223	$3.52*10^{-6}$	$5.68*10^{6}$
150	505	1	6.1	135	490	932	58	0.0320	$3.83*10^{-6}$	$7.78*10^{6}$
150	505	2	6.1	105	456	899	54	0.0267	$3.52*10^{-6}$	$6.82*10^{6}$
200	505	1	6.1	180	490	932	58	0.0426	$3.83*10^{-6}$	$1.04*10^{7}$
200	505	2	6.1	140	456	899	54	0.0356	$3.52*10^{-6}$	$9.09*10^{6}$
250	505	1	6.1	225	490	932	58	0.0533	$3.83*10^{-6}$	$1.30*10^{7}$
250	505	2	6.1	175	456	899	54	0.0445	$3.52*10^{-6}$	$1.14*10^{7}$
300	505	1	6.1	270	490	932	58	0.0639	$3.83*10^{-6}$	$1.56*10^{7}$
300	505	2	6.1	210	456	899	54	0.0534	$3.52*10^{-6}$	$1.36*10^{7}$

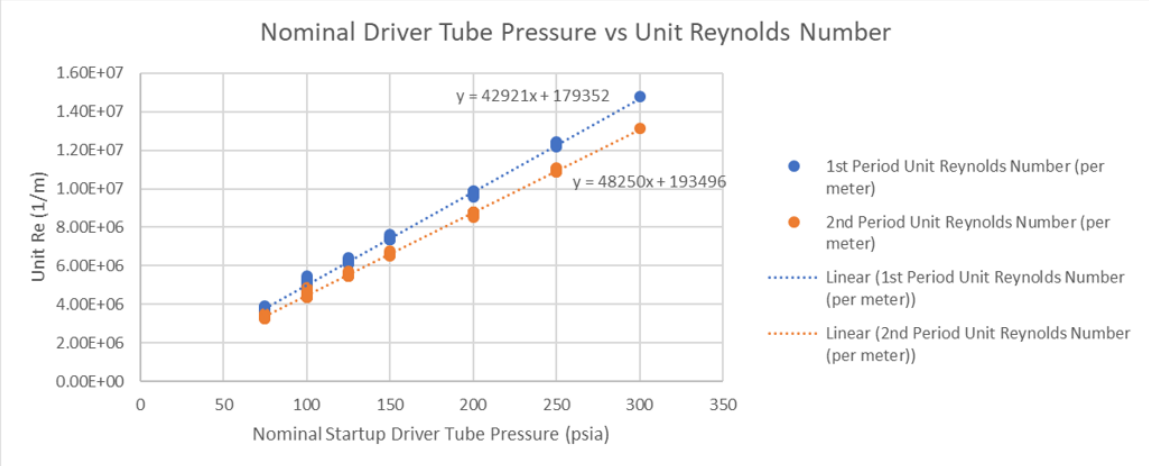


Figure 49. Nominal driver tube pressure vs unit Reynolds number for both quasi-steady periods

3.2 Seven Degree Half Angle Sharp Cone

Across the hypersonic instability and transition research community, the standard geometry used for determining tunnel instability measurement capabilities is the sharp tipped, circular cone [79, 9, 15, 70]. Referred to by this author as one of the "canonical conicals" due to it's frequent appearance in the hypersonic transition research community, the seven degree half angle cone is a well documented geometry with many experimental and computational stability results from a variety of researchers and facilities [11, 15, 70]. For this study, a seven degree half angle cone utilized and described in a thesis by Second Lieutenant Ryan Oddo was used as a verification geometry for the instability measurement techniques used [22].

3.2.1 Geometry.

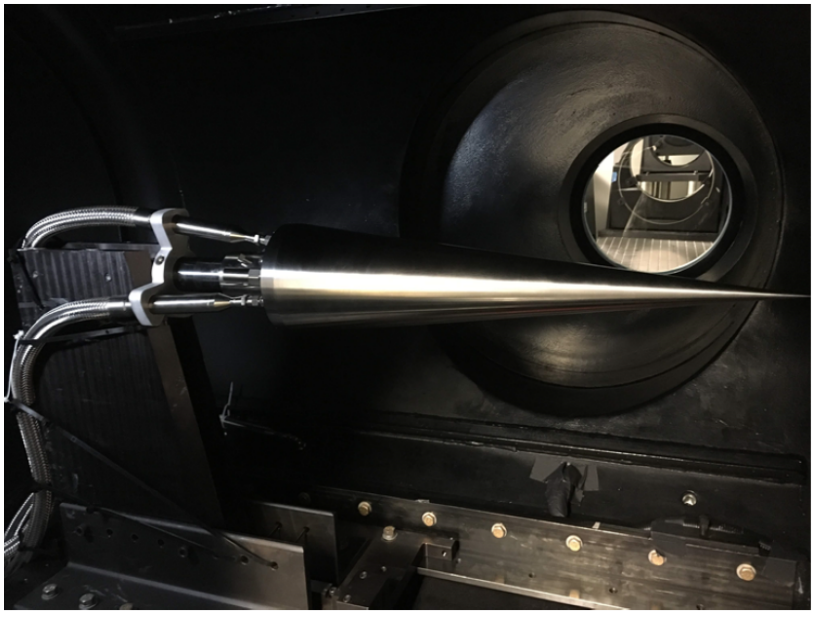


Figure 50. Oddo's seven degree half angle sharp cone mounted in the AFRL Mach 6 Ludwieg tube [22]

Pictured in Figure 50, the cone designed by Oddo is 60.96cm ($\tilde{2}$ft) in length with a seven degree half angle and a base radius of 15.11cm. The cone was machined by

the AFIT machine shop from 303 stainless steel and uses a custom sting mounting adapter that is also fabricated from 303 stainless steel [22].

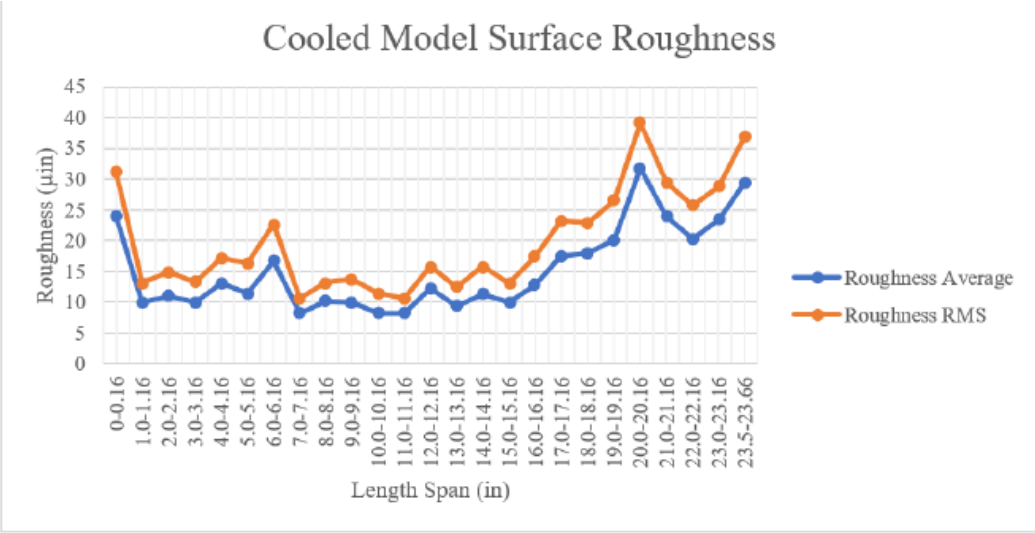


Figure 51. Roughness distribution of Oddo's seven degree half angle sharp cone [22]

The tip of the cone is as sharp as the AFIT machine shop could possibly make with an estimated spherical bluntness radius of approximately 0.1mm ($\tilde{0}$.066% bluntness). Shown in Figure 51, the arithmetic roughness average (RA) of the of the cone's surface was determined to be between 32 μin near the tip and 12 μin near the base [22].

Designed for use in experiments on hypersonic surface temperature instability effects, Oddo's cone is hollow and capable of storing either chilled or heated fluids internally. A diagram of the cone showing the hollow interior is shown in Figure 52. The rear of the cone has access ports capable of delivering cryogenic liquids into the cone such as liquid nitrogen that are pumped into the cone and then exhausted back out. The cooling capability of this cone was not used for the present study, but was explored extensively by Oddo [22].

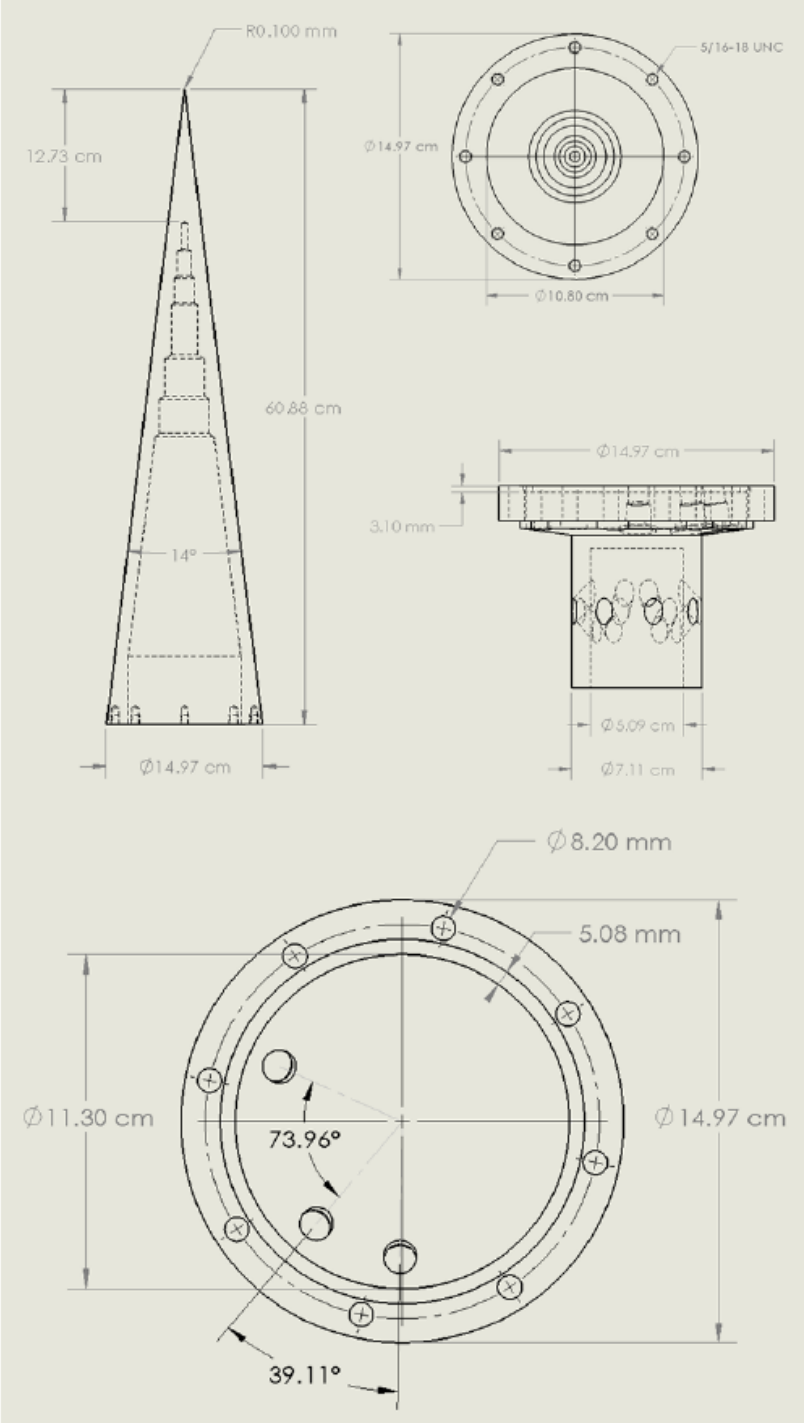


Figure 52. Diagram of Oddo's seven degree half angle sharp cone [22]

3.2.2 Run Conditions.

For this study, Oddo's seven degree half angle sharp cone was run in the AFRL Mach 6 Ludwieg tube at nominal driver tube pressures ranging from 100 to 300 psia with corresponding unit Reynolds numbers varying from $5.2 * 10^6/m$ to $2.07 * 10^7/m$. The cone surface was kept at ambient temperatures. The ambient surface temperature was chosen due to the understanding that the ambient temperature cone should produce strong second Mack mode instabilities along its length. The second Mack mode is known to produce strong flow features over this geometry type which would be useful for characterizing the validity of FLDI and Schlieren in measuring hypersonic instabilities in the AFRL Mach 6 Ludwieg tube [9].

FLDI and high speed Schlieren were used to capture flow features and determine the frequency of passing instabilities. It was found that the range of Reynolds numbers used produced strong second mode features that could be observed in both measurement techniques. Section 4.1 of this report provides an in depth look at the results from experiments over the geometry.

Runs 10-17 and 102 (details in Appendix A) are the runs where FLDI was used over Oddo's cone. The Schlieren images were captured and provided by Oddo in a set of runs completed by the AFRL and AFIT team at similar run conditions to the FLDI runs in this study [22].

3.3 Ogive-Cylinder Model

With the unique results produced by Purdue's findings in the Mach 6 quiet tunnel (as previously discussed in Section 2.5) it was determined by this study's research team that a further exploration of hypersonic instabilities over ogive-cylinder models is an appropriate area of further research. With this in mind, a modular ogive-cylinder model with variable length and nosetip geometries was designed. This model

takes inspiration from Purdue's original cone-ogive-cylinder models, but there are some significant design changes/choices that will be discussed in greater detail in this section. Experiments were conducted using the ogive-cylinder model at zero angle of attack in the AFRL Mach 6 Ludwieg Tube at Reynolds numbers ranging from $3.25 * 10^6/m$ to $1.48 * 10^7/m$ with corresponding driver tube pressures of 71.7psia and 290.79psia respectively. Diagnostics including FLDI, surface mounted pressure sensors, and high speed Schlieren were used to capture flow features and measure hypersonic boundary layer instabilities over the model.

3.3.1 Overall Design.

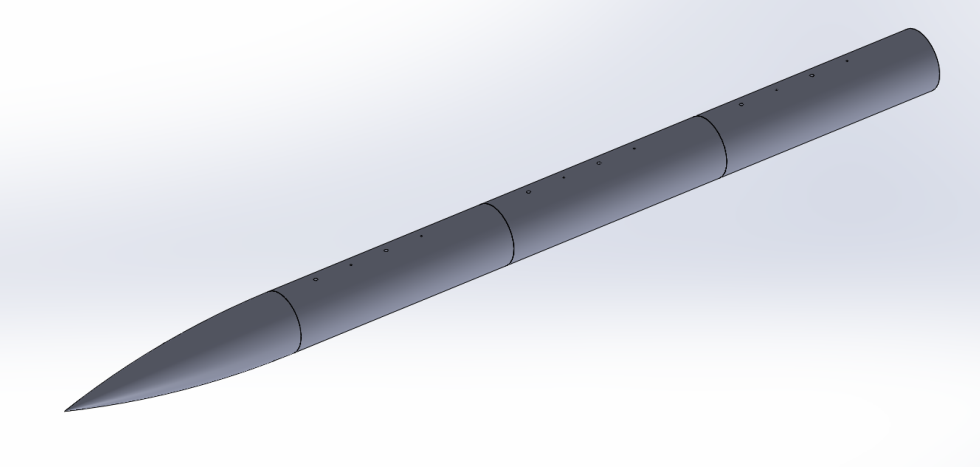


Figure 53. Rendering of Hill's ogive-cylinder model

The ogive-cylinder model used in this study is rendered in Figure 53. The model measures 1 meter in length when fully assembled and is capable of being shortened and lengthened by adding or removing body sections to the cylindrical portion of the model. The fully assembled model uses three cylindrical body sections and a single nose section. Each component is approximately 1/4 meter long and the base radius of the cylinder is 2.45in (6.223cm). It should be noted that while the length of this model is approximately the same as Purdue's, the diameter of this model is

approximately 1/2 inch larger.



Figure 54. Photo of cylindrical body with mounting adapter attached

The model was manufactured by the AFIT machine shop from 2.5in diameter 6061 aluminum rods. Each section of the cylindrical body was individually milled, but the entire cylindrical body was fully assembled before the final finishing pass was applied. This finishing pass brought the diameter down to down to 2.45in. By adding the finishing pass with the cylindrical body fully assembled, a smooth finish was achieved across the length of the body. The average roughness across the cylindrical portion of the body is below 15 Ra and the seams between the body sections are unobservable to the human eye and cannot be felt when passing a finger over the model. A photo of the finished body with all three sections fully assembled can be observed in Figure 54

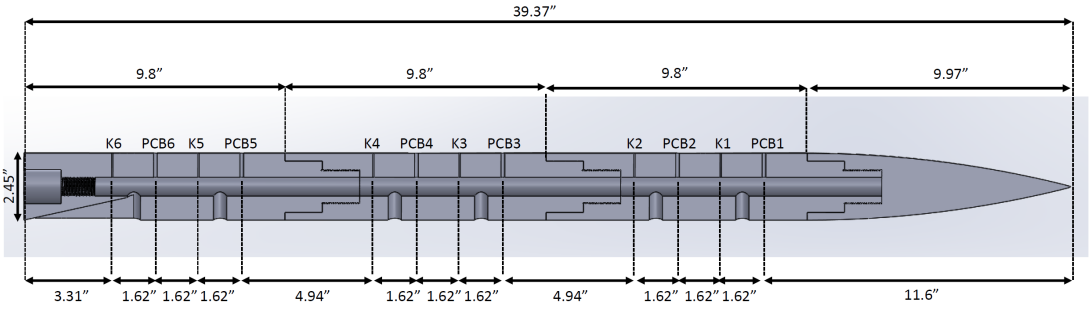


Figure 55. Slice view with dimensions of the ogive-cylinder model

The nose sections of the model were also manufactured from 6061 aluminum rods. The machine shop ensured each nose section was brought to as smooth of a finsh as possible while maintaining a smooth transition to the cylindrical body, but due

to the complex/curved surface of the tips, no accurate measures of average surface roughness were made. More details on the specifics of each nose section designed, manufactured, and tested in this study will be provided in Section 3.3.2.

As can be observed in Figure 55, the cylindrical body of the model was hollow and lined with various ports for surface mounted pressure sensors. Two types of surface mounted pressure sensors were used, the Kulite XCE-062-15A and the PCB 132B38. More specifics on these sensors and why they were chosen are discussed in Section 3.4.1. The sensors were mounted flush to the surface along the centerline of the cylindrical body with each sensor alternating down the length. The sensor wires were run through the centerline of the body and out the rearmost port on the bottom of the cylinder as shown in Figure 56. Along the bottom of the cylinder, 1/2 inch diameter access ports were added to allow for easier installation of the sensors. A later modification to the cylindrical body added additional line of site cuts through these access ports to provide easier access, but the overall design stayed the same and had no effect on the 1/2 inch diameter access holes.

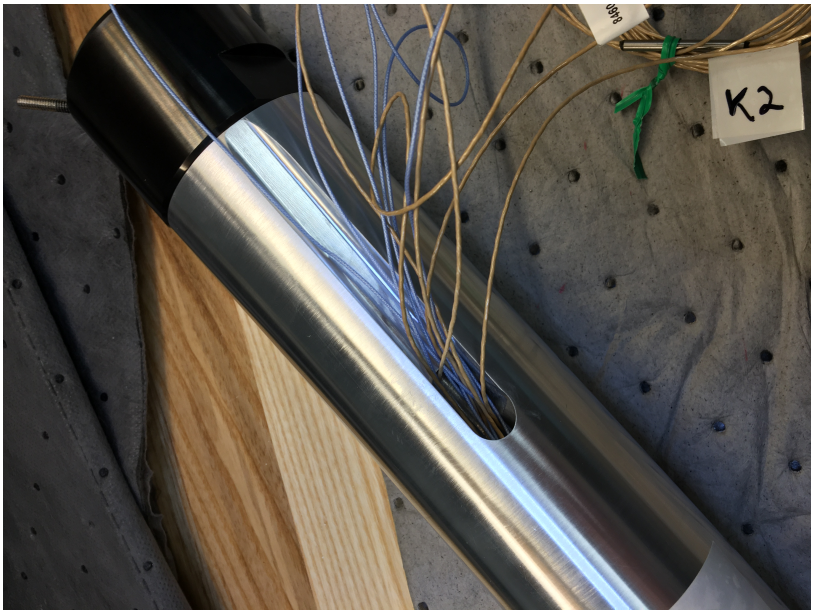


Figure 56. Sensor wires running out the back end of the model

3.3.2 Nose Tip Design.

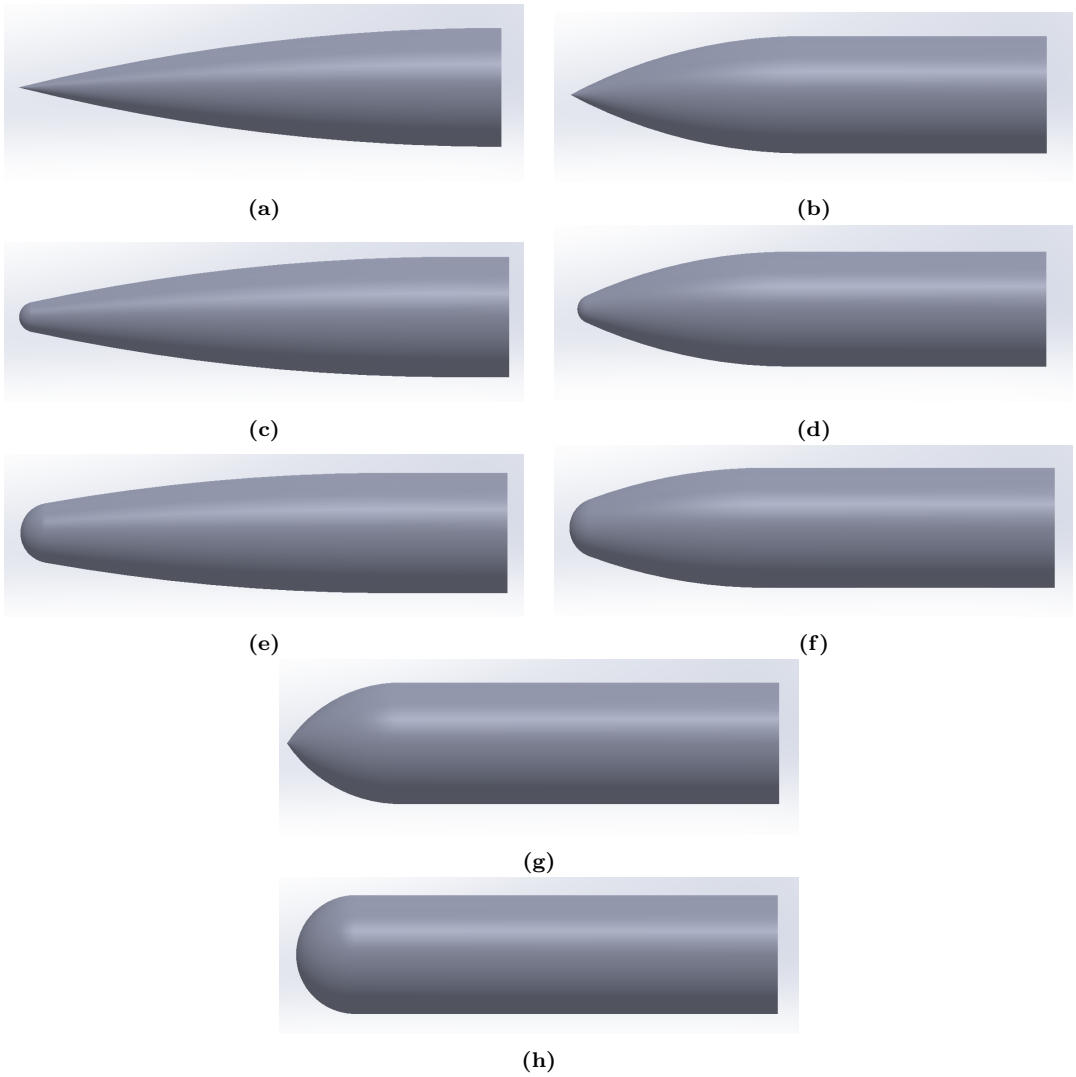


Figure 57. Tip renders (a) 14 degree sharp (b) 28 degree sharp (c) 14 degree 1/4R blunted (d) 28 degree 1/4R blunted (e) 14 degree 1/2R blunted (f) 28 degree 1/2R blunted (g) 56 degree sharp (h) fully blunted

Eight nose tip sections, rendered in Figured 57 were used in the experiments for this study. The key distinguishing factor between these geometries used in this study and those of Purdue's cone-ogive-cylinder work is how the nose tip sections were designed. In this subsection, the specific reasons for the design of the nose tips for the ogive-cylinder model will be discussed.

Theory.

In Purdue's work, a primary goal of the experiments was to study the effects of tip angle on downstream entropy layer measurements by using a cone-ogive-cylinder that was designed via a set of equations defining the nose geometry from Zucrow and Hoffman's 1984 textbook on gas dynamics [19, 76]. The method described in this book splits the tip into three sections: a conical tip, an ogive curve fit, and a cylindrical body. While this method gives the user the ability to choose a tip angle, there are large variations in the length of the conical sections when different angles are chosen and the ogive sections are simple quadratic curve fits between the cone and cylinder. As a result of these design methods, the tips created this way have inconsistent, non-constant curvature. This author hypothesized that the curvature of the tip section is crucial in understanding the shock structure and resulting entropy layer effects generated. If nose bluntness effects and entropy layer instabilities are to be studied effectively moving forward, a methodical approach to the tip geometry should be taken.

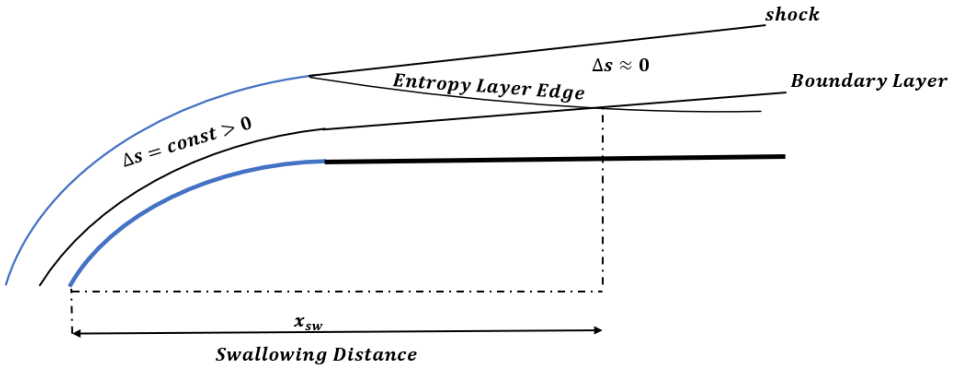
As is discussed by the Purdue research team in a dissertation, entropy layer instabilities are an inviscid phenomenon [19]. Looking back to Section 2.2.2, the inviscid nature of the entropy layer instability should make sense due to the fact that the entropy layer itself is an invisicid phenomenon that is entirely driven by shock curvature effects. With this inviscid quality of the entropy layer in mind, it is hypothesized by this author that entropy layer instabilities could be sensitive to inviscid stability criteria, such as the Rayleigh inviscid stability criterion, which are found in other flow features. As discussed in Section 2.1, the Rayleigh criterion states that the presence of an inflection point in an inviscid flow profile means that the flow is inherently inviscidly unstable [26]. Applying this same logic to entropy layers, it is possible that an inflection point in the curvature of a could have direct influences on entropy layer

instabilities.

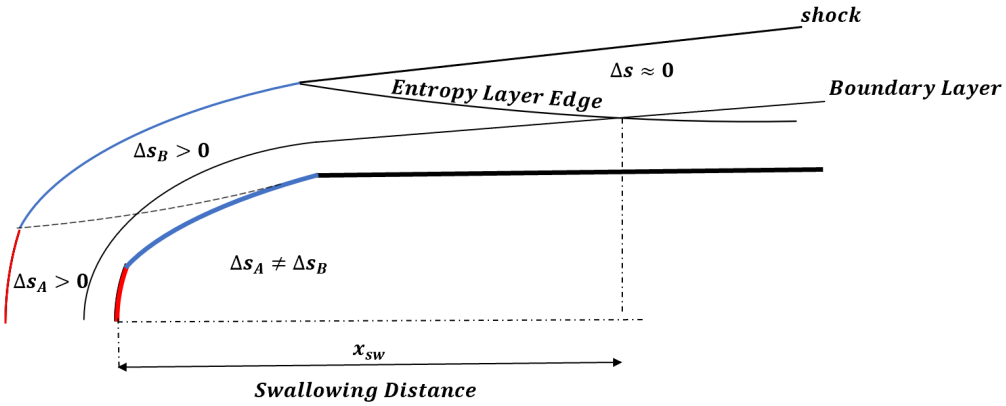
As discussed in Section 2.2.1, shocks formed in front of hypersonic bodies closely conform to the leading edge body contour of the geometry behind the shock. With this in mind, it is reasonable to assume that the curvature of the leading edge of a blunt hypersonic body will directly influence the curvature of the shock that forms in front of it at hypersonic speeds. Figure 58 provides a side-by-side diagram comparing a shock and resulting entropy layer that is formed when the body has constant and non-constant curvature. The shocks in these diagrams are colored to match the section of the body that influences the shape of that portion of the shock. It can be observed for the non-constant curvature case that an inflection point in the curvature of the shock is formed where the two shock sections influenced by different surface curvatures meet. As a result, there is a non-constant entropy gradient that forms between the shock and the body.

The inflection point in the shock curvature results in an inflection point in the entropy layer gradients. With this in mind, it is easy to speculate that this inviscid inflection point in the flow could affect instabilities downstream. It is conceivable that the entropy layer inflection point could serve as an instability mechanism for creating and amplifying entropy layer instabilities. Alternatively, this shock and entropy layer inflection point could also serve as a receptivity mechanism to freestream noise or other disturbances. These observations however are purely speculative and thus this author leaves further investigation of these theories to others in the community.

With the theory established on why surface geometry curvature is important when attempting to study hypersonic blunt body instabilities, a series of equation driven geometries were derived to provide quantifiable effects. The tips designed can be placed into two categories: sharp ogives and blunted ogives. Both tip category use a different method for determining the body profile, but the methods ensure that the



(a)



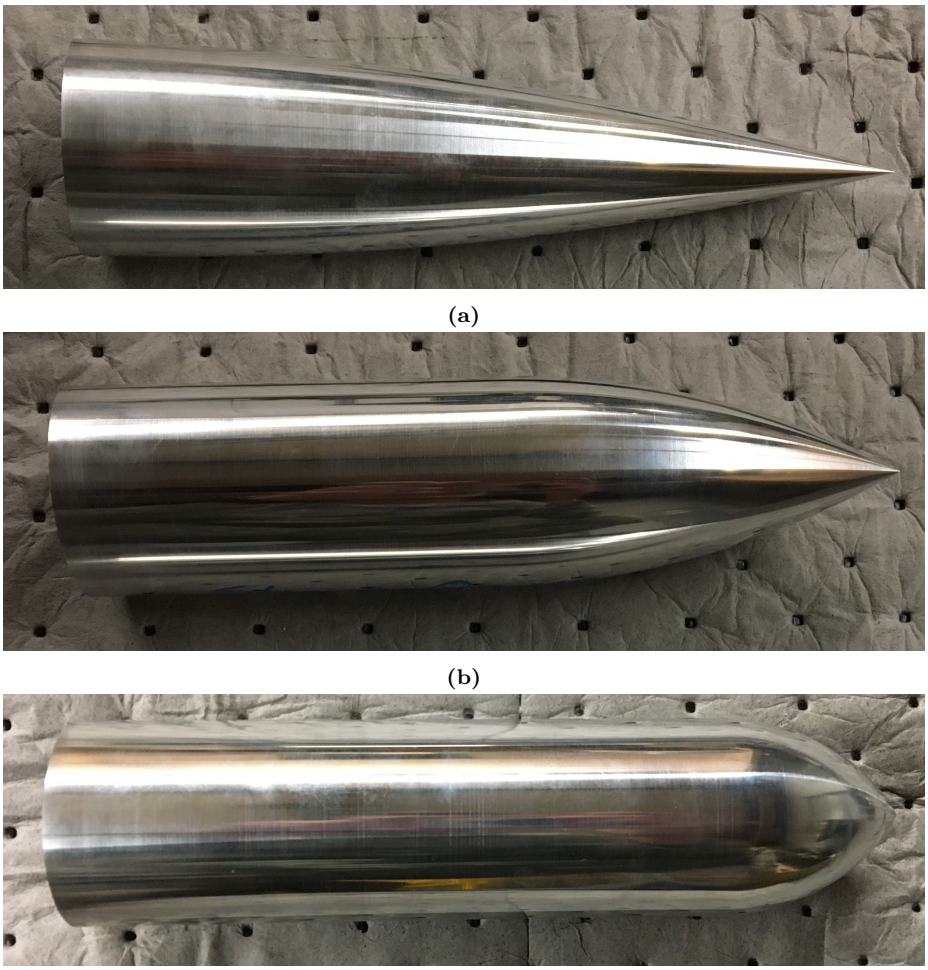
(b)

Figure 58. Shock curvature and entropy layer for (a) constant curvature ogive tip (b) non-constant curvature blunted ogive tip

tip curvature is well understood and characterized.

Sharp Ogive Tips.

Three sharp tip ogives were designed and manufactured with tip angles of 14, 28, and 56 degrees (pictured in Figure 59). The tip angles used were chosen to allow for a variety of constant curvature effects to be observed from shallow, to steep curvature. These sharp ogives were considered to be the "baseline" tips for this study due to their constant curvature ogive radius. In order to design these sharp tip ogives, the



(a)

(b)

(c)

Figure 59. Sharp ogive tips (a) 14 degree (b) 28 degree (c) 56 degree

tangent ogive equation shown in Equation 13 was used. The diagram in Figure 60 provides context for how this equation describes the tip geometry.

$$\begin{aligned} y &= \sqrt{\rho^2 - (L-x)^2} + R - \rho \\ \rho &= \frac{R^2 + L^2}{2R} \\ L &= \frac{R}{tan(\theta)} \end{aligned} \tag{13}$$

In this equation ρ is the constant ogive radius, L is the length of the ogive section, R is the base radius of the ogive, and θ is the angle of the tip on the ogive. A code was

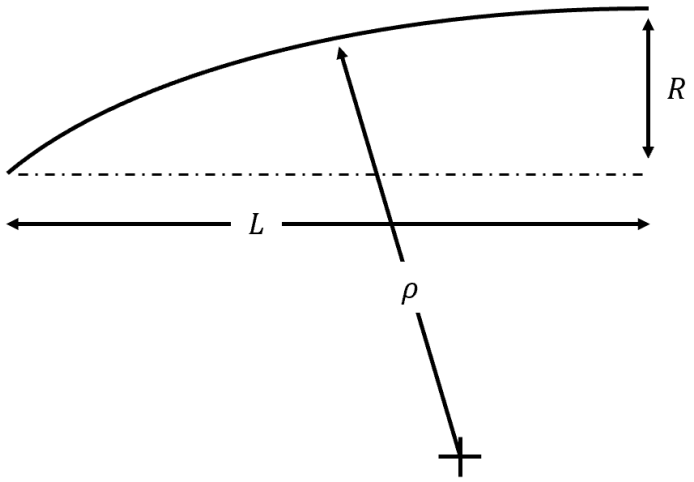


Figure 60. Tangent ogive diagram

developed in Matlab that assisted in developing the equations to achieve the desired geometry parameters. The resulting contours for the three sharp tip geometries can be found in Figure 61. It should be noted that the ogive length is inversely related to the tip angle desired, so the higher tip angles have shorter ogive lengths. To ensure that the overall length of each tip section remained the same, a cylindrical portion was added to the shorter ogives to maintain the 0.25m tip section length. The exact parameters and equations defining each tip contour can be found in Appendix C.

Blunted Ogive Tips.

Following a similar method to that found in Section 3.3.2, five spherically blunted ogive geometries were developed for this study. Unlike the sharp ogive tips where special care was taken to ensure the ogive maintained a constant curvature, the blunted ogive tips are designed specifically to introduce a distinct body contour inflection point. Using the ogive profiles for the 14 and 28 degree sharp ogives, spherically blunted tips were added with 1/4 and 1/2 the radius of the base radius of the cylin-

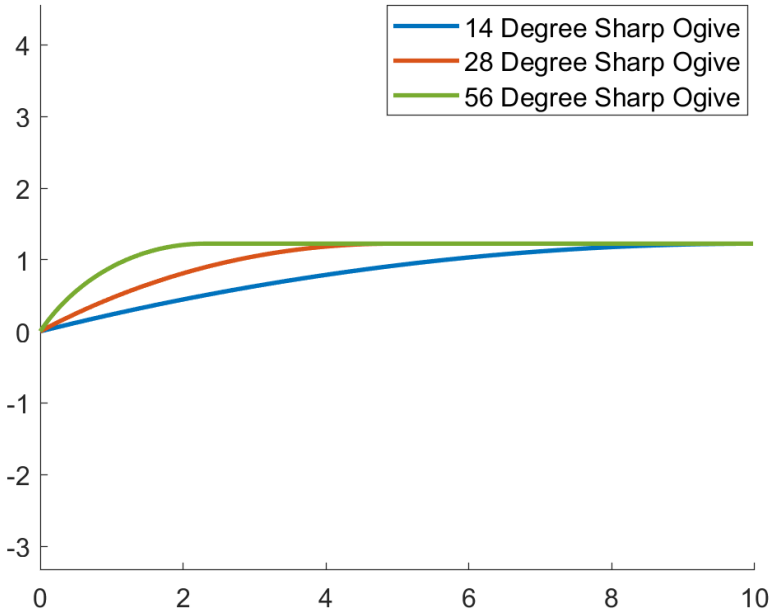


Figure 61. 14, 28, and 56 degree sharp ogive tip contours

der. A fully spherically blunted tip was also manufactured with a radius equivalent to that of the base radius to serve as a baseline case of the most extreme bluntness. Each of these blunted ogive tips was manufactured from the same 6061 aluminum rods as the other components. Again, the model shop attempted to create as smooth of a surface finish as possible, but no accurate measurements of te surface roughness values were taken. A picture of each of these spherically blunted ogive tips compared to their sharp counterparts can be found in Figure 62.

The spherically blunted ogives are designed using three separate equations to define the three main sections of the tip: the spherical bluntness, the ogive, and the cylindrical fit. Each section has its own set of equations defining the geometry contour. The spherical bluntness section is defined by using Equation 14. The diagram in Figure 63 is provided as a visual representation for where each parameter in this equation is physically derived from.

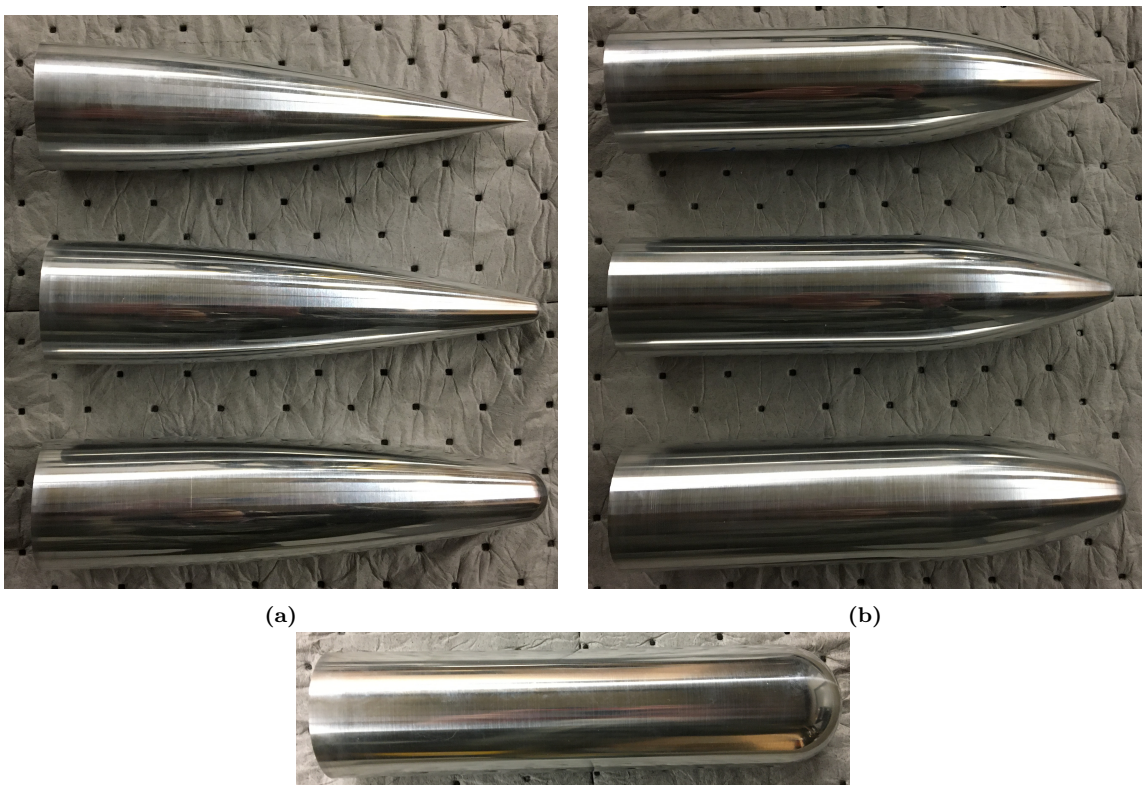


Figure 62. Blunted ogive tips (a) 14 degree ogives (sharp, 1/4R, 1/2R) (b) 28 degree ogives (sharp, 1/4R, 1/2R) (c) fully spherically blunted tip

$$
\begin{aligned}
y &= \sqrt{R_N^2 - (x - x_0)^2}; \\
x_0 &= L - \sqrt{(\rho - R_N)^2 - (\rho - R)^2} \\
&for\, x = x_a\, to\, x_t
\end{aligned}
\tag{14}
$$

where

$$
\begin{aligned}
x_a &= x_0 - R_N \\
x_t &= x_0 - \sqrt{R_N^2 - y_t^2} \\
y_t &= R_N * \frac{\rho - R}{\rho - R_N}
\end{aligned}
\tag{15}
$$

Once Equation 14 is used to define the spherical bluntness for a given tip, the same Equation 13 from the sharp tip variants is used to provide the ogive contour

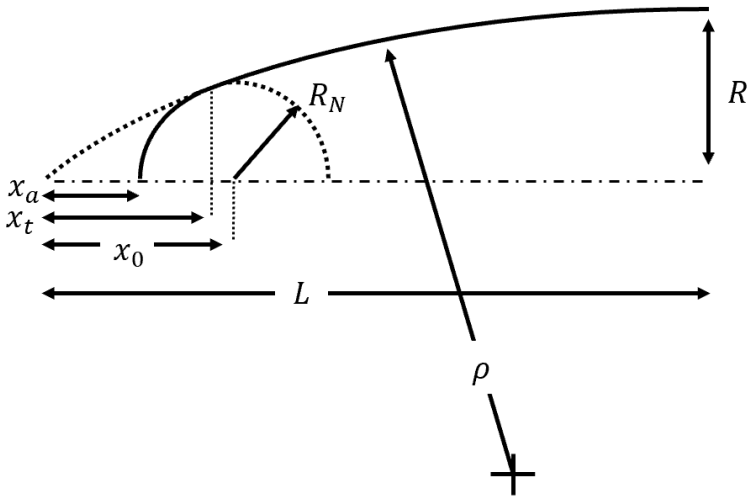
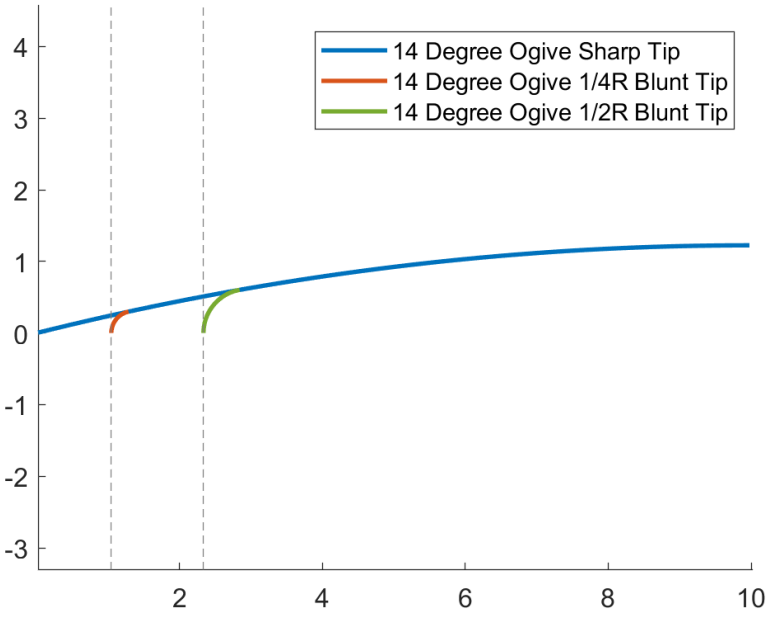


Figure 63. Spherically blunted tangent ogive diagram

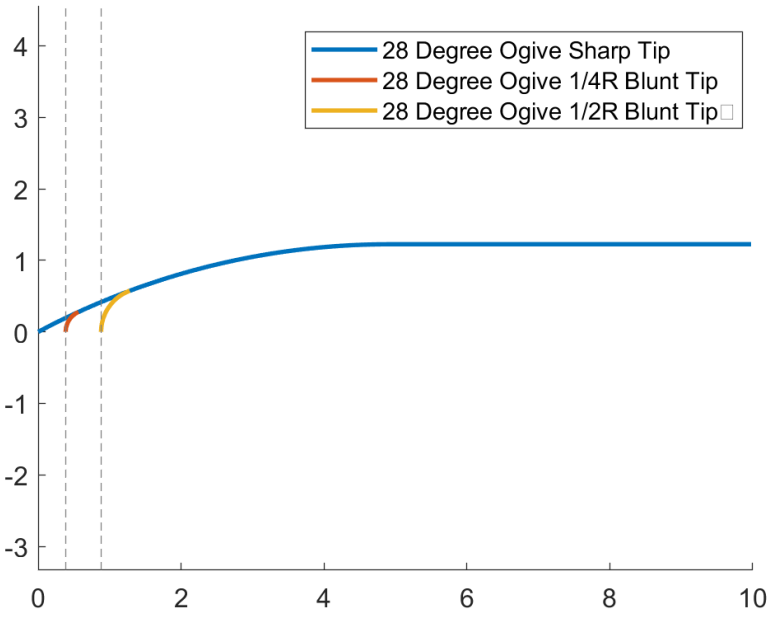
from the point of tangency, x_t, to the base radius of the cylinder. Again, just as the sharp ogive contours result in an inverse relationship between tip angle and ogive length, the higher bluntness levels result in a shorter ogive length. To compensate the for the shorter ogive lengths, a cylindrical portion was added to ensure that each tip was of equivalent length, ≈0.25m. The same Matlab code as before was used with an additional blunt tip function using the equations shown to create the contours as seen in Figure 64. The exact parameters and equations defining each tip contour can be found in Appendix C.

Unused Tips.

While the sharp and blunted ogive tips presented so far were the only ones used in this study, a variety of other tips were designed and manufactured, but were not used in any experiments due to time limitations. Two spherically blunted ogives were made for the 14 and 28 degree ogive tips with 3/4R nose bluntness. These unused highly blunted ogives can be seen in Figure 65. These highly blunted tips were not used due to their bluntness levels being well above the region where bluntness levels



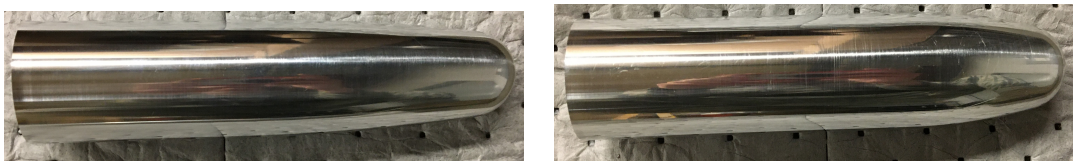
(a)



(b)

Figure 64. Blunted Tip Contours (sharp, 1/4R, 1/2R) (a) 14 degree ogives (b) 28 degree ogives

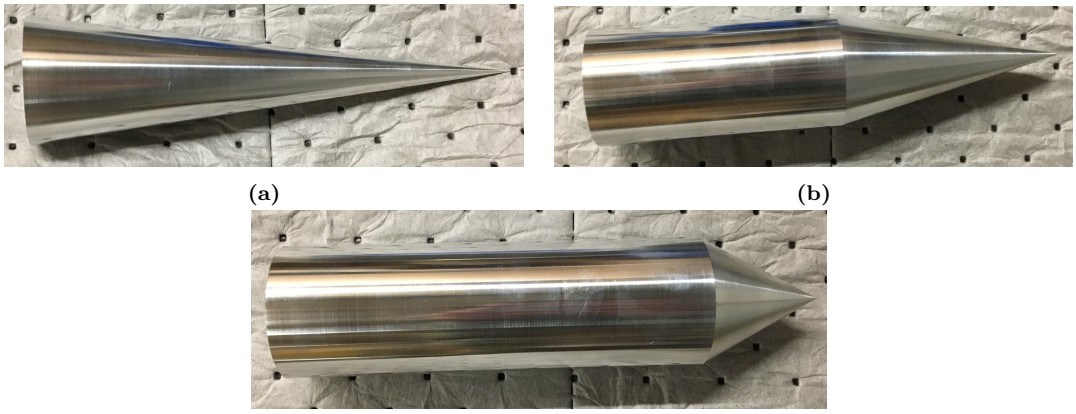
would be expected to have significant effects. It was believed that these tips would essentially perform just as the fully spherically blunted tip that was made. These tips were also made of 6061 aluminum.



(a) (b)

Figure 65. Unused 3/4R blunted ogive tips (a) 14 degree ogive (b) 28 degree ogive

In an attempt to create another set of baseline conditions for the experiment, a set of three conical tips were made for the model. These three tips had half angles of 7, 14, and 28 degrees and can be seen in Figure 66. These angles were chosen to provide a wide variety of angle effects on downstream instabilities. Inevitably, no runs were conducted using these tips due to concerns that there would be expansion issues at the intersection of the conical tip and cylindrical body that would skew the instability analysis. Time restraints also prevented further investigation of flow over these geometries, but further work could use these geometries to build up comparison data sets.



(a) (b)

(c)

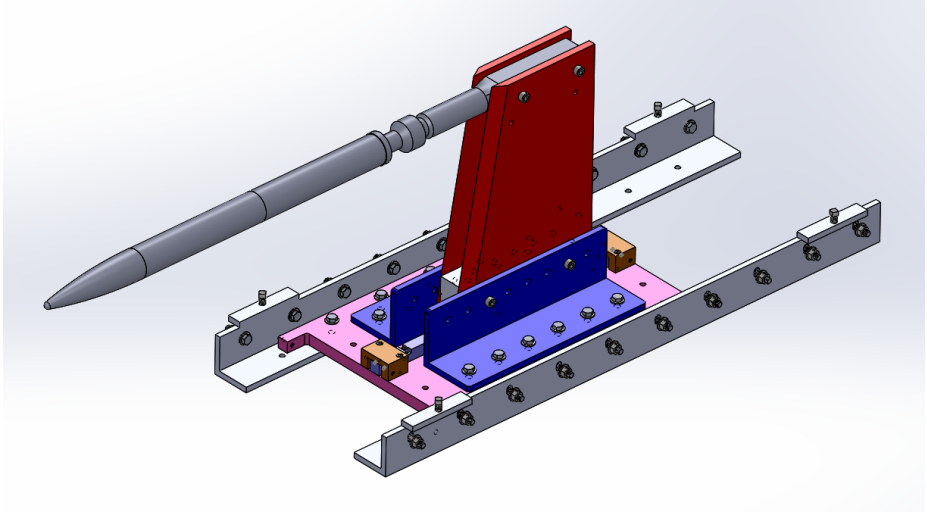
Figure 66. Unused conical tips (a) 7 degree (b) 14 degree (c) 28 degree

3.3.3 Run Conditions.

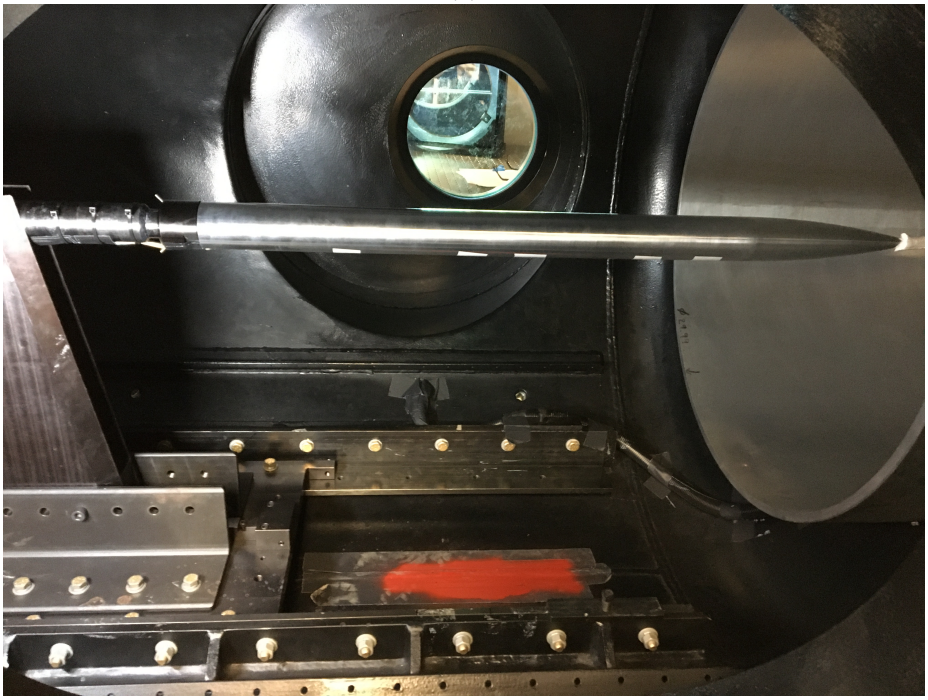
Once the eight primary ogive-cylinder geometries were designed and manufactured, a series of experiments were conducted in the AFRL Mach 6 Ludwieg tube at a variety of conditions. For each run, the stagnation temperature was held at the standard 505 Kelvin. Stagnation pressures for runs varied from a minimum of 64 psia (driver tube pressure of 72 psia) to a maximum of 218 psia (driver tube pressure of 244 psia). This in turn resulted in unit Reynolds number ranges from $3.25 * 10^6/m$ to $1.48 * 10^7/m$ with corresponding driver tube pressures of 71.7psia and 290.79psia respectively. Runs 18-101 use the ogive-cylinder geometry with its various tips. The specific flow details and stagnation conditions for each run can be found in Appendix A.

Not every tip geometry was run at the entire set of Reynolds numbers in this study, but were instead subjected to ever increasing Reynolds numbers until transition was consistently occurring to allow for a full study of Reynolds number effects on transition and instability propagation. It should be noted that the maximum driver tube pressure for this study was set to 250psia to ensure the meter long model would not face any overloading on the structure. Because of this safety limit, some of the tips were only able to produce transitional results and never became fully turbulent.

For every run completed with the ogive-cylinder model, the assembly was mounted at the rearmost position possible in the tunnel's test section. A rendering and picture of the model mounted at the run position with the 14 degree sharp ogive and all instruments installed can be observed in Figure 67. Due to the length of the model, the forward most tip section was approximately 200mm upstream of the nozzle exit and the base of the cylinder was approximately 800mm downstream of the nozzle exit. It was determined from the Mach contours of the flow profile, as talked to in Section 3.1.2, that there would be no significant issues with the tip of the model lying



(a)



(b)

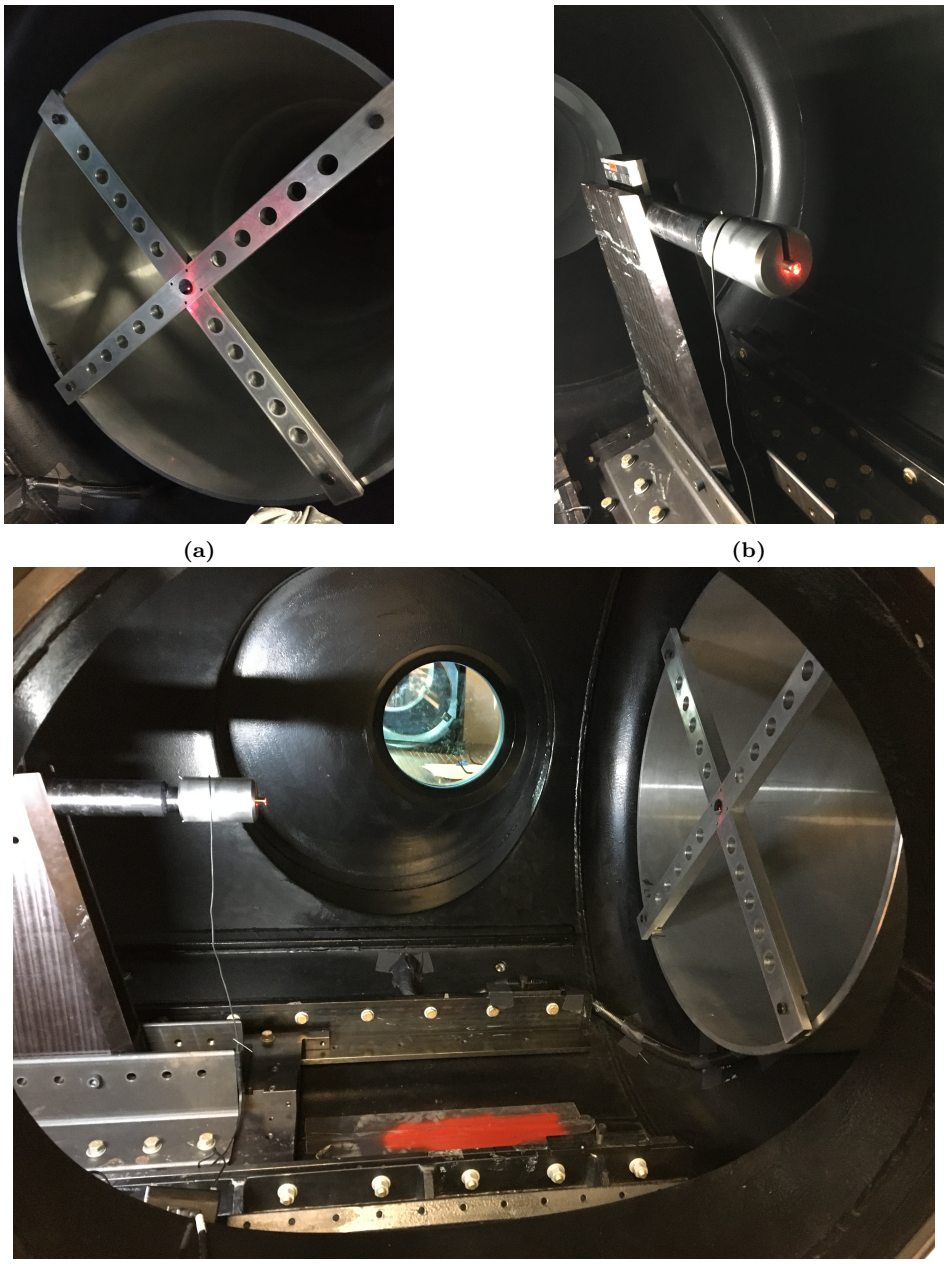
Figure 67. (a) Rendering of model mounted on the test section sting (b) picture of the assembled model and sensors on the test section sting

200mm upstream because the Mach number would still be approximately Mach 6.1. Further flow quality and pitot rake surveys are planned to experimentally verify the Mach number at all locations in the test section including slightly upstream of the nozzle exit, but none were completed at this upstream location as of the date of this

writing.

The ogive-cylinder model was held at zero degree angle of attack and sideslip for each run. One of the few shortcomings of the AFRL Mach 6 Ludwieg tube is the lack of high precision angle of attack and sideslip verification and tuning capabilities. For this study, the angle of attack and sideslip were verified by using both a laser based technique and a digital protractor. A picture of the laser based zeroing technique can be seen in Figure 68. Once the sting is mounted in the rear most position for each set of runs, a laser is attached to the end of the sting and a flat mirror is mounted at the center of the nozzle exit. The sting is then adjusted until the reflection of the laser off the mirror at the nozzle exit is pointed directly back at the emitting source. This method works well for getting the sting into the "ballpark" area for mounting, but the laser mount can sometimes vary between measuring attempts.

Once the laser based zeroing technique is finished, the ogive-cylinder model is mounted onto sting. A digital protractor is then placed at various axial positions along the length of the cylindrical body to find the exact angle of attack and make appropriate adjustments. Figure 69 shows an example measurement of the angle of attack. Again, this method has inherent flaws and large variation between measurement attempts, but was the only option available to this author. It was found using this technique in conjunction with the laser based method allowed for the angle of attack to be kept within 0.1 degrees of zero. It was often found that the protractor consistently measured downward angles of attack on the order of 0.05 degrees, even for surfaces which were considered to be flat and level in the test section room, so the estimate that the model was held to at least 0.1 degrees from zero angle of attack is conservative.



(a) (b)

(c)

Figure 68. Laser zeroing technique (a) laser sting mount (b) nozzle exit mirror (c) overall setup

3.4 Diagnostics

A variety of measuring techniques and diagnostic tools were utilized in this study including high speed surface mounted pressure transducers, high speed Schlieren, and



(a) (b)

Figure 69. Digital protractor angle of attack measurements (a) at the sting mount (b) at mid-length on the model

focused laser differential interferometry (FLDI). While each of these techniques and tools on their own are fully capable of performing hypersonic boundary layer instability measurements, for this study they were each used to cross-verify the findings of the others. As a result, the post-processing techniques and their findings explained later in this study have more credibility and verification sources.

3.4.1 Surface Mounted Pressure Sensors.

The ogive-cylinder geometry utilized high speed surface mounted pressure sensors to collect pressure fluctuation data. Alternating Kulite XCE-062-15A sensors with a face diameter of 0.066 inches and PCB 132B38 sensors with a face diameter of 0.125 inches were placed down the length of the model to allow for both sensors to gather data and be compared to one another. These two sensor types were chosen due to their common usage in the field of hypersonic boundary layer instability and transition research and due to each type having a different method of measuring pressure disturbances [80, 81].

Kulite XCE-062-15A.

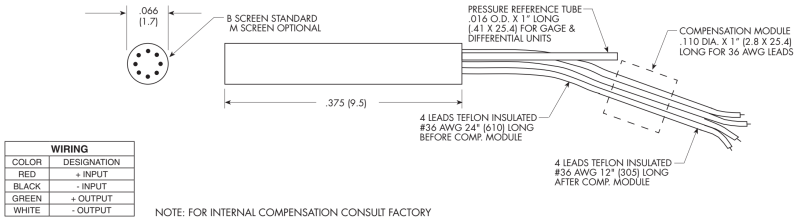


Figure 70. Kulite XCE-062-15A diagram [23]

The Kulite XCE-062-15A, shown in Figure 70, is an absolute pressure sensor that has excellent frequency resolution for frequencies below ≈150kHz. The use of this Kulite sensor and others like it in hypersonic research has been prominent in the community for a number of years due to the sensor's high dependability and frequency resolution.

For the ogive-cylinder model used in this setup, six Kulite XCE-062-15A sensors were used along the centerline of the cylindrical body (see Figure 55 for dimensions). The sensor wires were run through the centerline of the model's body, through the tunnel walls, and connected to the data acquisition system for the tunnel. A signal conditioner for the Kulite sensors was used to help amplify and clean up the signal before they were passed along to the data system. The data system for the Kulites used a sampling rate of 2MHz, thus tecnically allowing the Kulite data to resolve frequencies out to the Nyquist frequency of 1MHz. The high Nyquist frequency more than enough covers the Kulite viable frequency range which is on the order of 100kHz.

It was found during the experiments for this study that the first Kulite sensor was unresponsive and was unable to provide useful data for analysis. It was also found that all the Kulite sensors exhibited a high level of background noise. An example power spectra showing the background noise for the working Kulites can be observed in Figure 71. It was found that the large amount of noise in the line was due to

faulty wiring between the Kulite leads and the signal conditioner. This noise source was not isolated and corrected until after the study was completed. Despite the high noise floor, the sensors were still able to provide useful data for frequencies below ≈100kHz. It should be noted however, that due to the Kulite noise, much of the analysis performed in Chapter IV uses the much cleaner data of the PCB sensors.

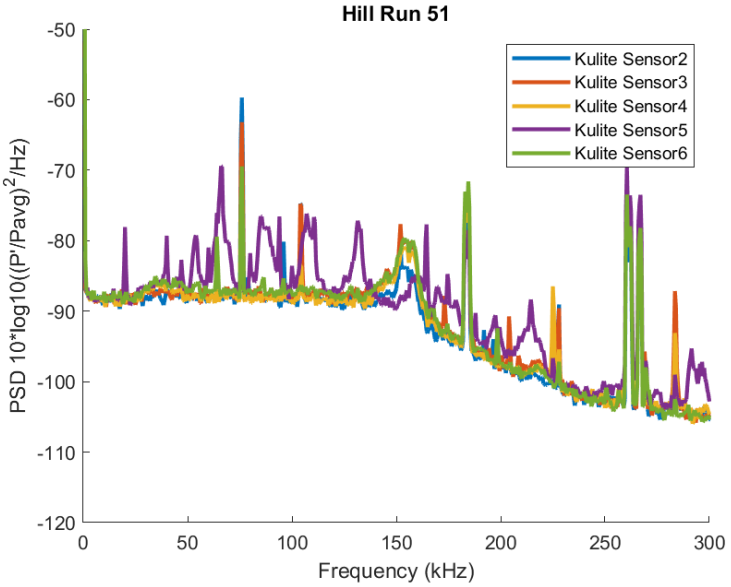


Figure 71. Kulite XCE-062-15A power spectral density noise levels

PCB 132B38.

The PCB 132B38, pictured in Figure 72 is a high frequency pressure sensor that has some unique characteristics that distinguish it from it is Kulite counterpart. Newer to the hypersonic boundary layer transition and instability research community than the Kulite models, the PCB 132B38 is becoming a relevant and widely used sensor in the community [81]. While the Kulite sensor is a passive sensor that provides absolute pressure measurements, the PCB 132B38 is inherently designed to only measure pressure fluctuations and not necessarily absolute pressure. At a high level, the PCB 132B38 uses a proprietary signal conditioning box to send a current to the

sensor to stimulate the sensor head. To compensate for this active sensor mechanism, the PCB 132B38 has a built in high-pass filter of 11 kHz. This means that the lowest frequency that the PCB can resolve is 11kHz and thus a 12kHz high pass filter was used for all PCB data sets in this study to help eliminate the hardware filtering effects. Despite this active stimulation of the sensor head resulting in an inherent high-pass filtering, the PCB 132B38 is in turn able to resolve much higher frequencies on the order of 1+MHz. This makes the PCB sensor extremely useful in cases where second Mack mode instabilities are expected to be present which can often reach frequencies in the 100s of kHz to 1+ Mhz.

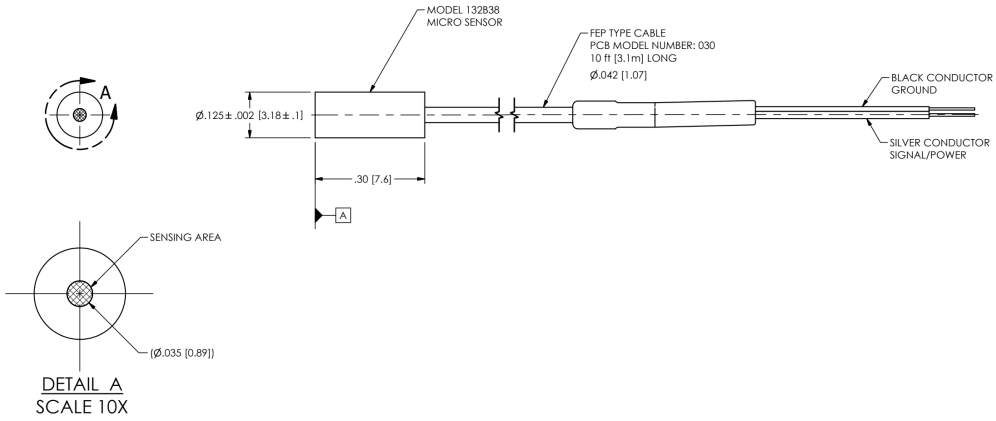
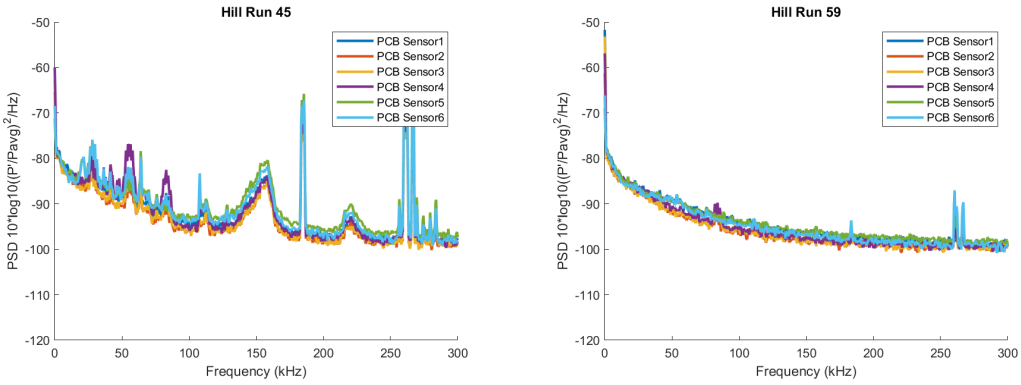


Figure 72. PCB 132B38 diagram [24]

For the ogive cylinder model, six PCB 132B38 sensors were used down the centerline of the model (see Figure 55 for dimensions). The wires for the sensors were run down the center of the model just as with the Kulite sensors. The wires were then plugged into the PCB signal conditioner box where another line to the data acquisition system was run for each sensor. The sampling rate for the PCB sensors is 5MHz which is more than enough to capture all of the frequencies that the sensor can resolve.

It was found during the early runs with the ogive-cylinder model, that a moderate



(a) **(b)**

Figure 73. PCB signal background noise (a) prior to solution (b) after solution

amount of noise was appearing in the PCB signal. It was identified around run 52 of the study that the source of the signal background noise was due to bad coaxial cables and electrical noise from a bad wall socket. After changing the coaxial cables and moving the plug for PCB signal conditioners to an electrically isolated socket, the background noise was significantly reduced to more reasonable levels. Figure 73 shows the drop in background noise after the solution to the problem was discovered. For Chapter IV, it should be noted that many of the figures will use data from before the noise fix was applied and thus the ∼150kHz noise is observed in the results and should be discounted. For most of the results though, these noisy runs did not effect the overall trends of the frequency analysis.

3.4.2 Focused Laser Differential Interferometry.

Originally introduced by Smeets in 1971, the concept of using focused laser differential interferometry (FLDI) for hypersonic boundary layer experimental measurements is not a new concept. Ironically enough, Smeets had enough foresight into the possible application of his technique to even include a hypothetical use case in his report for hypersonic boundary layer and entropy layer measurements over a cone as shown in Figure 74 [25]. Despite Smeets's foresight, the technical complexities

and lack of appropriate/afforable equipment to utilize his flow measurement technique would limit the use of FLDI within the hypersonic boundary layer transition community for a number of years. It is only recently with advancements in laser and imaging technology that FLDI has seen a resurgence in hypersonic experimental work [82]. This resurgence in FLDI use is why this author decided to bring online a viable FLDI system for the AFRL Mach 6 Ludwieg tube.

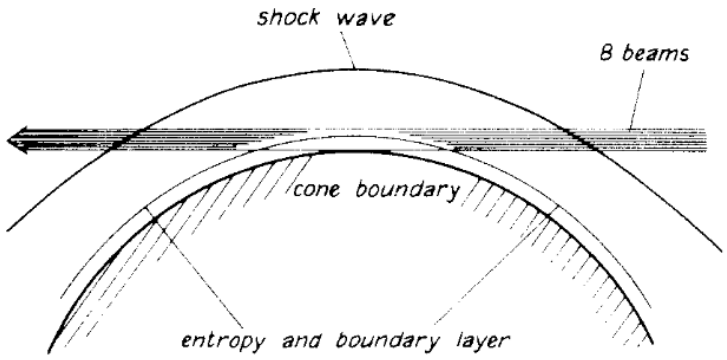


Figure 74. Hypothetical hypersonic use case for FLDI [25]

Theory.

While there is a great deal of underlying complicated theory involving laser and optical characteristics that influence the setup of an FLDI system, an effective high level background on the basic principles that make FLDI work are sufficient to provide the reader with the level of knowledge needed to move forward. With that in mind, this subsection will focus on the high level principles of FLDI.

A laser differential interferometer (LDI) is a non-intrusive density fluctuation measurement device that utilizes a laser, a series of focusing optics, and a photodiode. A simple diagram of an LDI setup can be observed in Figure 75. In short, LDI works as follows: First, a continuous wave laser emits a beam through a diverging lens to expand the beam. While the beam is expanding, it is passed through a polarizer

Label	Component
A	Laser Source
B	Diverging Lens
C	Polarizer
D	Wollaston Prism
E	Field Lens
F	Photodiode

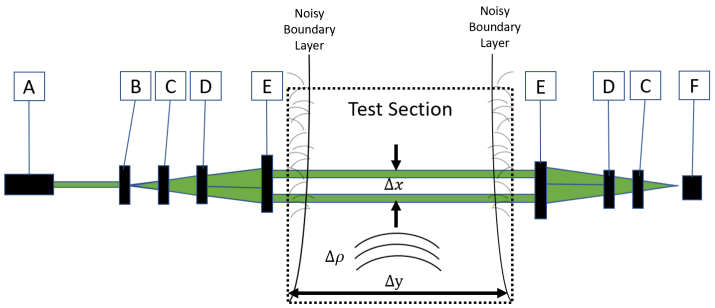


Figure 75. Example LDI diagram

(often a linear polarizer) and then a Wollostan prism to create two separate beams of orthogonal polarization. The expanding beam is then collimated by a field lens into two parallel beams separated by a distance, Δx, that are passed through the test section. On the far side of the test section, the same set of optics are used to recombine the two beams so that they interfere and are focused onto a photodiode. As density fluctuations in the test section pass by the two beams, each beam is slightly diffracted, causing the beams to interfere and change the corresponding voltage readout from the photodiode. This allows for extremely fast density fluctuation measurements across the distance Δx to be made within the test section, but there are some limitations. The biggest limitation of LDI is that the density fluctuation effects across Δx are integrated across the entire test section width of Δy. This means that density fluctuations that occur outside the region of concern within the test section can affect the measurements made at the photodiode. Effects such as boundary layer noise at the edges of the test section thus become a limitating factor for the use of LDI [25].

To overcome the shortfalls of its simpler counterpart, focused LDI (FLDI) uses the same basic principles as LDI, but with some key differences that make it a very valuable, pin-point accurate, non-instrusive, density fluctuation measurement technique. A diagram of a basic FLDI setup is shown in Figure 76. Just as in LDI,

Label	Component
A	Laser Source
B	Diverging Lens
C	Polarizer
D	Wollaston Prism
E	Field Lens
F	Photodiode

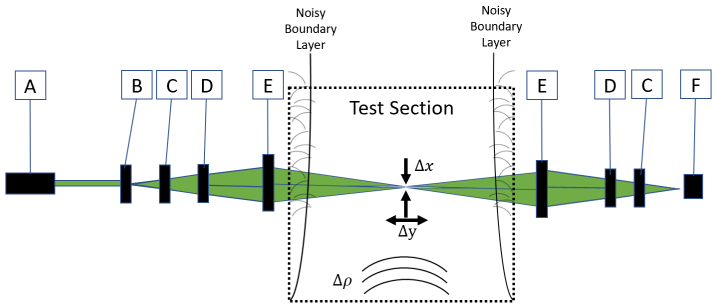
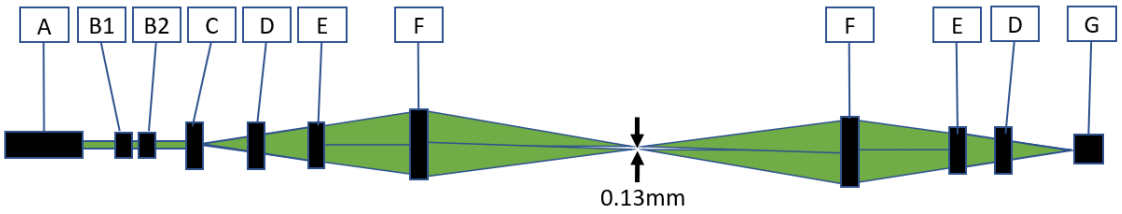


Figure 76. Example FLDI diagram

FLDI polarizes and splits a laser beam into two orthogonally polarized beams, but instead of collimating the beams, FLDI refocuses the beams into the test section. As a results, the two beam come to two separate focal points within the test section separated by a distance, Δx. The beams then are recombined on the far side of the test section and allowed to interfere with their focal points lying on a photodiode. While at first this setup looks almost identical to the LDI setup, the key difference in FLDI is that it is able to effectively eliminate freestream and non-important density fluctuations from its signal. This inherent filtering quality of FLDI is a result of the two beams having significant overlap at all points in the test section except at exactly the focal point locations. In the regions of the beams where the two beams overlap, any density fluctuations that affect one beam affect the other at the same time which in turn results in little to no interference on the photodiode. This means that only density fluctuations across Δx in the region defined by Δy are integrated and show interference effects on the photodiode. It should be noted that this Δy distance is known as the Rayleigh distance and is the region where the two beams no longer overlap and density fluctuations affect the readings [25].



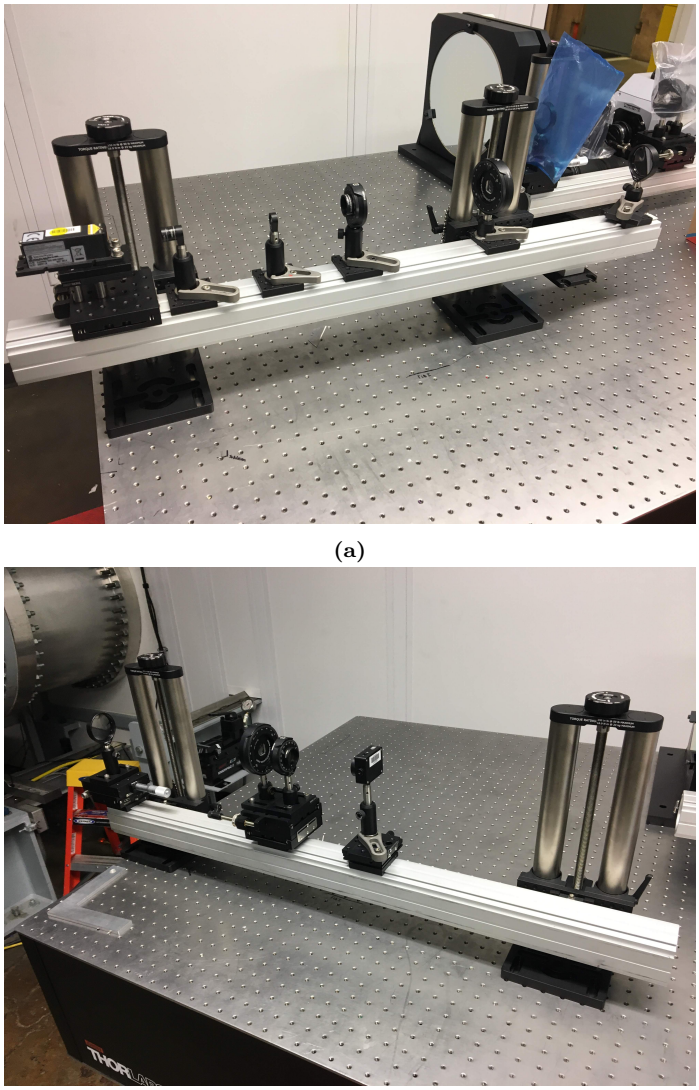
Label	Component
A	Solid State Continuous Wave Laser (532 nm, 200 mW)
B1	Neutral Density Filter 2.0 (1%)
B2	Neutral Density Filter 1.3 (5%)
C	10mm Focal Length Achromatic Doublet
D	Linear Polarizer (500-720 nm)
E	Wollaston Prism (2 arc minutes beam separation)
F	300 mm Focal Length Plano Convex Lens
G	Si Photodetetector (350-1100 nm)

Figure 77. Current FLDI setup diagram

Setup.

Using FLDI components initially gathered by Dr. Joseph Jewell at AFRL for testing purposes, a new FLDI setup was developed by the author for the AFRL Mach 6 Ludwieg tube. A basic diagram of this setup along with all of the major components is shown in Figure 77 and a list of all the components used can be found in Appendix B. It was found that this setup was capable of focusing the beams directly over the models with a measured focal point separation distance of approximately 0.13mm. With this setup, measurements were taken over Oddo's sharp seven degree cone and the ogive-cylinder model with various nosetips. A 10in traversal rail was mounted to both sides of the FLDI setup which then allowed for precise, incremental sweeps of the FLDI beams between runs.

Pictures of the emitting and receiving side of the FLDI setup can be seen in Figure 78. On both sides, the entire optical rail could be moved at precise increments using



(a)

(b)

Figure 78. FLDI setup rails (a) emitting rail and optics (b) receiving rail and optics

10in vertical traverses from ThorLabs. For this study, increments of 2mm were used to perform the vertical FLDI sweeps.

A series of beam profiler measurements of the two focal points of the FLDI setup were taken using a Coherent LaserCam IIID profiler alongside the Beamview Analyzer 3.2.3 software. It should be noted that, while the beam profiler setup is an older unit, it was capable of capturing the qualitative characteristics of the beam and verified the focal point spread distance of 0.13mm. Images from the beam profiler can be

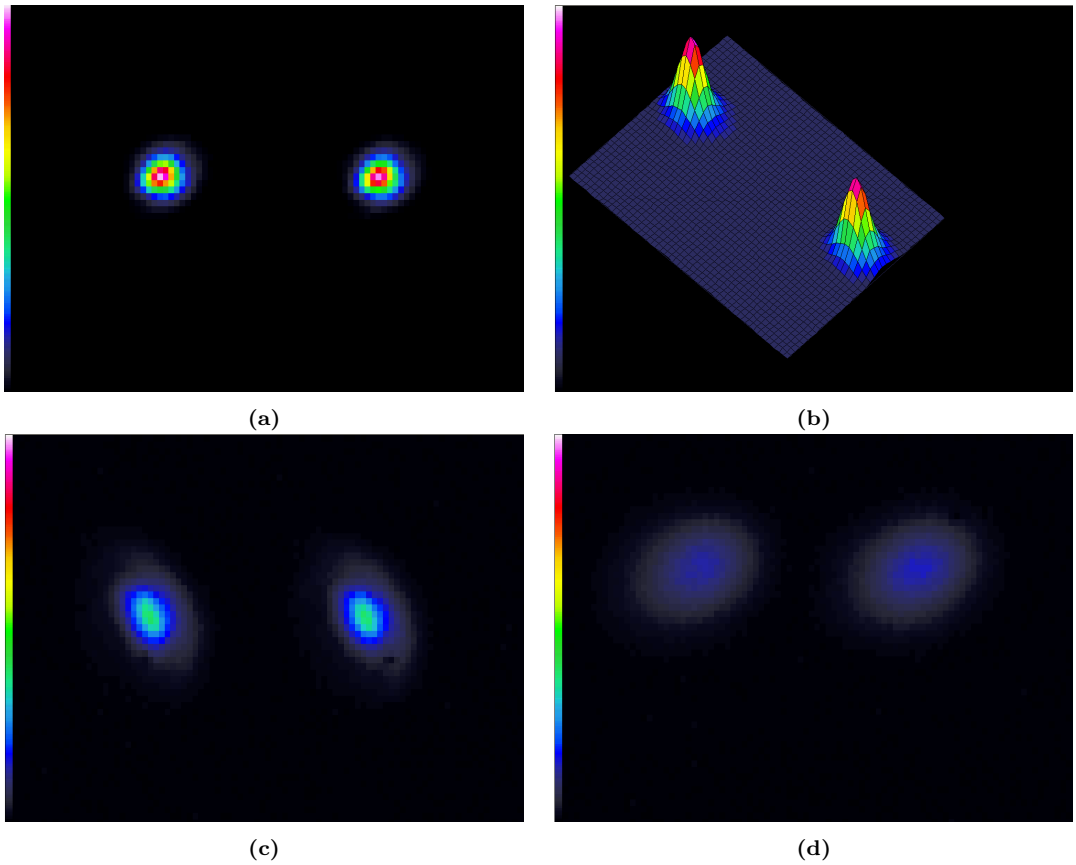


Figure 79. Beam profile of the FLDI beams (a) 2D view the focal point (b) 3D view at the focal point (c) 2D view 3/4in forward (d) 2D view 3/4in rearward

seen in Figure 79. From the beam profiler results, the Gaussian nature of the beam can be observed at the focal points and the merging of the two beams can be seen as the profiler is moved forward and aft of the beam focal points.

The signal from the photodiode used in this setup was amplified 25 times via a SR445 Stanford Research Preamplifier before being sent to the data acquisition system. The data acquisition system used a sampling frequency of 100MHz to gather the data from the photodiode. This sampling frequency is more than enough to resolve the frequencies to which the photodiode can respond.

While there were two neutral density filters available for use in this study, they were not used due to a clear signal from the unfiltered beams being observed in the photodiode readouts. It was found at the end of this study, that the lack of density

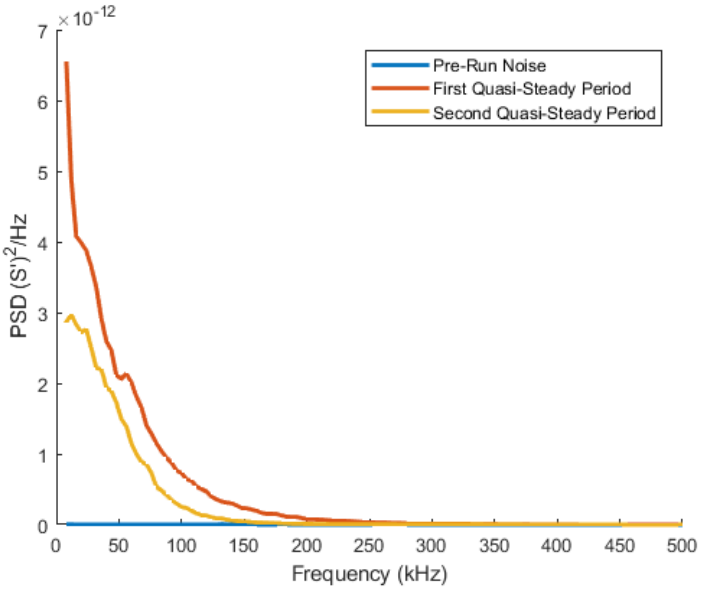


Figure 80. FLDI pre-run noise compared to first and second quasi-steady period signals from example run

filters prevented the ability to take quantitative density gradient measurements with the FLDI setup, but did not affect the ability to take quantitative density fluctuation measurements. Since the main goal in using the FLDI setup was to take frequency content and not necessarily measure absolute density fluctuation amplitudes, this side effect of not using the neutral density filters did not detract from the main goal of the study.

For future work, the following provides a description of how the neutral density filters can allow for the FLDI setup to measure absolute density fluctuations in addition to frequency content. On the receiving end of the FLDI setup, it is ideal to position the polarizer and Wollaston prism in an orientation so that the focal points are on the edge of an interference fringe of the combined beams. As the Wollaston prism is translated across the width of the converging beam, the phase of the interference pattern can be finely adjusted. The resulting voltage readout from the photodiode as the Wollaston prism is translated follows a sinusoidal pattern from maximum to

minimum voltage where the least and most interference is experienced between the two beams. At the inflection point of the sinusoidal response of the photodiode, the response of the FLDI system can be considered linear. This linear region allows for a quantitative estimate of the shift in density across the beams to be made. Before each run, the maximum and minimum voltages are recorded and then the Wollaston prims is positioned so that the voltage readout is exactly halfway between these two values, placing it in the center of the linear response regime. For this study, the 25 times amplifier was unknowingly overloaded when no neutral density filters were used. This overload prevented a maximum voltage from being recorde and thus quantitative density fluctuation magnitudes could not be made. For future studies, adding the neutral density filters to prevent an overload of the amplifier should solve this complication and add another set of data returned from the FLDI setup.

As is shown in Figure 80, the FLDI system used produced very low electrical noise. This low level of noise is most likely attributed to the photodiode using a battery energy source as opposed to a wall plug where the other sensors saw high electrical noise and interference.

3.4.3 High Speed Schlieren.

Setup.

For the seven degree half angle sharp cone and the ogive-cylinder model, high speed Schlieren was used to capture images of flow features and boundary layer instabilities. The setup used for this study was a modified z-type Schlieren assembly. A basic diagram of the setup can be viewed in Figure 81. A continous light Newport 66921 Arc Lamp with a 450W ouput power was used as the light source for this experiment. A plano-convex lens was used to focalize the light from the lamp to a focal point where an iris aperture ($< 2mm$) was used to create an artificial point source for the

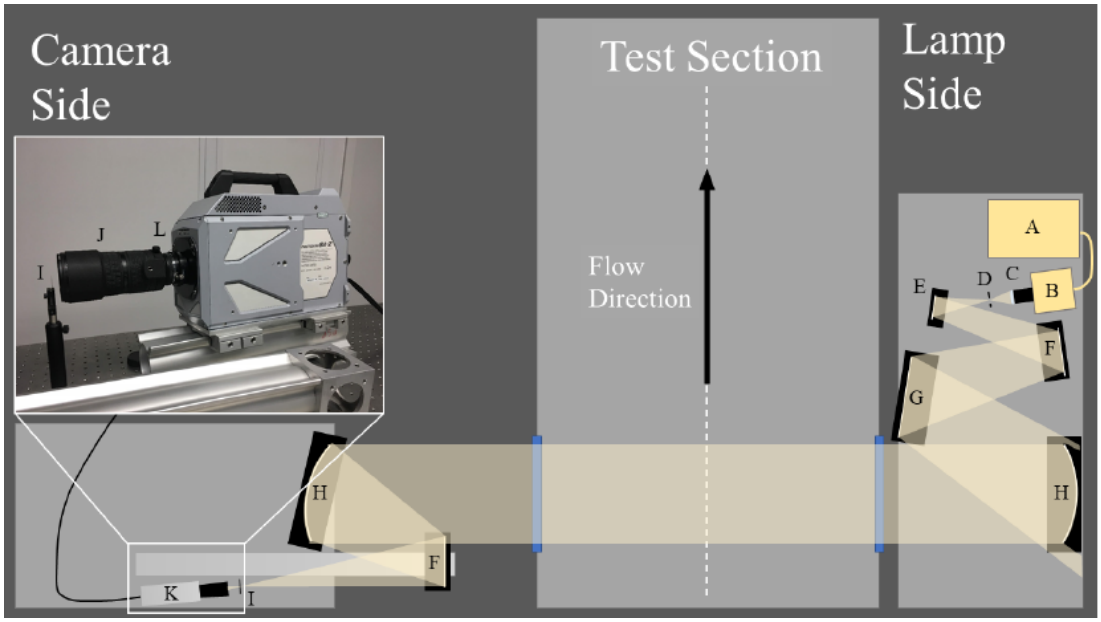


Figure 81. Schlieren setup diagram

Table 5. Schlieren setup components

Component	Description
A	Oriel OPS-A1000 Arc Lamp Power Supply
B	Newport 66921 Arc Lamp, 450W
C	BK7 A Coated Plano-Convex Lens, 2" Diameter, F = 150.0 mm
D	Circular Aperture, 2.5" Diameter
E	Planar Mirror, 3" Diameter
F	Planar Mirror, 6" Diameter
G	Planar Mirror, 10" Diameter
H	Concave Mirror, 12" Diameter, Parabolic, F = 75"
I	Razor Blade, 2.4375" Length
J	Camera Lens, Nikon Nikkor 80-200mm 1:2.8D
K	Photron Fastcam SA-Z-2100K-M-32GB
L	2x Zoom Teleconverter, Nikon **(not used with Viewing Window 1)**

Schlieren optical path. A series of flat mirrors are then used to reflect the light to allow for the 75in focal length of the large 12in diameter concave mirror to be met in the confined space between the tunnel and the wall. The large concave mirror collimates the light through the test section before being received by an identical mirror on the far side of the test section. This second concave mirror focuses the light another 75in to a focal point. A flat mirror is used to allow for the light to be

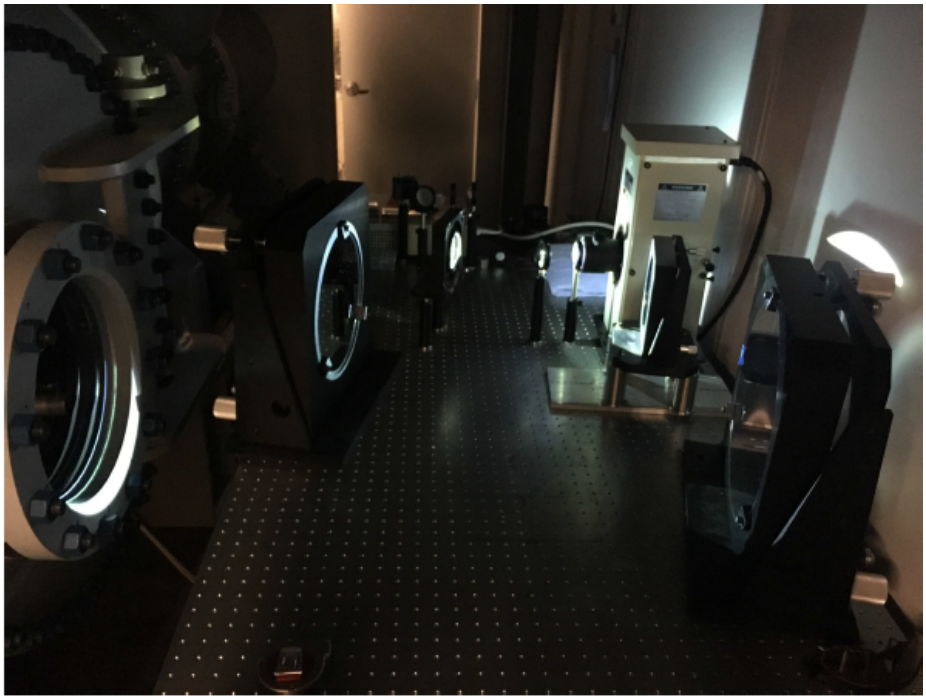
redirected back onto the optical table. At the focal point on the receiving side of the setup, a horizontal knife edge is used to create the full Schlieren effect. The light is then received by a Photron Fastcam SA-Z-2100K which is capable of framerates up to 2 million frames per second (fps) with minimum shutter speeds of 150 nanoseconds. Figure 82 shows the emitting and receiving sides of the Schlieren setup in the tunnel test section room.

For the Schlieren images captured over Oddo's cone, two viewing windows were used with varying window size and framerates. These viewing windows can be seen in Figure 83 with their corresponding imaging specifications tabulated in Table 6. The lower framerate, wider view window 1 was used for a majority of the runs over the cone. The wide viewing window allows for the boundary layer and instabilities to be clearly observed. The 300kHz framerate was found to be undersampled relative to the frequencies passing by for viewing window 1. This undersampled framerate meant that traditional temporal fast Fourier transforms (FFT) could not be performed to resolve the instability frequency content. A post-processing technique was developed and tested over this geometry that allows for spatial frequency to be translated into temporal frequency. Viewing window 2 was used for a couple of run conditions at a much higher framerate of 900kHz to allow for traditional FFT analysis to be used to cross-verify the spatial to temporal frequency analysis.

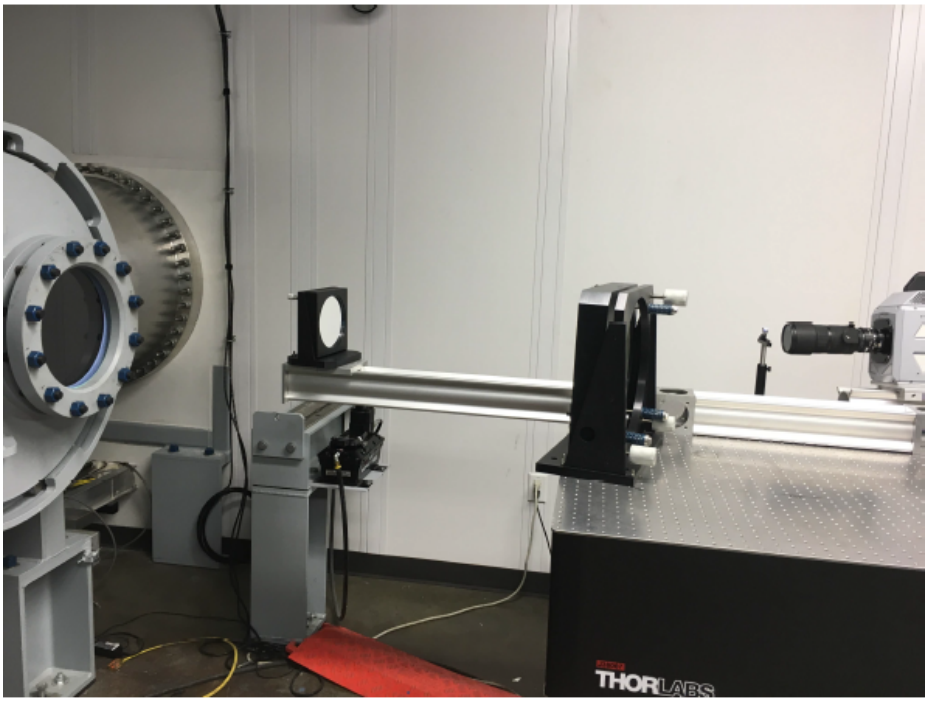
Table 6. Oddo Schlieren imaging specs

Window Number	Pixel Resolution	Pixel Scale (Pixels per mm)	Visible Span Axially from Tip (mm)	Visible Height Above Surface (mm)	FPS	Shutter Speed (sec)
1	1024 x 56	9.65	191-292 (6-10in)	5.3	300,000	1/2880000
2	128 x 48	9.65	235-248 (9.25-9.75in)	4.8	900,000	1/2880000

For the Schlieren images captured over the ogive-cylinder geometry, three primary windows were used. These windows and there corresponding specifications can be seen



(a)



(b)

Figure 82. Schlieren setup (a) emitting side (b) receiving side

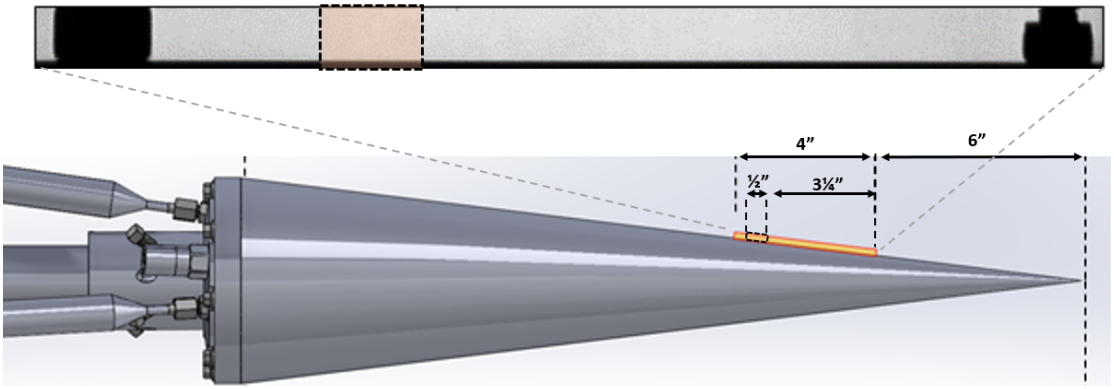


Figure 83. Oddo Schlieren imaging window

in Figure 84 and Table 7. The first window uses the lowest framerate and is used as an angle of attack verification source due to its ability to capture the boundary layer above and below the model. Results of the angle of attack measurements for the first window are shown in Section 4.2. The primary two windows that are used for instability observation are windows 2 and 3. These two windows are effectively identical and focus on the upper surface of the model.

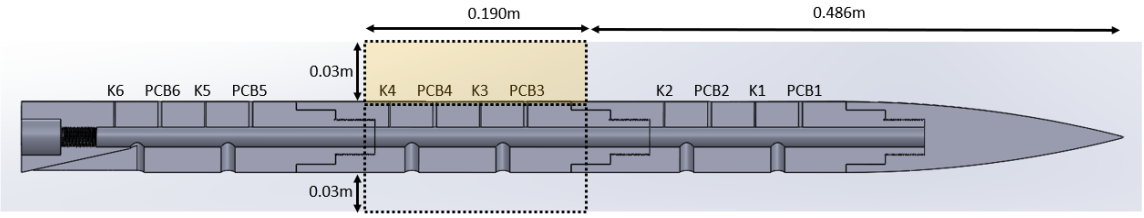


Figure 84. Ogive-cylinder Schlieren imaging window diagram

Table 7. Ogive-cylinder Schlieren imaging specs

Window Number	Run Numbers	Pixel Resolution	Pixel Scale (Pixels per mm)	Visible Span Axially from Tip (mm)	Visible Height Above Surface (mm)	FPS	Shutter Speed (sec)
1	18-23	1024 x 632	5.03	486-676	36.59	32000	1/4032000
2	24-37	1024 x 152	5.11	486-676	28.76	112000	1/4032000
3	97-101	1024 x 152	5.11	486-676	27.98	112000	1/4032000

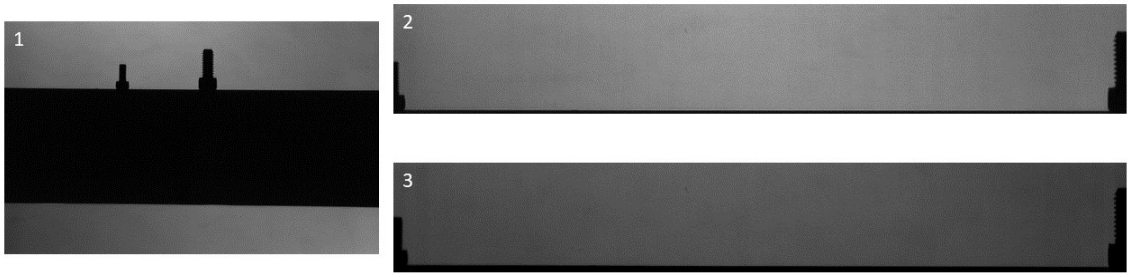


Figure 85. Ogive-cylinder Schlieren imaging window with screws used for pixel scaling

At the time that the Schlieren setup was used for this model, it was assumed during the experiments would see frequencies between 10-50kHz as Purdue observed [19]. As will be shown in Chapter IV, much of the frequency content that was observed over this model was between 50-60kHz. These frequencies fall too close to and slightly above the Nyquist frequency of $\approx 56kHz$ for the 112,000 fps framerate, thus no traditional temporal FFT frequency analysis could be performed. The same spatial to temporal frequency analysis that was developed and verified over Oddo's cone was thus used for this geometry as well to make estimates of wave packet frequencies from the Schlieren images.

Spatial to temporal frequency analysis.

The basic premise of the spatial to temporal frequency conversion analysis is that the frequency of a wave can be estimated if the wavelength, λ, and propagation speed, u_{wave}, of the wave is known via the equation $f_{temporal}(Hz) \approx \frac{u_{wave}(m/s)}{\lambda(m)}$. The method is split into three main parts: 1) spatial fast fourier transform (FFT) of frame to determine most prominent wavelength, 2) cross-correlation between two frames to determine estimated wave speed, 3) vertical sweep to determine frequency vs height.

As is shown in Figure 86, the spatial to temporal frequency analysis begins with pulling a frame where an instability is visible and a spatial FFT is performed on of a

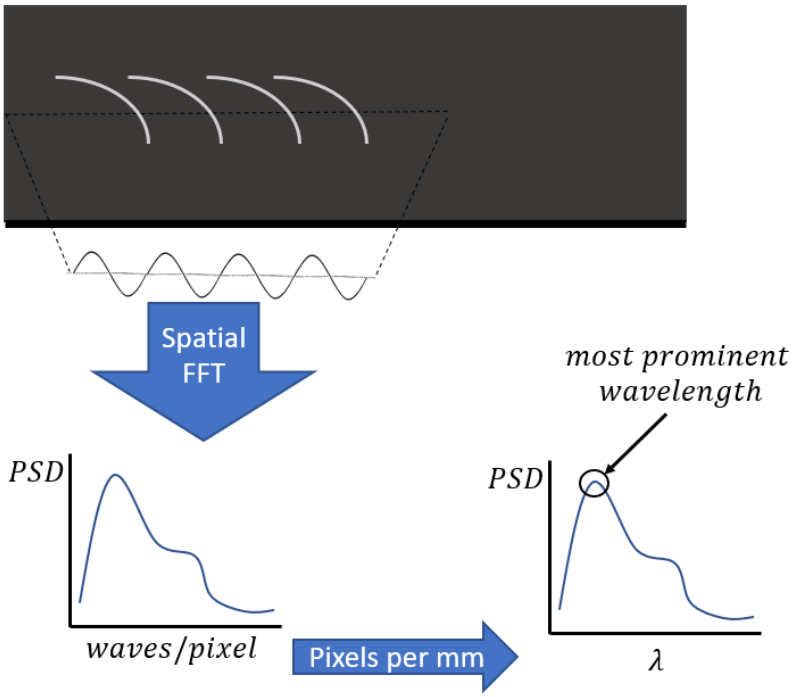


Figure 86. Spatial frequency estimate used to determine most prominent wavelength

line of pixels crossing the width of the observed instability. This spatial FFT's output is a spectral estimate of the most prominent number of waves per pixel. Multiplying the x-axis of this resulting FFT which has units of *waves/pixel* by the known parameter of *mm/pixel* for the Schlieren image returns a spectral estimate of the most prominent wavelength in the frame. The largest wavelength that can be estimated via this method is the length of the number of spanwise pixels in the frame used to perform the analysis. The smallest wavelength that can be resolved via this method is two pixels wide. This minimum wavelength is due to the effective "sampling rate" of the spatial FFT being one sample per pixel resulting in a "spatial Nyquist frequency" of 1/2 sample per pixel (i.e. wavelength must span two pixels to be resolved at a minimum).

As is depicted in Figure 87, after the wavelength is estimated for a frame, the same row of spanwise pixels used for the first frame are pulled from the next frame

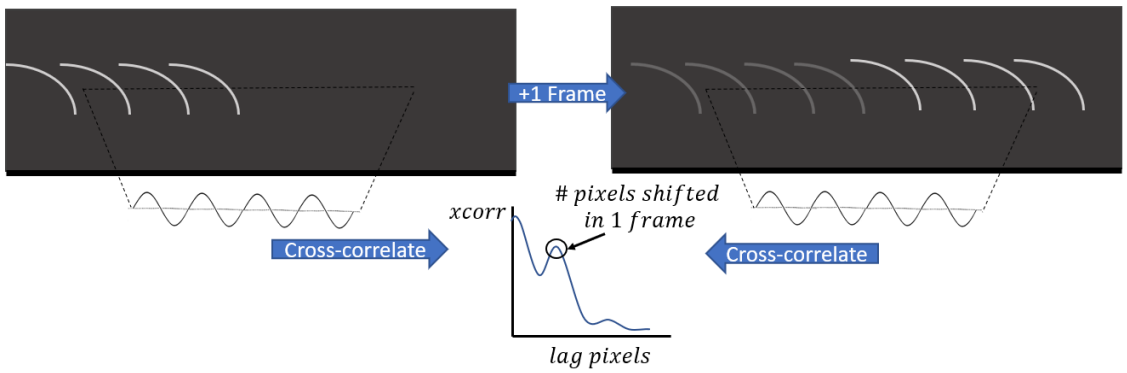


Figure 87. Cross-correlation between frames used to estimate wave propagation speed

and the two rows are compared to one another using a cross-correlation function. The output of the cross-correlation function is an estimate of the number of "lag pixels" that occur between frames (i.e. how many pixels did the signal from frame one shift as it moved to frame two). With this estimate of the number of pixels the signal shifted, an estimated wave propagation speed can be acquired via the equation $u_{wave}(m/s) \approx \frac{pixels\ shifted}{frame} * \frac{meters}{pixel} * \frac{frames}{second}$. The resulting output of this equation is the cross-correlation x-axis being converted into wave propagation speed. The highest peak in the cross-correlation in turn is the most prominent wave speed measured in the data. The automated version of this method attempts to find the first most prominent peak in the cross-correlation to find the wave propagation velocity. If the frame has no clear wave in frame, the estimate of this propagation speed will either drop to near zero or go towards infinity. A simple filter is used to ensure the algorithm does not allow for nonsensical propagation estimates below 0m/s or greater than 1000 m/s. It should be noted that a key assumption for this wave speed estimate is that there is negligible phase velocity of the waves between frames and that the wave propagation velocity dominates the shift in the apparent wave structure from frame to frame.

With the wavelength and wave propagation speed estimated for a given frame and

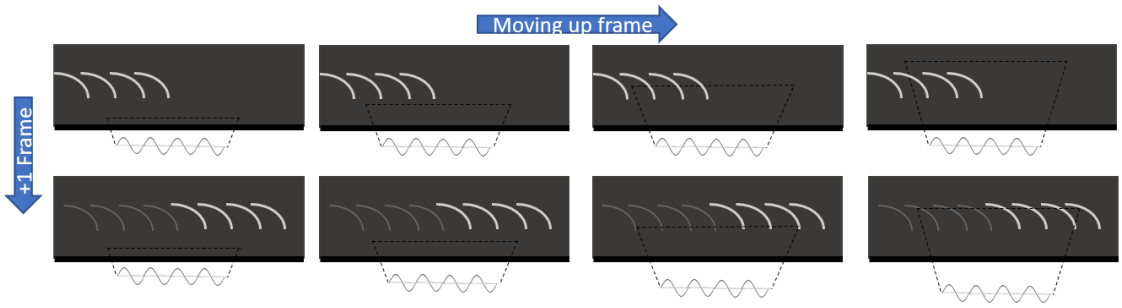


Figure 88. Iterate across rows of x-pixels and frames to build time accurate average frequency content

row of x-pixels, the same process is then iterated on for each row of desired x-pixels sweeping upward across a frame for each frame desired to be analyzed. As is depicted in Figure 88, this process allows for a time accurate estimate of frequency vs height for the selected number of frames and heights selected by the user. This is shown to be a powerful tool for undersampled Schlieren images where the instabilities observed in the frame are too close to and above the Nyquist frequency. This spatial to temporal frequency analysis is also analogous to a short time Fourier transform in that it is also a very strong tool for finding highly random and intermittent packets of frequencies by providing time-accurate estimates of the presence of waves with a given frequency for a desired row of pixels above the surface of the model.

Figure 89 shows an overview of the end product capability of this analysis technique for one of the 14 degree sharp tip ogive-cylinder cases where 100 Schlieren frames were analyzed for frequency content. All of the spanwise pixels were used for this example analysis and frequency content was taken for each row of pixels across the height of each frame. The resulting product is a multitude of powerful frequency spectra insights. First, the most prominent frequency at each row of pixels across the frame can be plotted or it can be normalized the amount of wave packets at that frequency that are observed across the frames. Pulling a row of pixels at any given

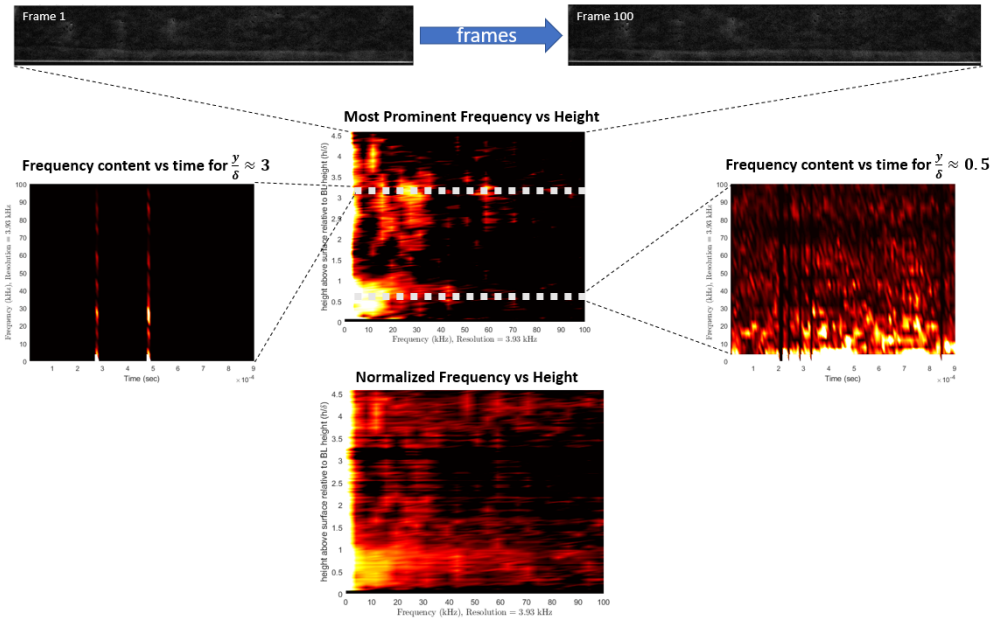


Figure 89. Resulting outputs of the spatial to temporal frequency analysis

height can then show the frequency content of that row of pixels vs time. This can allow for the user to determine the amount of wave packets of a given frequency cross the window during the selected set of frames.

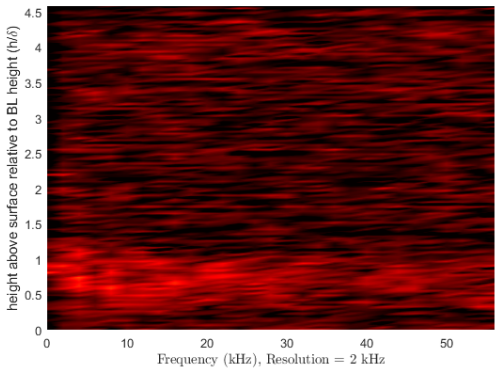


Figure 90. Example output of traditional temporal FFT using same data set

For situations where the instabilities have long and random intermittency between packets, this spatial to temporal frequency analysis can be more useful than a traditional temporal FFT of the frames at finding passing wave packets. Figure 90 shows

the result of using a traditional temporal FFT on the same set of frames as in Figure 89. It is observed that, while the traditional FFT resolves the most prominent frequencies with many wave packets, the heights where the wave packets are more intermittent, the traditional FFT loses fidelity and "washes" out the frequency of the intermittent packets in the background noise of the rest of the samples.

IV. Results and Analysis

A series of experiments using a seven degree half angle sharp cone and an ogive-cylinder model with various nose geometries were conducted in the AFRL Mach 6 Ludwieg tube. These experiments revealed instabilities that were analyzed through a variety of measurement and post-processing techniques. In this chapter, the results from the cone and ogive-cylinder models are presented and analyzed. Since the seven degree half angle cone is a well documented case that has been shown in previous experiments to exhibit strong second Mack mode instabilities, the results from the experiments on this geometry are presented first as a validation of the FLDI setup and Schlieren imaging techniques before being utilized over the more complex and less documented ogive-cylinder geometry. After the techniques are shown to be valid for the conical geometry, an in-depth break down of the results from the ogive-cylinder experiments is presented.

4.1 Seven Degree Half Angle Cone

While the use of pressure sensors, Schlieren imaging, and focused laser differential interferometry (FLDI) to perform boundary layer instability measurements is not new, experiments using of all of these techniques together in the AFRL Mach 6 Ludwieg tube have not been extensively conducted prior to this investigation. This study is also the first time this author is using all of these measurement techniques together on a geometry. In order to provide a validation of the FLDI and Schlieren imaging techniques in this facility, experiments were conducted over a seven degree half angle cone to allow for a refinement of the measurement techniques and for an initial cross-validation between the methods. The seven degree half angle sharp cone is a well documented geometry at Mach 6 conditions, thus it was determined to be a

useful starting point for ensuring the FLDI and Schlieren measurements are capable of measuring these instabilities and that they are seeing the same instabilities.

4.1.1 Schlieren visualization resolves the boundary layer and second mode instabilities.

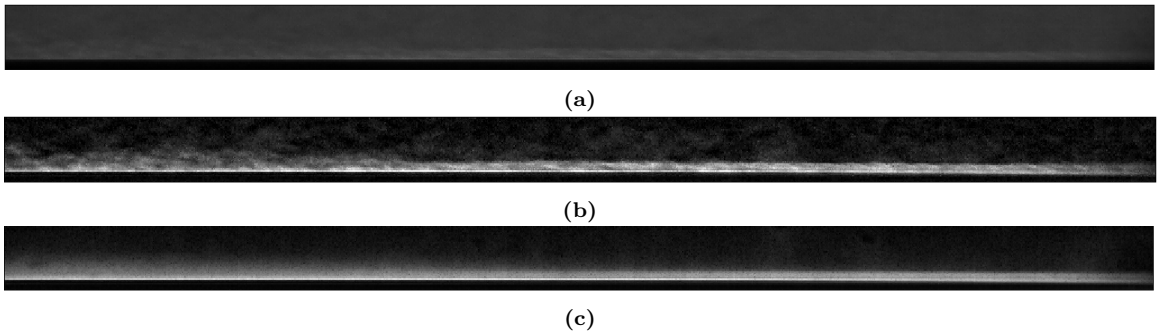


Figure 91. Schlieren images of boundary layer over Oddo's cone at nominal 300psia driver tube pressure(a) raw frame (b) background subtracted frame (c) average of 1000 background subtracted frames

The first verification study performed is a qualitative assurance that the Schlieren setup used is capable of spatially resolving the boundary layer and collecting time accurate information about instabilities in the boundary layer. Using Viewing Window Two of Oddo's Schlieren images (see Section 3.2), a series of images were taken at a frame rate of 300,000 frames per second (fps) and a shutter speed of 1/2,880,000 per second over the cone geometry at various run conditions. Five separate driver tube pressure conditions were analyzed in this study. For each of the run conditions, the Schlieren images were collected and processed via a simple frame averaging technique to determine each run's approximate boundary layer height. In order to consistently find the average boundary layer height for each run condition, a process was developed using ImageJ to manipulate the raw images to a form where the boundary layer edge is easily observed. First, approximately 1000 frames at the beginning of the second quasi-steady state period of each run are pulled and a background subtraction

is applied to the raw images. A contrast enhancement normalizing all of the pixels between 0 and 1 is then applied to the background subtracted frames to make any features present stand out better. The effect of this background subtraction and subsequent contrast enhancement can be observed between Figure 91 (a) and (b) where the raw and processed images are presented. It can be clearly observed that this subtraction and enhancement process makes the structures present in the boundary layer much easier to identify. In order to find the average boundary layer height, an average intensity of the 1000 processed frames is taken, resulting in a final image as shown in Figure 98 (c) where the average boundary layer height across the frame can be measured.

Table 8. Boundary layer heights determined from Schlieren for Oddo's cone at various driver tube pressures

Oddo 7° Cone					
Desired P_{DT} (psia)	100	150	200	250	300
Boundary Layer Height (mm)	1.45	1.40	1.35	1.14	0.98

Using this image processing method, Table 8 is created showing the estimated boundary layer heights for the nominal driver tube set pressures that were used. It can be easily observed from this table that an increase in driver tube pressure (which correspondingly means an increase in unit Reynolds number) causes the boundary layer to become thinner. This trend of decreasing boundary layer thickness with increased Reynolds number is expected and shows the Schlieren is able to capture features of the boundary layer effectively. It should be noted that this method only provides a "ballpark" estimate of the boundary layer height for each configuration and driver tube pressure. During the course of a single run, the stagnation conditions drop considerably along with the Reynolds number which in turn means that each run will have a boundary layer that changes height from one quasi-steady state to

the next during the run. With this in mind, the results shown here should be taken as a rough estimate of each run condition's boundary layer height and are meant to be used for comparison's sake. For a more in depth verification of the boundary layer measured heights against theory, the author directs the reader towards Oddo's thesis [22].

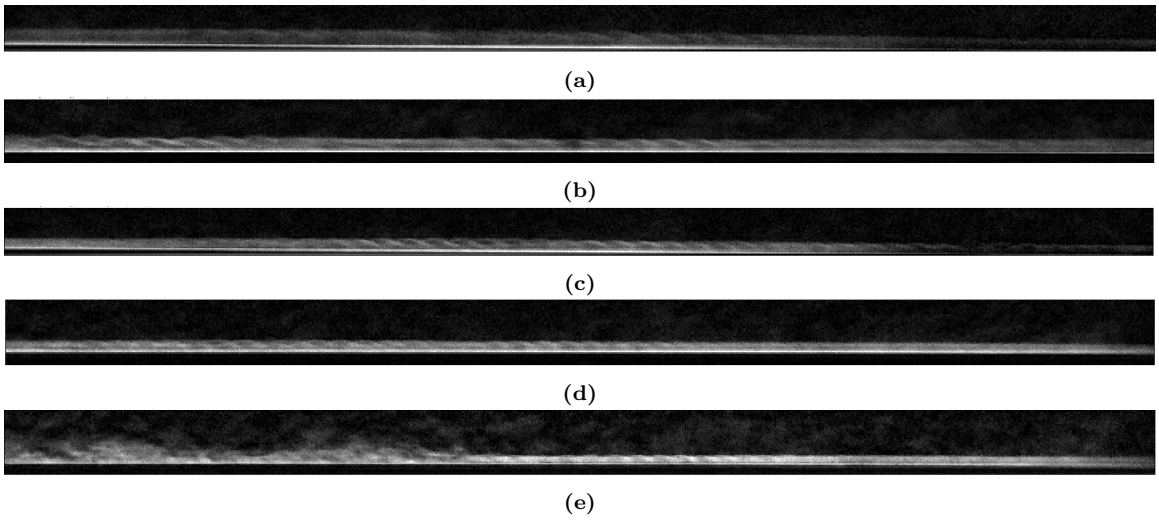


Figure 92. Second mode instabilities over cone (a) $P_{DT} = 100psia$ **(b)** $P_{DT} = 150psia$ **(c)** $P_{DT} = 200psia$ **(d)** $P_{DT} = 250psia$ **(e)** $P_{DT} = 300psia$

Beyond finding the average boundary layer height, the Schlieren images captured over Oddo's cone show clear boundary layer instabilities. Figure 92 shows the "rope-like" structures indicative of second Mack mode waves present at every run condition used for this study over this geometry. It can be noted that the intensity of the second mode waves in the Schlieren images increases with increasing driver tube pressure. It is observed for the 100psia case that the second mode waves are very sparse and low in intensity making them difficult to identify for this run case. The 150psia and 200psia cases show much more prominent second mode packets with little to no turbulent spotting. The 250psia case shows strong second mode packets with intermittent turbulent spotting on the downstream edge of the frame. The highest pressure of 300psia shows consistent turbulence on the downstream portion of the

frame.

4.1.2 FLDI and Schlieren measure the same second mode instabilities.

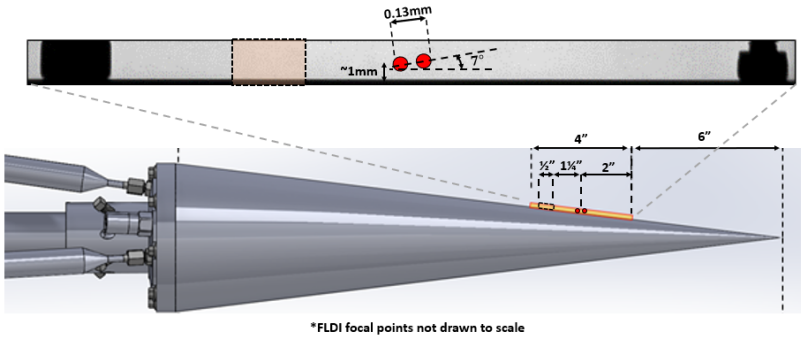


Figure 93. FLDI and Schlieren viewing window diagram

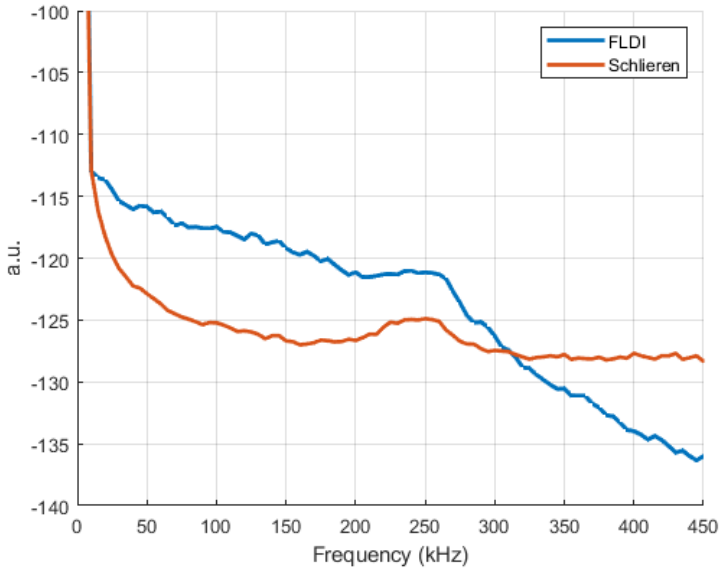
Moving from the primarily qualitative observations of the Schlieren setup's ability to capture second mode waves over Oddo's cone, a quantitative analysis comparing the frequency content of the Schlieren and FLDI for similar run conditions is made. Figure 93 shows the location of the FLDI focal points relative to the viewing windows for Oddo's cone. It should be noted that this diagram is not to scale, but provides a relative positioning and orientation for the two diagnostics. The FLDI beams were positioned 8 inches downstream from the tip of Oddo's cone with a horizontal focal point orientation at approximately 1 millimeter above the surface as close as the beams could be resolved without touching the model's surface. Viewing window 2 of the Schlieren images, while slightly downstream of where the FLDI focal points were taking measurements, used a framerate capable of adequately performing traditional temporal Fourier transform frequency analysis and resolved similar frequencies to those found using FLDI. Two run conditions (nominal $P_{DT} = 150psia$ and $P_{DT} = 200psia$) were captured with this Schlieren window's high framerate and were found to be sufficient for comparing with the FLDI results. Figure 94 shows the results of FLDI and Schlieren frequency analysis compared to one another in arbitrary units.

These results were achieved by using Matlab's Welch's power spectral approximation function (pwelch) with a frequency resolution of 5kHz. The 150psia case corresponds to Oddo's run 85 and this study's run 102. The 200psia case corresponds to Oddo's run 86 and this study's run 12. It should be noted that, while Oddo's runs were completed at the same nominal driver tube pressure (P_{DT}), each run in the tunnel has a slight variance in stagnation conditions, but the overall flow properties are fairly consistent.

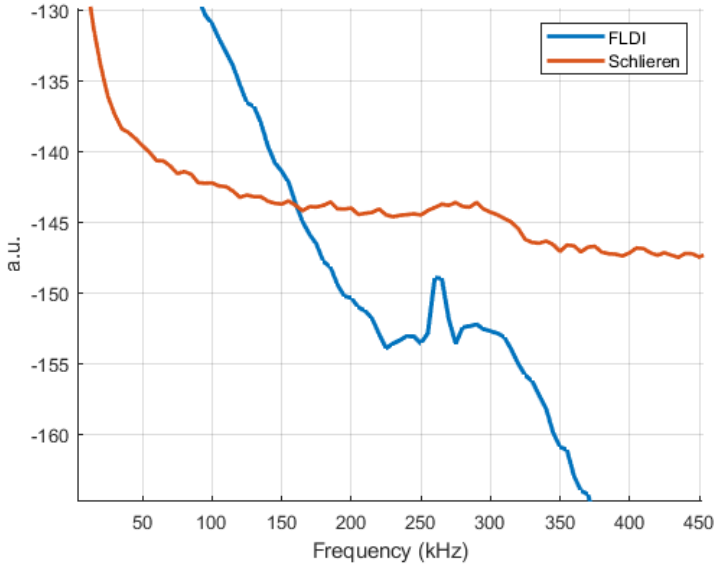
It can be observed from Figure 94 that the FLDI and Schlieren results for the high framerate runs are capable of resolving the same frequencies and are most likely measuring the same second mode instabilities. It can be seen that the 150psia case resolves a frequency of $\sim$ 250kHz and the 200psia case resolves a frequency of $\sim$ 275kHz. This increase in frequency is expected since the higher driver tube pressure results in a higher unit Reynolds number and thus a thinner boundary layer which supports higher frequency second mode packets.

From the Schlieren images, the same power spectra technique can be applied for each row of pixels above the model to produce Figure 95. It can be observed in this figure that the Schlieren images produce a clear peaks in frequency content between 60% to 100% of the boundary layer height with the same frequencies being resolved as before. This location of frequency content is expected since the "rope-like" structures of second mode waves are bounded by the relative sonic line ($\sim$ 60% of the boundary layer height) and the upper edge of the boundary layer [10]. Dimensionalizing these heights using the Table 8, it is found that the frequencies are located around 1mm above the cone's surface. The FLDI focal points are located at approximately this height, thus further verifying that Schlieren and FLDI are measuring the same instabilities.

With this mutual verification of FLDI and Schlieren showing that FLDI is capa-



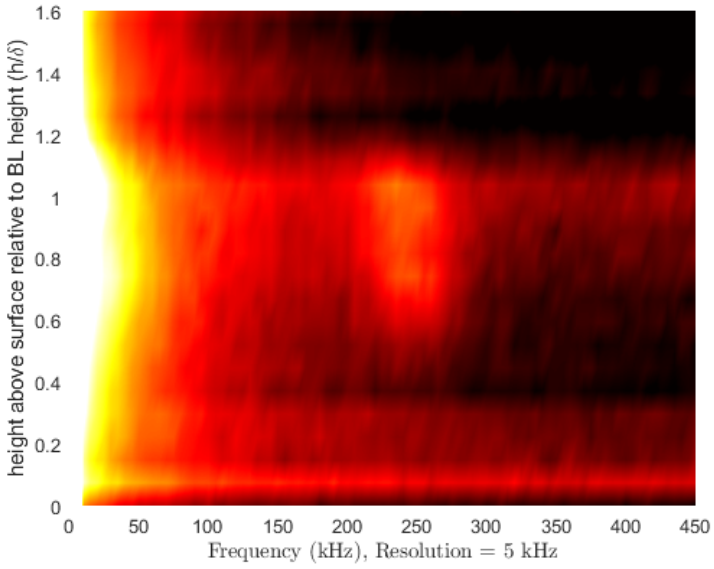
(a)



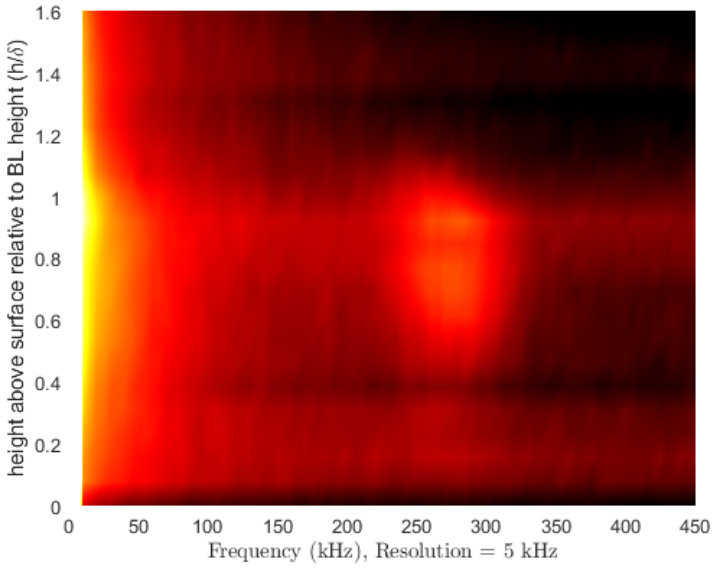
(b)

Figure 94. PSD comparison between FLDI and Schlieren (a) $P_{DT} = 150psia$ **(b)** $P_{DT} = 200psia$ **(y-axis uses arbitrary units)**

ble of measuring the frequencies associated with second mode instabilities found in Schlieren, a frequency analysis for the remaining FLDI cases that were run can be completed. Figure 96 shows the PSD results from FLDI over Oddo's cone for the second quasi-steady period for nominal driver tube pressures of 100, 150, 200, 250,



(a)



(b)

Figure 95. Traditional FFT PSD results from Schlieren vs height above cone normalized by boundary layer height (a) $P_{DT} = 150psia$ **(b)** $P_{DT} = 200psia$

and 300 psia (runs 13, 16, 15, 11, 14 respectively). It is clearly observed in this figure that the FLDI is able of capturing the peak frequencies for each driver tube setting. It should be noted that each of the FLDI runs had different scaling and thus are presented in arbitrary units, but the peak frequencies can still be compared. It can

be observed that the 100psia case shows no clear peak frequency, but as the pressure is increased a clear second mode frequency is observed. With increasing driver tube pressure, a clear second mode frequency peak appears and it can be seen that the peak frequency increases as the drive tube pressure (and the unit Reynolds number in turn) increases. This increase in frequency with increased driver tube pressure is expected due to the thinner boundary layers at the higher unit Reynolds numbers.

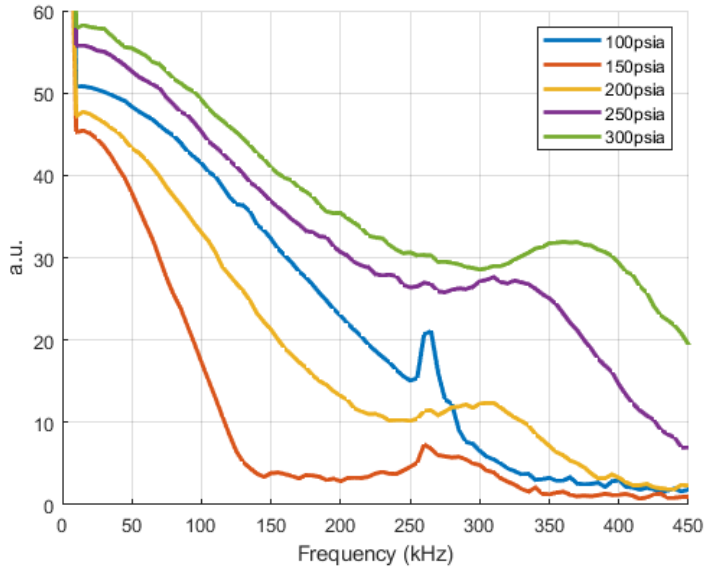
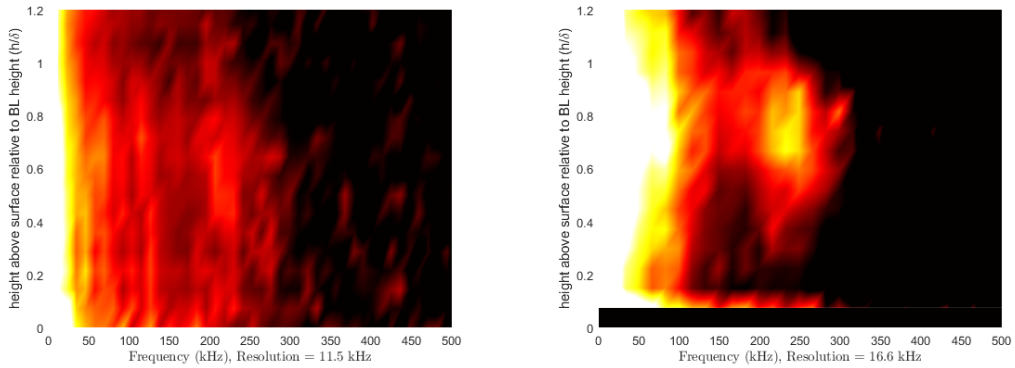


Figure 96. FLDI measurements with increasing driver tube pressure (the 100psia case shows a non-physical electrical noise peak)

4.1.3 Spatial to temporal frequency analysis of Schlieren reveals more instability features.

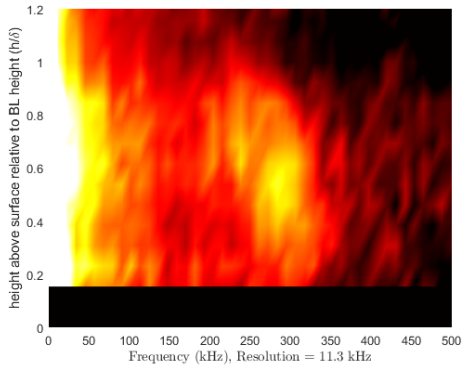
While only two cases were run with high enough frame rates to allow for proper Fourier transform frequency analysis, a process was developed to allow for spatial frequencies resolved in undersampled Schlieren frames to be transformed into temporal frequencies.

The spatial to temporal frequency analysis was performed for Schlieren images over

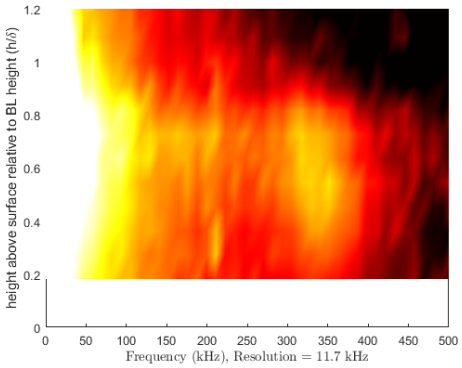


(a)

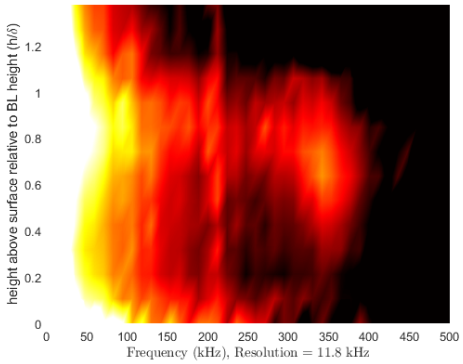
(b)



(c)



(d)



(e)

Figure 97. Spatial to temporal frequency PSD over Oddo's cone vs normalized height above model (a) $P_{DT} = 100psia$ **(b)** $P_{DT} = 150psia$ **(c)** $P_{DT} = 200psia$ **(d)** $P_{DT} = 250psia$ **(e)** $P_{DT} = 300psia$

Oddo's cone at driver tube pressures of 100, 150, 200, 250, and 300 psia (runs 36, 76, 35, 52, and 62 of Oddo's runs respectively [22]). The results of this analysis are shown in Figure 97 for each of these runs conditions during the first quasi-steady period

except for the 300psia case where the only clear PSD that could be accomplished was with the second quasi-steady period. It is clear from this figure that, while the spatial to frequency conversion has a lower temporal frequency resolution than the traditional FFT PSD results seen in Figure 95, this method is capable of resolving the peak frequencies for each run condition and consistently measures the height of the frequencies to be appropriately bounded appropriately between 60% to 100%. A clear increase in peak frequency from ∼275kHz to ∼350kHz is observed with the increase in driver tube pressure. This increasing frequency trend is expected and confirms that the spatial to temporal frequency conversion is capable of capturing the flow instabilities for undersampled framerates.

Table 9. Estimated wavelengths and wave propagation speeds over Oddo's cone

Oddo 7° Cone					
Desired P_{DT} (psia)	100	150	200	250	300
Estimated wavelength (mm)	3.25	2.9	3.28	2.9	2.4
λ/δ	2.24	2.07	2.43	2.54	2.35
Estimated wave propagation velocity (m/s)	819 ± 46	816 ± 37	789 ± 49	816 ± 38	805 ± 31

From the spatial to temporal frequency analysis, estimates of wavelength and propagation speed can also be made. Table 9 shows the results of these estimates. It can be observed that the wavelength at each run condition is approximately twice the thickness of the observed boundary layer from Schieren. This directly aligns with theory and further confirms the spatial to temporal frequency conversion method [44]. The wave propagation velocities also closely align with Oddo's estimates of boundary layer edge velocities [22]. It has been shown that second mode wave propagation velocity is approximately the same as boundary layer edge velocity, so the alignment here is another verification of this method's applicability [44].

4.2 Ogive-Cylinder Model

From the seven degree half angle cone results, confidence is increased in the ability of the current Schlieren and FLDI setups to measure hypersonic flow instabilities in the AFRL Mach 6 Ludwieg tube. Experiments were then performed over the ogive-cylinder geometry using surface mounted pressure sensors, FLDI, and Schlieren imaging to study tip geometry effects on downstream instabilities. This section will provide analysis on the results gathered from the experiments conducted over this geometry and its tip variants.

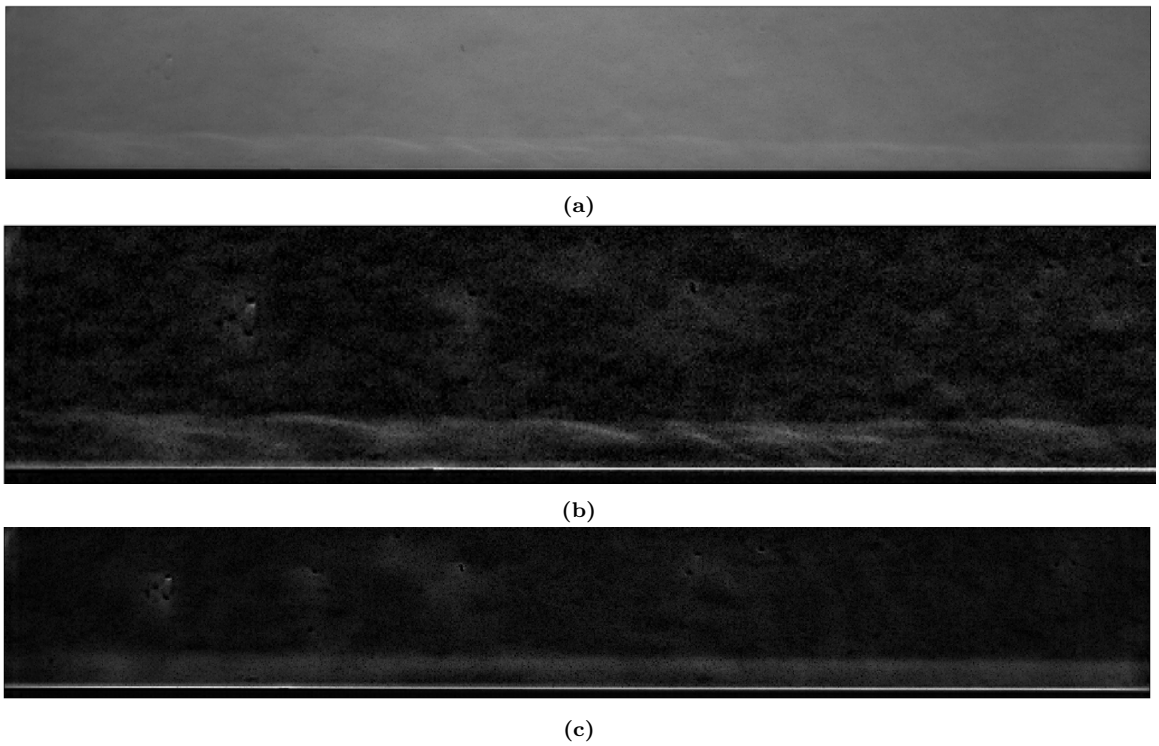
4.2.1 Schlieren results.

Schlieren images were taken over each of the ogive-cylinder configurations at a variety of run conditions. This section shows the results of this study in using Schlieren to shed light on the qualitative structure and quantitative behavior of the boundary layer instabilities over the ogive-cylinders.

Schlieren resolves the boundary layer.

Initial experiments of the ogive-cylinder geometry in the AFRL Mach 6 Ludwieg tube used Schlieren imaging to capture the boundary layer and instabilities present in the window. The imaging window, shown in Section 3.4.3, captured images between between 496mm to 676mm from the model's tip at a frame rate of 112,000 fps and a shutter speed of 1/4032000 sec. At this framerate and shutter speed, the boundary layer was clearly resolved and instabilities were "frozen" in each frame. For each geometry and run condition, the same method as that used in Subsection 4.1.2 is applied to the Schlieren images to resolve the average boundary layer height for the run. Figure 98 shows an example raw, processed, and averaged frame from the 14 degree sharp ogive tip with a nominal driver tube set set pressure of 125psia. Again,it

can be clearly observed that this subtraction and enhancement process makes the structures present in the boundary layer much easier to identify.



(a)

(b)

(c)

Figure 98. Schlieren images of boundary layer over the ogive-cylinder (a) raw frame (b) background subtracted frame (c) average of 1000 background subtracted frames

The resulting estimated boundary layer heights determined from the image processing technique are shown in Table 10 for each tip and driver tube pressures that Schlieren images were taken. As mentioned before, it should be noted that this method only provides a "ballpark" estimate of the boundary layer height for each configuration and driver tube pressure. During the course of a single run, the stagnation conditions drop considerably along with the Reynolds number which in turn means that each run will have a boundary layer that changes height from one quasi-steady state to the next during the run. With this in mind, the results shown here should be taken as a rough estimate of each geometry's and run condition's boundary layer height and are meant to be used for comparison's sake.

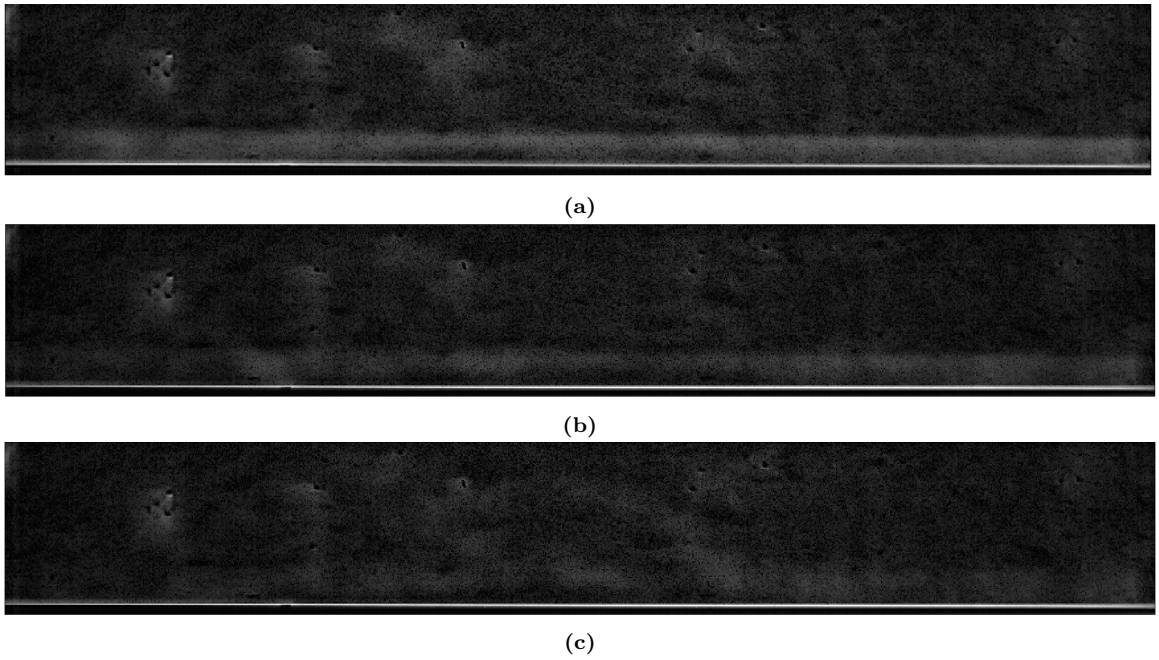
It can be observed from Table 10 that as the tip angle is increased for the sharp

Table 10. Boundary layer heights determined from Schlieren

14° Sharp Ogive						
Desired P_{DT} (psia)	75	100	125	150	200	250
Boundary Layer Height (mm)	6.07	5.28	5.09	4.7	N/A	N/A
14° 1/4R Blunt Ogive						
Desired P_{DT} (psia)	75	100	125	150	200	250
Boundary Layer Height (mm)	N/A	N/A	N/A	N/A	5.28	N/A
14°1/2R Blunt Ogive						
Desired P_{DT} (psia)	75	100	125	150	200	250
Boundary Layer Height (mm)	N/A	N/A	N/A	N/A	N/A	5.09
28° Sharp Ogive						
Desired P_{DT} (psia)	75	100	125	150	200	250
Boundary Layer Height (mm)	6.65	6.07	5.68	5.09	N/A	N/A
28° deg 1/4R Blunt Ogive						
Desired P_{DT} (psia)	75	100	125	150	200	250
Boundary Layer Height (mm)	N/A	N/A	N/A	N/A	N/A	5.68
28° 1/2R Blunt Ogive						
Desired P_{DT} (psia)	75	100	125	150	200	250
Boundary Layer Height (mm)	N/A	N/A	N/A	N/A	N/A	5.68
56° Sharp Ogive						
Desired P_{DT} (psia)	75	100	125	150	200	250
Boundary Layer Height (mm)	N/A	6.07	5.87	5.68	5.09	4.7
Spherically Blunted						
Desired P_{DT} (psia)	75	100	125	150	200	250
Boundary Layer Height (mm)	N/A	N/A	N/A	N/A	5.09	N/A

ogives (14 to 28 to 56 degrees), the boundary layer height for a given nominal driver tube pressure setting increases with increasing tip angle. The same holds true for a sharp ogive when bluntness is added. With increasing bluntness, the boundary layer height increases. This increase in observed boundary layer height is most likely due to the higher tip angles and bluntness creating a stronger shock front that decelerates the flow behind the shock more than the more oblique cases. This stronger deceleration

of the higher tip angles and blunt tips effectively drops the local Reynolds number for the flow behind the shock and allows for a thicker boundary layer to grow along the length of the cylinder.



(a)

(b)

(c)

Figure 99. Average boundary layer height Schlieren images at $P_{DT} = 125psia$ (a) 14 degree sharp ogive (b) 28 degree sharp ogive (c) 56 degree sharp ogive

The effect of the entropy layer and shock deceleration is also observed in the Schlieren image clarity. For the 14 and 28 degree half angle sharp ogives (the shallowest tip angle ogives used), the boundary layer was clearly resolved and instabilities were clearly observed in the Schlieren images. As the tip angle is increased, or if bluntness is added to the sharp ogive variants, it is observed that the boundary layer becomes more difficult to resolve as is shown in Figure 99. This is believed to be a side effect of the higher tip angles and blunted tips creating a stronger entropy layer that "blends" the density gradient of the boundary layer into the region of flow above the boundary layer. This blending of the boundary layer into the entropy layer makes estimates of the average boundary layer height difficult for the higher tip angles and bluntness values, and thus the boundary layer height measurements with these

tips have a higher chance for error. Regardless, the overall trends of the observed boundary layer heights make sense and are expected.

Schlieren shows changing instability structures.

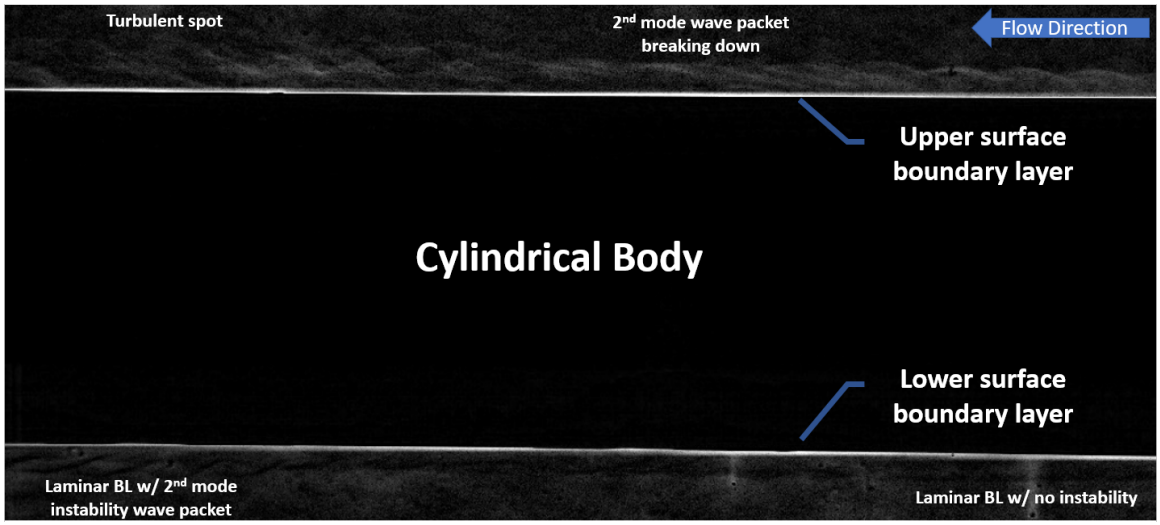
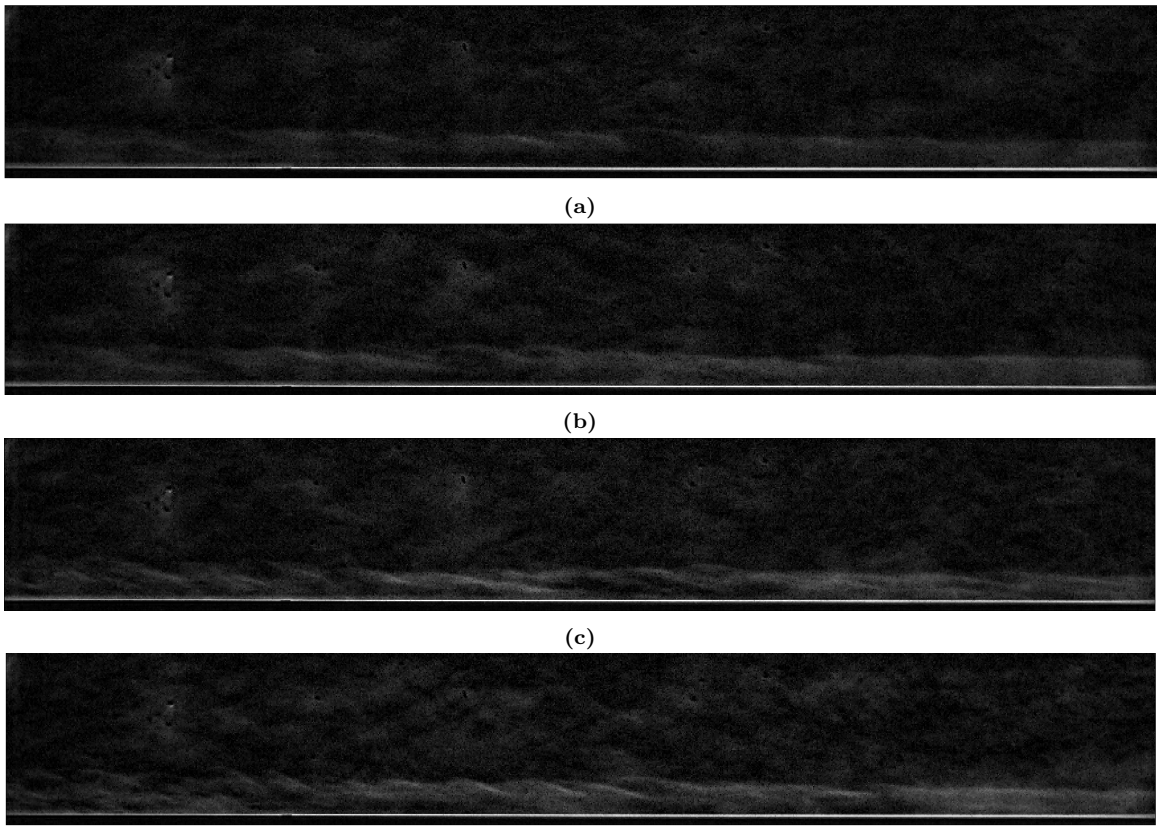


Figure 100. Schlieren image of modal instabilities forming and breaking down within the upper and lower boundary layers over the body of the 14 degree sharp ogive-cylinder at $P_{DT} = 100psia$

The Schlieren images used to find the average boundary layer were also capable of resolving clear boundary layer instabilities for the various tip geometries and run conditions. It was found that the 14 degree tip exhibited strong instability structures reminiscent of the "rope-like" structures of second Mack mode packets. Figure 100 shows a prime example of this "rope-like" modal instability above and below the model for the 14 degree sharp ogive tip with a nominal driver tube pressure of 100psia. This frame in particular provides some key insight into the behavior of this modal instability because the lower boundary layer shows a packet forming while the upper boundary layer shows a packet breaking into turbulence. Starting with the lower boundary layer where the packet is forming, it can be observed that the thickness of the boundary layer leading up to the packet forming is significantly smaller than after

the packet forms. The packet physically thickens the observable boundary layer edge and has clear structures that appear to be reminiscent of the classical second mode structures. Looking next to the upper boundary layer, it can be seen that as the wave packet breaks down, the packet structure becomes less defined and the packet appears to elongate and flatten before extending into the flow above the boundary layer and breaking down into turbulence. In the region where the packet elongates before breaking down, the packet structure appears to become more tightly packed and the striations extend all the way from the model's surface into the flow above the boundary layer.



(a)

(b)

(c)

(d)

Figure 101. Boundary layer instabilities for the 14 degree sharp ogive tip (a) $P_{DT} = 75psia$ **(b)** $P_{DT} = 100psia$ **(c)** $P_{DT} = 125psia$ **(d)** $P_{DT} = 150psia$

Figure 101 shows the development of the observed boundary layer modal instabilities for the 14 degree sharp ogive tip. As the nominal driver tube pressure is

increased it is clear that the modal instabilities strengthen in intensity and appear to be the primary driver for transition over the model. The consistency and frequency of intermittent turbulent spotting increases in the Schlieren images as the driver tube pressure increases with the 150psia case showing consistent turbulent spotting on the downstream end of the frame. The characteristics of the modal packets do not appear to change their behavior or structure with increased driver tube pressure. Instead, it is observed in the Schlieren that the higher pressures increase the intensity and intermittency of the modal packets and result in more turbulent spots forming.

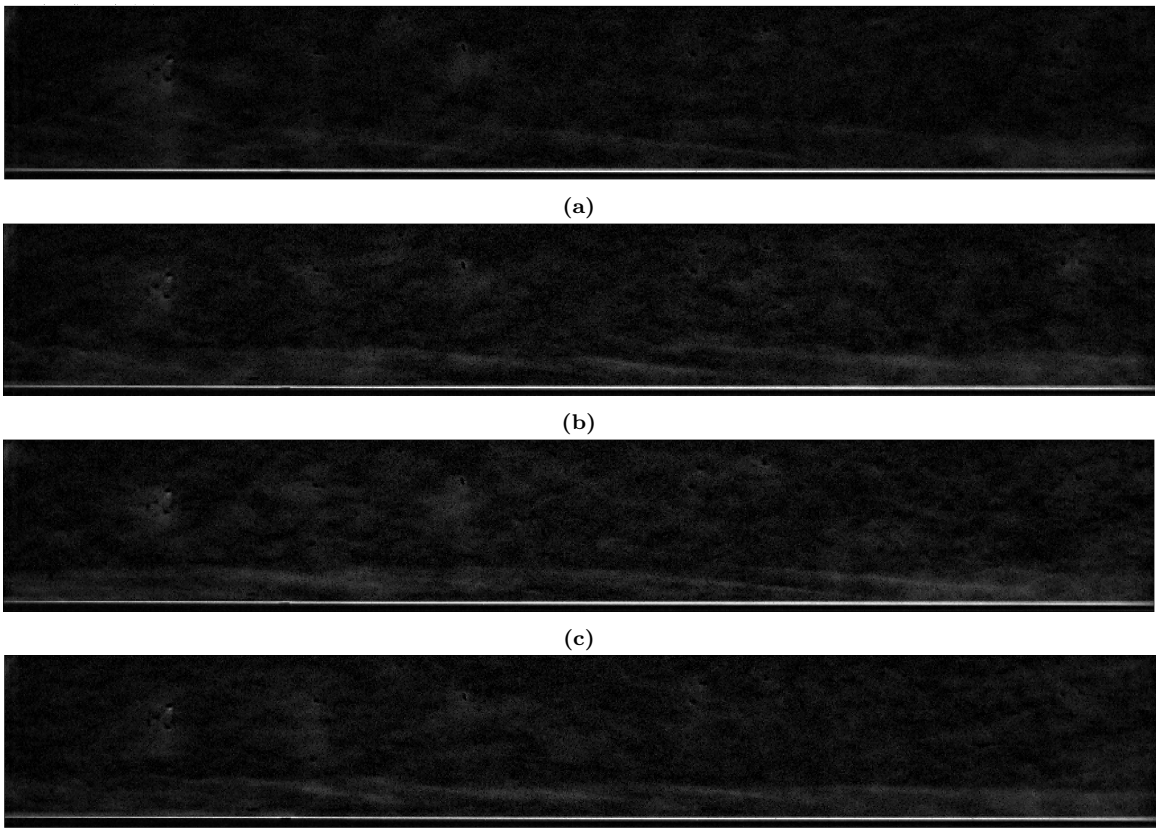
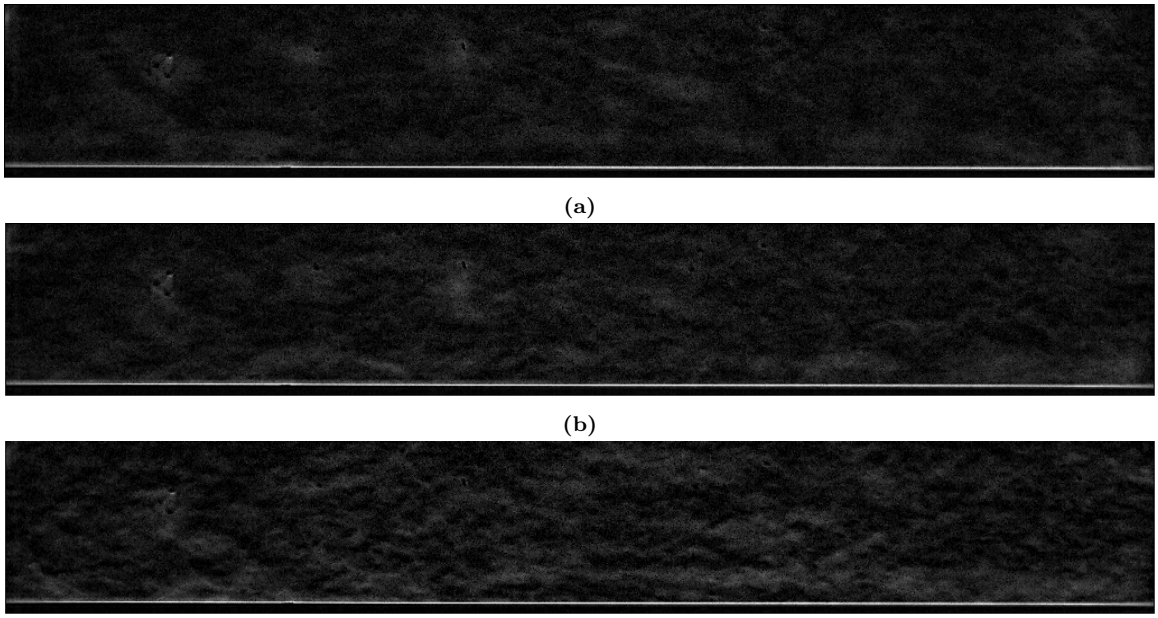


Figure 102. Boundary layer instabilities for the 28 degree sharp ogive tip (a) $P_{DT} = 75psia$ **(b)** $P_{DT} = 100psia$ **(c)** $P_{DT} = 125psia$ **(d)** $P_{DT} = 150psia$

As the tip angle of the sharp ogive is increased to 28 degrees, a clear change in the structure of the observed instabilities occurs. Figure 102 shows the instabilities observed with the 28 degree tip as the driver tube pressure is increased. These

instability waves are clearly elongated and much flatter than the typical curved, "rope-like" structure of the typical second mode wave. These waves still appear to have modal qualities and appear to elongate and flatten more as the driver tube pressure is increased, but their structure is fairly consistent. With this geometry, the amount of intermittent turbulent spotting was observed to be significantly reduced for all driver tube pressure settings. That being said, the behavior of the packets as they break down into turbulence is similar to that of the more "rope-like" packet observed over the 14 degree tip variant.



(a)

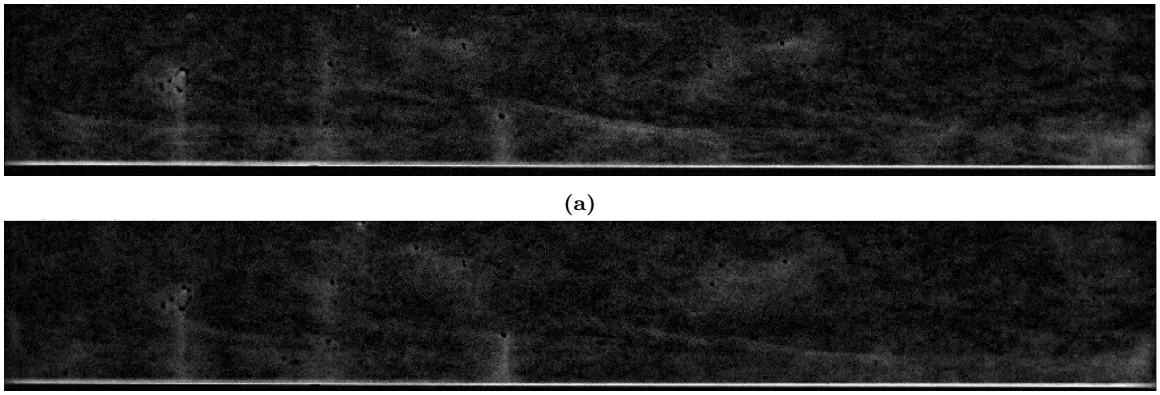
(b)

(c)

Figure 103. Schlieren above the 56 degree sharp ogive tip (a) $P_{DT} = 75psia$ **(b)** $P_{DT} = 150psia$ **(c)** $P_{DT} = 250psia$

For the 56 degree sharp tip ogive, no clear instabilities could be observed over the model, regardless of driver tube pressure used (P_{DT} was varied from 75 to 250psia for the Schlieren images). The only clear difference between the 56 degree sharp ogive and the other two shallower tips is the significant increase in noise across the frame as the driver tube pressure is increased as is shown in Figure 102. This is most likely due to the higher tip angle creating a stronger shock and thus a stronger entropy

layer. This also results in the boundary layer being almost indistinguishable without performing an averaging of many frames.

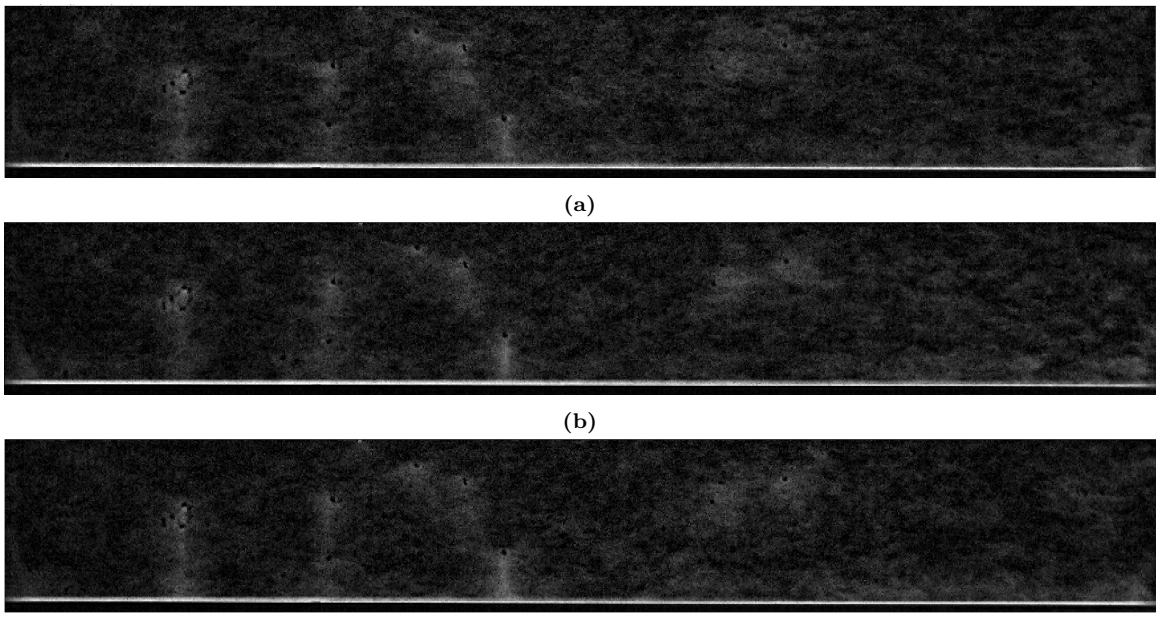


(a)

(b)

Figure 104. Instabilities observed over 1/4R blunted ogives (a) 14 degree ogive with 1/4R bluntness at $P_{DT} = 200psia$ (b) 28 degree ogive with 1/4R bluntness at $P_{DT} = 250psia$

When the sharp tipped 14 and 28 degree half-angle ogives are spherically blunted with 1/4 of the base radius, the instability observed again show a change in structure and behavior. Figure 104 shows an example of a wave structure over both models. It is clear that the structure of the instabilities over these 1/4R blunted models are even more elongated than the instabilities observed over the 28 degree sharp tip. The instabilities appear to be much higher in the boundary layer and extend well into the flow above the boundary layer as they pass. This behavior of the waves to have whisps extending into the freestream are reminiscent of the waves observed by Kennedy et al. over a blunted cone as shown in Figure 20 [15]. It can also be observed that the structure of the instability between the two models are very similar. This suggests that the mechanism driving the instability generation is the same between the two models and is most likely due to the nose bluntness. While the 28 degree sharp tip caused the rope-like structures of the 14 degree tip to elongate within the boundary layer, it is clear that the introduction of bluntness causes the instabilities to extend outward from the boundary layer.



(a)

(b)

(c)

Figure 105. Schlieren over 1/2R blunted ogives and the fully blunted tip (a) 14 degree ogive with 1/2R bluntness at $P_{DT} = 250psia$ (b) 28 degree ogive with 1/2R bluntness at $P_{DT} = 250psia$ (c) fully spherically blunted tip at $P_{DT} = 200psia$

As the tip bluntness is increased for the 14 and 28 degree ogives to 1/2 the base radius, no clear instabilities can be observed in Schlieren. The same holds true for the fully spherically blunted model. Schlieren above all three high bluntness variants are shown in figure 105. Similar to the 56 degree sharp tip ogive, the lack of observable instabilities over these geometries is due to the presence of a strong entropy layer causing a density gradient between the curved shock and the body's surface that makes the Schlieren unable to resolve instabilities.

Traditional frequency analysis shows low frequency instability content within boundary layer over the sharp ogives.

With the confirmation of the presence of second-mode like waves in the Schlieren images, attempts at performing traditional Fourier transform frequency analysis are attempted. Samples are taken from a column of pixels spanning the height of the

frames for 2000 frames at the beginning of the second quasi-steady period of each run. Using a Welch's PSD approximation (Matlab's pwelch command), 2 kHz resolution PSD's were generated for a variety of model geometry variants and run conditions.

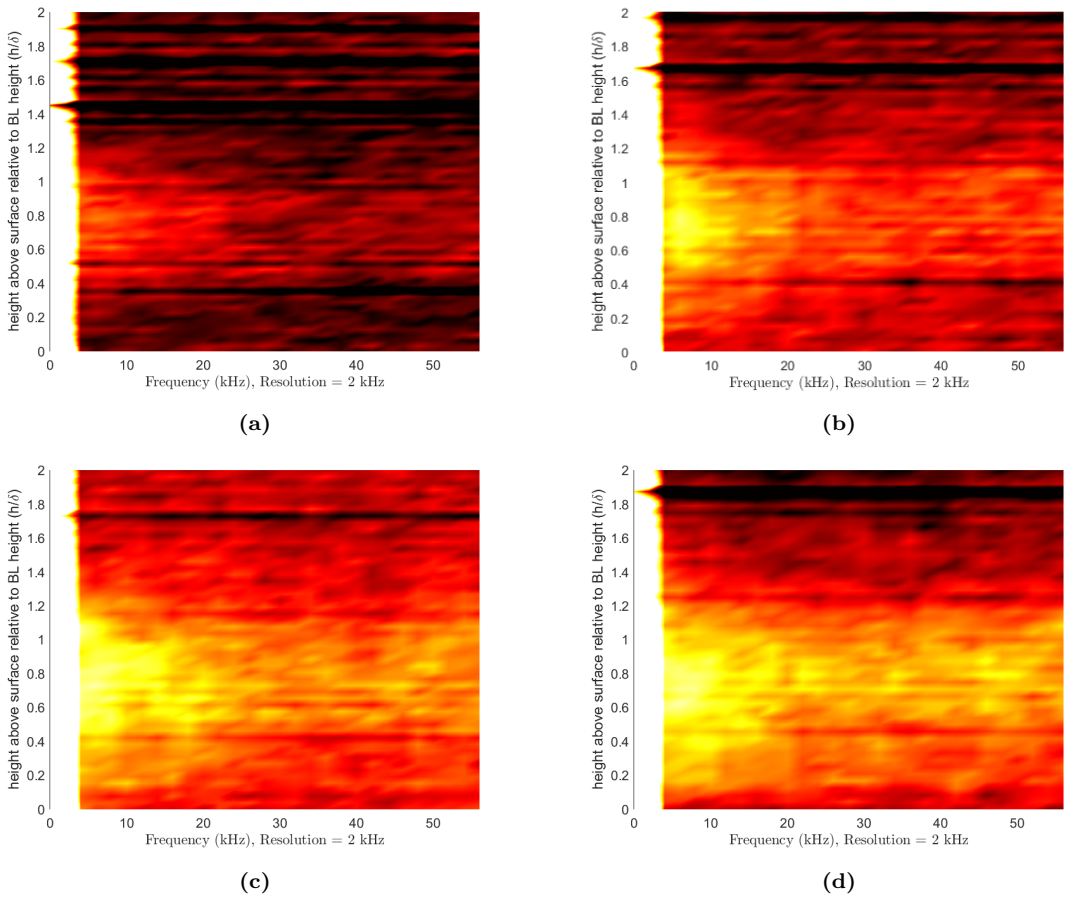


Figure 106. PSD of Schlieren over the 14 degree sharp ogive (a) $P_{DT} = 75psia$ **(b)** $P_{DT} = 100psia$ **(c)** $P_{DT} = 125psia$ **(d)** $P_{DT} = 150psia$

Figure 106 shows the PSD results for the 14 degree sharp ogive variant at increasing driver tube pressures (runs 30, 29, 31, and 32 respectively) . A frequency band centered at ∼6kHz and bounded between 60% and 100% the boundary layer thickness emerges as the driver tube pressure is increased. This low frequency band intensifies and broadens as the driver tube pressure is increased.

Performing the same analysis for the 28 degree sharp ogive shows a similar behavior. Figure 107 shows the PSD results for the 28 degree sharp ogive variant at the

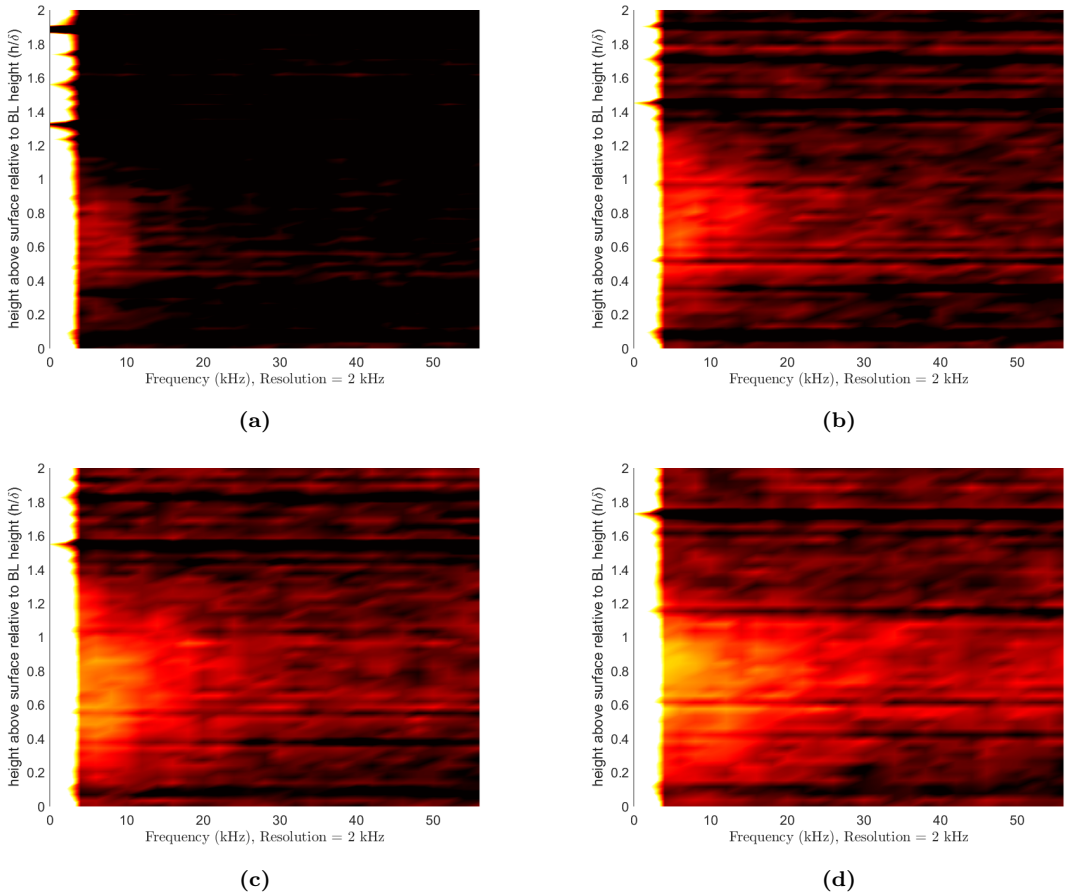


Figure 107. PSD of Schlieren over the 28 degree sharp ogive (a) $P_{DT} = 75psia$ **(b)** $P_{DT} = 100psia$ **(c)** $P_{DT} = 125psia$ **(d)** $P_{DT} = 150psia$

same driver tube pressures as the 14 degree tip variant in Figure 106 (runs 25, 24, 26, and 27 respectively). A similar, low frequency band around ∼6-10kHz emerges as the pressure is increased. This low frequency band appears to have a lower intensity than the 14 degree variant which agrees with the qualitative observations of the Schlieren images where the 28 degree ogive had much less frequent wave packets.

Further increasing the ogive angle to the 56 degree sharp ogive shows a trend similar to that of the first two ogives. Figure 108 shows the PSD results for the 56 degree sharp ogive variant at increasing pressures up past the pressures used for the other two ogives (runs 33, 34, 35, 36, and 37 respectively). It is observed that the low frequency band does not emerge until a higher driver tube pressure is reached. At

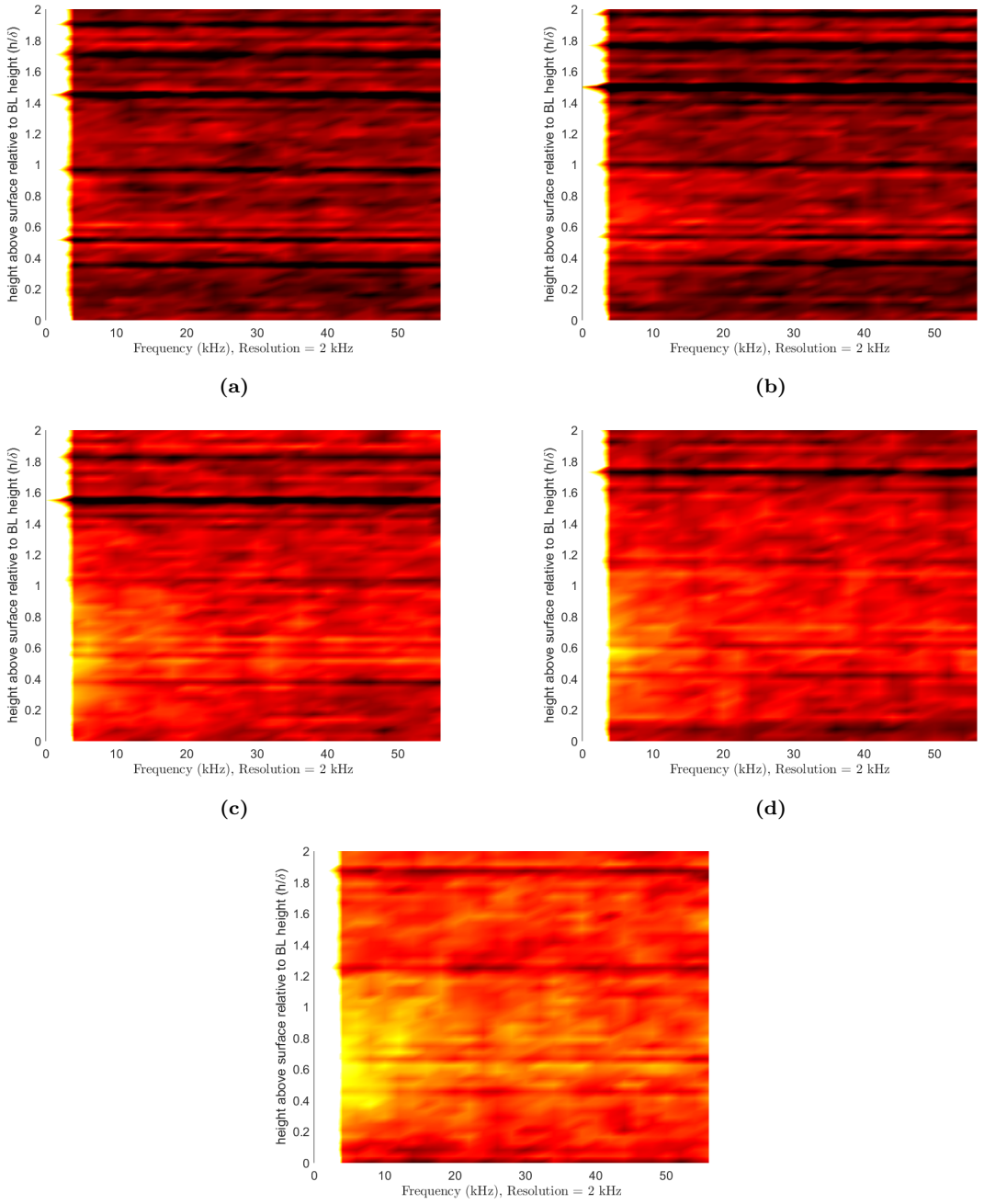


Figure 108. PSD of Schlieren over the 56 degree sharp ogive (a) $P_{DT} = 100psia$ **(b)** $P_{DT} = 125psia$ **(c)** $P_{DT} = 150psia$ **(d)** $P_{DT} = 200psia$ **(e)** $P_{DT} = 250psia$

the highest pressure, the low frequency band appears to broaden across 10kHz and overall frequency content begins to increase in noise.

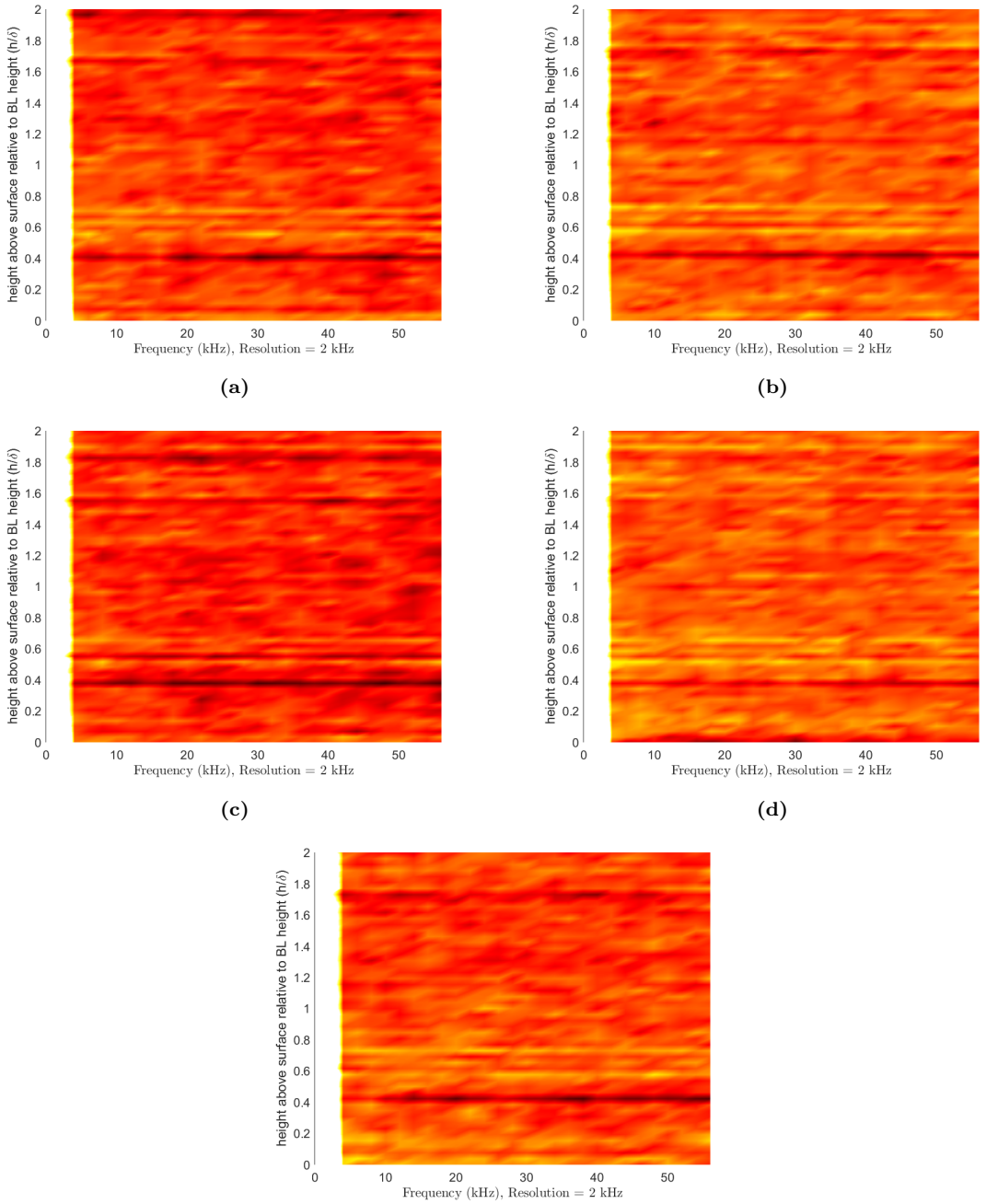


Figure 109. PSD of Schlieren over the blunted ogives (a) 14 degree ogive with 1/4R bluntness at $P_{DT} = 200psia$ (b) 14 degree ogive with 1/2R bluntness at $P_{DT} = 250psia$ (c) 28 degree ogive with 1/4R bluntness at $P_{DT} = 250psia$ (d) 28 degree ogive with 1/2R bluntness at $P_{DT} = 250psia$ (e) fully spherically blunted tip at $P_{DT} = 200psia$

The blunted ogives have entirely different frequency content.

Further utilizing tradtional PSD to make observations over the spherically blunted tips reveals an inherently different spectra than the sharp tip variants. It was observed

that regardless of driver tube pressure, the blunted ogives exhibited no low frequency band detectable via Schlieren visualization like the sharp tip ogives. Figure 109 shows the PSD results for each of the blunted tip configurations at the highest driver tube pressures measurements were taken at (runs 8, 99, 100, and 101 respectively). It is clearly observed that the spectra is entirely broadband with no clear peak in frequencies. This seemingly implies that the blunted ogives have a entirely different instability mechanism occurring or that the density gradients due to any passing instabilities are not strong enough to be resolved via Schlieren imaging.

Spatial to temporal frequency analysis reveals two frequency bands for the sharp tip ogives.

Due to the framerate used to capture the Schlieren images only being 112,000 fps, the highest frequency resolvable via traditional PSD techniques is ∼56kHz, the Nyquist frequency. It is suspected that the frequency band of the observed second mode packets is close to if not above this Nyquist frequency, so a spatial to temporal frequency analysis is needed to estimate the frequencies. The same spatial to temporal frequency analysis that was used to reveal the 300kHz peaks over Oddo's cone for the undersampled framerate is applied to this geometry. It was found during this analysis that this technique is very dependent on the presence of consistent instability structures to be in the frames being analyzed. For Oddo's cone, this was not an issue since consistent, clear second mode waves are nearly always in frame for the run conditions used. For the ogive-cylinders, it was found that instability structures were sparse with randomly spaced intermittency. Fortunately, the algorithm used for this analysis does an excellent job at findings intermittent wave packets and pulling their frequencies out from the frames, so many new observations were still made from the Schlieren images over these geometries.

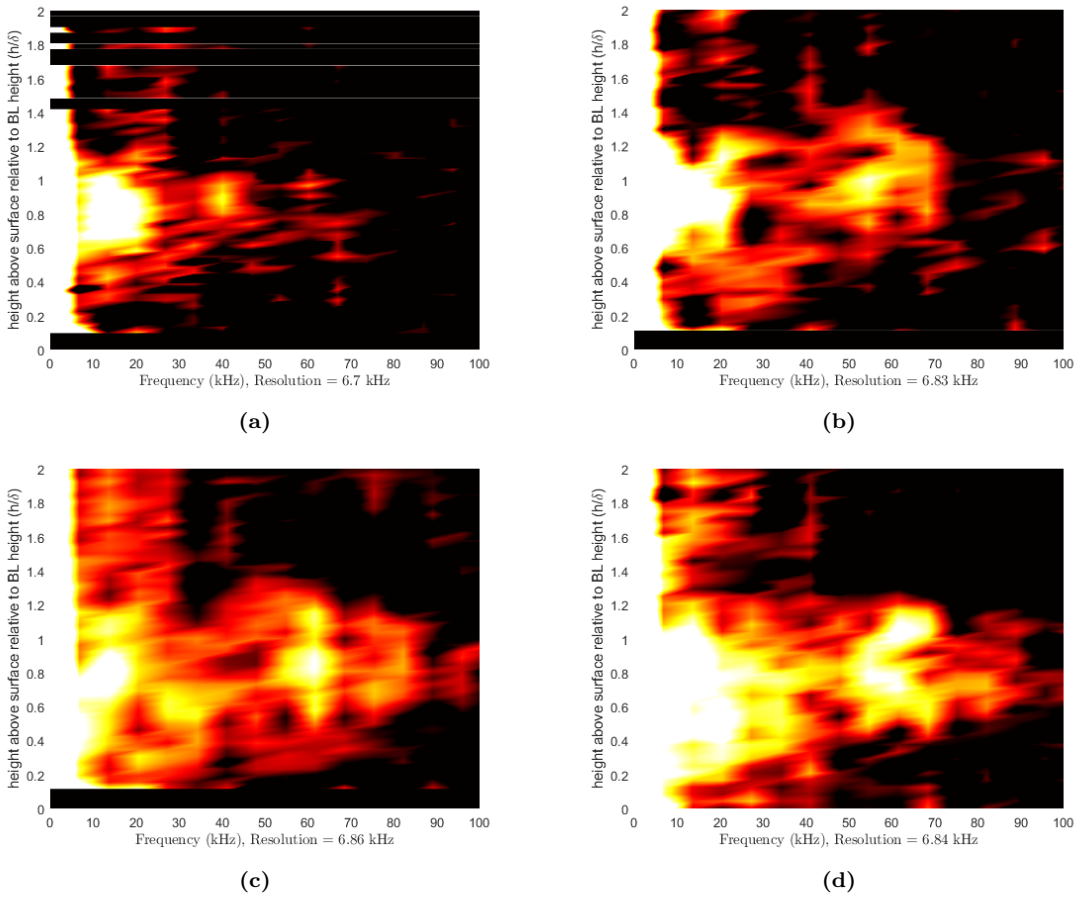
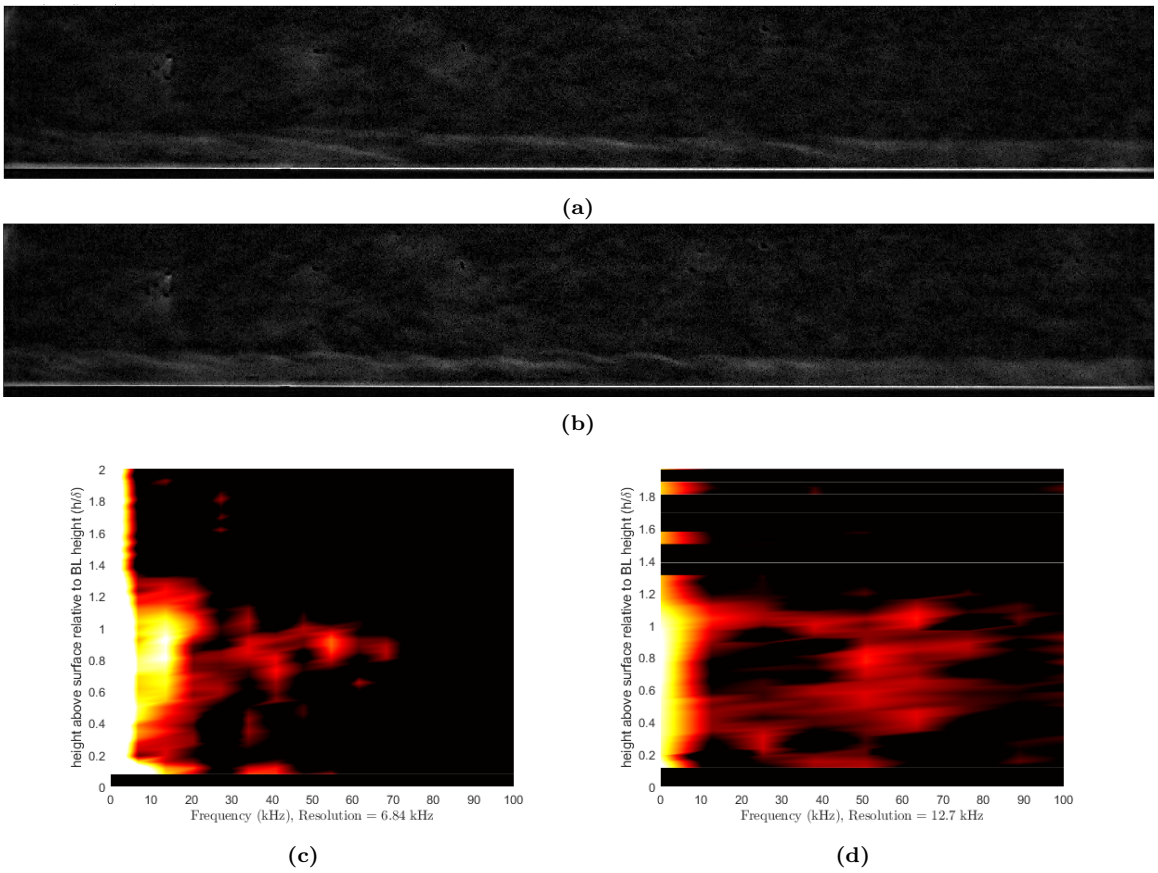


Figure 110. Spatial to temporal PSD of Schlieren over the 14 degree sharp ogive (a) $P_{DT} = 75psia$ **(b)** $P_{DT} = 100psia$ **(c)** $P_{DT} = 125psia$ **(d)** $P_{DT} = 150psia$

Figure 110 shows the spatial to temporal frequency PSD for the 14 degree sharp ogive at several run conditions (runs 30, 29, 31, and 32 respectively). A broad, ∼10kHz band can be observed in all of the run conditions between 60% to 100% the boundary layer thickness and is most likely the same band observed in the traditional FFT PSDs. A second band is observed at ∼40kHz for the lowest pressure. As the preesure is increased, this second band increases in frequency to end at ∼60-70kHz. This second band also appears to extend above the boundary layer edge and appears to be separate from the lower frequency band.

It is determined by this author that the low, 10kHz band and the higher, 50kHz band found in the frequency content above the 14 degree ogive-cylinder are most



(a)

(b)

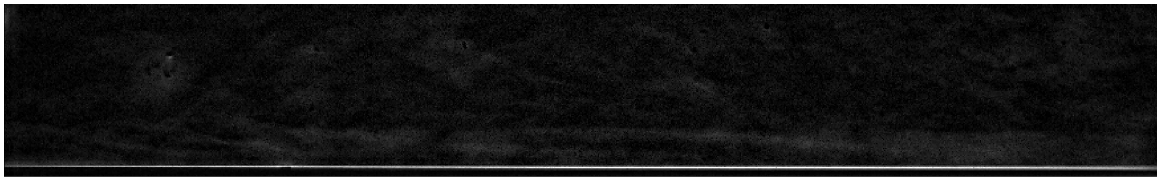
(c)

(d)

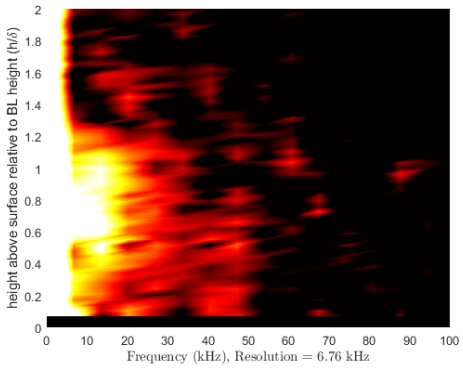
Figure 111. Wave structure observed in Schlieren and the corresponding spatial to temporal PSD for the 14 degree ogive-cylinder at $P_{DT} = 125psia$ (a) low frequency elongated, flat structure (b) high frequency rope-like structure (c) low frequency PSD (d) high frequency PSD

likely caused by two separate structures observed in the Schlieren images. Figure 111 shows an example of the two structure types observed and the corresponding spatial to temporal frequency PSDs associated with those instabilities. The higher frequency, ∼50kHz instability takes on a rope-like structure similar to that of traditional second mode waves. These rope-like waves have a shorter wavelength and thus a higher frequency. The lower, 10kHz band instability structure is elongated and flat. As is shown in Subsection 4.2.1, this flat structure is most prevalent over the 28 degree ogive, but it also appears for the 14 degree ogive as well, causing the low frequency band to appear in the spectra.

To further confirm that the elongated structures observed over the 14 degree



(a)



(b)

Figure 112. Wave structure observed in Schlieren and the corresponding spatial to temporal PSD for the 28 degree ogive-cylinder at $P_{DT} = 100psia$ (a) instability structure (b) instability PSD

ogive variant are the cause of the low frequency band observed, the same analysis is performed for the 28 degree ogive where these structures are more prevalent. Figure 112 shows an example wave from above the 28 degree model at a driver tube pressure of 100psia and the corresponding PSD. A clear band at ∼10kHz is again observed, thus confirming that this structure is most likely the cause of the low frequency spectra.

Performing the spatial to temporal frequency analysis for the 28 degree ogive-cylinder for increasing driver tube pressures shows an ever increasing strength of the low frequency band within the boundary layer as depicted in Figure 113 (runs 24-27). There is no clear emergence of a higher frequency band and the low frequency band is bound to the boundary layer. Despite this immediate obserance of high frequency content, small numbers of frames from the Schlieren images do show higher frequency content.

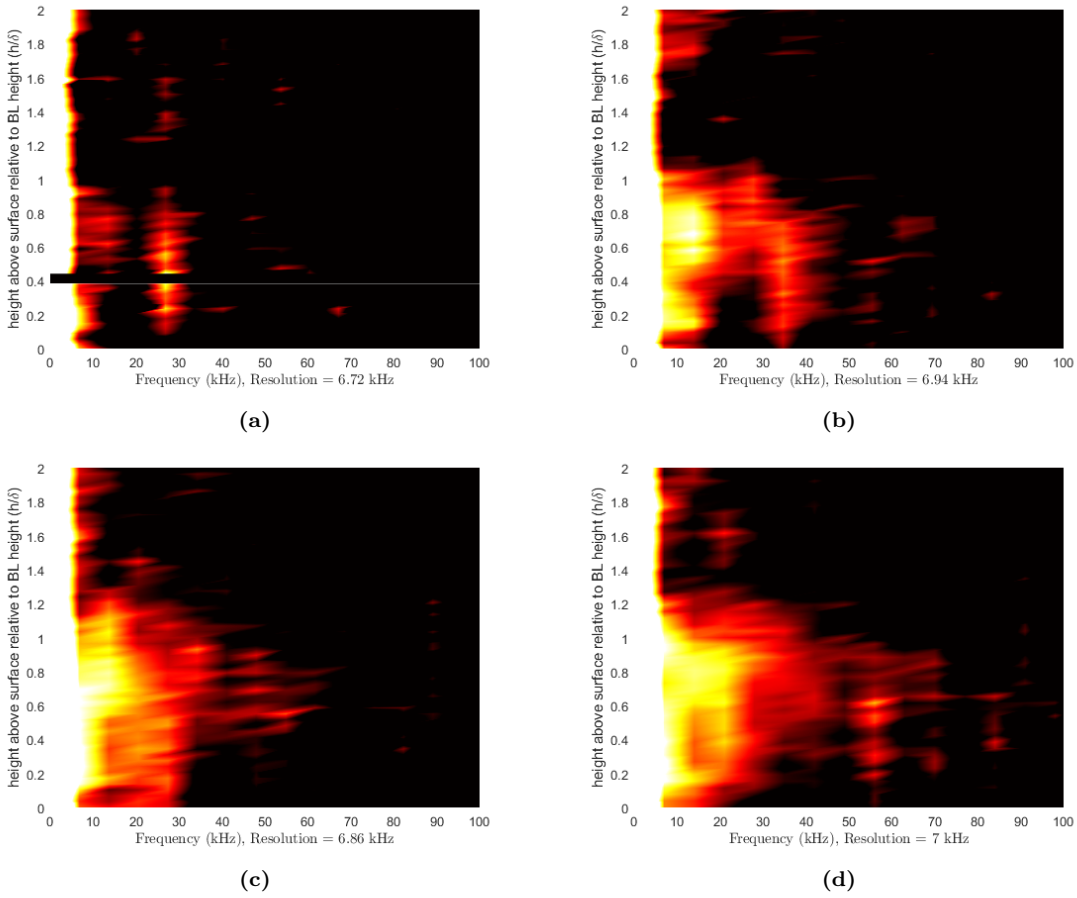


Figure 113. Spatial to temporal PSD of Schlieren over the 28 degree sharp ogive (a) $P_{DT} = 75psia$ **(b)** $P_{DT} = 100psia$ **(c)** $P_{DT} = 125psia$ **(d)** $P_{DT} = 150psia$

At the higher driver tube pressures, the elongated waves of the lower frequency band appear to show signs of non-linear interactions and breakdown. Figure 114 shows a set of frames over the 28 degree sharp ogive as a strong wave cross through the viewing window and breaks down. The power spectra of the window for each frame is shown on the right hand side of the window. The wave first enters into the frame as an elongated, flat wave of an approximate wavelength of 30mm and a propagation velocity of $\sim 438m/s$. Performing a simple estimate of the frequency of this wave via $f = u_e/\lambda$, the approximate frequency of this wave entering the window is $\sim$15kHz which aligns with the PSD of the first frame. As the wave crosses the frame, striations form along the length of the wave and it begins to lift up from the boundary layer.

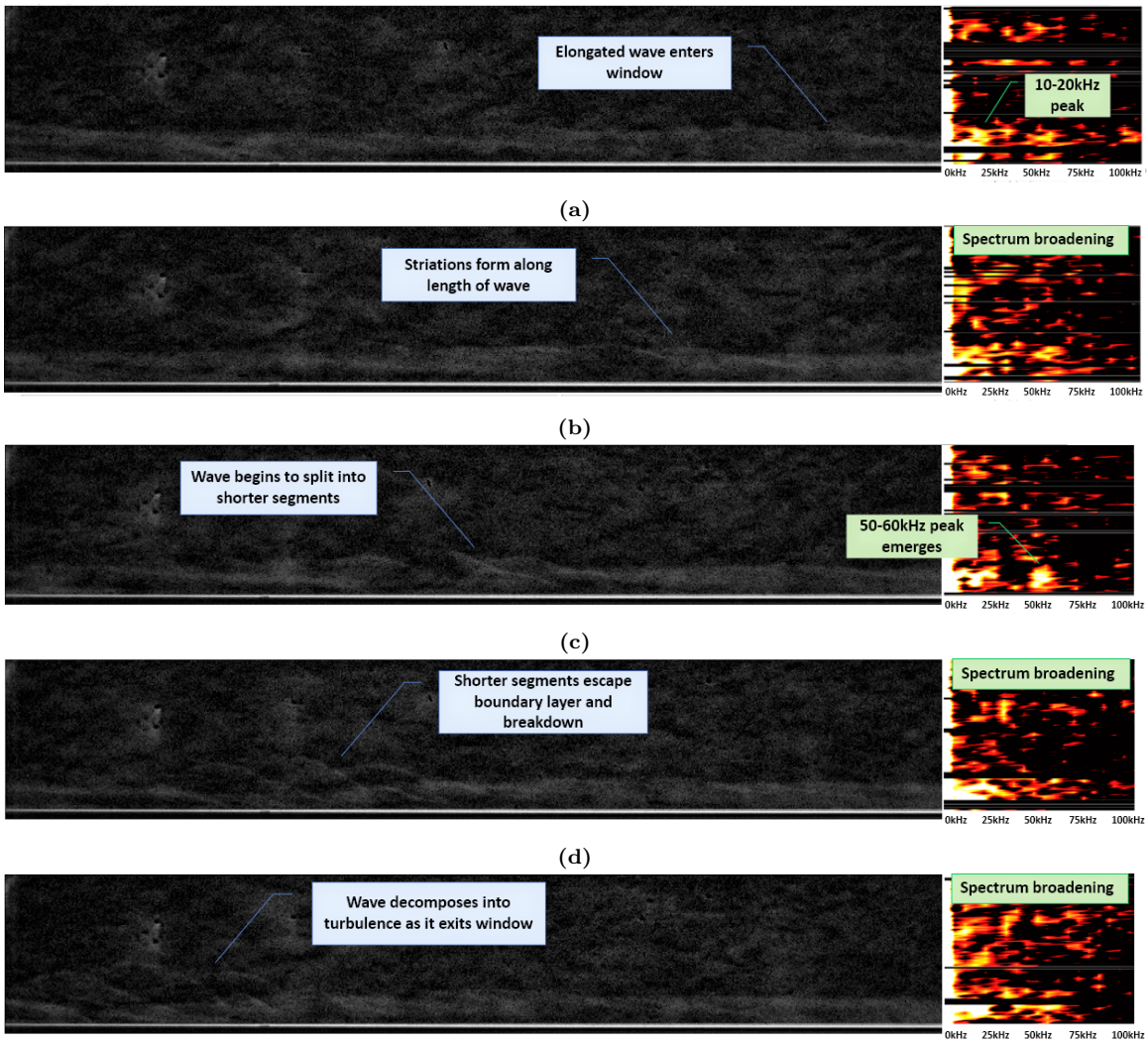


Figure 114. Elongated wave exhibiting nonlinear interaction and breakdown over the 28 degree sharp ogive at $P_{DT} = 100psia$ **(a)** $t = 0\mu s$ **(b)** $t = 17.9\mu s$ **(c)** $t = 35.7\mu s$ **(d)** $t = 53.7\mu s$ **(e)** $t = 71.4\mu s$ **(f)** $t = 89.3\mu s$

The power spectra broadens until the wave reaches a critical point and separates into several smaller wavelets. These wavelets have an approximate wavelength of 7.8mm and a propagation velocity of $\sim 874\ m/s$ for a resulting frequency estimate of ∼56kHz. This emergence of the the higher frequency wave is captured in the PSD at the same frequency as the estimate. As the wave continues to rise out of the boundary layer and breakdown to turbulence, the PSD shows a spectral broadening and a rise in frequency content above the boundary layer. This behavior of the elongated, low

frequency wave breaking down into smaller high frequency waves appears to be a nonlinear behavior. As the different frequency modal instabilities progress through the boundary layer, they nonlinearly interact which can lead to complex interactions such as the breakdown of the disturbances to turbulence like is seen here.

Figure 115 shows the progression of frequency content over the 56 degree ogive-cylinder body as the driver tube pressure is increased (runs 33-37). It is clear that the spectra is almost entirely dominated by the low frequency band. It is also observed that the spectra broadens much more intensely than the other two sharp ogives at the highest pressures.

Spatial to temporal frequency analysis reveals possible entropy layer instability above the boundary layer.

While the spatial to temporal frequency analysis is very capable of revealing the two distinct frequency bands within the boundary layer for the sharp ogive-cylinders, a similar analysis of the flow above the boundary layer reveals new insights. This analysis uses the same spatial to temporal frequency technique as before, except more frames are used to gather information over the entire height of the frame and a normalization is applied to each frequency to scale its PSD by the prevalence of wave packets at that frequency. As a result, this section will present the frequencies present in the flow over each geometry and will scale the PSD return of those frequencies by how often the algorithm observes waves at that frequency.

Beginning with the 14 degree sharp ogive in Figure 116, the normalized frequency content above the model can be observed (runs 29-32). At the lowest driver tube pressure of 75psia there is almost no frequency content above the boundary layer and the 10-20kHz band appears to have the highest prevalence of wave packets. As the pressure is increased to 100 and 125psia, the boundary layer spectra broadens and the

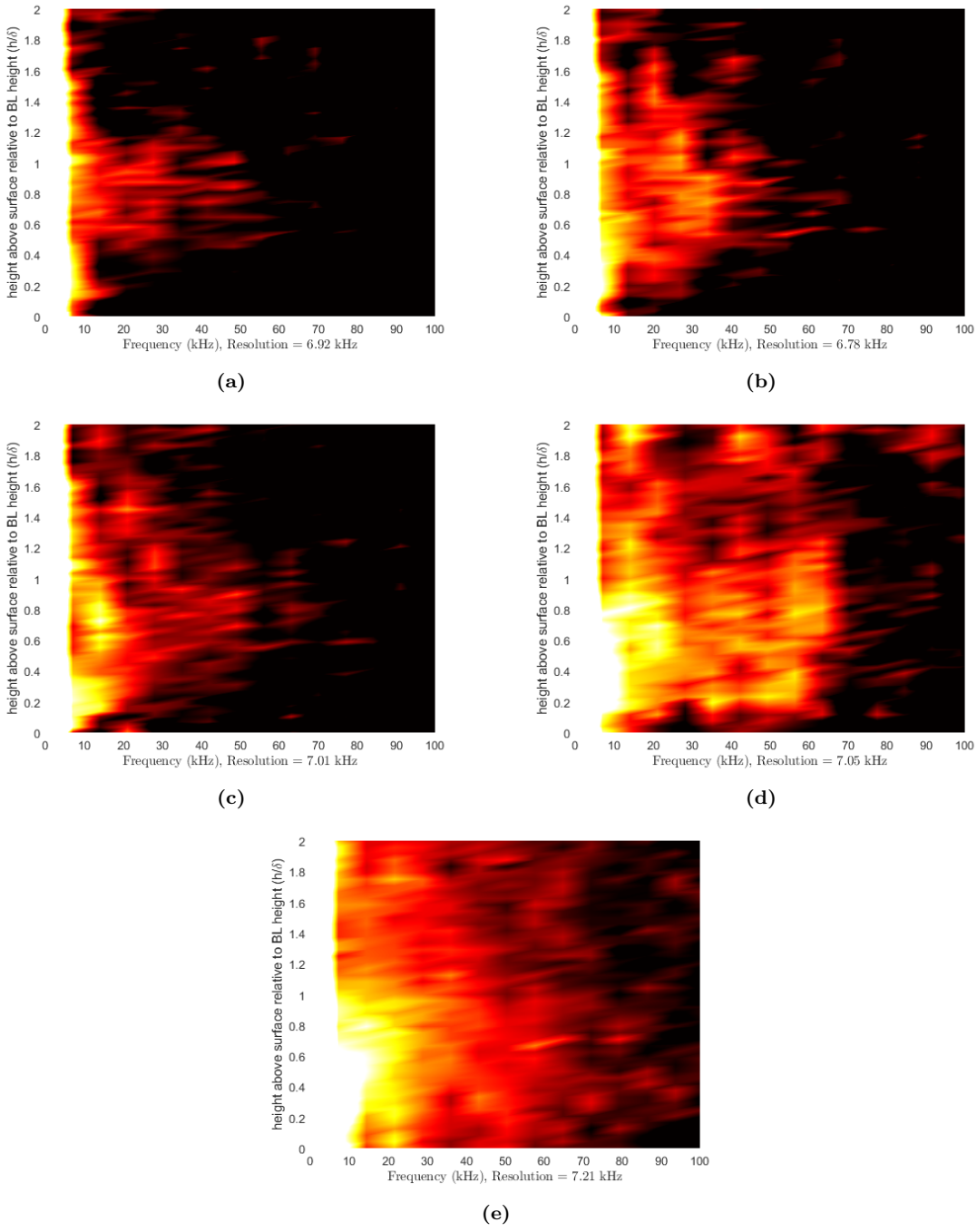


Figure 115. Spatial to temporal PSD of Schlieren over the 56 degree sharp ogive (a) $P_{DT} = 100psia$ **(b)** $P_{DT} = 125psia$ **(c)** $P_{DT} = 150psia$ **(d)** $P_{DT} = 200psia$ **(e)** $P_{DT} = 250psia$

10-20kHz band and the 50-60kHz bands emerge. It appears that the 10-20kHz band has a higher prevalence of wave packets and the broad spectra between the 10-20kHz band and the 60kHz band implies the presence of waves breaking down from the lower

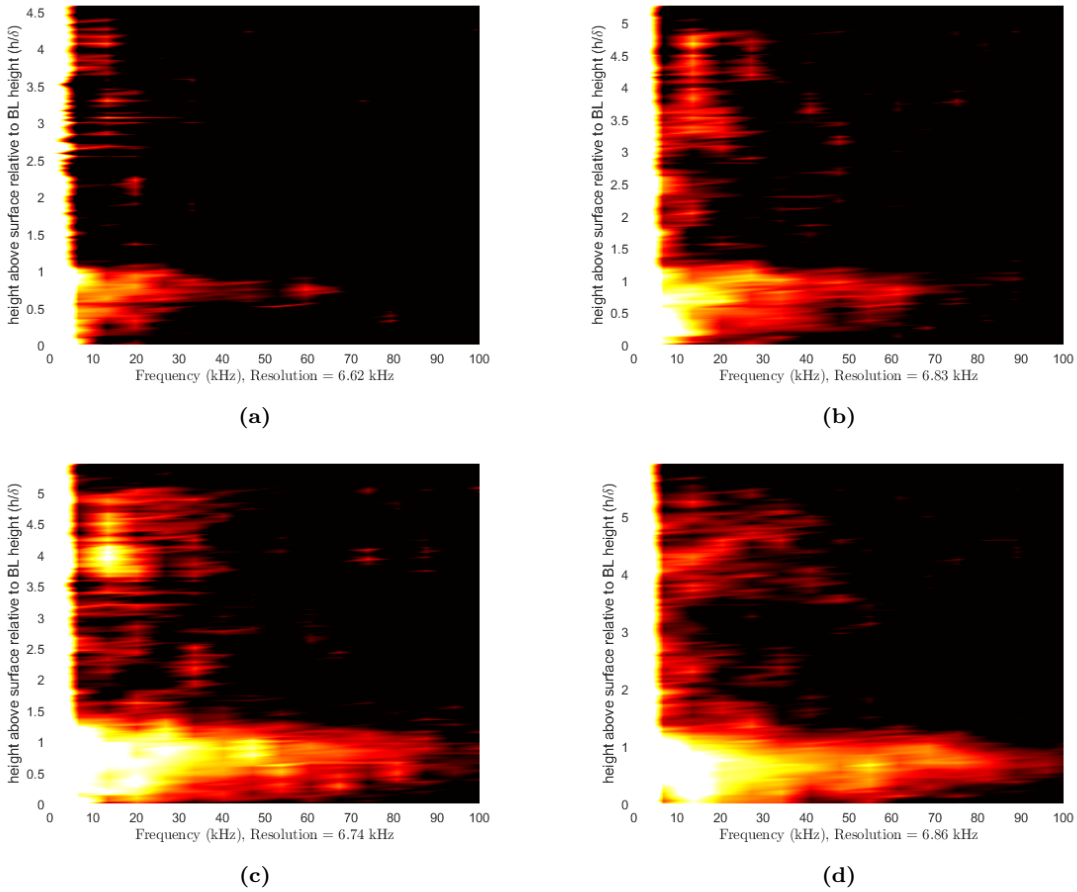


Figure 116. Normalized spatial to temporal PSD of Schlieren over the 14 degree sharp ogive for entire frame height at (a) $P_{DT} = 75psia$ **(b)** $P_{DT} = 100psia$ **(c)** $P_{DT} = 125psia$ **(d)** $P_{DT} = 150psia$

frequency band into the higher frequency band as discusses at Figure 114 where an apparent non-linear breakdown occurs with the 10-20kHz band. It can also be noted that as the pressure is increased, a clear 10-20kHz band emerges between 3-5 times the boundary layer height. This band appears to grow in intensity up to the 125psia driver tube pressure and then broadens for the 150psia case.

Increasing the tip angle to the 28 degree sharp ogive in Figure 116, a new set up observations can be made (runs 24-27). Across each driver tube pressure, it is evident that the frequency content is significantly reduced when compared to the 14 degree sharp ogive. It is clear that the lowest pressure of 75psia has almost no consistent

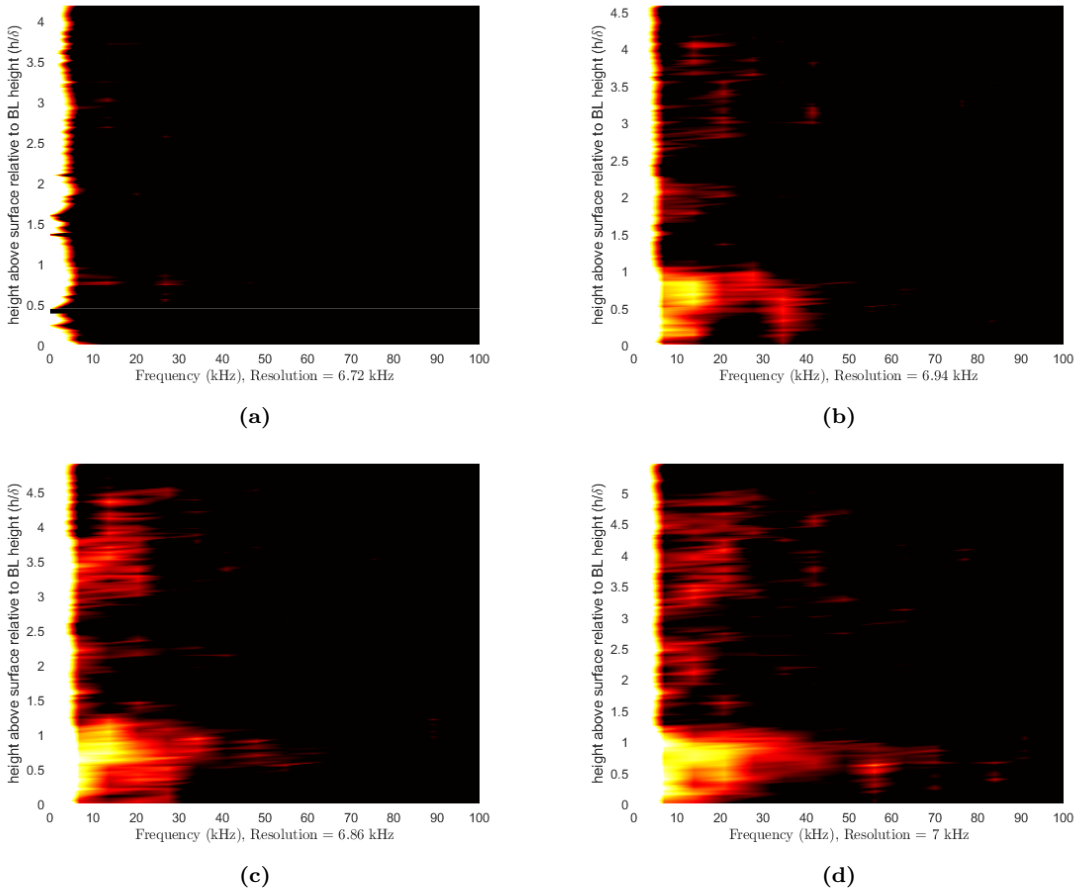


Figure 117. Normalized spatial to temporal PSD of Schlieren over the 28 degree sharp ogive for entire frame height at (a) $P_{DT} = 75psia$ **(b)** $P_{DT} = 100psia$ **(c)** $P_{DT} = 125psia$ **(d)** $P_{DT} = 150psia$

frequency content above the sub-10kHz background noise. With increasing driver tube pressure, the 10-20kHz band clearly resolves itself. Again, a 10-20kHz band at 3-5 times the boundary layer height is observed forming at the higher driver tube pressures, but the intensity of this band appears to be reduced compared to the 14 degree ogive case. The 50-60kHz band does not appear to resolve until the highest driver tube pressure of 150psia.

Further increasing the sharp ogive tip angle to 56 degrees produces the results in Figure 118 (runs 33-37). At this ogive angle, it is observed that the presence of frequency content within the boundary layer is greatly reduced and the presence of

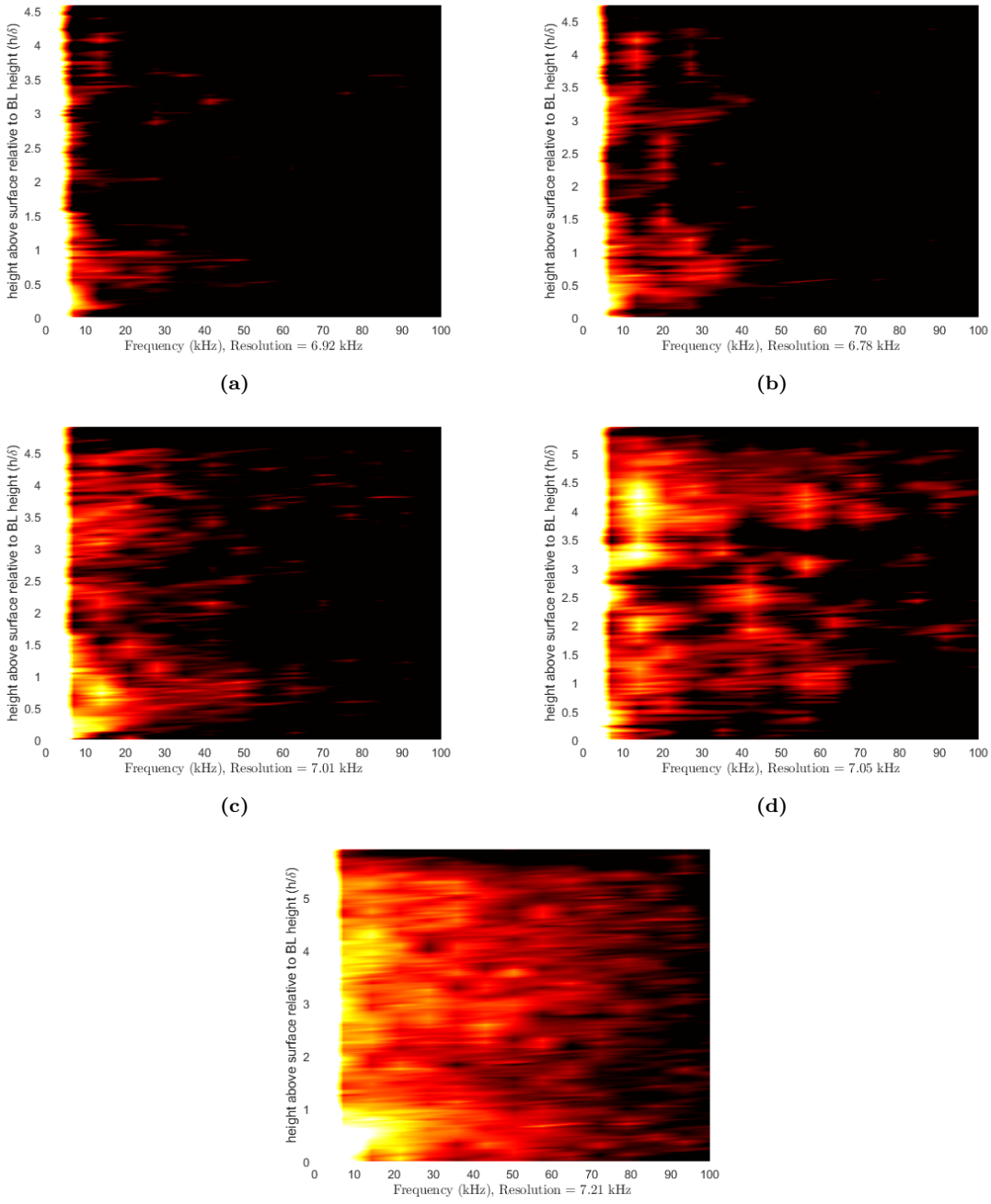


Figure 118. Normalized spatial to temporal PSD of Schlieren over the 56 degree sharp ogive for entire frame height at (a) $P_{DT} = 100psia$ **(b)** $P_{DT} = 125psia$ **(c)** $P_{DT} = 150psia$ **(d)** $P_{DT} = 200psia$ **(e)** $P_{DT} = 250psia$

frequency content above the boundary layer is increased. Again, the emergence of a 10-20kHz band is observed above between 3-5 times the boundary layer height as

the pressure is increased to 200 psia. As the pressure is further increased, the low frequency band extends downward towards the boundary layer and a strong 10kHz band is observed withing the boundary layer. The data suggests that the behavior of the emergence of this band above the sharp ogives and its influence on the boundary layer frequency content of the 56 degree ogive indicates that the observed band is an entropy layer instability that increases in strength and influence on the boundary layer as the driver tube pressure is increased (an increase in unit Reynolds number).

Adding spherical bluntness to the ogive tips further reinforces the hypothesis that the observed 10-20kHz band above the boundary layer is an entropy layer. Figure 119 shows the normalized spatial to temporal frequency content of each blunted ogive run that Schlieren images were captured (runs 98-101). A clear 10-20kHz band is observed over each geometry at approximately 3-5 times the boundary layer height. For the 14 and 28 degree blunted ogives, as the bluntness is increased from 1/4 base radius to 1/2 base radius, the 10-20kHz band extends downward towards the boundary layer and an emergence of the frequency is observed within the boundary layer. The 28 degree ogive with 1/2 base radius bluntness in particular shows a large spectral broadening above the boundary layer implying the possibility of turbulent bursts occurring at the boundary layer edge due to the 10-20kHz band influence.

With the hypothesis that the 10-20kHz band observed between 3-5 times the boundary layer height in the spatial to temporal analysis is an entropy layer instability, a set of Schlieren frames were selected above the 28 degree ogive with 1/2 base radius bluntness where an apparent entropy layer instability is observed. A spatial to temporal frequency analysis is performed for each frame and then averaged across the frames to produce Figure 120. The 28 degree ogive with 1/2R bluntness was chosen due to the frequency content above the boundary layer for this tip being the strongest when compared to the other blunted ogives. An elongated whisp structure with a

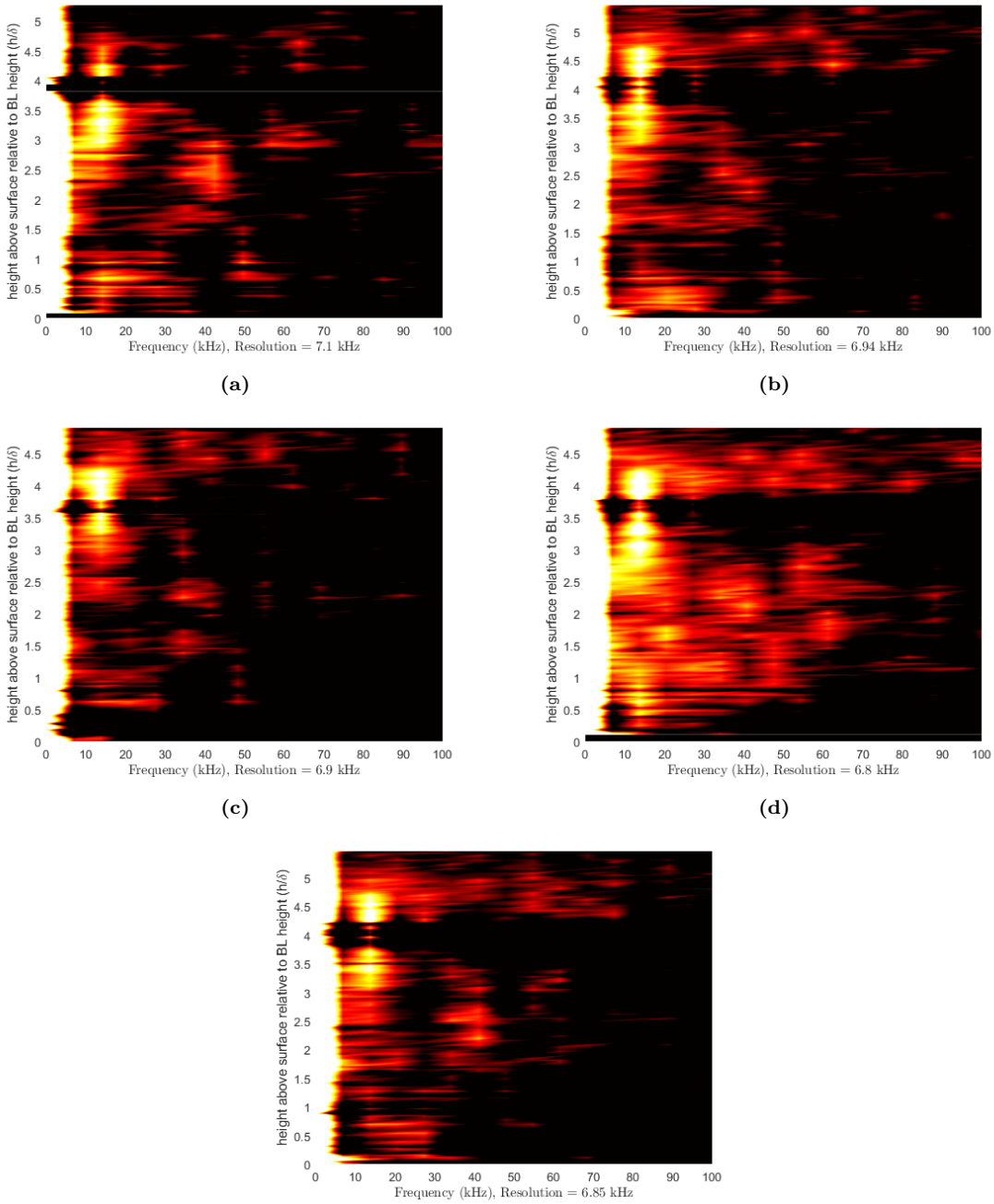
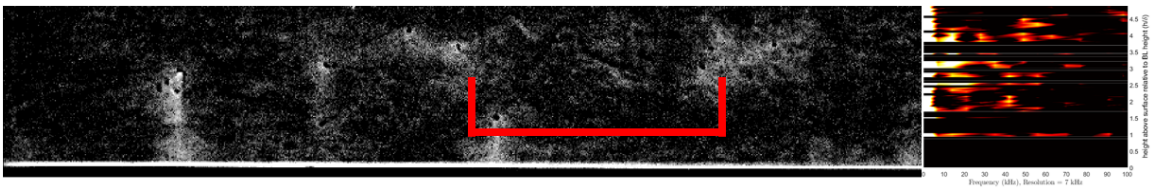
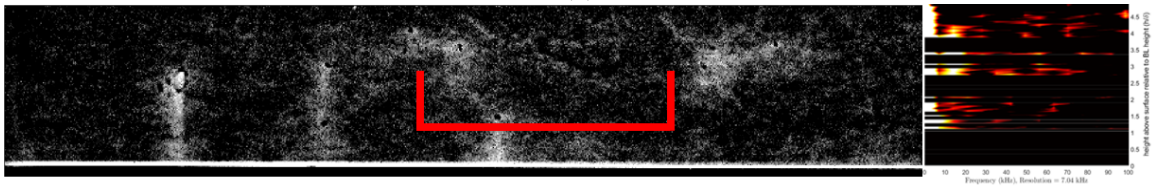


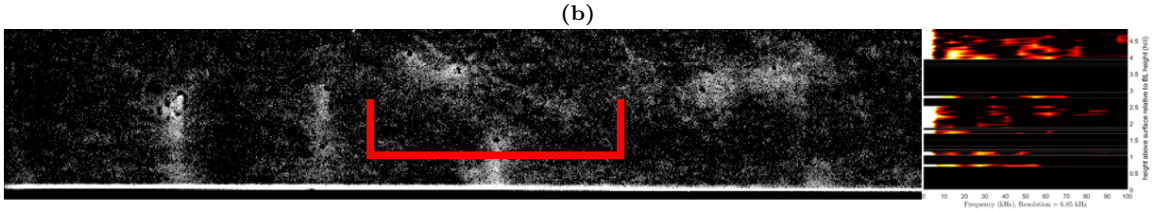
Figure 119. Normalized spatial to temporal PSD of Schlieren over the bluinted ogives for entire frame height (a) 14 degree ogive with 1/4R at $P_{DT} = 200psia$ (b) 14 degree ogive with 1/2R at $P_{DT} = 250psia$ (c) 28 degree ogive with 1/4R at $P_{DT} = 200psia$ (d) 28 degree ogive with 1/2R at $P_{DT} = 250psia$ (e) fully spherically blunted tip at $P_{DT} = 200psia$



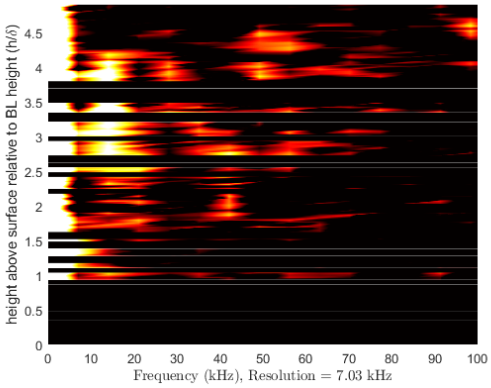
(a)



(b)



(c)



(d)

Figure 120. Schlieren images and spatial to temporal frequency analysis of entropy layer instability above the 28 degree ogive with 1/2R bluntness at $P_{DT} = 250psia$ (a) frame 1 at $t = 0\mu s$ (b) frame 2 at $t = 8.9\mu s$ (c) frame 3 at $t = 17.9\mu s$ (d) spatial to temporal FFT PSD of all shown frames

frequency of 10-20kHz that is similar to the whisp structures observed in Figure 104 is resolved. This author believes that this observed passing instability is separate from the previously discussed whisp structures that were closer to the boundary layer edge. In each blunted ogive's frequency spectra shown in Figure 119, there is a clear separation between the frequency bands bound to the boundary layer and the

frequency band well above the boundary layer. These bands only begin to merge together at the viewing window as the driver tube pressure is increased, implying a more upstream influence of the entropy layer as the driver tube pressure is increased.

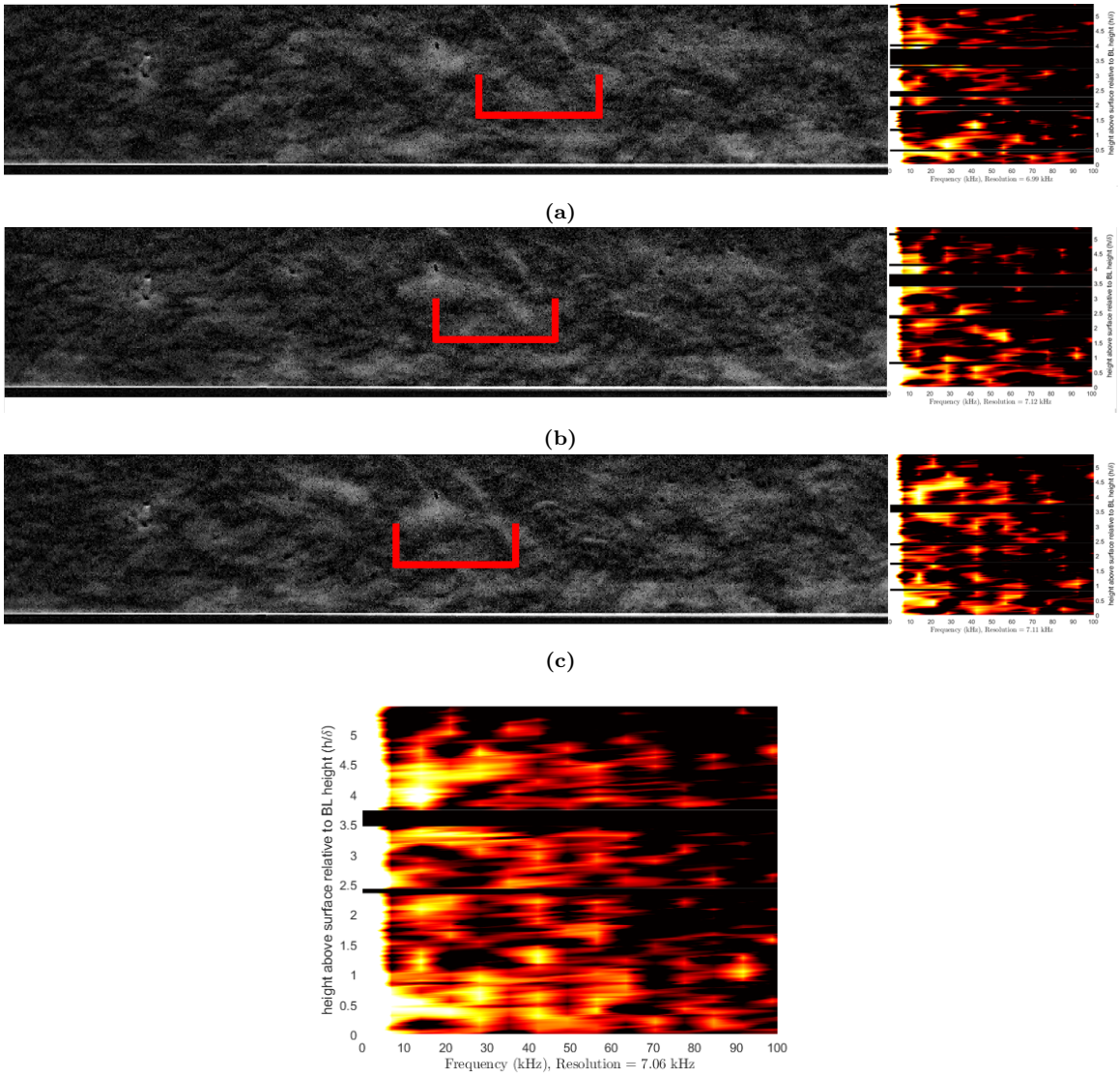


Figure 121. Schlieren images and spatial to temporal frequency analysis of entropy layer instability above the 56 degree sharp ogive at $P_{DT} = 200psia$ (a) frame 1 at $t = 0\mu s$ (b) frame 2 at $t = 8.9\mu s$ (c) frame 3 at $t = 17.9\mu s$ (d) spatial to temporal FFT PSD of all shown frames

To further iterate the point that the hypothesized entropy layer instability is separate from the boundary layer whisp structures, the same process is performed for

the 56 degree sharp ogive in Figure 121. A similar wave structure is observed well above the boundary layer in the Schlieren image what has a 10-20kHz frequency and is completely separate from the frequencies bound to the boundary layer.

4.2.2 FLDI results.

With the Schlieren results providing context for the structure, location, and frequency of the instabilities being produced by the different tip geometries, FLDI was used in an attempt to measure off surface density fluctuation instabilities. It was found during this study that the current FLDI setup is capable of measuring the observed flow instabilities, but some key comments are also provided for future work using FLDI for similar studies. This section will discuss the observations made after processing the FLDI data.

FLDI captures the strong modal instabilities.

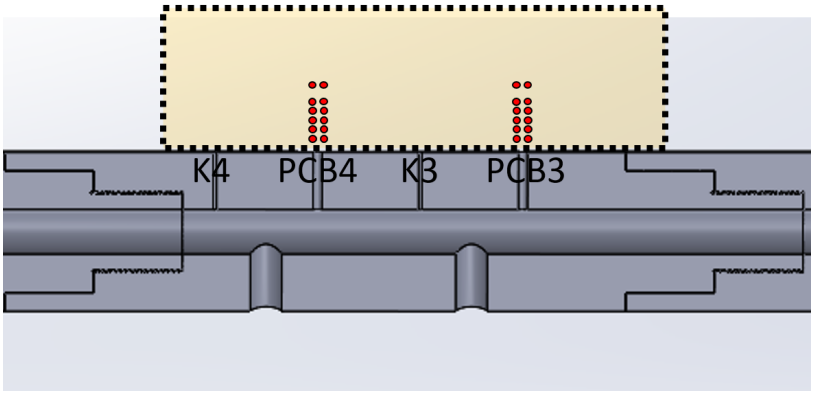


Figure 122. FLDI and Schlieren viewing window diagram for the ogive-cylinder

Measurements using FLDI were taken over the model for each tip variant. As shown in Figure 122, the FLDI focal points were positioned over PCB3 (x=0.543m, 21.4in) for half of the measurements and over PCB4 (x=0.625m, 24.6in) for the other

half of the measurements. The beams were moved upward between runs at ∼2mm increments above model's surface up to 8mm above the surface and then a final measurement was taken at 12mm above the surface to ensure the beams were outside of the boundary layer. This incremental FLDI survey was completed in an attempt to measure instabilities both within and outside the boundary layer.

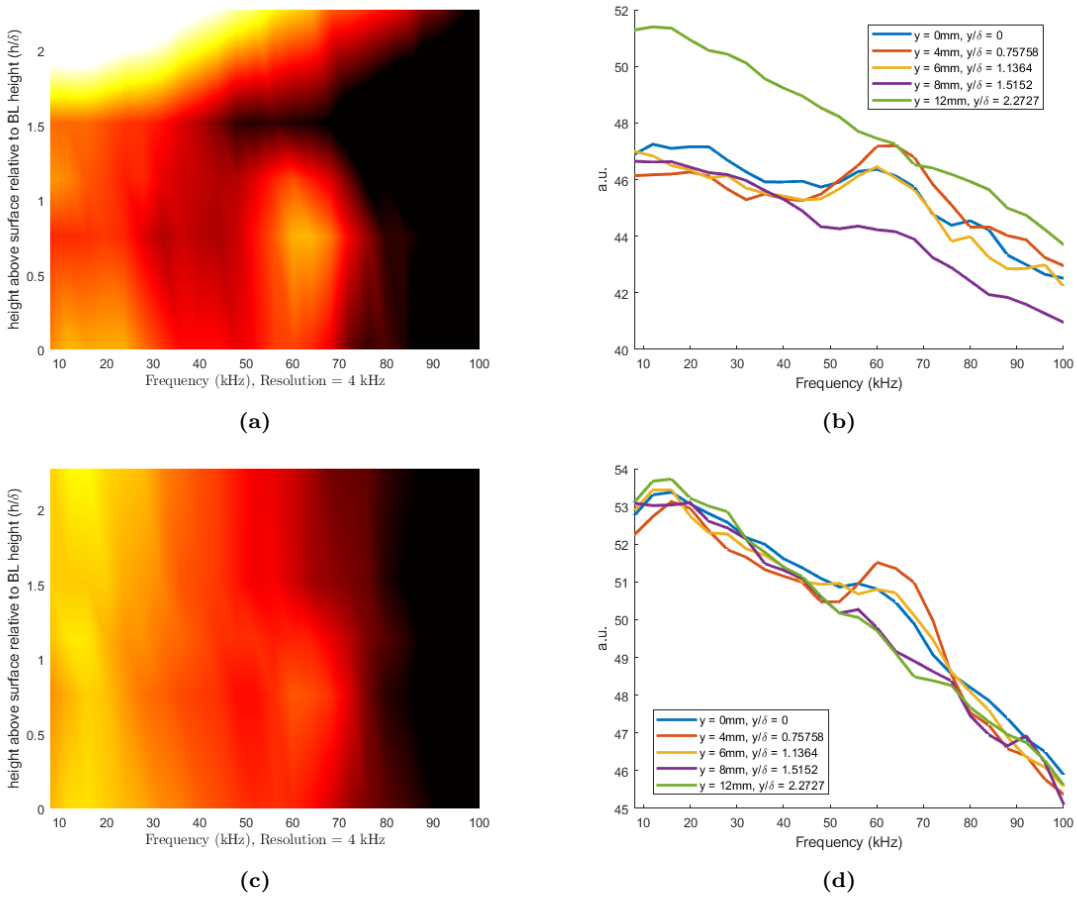


Figure 123. FLDI PSD vs normalized height above the 14 degree ogive model at the PCB3 location and $P_{DT} = 100psia$ (a) and (b) first quasi-steady period peak frequencies vs height (c) and (d) second quasi-steady period peak frequencies vs height

The FLDI used in this study was found to only have sensitivity for the strongest of modal instabilities over the model. This finding coupled with a limited timeline prevented extensive investigation into the intricacies of the FLDI setup for this study. Despite the shortfalls of the technique that were experienced, a few critical observa-

tions were made. A full FLDI sweep was completed above PCB3 for the 14 degree sharp ogive variant at a driver tube pressure of 100psia. Figure 123 shows the power spectra of the FLDI measurements plotted against height above the model for these runs (runs 63, 64, 65, 66, and 67).

It is clear from Figure 123 that the FLDI resolves a strong ∼60kHz band in the first quasi-steady period of the run and then resolves both the ∼10-20kHz and ∼60kHz bands in the second quasi-steady period. The instabilities are bounded between 60% to 100% the boundary layer thickness, matching the findings of the Schlieren analysis. The lack of the ∼15kHz band in the first quasi-steady period is most likely due to a higher noise floor for this half of the run washing out the signal. It is observed that, while the first steady period shows broadband noise above the boundary layer, the second-quasi steady period appears to show the lower frequency band extending up above the boundary layer to twice the boundary layer height. This frequency band was limited to the boundary layer in the Schlieren analysis, so there is a possibility that this is an artifact of the FLDI technique or is unresolved by the spatial to temporal frequency analysis that was performed on the Schlieren images.

Moving downstream for the same geometry and run conditions, another FLDI sweep was completed over PCB4. Figure 124 shows the PSD results for this downstream location during the fist and second quasi-steady period (runs 38, 61, 40, 42, 43, and 44). It should be noted that the runs used to complete this sweep are completely separate than the runs over PCB3, so no cross-correlation analysis can be completed on the signals, but some observations can still be made by comparing the spectra. For the first quasi-steady period, the same ∼60kHz band can be observed and the freestream above the boundary layer still maintains a high broadband noise floor. For the second quasi-steady period, both the ∼15kHz and ∼60kHz are more clearly resolved than at the upstream position. It is also observed that the heights above the

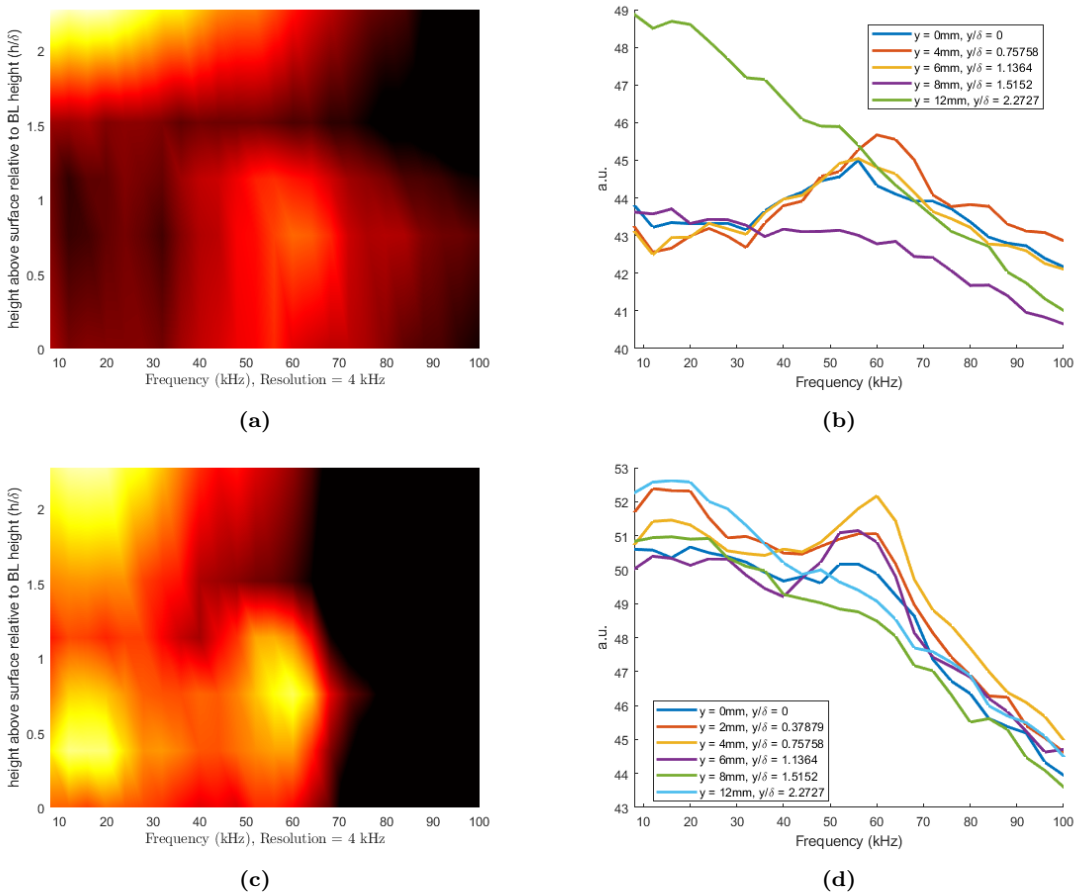


Figure 124. FLDI PSD vs normalized height above the 14 degree ogive model at the PCB4 location and $P_{DT} = 100psia$ (a) and (b) first quasi-steady period peak frequencies vs height (c) and (d) second quasi-steady period peak frequencies vs height

model surface where the max frequency content is located for the two bands is not the same. The location of max 15kHz content is 2mm above the surface ($y/\delta = 0.38$) while the location of max 60kHz content is 4mm above the surface ($y/\delta = 0.76$). This is consistent with the Schlieren observations where the lower frequency band's structure was elongated and flat within the boundary layer while the higher frequency band's structure was rope-like and bound between 60% and 100% the boundary layer thickness. It can be noted that the frequencies of the two bands have little to no shift between the measurements taken above PCB3. This is most likely due to a negligible increase in boundary layer thickness between these two axial locations. Figure 125

shows that the FLDI is capable of resolving a shift in peak frequency when an entirely different driver tube pressure is used. This further confirms that the higher ∼60kHz band is most likely a second mode instability as it exhibits the "tuning" effect of the boundary layer thickness on the instability frequency. Again it can be observed that the 10-20kHz band dissipates at the boundary layer edge, but at approximately twice the boundary layer thickness, the band re-emerges. This is most likely the same 10-20kHz band that is observed above the boundary layer from the spatial to temporal analyis of the Schlieren images.

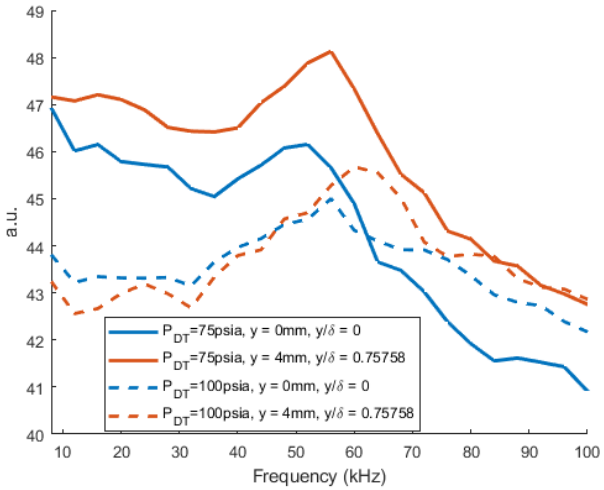


Figure 125. Shift in FLDI PSD peak frequency between $P_{DT} = 75$ and $P_{DT} = 100$ for the 14 degree sharp ogive

FLDI measurements were also successful in capturing instabilities over the 28 degree sharp ogive-cylinder. Vertical surveys above PCB3 and PCB4 were completed at a driver tube pressure of 125psia. Figure 126 shows that the forward most survey location above PCB3 has no clear 60kHz frequency peak. There is a slight peak at 10-15kHz, but it is unclear if the peak is truly a measured instability or simply low frequency noise. If the 10-20kHz band is in fact a resolved frequency band and not noise, it can be noted that the frequency extends to twice the boundary layer height

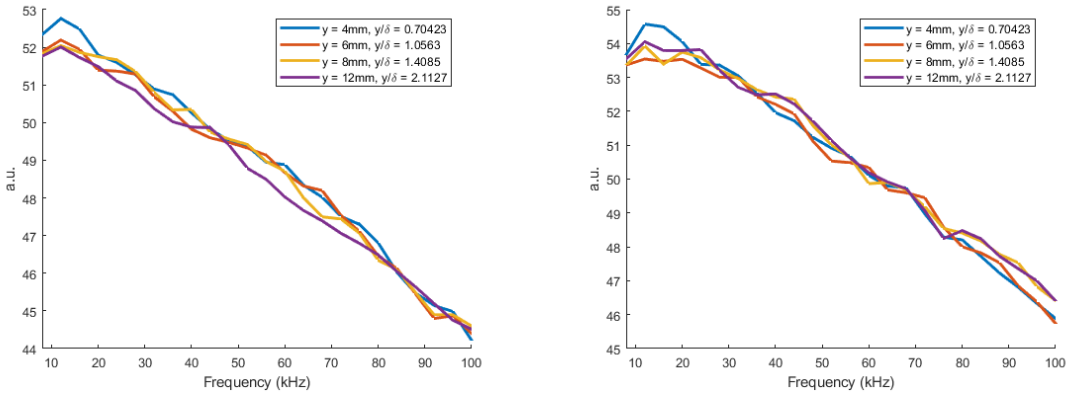


Figure 126. FLDI PSD vs normalized height above the 28 degree ogive model at the PCB3 location and $P_{DT} = 125psia$ (a) first quasi-steady period peak frequencies vs height (b) second quasi-steady period peak frequencies vs height

during both periods.

While the measurements above PCB3 on the 28 degree sharp ogive show no clear sign of a prominent instability, the FLDI results downstream over PCB4 show the clear emergence of both the lower and higher frequency band. Figure 127 shows the FLDI PSD results for both quasi-steady period over PCB4 on the 28 degree ogive at a driver tube pressure of 125psia. While the second quasi-steady period appears to only show a peak at the 15kHz band, the first quasi-steady period shows peaks at both the 15kHz band and the 60kHz band. Both bands appear to be strongest at the boundary layer height, but unfortunately no measurements above the boundary layer were completed using FLDI for this configuration. It should be noted however that the FLDI measurement closest to the surface appears to show a peak at $\sim$ 50kHz while the measurements at 70% and 100% the boundary layer thickness see a $\sim$58kHz response. It can also be noted that the low frequency band for the first period is strongest at the highest measurement point (the boundary layer edge) where it is broader, spanning 10-30kHz, than in the other measurements. For the second period, only the 10-20kHz band is resolved.

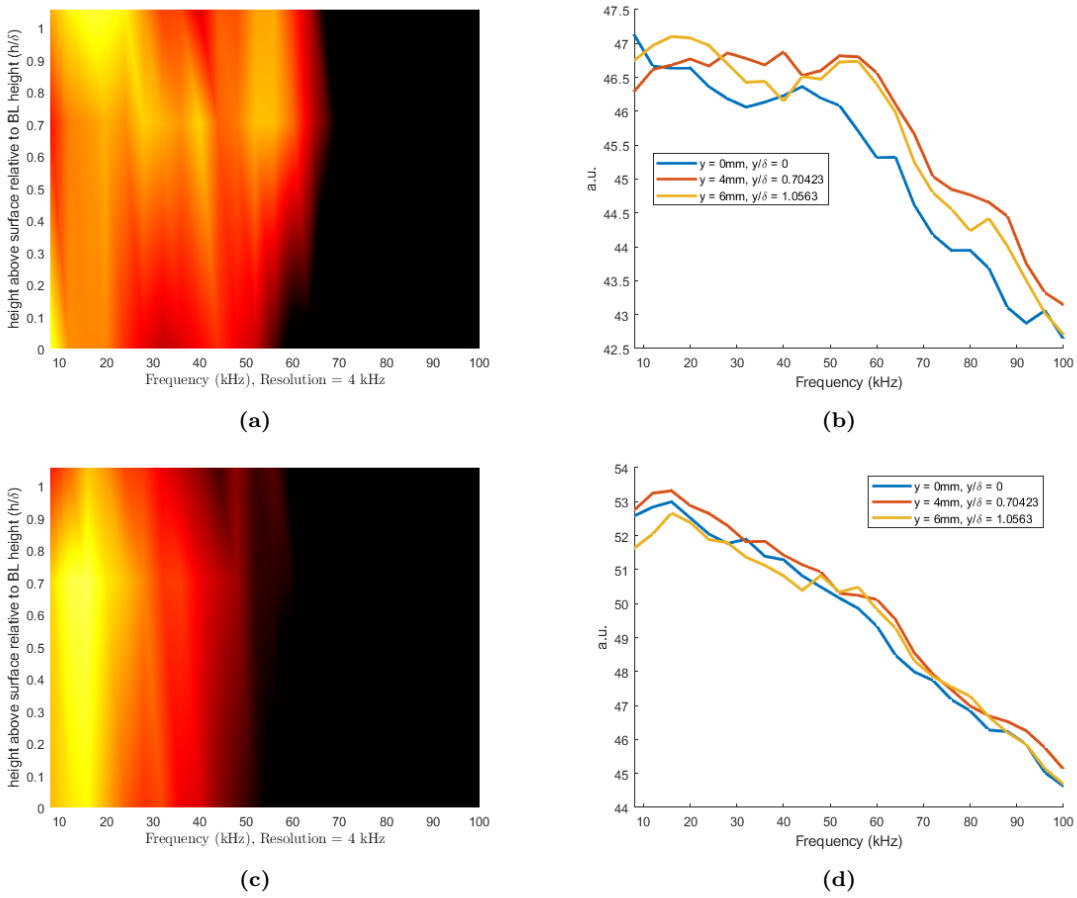


Figure 127. FLDI PSD vs normalized height above the 28 degree ogive model at the PCB4 location and $P_{DT} = 125psia$ (a) and (b) first quasi-steady period peak frequencies vs height (c) and (d) second quasi-steady period peak frequencies vs height

FLDI spacing and orientation affected ability to measure instabilities.

Measurements using FLDI were also completed for the 56 degree sharp ogive and all of the blunt tip configurations with little success in resolving dominant frequency bands. Figure 128 shows the PSD results for each of these tips at a driver tube pressure of 125psia and 200psia. These high angle and blunted tips all exhibit very similar broadband frequency behavior in the FLDI results for all of the run conditions measured. At first glance, this result appears to suggest that FLDI shows little to no

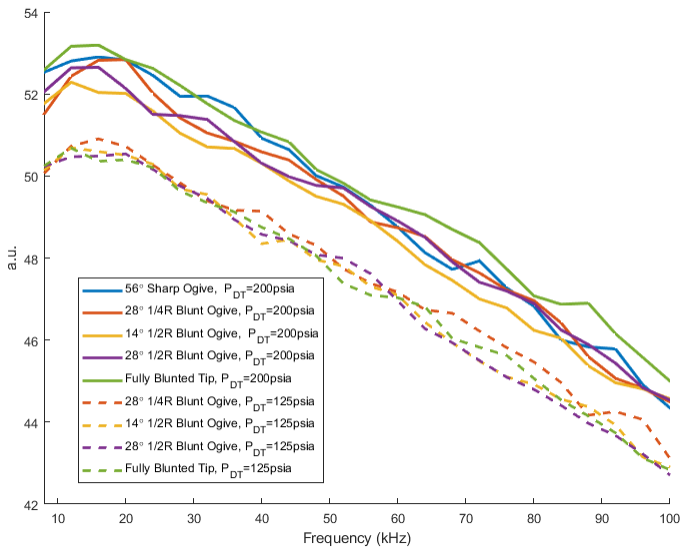


Figure 128. FLDI PSD at 4mm above PCB3 for the 56 degree sharp ogive, 14 degree and 28 degree ogives with 1/4R and 1/2R bluntness, and the fully blunted tip at $P_{DT} = 125psia$ and $P_{DT} = 200psia$

frequency content above the body for these tips, but upon further inspection, some key insights into the nature of FLDI and suggestions for future work can be made.

While it is very possible that the FLDI measurements made in this study did not sample high enough above the surface for each configuration, there appears to be a scaling and orientation issue between the FLDI focal points and the wavelengths of the measured instabilities. FLDI is inherently dependent on a phase shift between the two beams of the setup due to a difference in density between the two focal points. The focal points in this setup have a separation distance of approximately 0.13mm across which the setup is sensitive to changes in density. For second mode waves, the wavelength of the wave packets is approximately two times the boundary layer thickness [44]. The Schlieren results for this study indicate that the elongated, flat waves observed propagating over the ogive-cylinders are at least three to five times the the thickness of the boundary layer. In order for the FLDI setup to measure the presence of a passing instability wave, the wave needs to cause a density shift for one

beam while leaving the other one relatively untouched so that the two FLDI beams interfere further along the beam path. In the case of second mode packets which have a distinctive "s" shape to the individual waves in the "rope-like" structure, FLDI has the best sensitivity if the focal points are positioned at the height of and oriented normal to the inflection point in the curvature of the wave. This location along the length of the wave has the strongest density gradient across the flow direction and thus is where FLDI has the strongest returns.

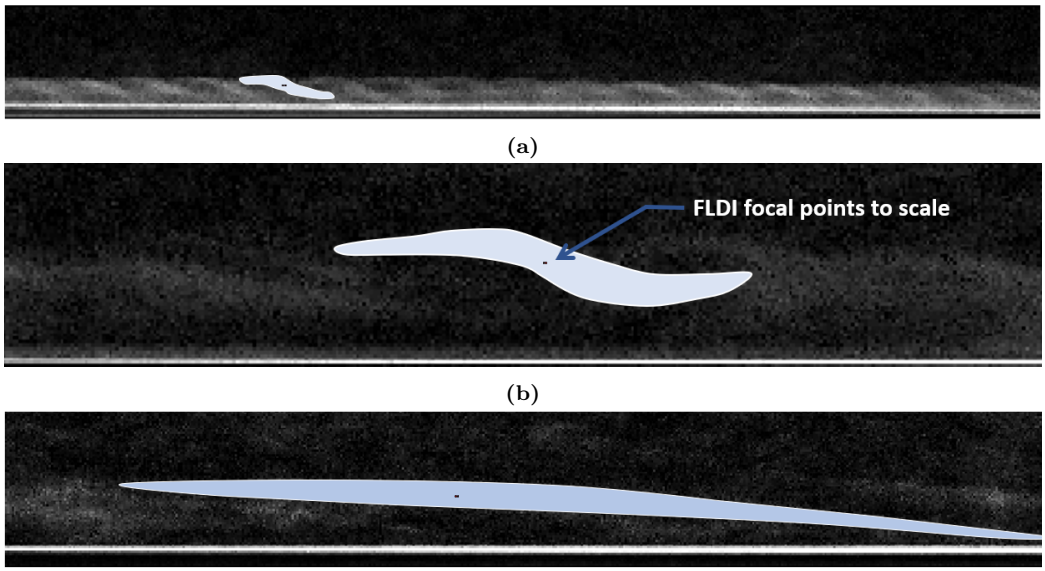


Figure 129. Comparison of instability waves in the boundary layer relative to the FLDI focal points (a) Oddo's cone second mode instability (b) 14 degree sharp ogive second mode instability (c) 28 degree sharp ogive low frequency instability

The elongated waves of the instabilities passing over the blunter ogive-cylinders may be too large for the spacing of the FLDI focal points and thus cause a reduction in sensitivity to the passing disturbances. The "flat" nature of the elongated waves may also affect the ability of the horizontally oriented focal points to effectively measure the passing disturbances. Figure 129 provides an example of the relative sizes and shapes of the waves observed over the cone, the 14 degree sharp ogive, and the 28 degree sharp ogive with respect to the FLDI focal points. It is clear from this figure that the FLDI

focal point spacing for the current setup is relatively narrow in comparison to ogive-cylinder disturbance wavelengths. As is shown in Table 8 for the cone, the wavelengths of the second mode waves over the cone geometry are 2-3mm (approximately two times the boundary layer thickness the boundary layer). While the overall wavelength of the wave packet is much larger than the focal point separation distance of 0.13mm, at the inflection point of the second mode wave packets, the width of the density gradient is approximately 0.5mm. This means the focal point separation distance is at the same order of magnitude of the width of the wave inflection point of the passing instabilities. The ogive-cylinder's second mode waves are approximately 12-15mm in wavelength with an inflection point density gradient width of approximately 2-4mm. This significant increase in the width of the density gradient region places it at least an order of magnitude larger than the separation distance of the FLDI focal points. For the lower frequency waves with wavelengths around 30-40mm and that are much flatter and have little to no inflection point, the disparity between the FLDI focal point separation distance and the density gradient width are only further exacerbated.

For the ogive-cylinder cases, the increase in the density gradient thickness reveals itself as a "washing-out" effect of the FLDI signal. This effect is exemplified in Figure 130 where the FLDI traces for the cone, the 14 degree sharp ogive, and the 28 degree sharp ogive are shown. Note that each of these plots show a passing instability at the same time scale. It is clear that the ogive-cylinder disturbances are being washed out by the width of the passing instabilities, resulting in a noisy response by the FLDI system. As the tip angle is increased and the low frequency waves emerge more consistently with their elongated, flat structure, the FLDI beam focal point separation distance becomes too small to resolve any significant changes in beam interference due to phase shifts at the focal point. Also, the "flatness" of these elongated waves

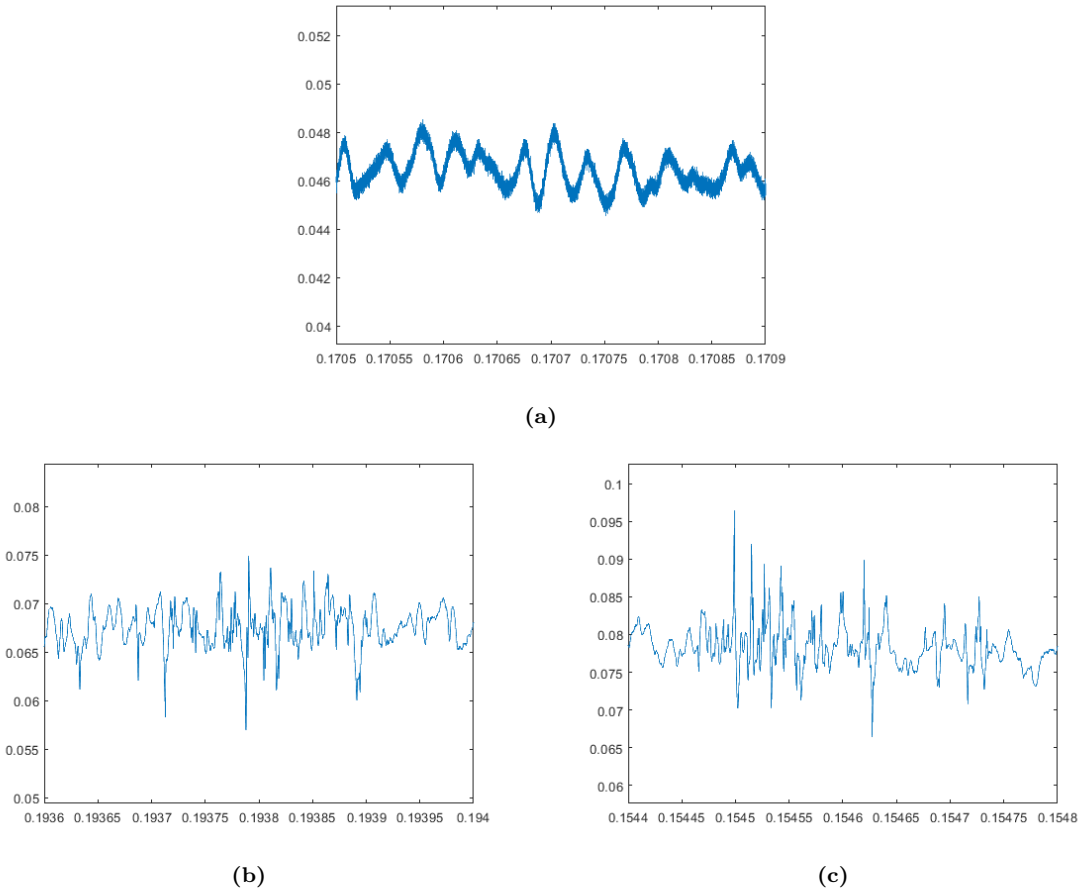


Figure 130. Examples of FLDI traces (y-axis) vs time (x-axis) (a) Oddo's cone (b) 14 degree sharp ogive (c) 28 degree sharp ogive

cause the horizontally oriented focal points to no longer be normal to the oncoming wave front of the passing disturbances, further decreasing the sensitivity of the setup. Continuing to increase the tip angle or adding spherical bluntness to the ogive tip only further accentuates these issues.

4.2.3 Surface pressure sensor results.

The final diagnostic used to capture frequency content in this study is an array of alternating Kulite and PCB surface mounted pressure sensors along the length of the cylindrical body of the ogive-cylinder configurations. It was found during this study that the surface mounted sensors provided consistent measurements and

exposed more behaviors of the measured instabilities. This section will explore the results of the surface mounted pressure sensor measurements. It should be noted that the PCB sensors used in this study have an inherent 11kHz highpass filter that creates an artificial spike at this frequency in the power spectras displayed. Also, the Kulite data and the PCB data experienced a great deal of electrical noise as is noted in Section 3.4.1. Because of this electrical noise, there is a broad spike in the PCB data around 150kHz for many of the runs and the Kulite data was rendered unusable above 100kHz. Despite these complications, both sensors provided valuable insights.

The 15kHz and 60kHz bands are measured by the pressure sensors for the sharp ogives.

As discussed in Section 3.4.1, the Kulite sensors used in this study were unfortunately plagued with a high noise floor due to faulty wiring during this study. This high noise floor resulted in no usable frequency data above ∼100kHz being resolved from the PSD's completed for the Kulites, but fortunately the low frequency content of the sensors was preserved. Since the PCB's are unable to resolve frequencies below ∼11kHz due to their filtering, the Kulites are more useful for measuring low frequency content and are the primary source of the low frequency analysis for this portion of the study. From the measurements of the Kulite sensors, the same 15kKz and 60kHz bands that were measured in the Schlieren images and FLDI measurements over the 14 and 28 degree sharp ogives are resolved.

Figure 131 shows Kulite frequency content above the 14 degree sharp ogive at a variety of run conditions. Each PSD shows the Kulites down the length of the model for a given run condition. The same ∼15kHz and ∼60kHz bands are clearly seen in the PSD results for each of the run conditions at every sensor. This shows that the both instability bands measured in the Schlieren and FLDI reach to the surface

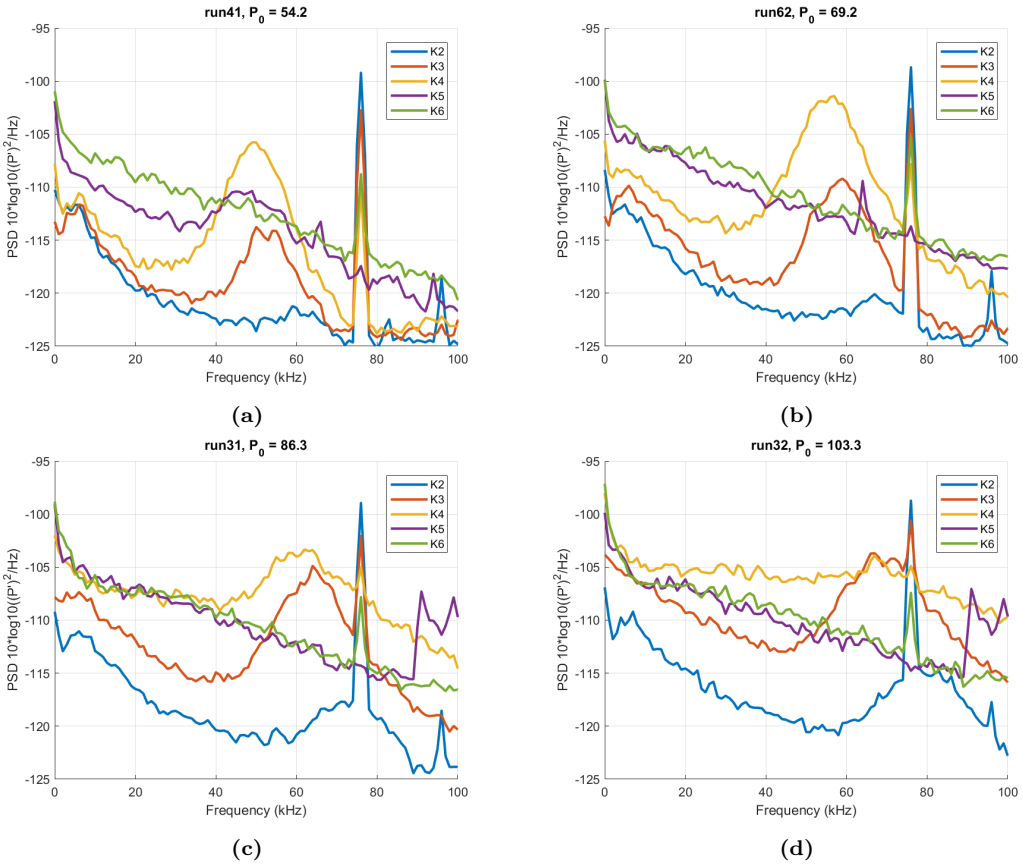


Figure 131. PSDs at each run condition for the Kulites down the length of the 14 degree sharp ogive sampled during second quasi-steady periods (a) $P_{DT} = 75psia$ (b) $P_{DT} = 100psia$ (c) $P_{DT} = 125psia$ (d) $P_{DT} = 150psia$ (note: the ≈75kHz spike is electrical noise)

of the model for this geometry. The higher frequency band drops in frequency as it progresses downstream and as the driver tube pressure is increased. The lower frequency band however does not appear to change frequency, regardless of axial position or driver tube pressure. This further implies that the lower frequency band is not a modal instability bound to the boundary layer thickness while the upper frequency exhibits clear second mode behavior.

The behavior of the lower frequency band remaining unaffected by the change in run conditions while the higher frequency is affected is perhaps shown best in Figure 132 where the PSD of each Kulite over the 14 degree ogive is plotted against run condition. The steadfastness of the ∼10kHz band can clearly be observed while the

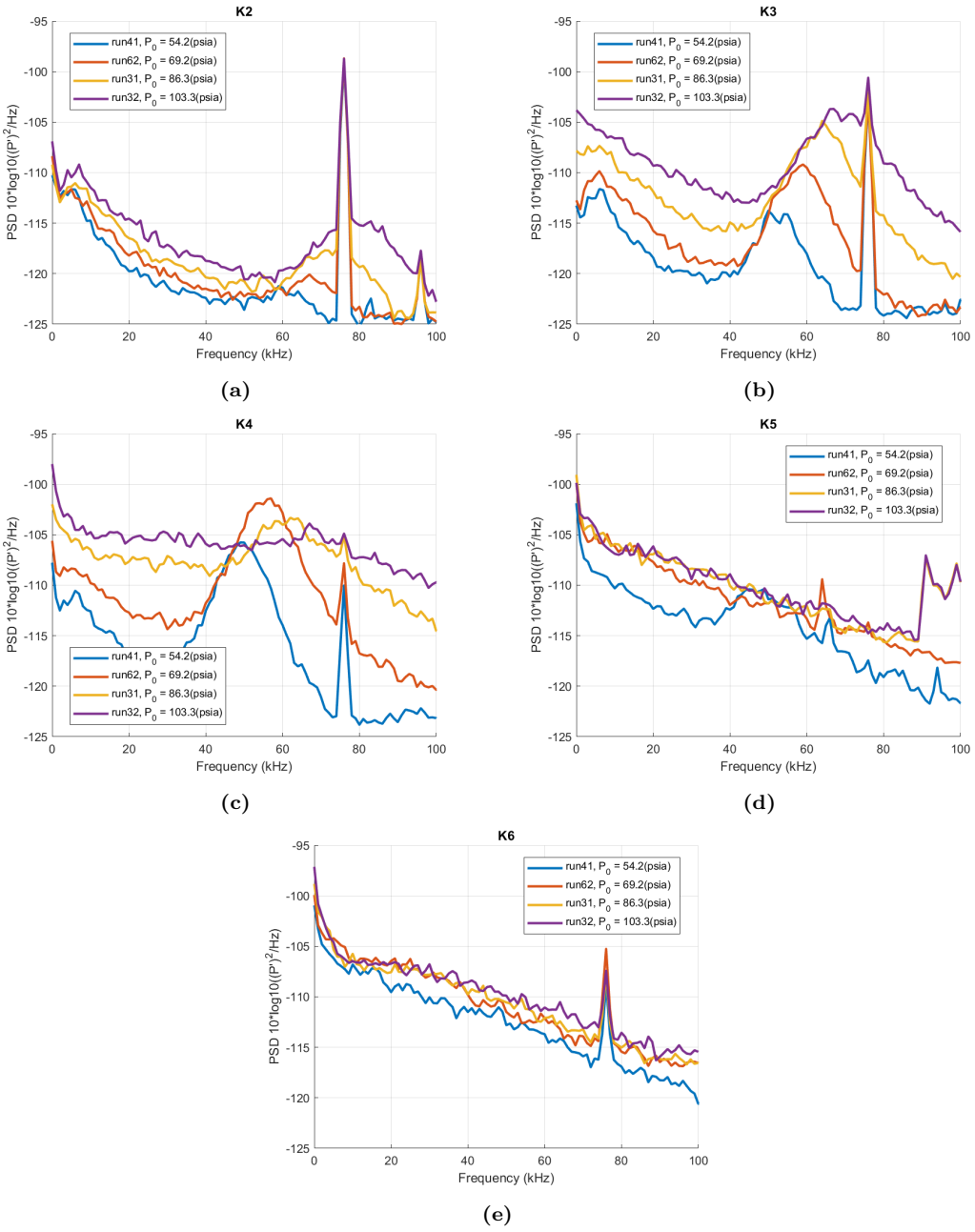


Figure 132. PSDs of each Kulite sensor at various driver tube pressures over the 14 degree sharp ogive sampled during second quasi-steady period (a) Kulite 2 (b) Kulite 3 (c) Kulite 4 (d) Kulite 5 (e) Kulite 6 (note: the ≈75kHz spike is electrical noise)

higher frequency band can be seen ranging from ∼50kHz to ∼80kHz depending on sensor location and run condition. From this view of the Kulite PSD's over the 14 degree sharp ogive, it appears as if the higher frequency, modal instability band is

dominating the transition behavior over the flow. The model appears to be fully transitioned for each run condition by Kulite sensor 5. There is also a valid argument to be made that the sensors appear to broaden across the 10-60kHz range possibly suggesting interactions between the upper and lower frequency bands as transition occurs.

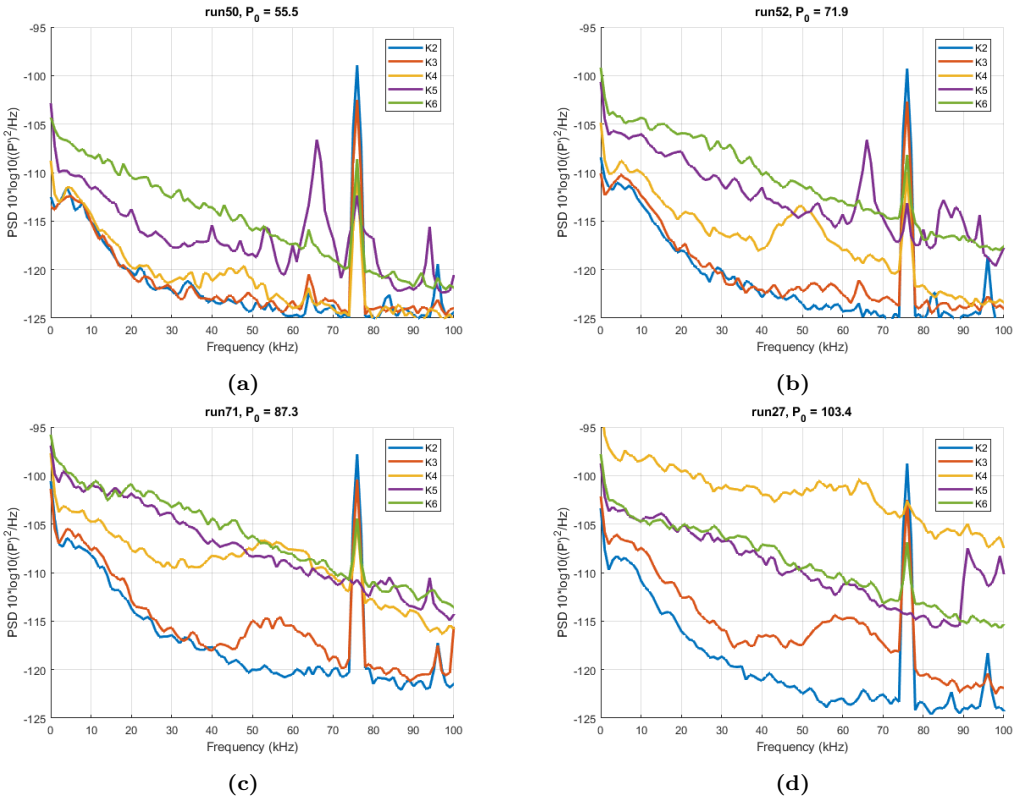


Figure 133. PSDs at each run condition for the Kulites down the length of the 28 degree sharp ogive sampled during second quasi-steady periods (a) $P_{DT} = 75psia$ **(b)** $P_{DT} = 100psia$ **(c)** $P_{DT} = 125psia$ **(d)** $P_{DT} = 150psia$ **(note: the ≈65-75kHz spike is electrical noise)**

Performing the same exercise for the 28 degree ogive tip at the same run conditions as Figure 131 produces Figure 133. These PSDs again show all of the Kulite sensors over the length of the model for a given run conditon. It is evident from this result that the 28 degree ogive ogive tip has a strong and consistent low frequency band, but the higher frequency band exhibits a different behavior than the 14 degree ogive case. The higher frequency band appears to be significantly delayed in its emergence

compared to the 14 degree ogive and transitions with a broader spectrum. Despite this later emergence and broader spectral behavior of the instability, the data suggests the possibility of a faster amplification of the instability and transition to turbulence once the instability forms.

Plotting the PSD results of each Kulite at each run conditions for each sensor in Figure 134 provides a useful perspective of the frequency content once again. First it can be noted that Kulite 2 exhibits no clear high frequency band, but does show a strong low frequency band. Kulite 3 shows indications of the higher frequency band for the two highest pressures. Continuing downstream to Kulite 4, it is observed that there is a spectral broadening and merging of the two frequency bands as the pressure is increased. By Kulite 5 and 6, there is no clear lower or upper frequency band peak. For these final two sensors, the spectra increases linearly in a broadband fashion which may indicate a non-modal progression to turbulence.

Increasing the tip angle again to the 56 degree sharp ogive and plotting resulting PSDs for each run condition produces Figure 135. A distinctly different spectral behavior is observed for this range of frequencies using the Kulite sensors. The transition behavior appears to be dominated by a broadband, nonmodal progression for each run condition.

Plotting each sensor individually against pressure for the 56 degree sharp ogive in Figure 136 helps to reveals the presence of the expected 10-15kHz peak and the emergence of an apparent frequency peak at $\sim$20kHz. This peak was not clearly observed in the other measurement techniques and appears to dominate the initial onset of transition. After transition begins, it appears as if the progression to fully turbulent flow follows a broadband linear increase in spectral intensities with no clear frequency peaks.

The blunted geometries produced no clear low frequency content or trends from

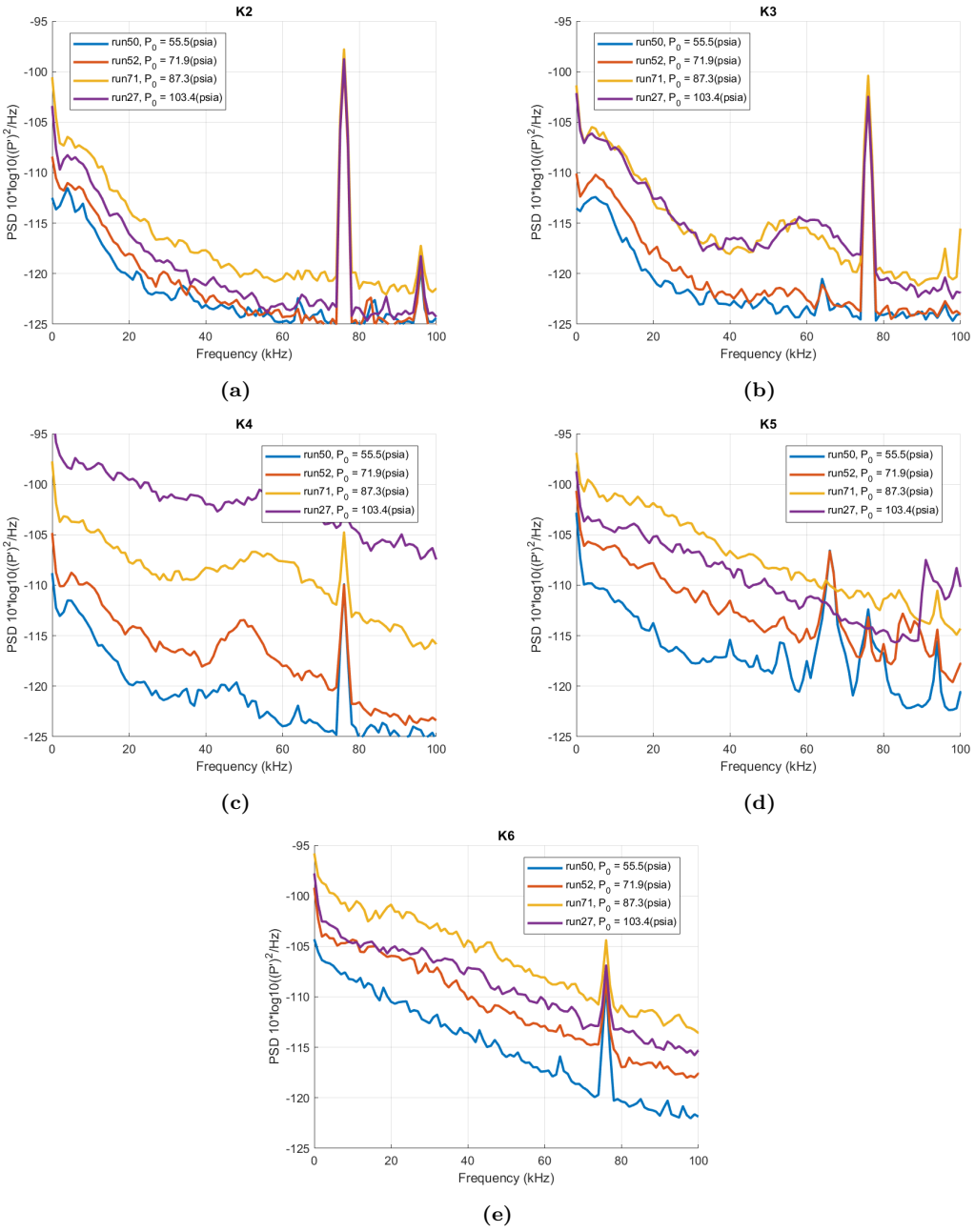


Figure 134. PSDs of each Kulite sensor at various driver tube pressures over the 28 degree sharp ogive sampled during second quasi-steady periods (a) Kulite 2 (b) Kulite 3 (c) Kulite 4 (d) Kulite 5 (e) Kulite 6 (note: the ≈75kHz spike is electrical noise)

the Kulite sensors and thus are not discussed in this study. Fortunately, spectral information for these blunted geometries are found from the PCB sensors.

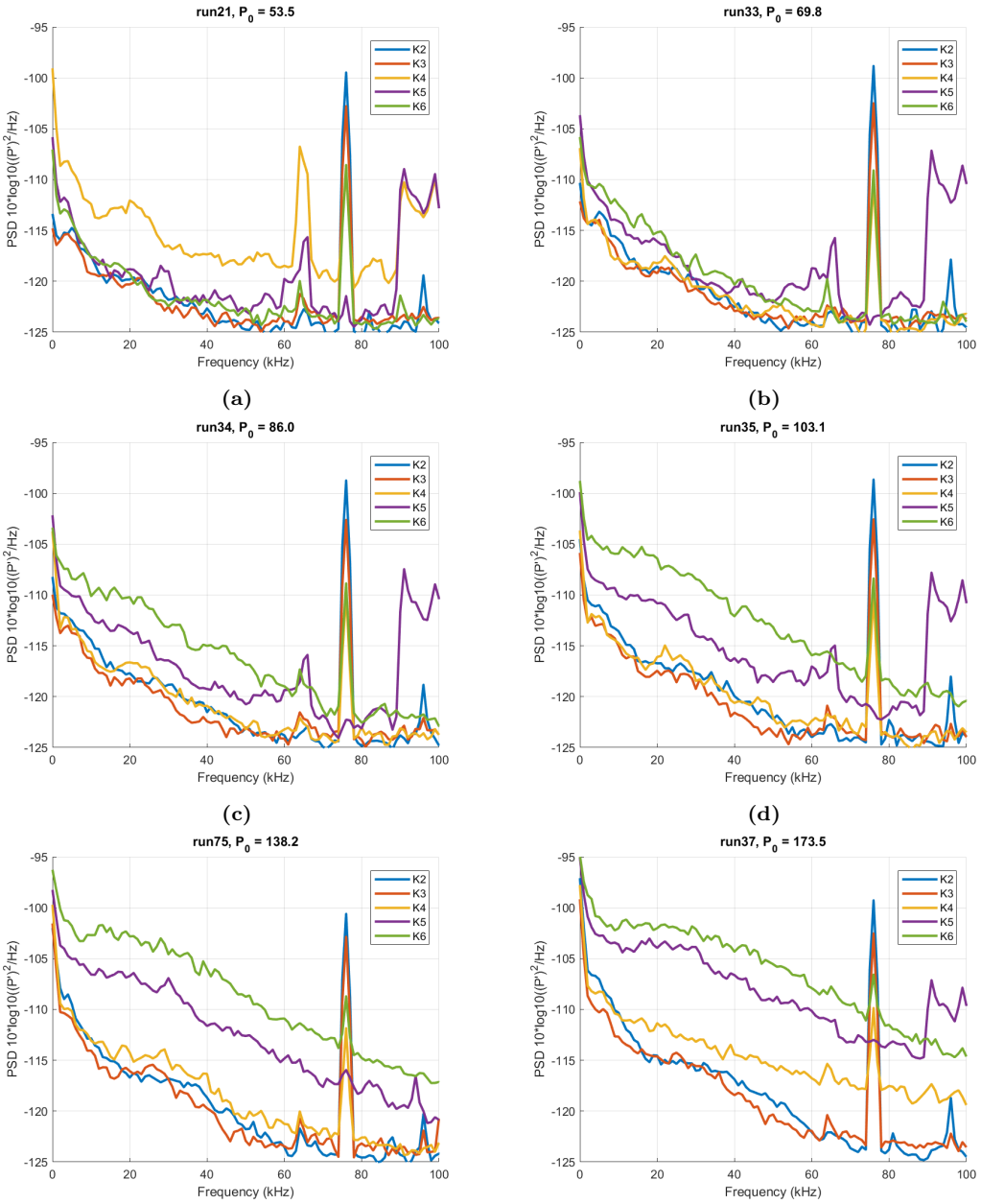


Figure 135. PSDs at each run condition for the Kulites down the length of the 56 degree sharp ogive sampled during second quasi-steady periods (a) $P_{DT} = 75psia$ (b) $P_{DT} = 100psia$ (c) $P_{DT} = 125psia$ (d) $P_{DT} = 150psia$ (e) $P_{DT} = 200psia$ (f) $P_{DT} = 250psia$ (note: the ≈65-75kHz spike is electrical noise)

The sharp ogives show strong modal instabilities with non-linear interactions.

With the Kulite measurements over the 14 and 28 degree sharp ogives showing the presence of the same two frequency bands that were observed in the off-surface mea-

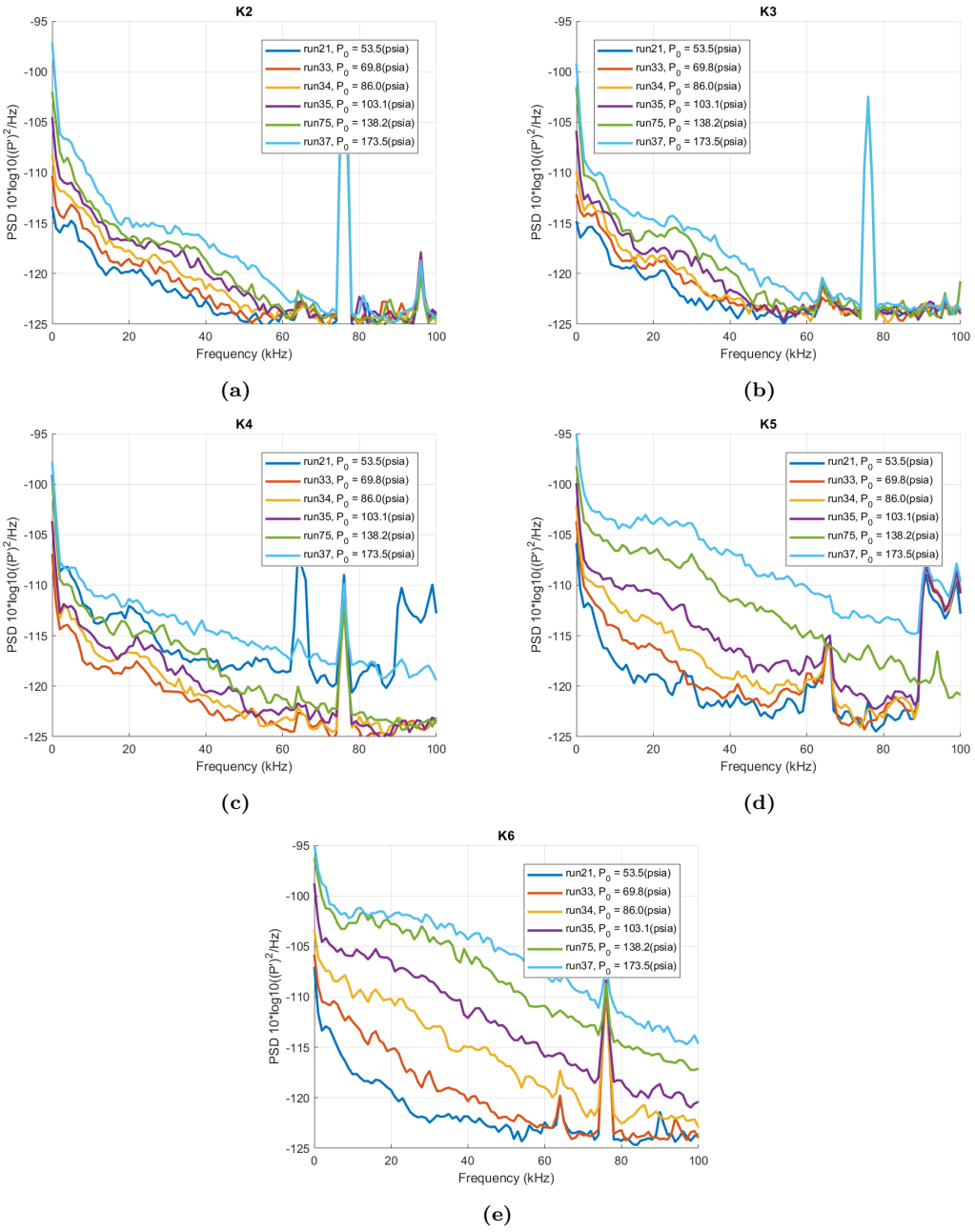


Figure 136. PSDs of each Kulite sensor at various driver tube pressures over the 56 degree sharp ogive sampled during second quasi-steady periods (a) Kulite 2 (b) Kulite 3 (c) Kulite 4 (d) Kulite 5 (e) Kulite 6 (note: the ≈65-75kHz spike is electrical noise)

surements, the PCB sensors were then used to explore the higher frequency content of the flow over these two geometries at the same run conditions.

Figure 137 shows the PCB power spectra for the flow above the 14 degree sharp

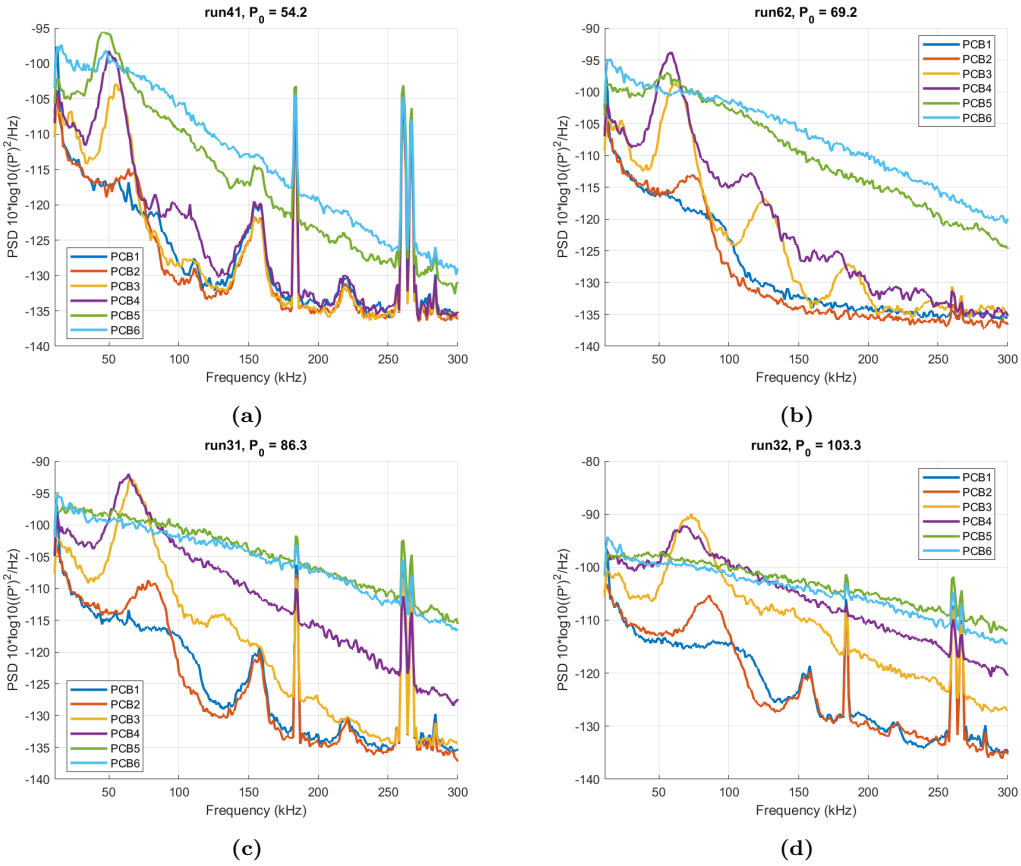


Figure 137. PSDs at each run condition for the PCBs down the length of the 14 degree sharp ogive of second quasi-steady periods (a) $P_{DT} = 75psia$ (a) $P_{DT} = 100psia$ (a) $P_{DT} = 125psia$ (a) $P_{DT} = 150psia$ (note: the ≈150kHz spike and other higher frequency spikes are electrical noise)

ogive geometry at multiple driver tube pressures. The same primary frequency peak at ∼50-80kHz that is observed in the Kulite traces of Figure 131 are observed in this figure as well. On top of the peak frequency being measured by the PCB's however, a clear harmonic is observed in the traces at a variety of PCB locations. At a driver tube pressure of 100psia, the third PCB is able to resolve at least three harmonic peaks on top of the primary ∼60kHz peak. It is immediately evident that each run condition experiences transition due to a domination of this highly modal instability with harmonic peaks. This transition after the appearance of the harmonics implies that nonlinear interactions could be causing a breakdown of the modal instabilities. It also appears that a low frequency band does emerge from the PCB 11kHz filter

centered around 20kHz in each run. It is not immediately evident however if this lower frequency band is directly impacting transition since the nonlinear harmonics appear to dominate the spectra. It should also be noted again here that the seemingly random broad spike at 150kHz is electrical noise that was present in runs up to run 52 of this study and is not a physical peak in the spectra.

Plotting each PCB sensor individually against the driver tube pressures produces Figure 138. This visualization of the of the frequency space confirms the strong modal behavior of the ∼50-60kHz band that sees an increase in peak frequency with increased unit Reynolds number. At PCB1, the modal instability begins to emerge as a spectral broadening before forming a clear peak by PCB2 for every run condition. The harmonics forming by PCB3 appear to dominate the progression to turbulence. Once transition initiates, the modal peak appears to broaden and the harmonics fall away into broadband transitional noise. This implies a nonlinear domination of transition and agrees the Schlieren analysis which saw complex frequency interactions causing turbulent bursts such as was shown in Figure 114.

To further ensure that the observed PSD results are indeed nonlinear effects, bicoherence analysis was performed on the PCB traces for the 100psia driver tube pressure case (run 62). This analysis was accomplished via a bicoherence Matlab code that was written by Joshua Edelman for his dissertation at Purdue in 2016 [83]. In hypersonic boundary layer instability research, bicoherence is often used as a measure of the nonlinear interaction a given instability has with itself [83]. When the bicoherence between two frequencies is high, that is a strong indication of nonlinear interactions occurring between those frequencies. Figure 139 shows the resulting bicoherence diagrams for PCBs 2 through 5 for the 100psia case (run 62). PCB2 shows no signs of nonlinear effects, but by PCB3, a significant amount of bicoherence is observed at the intersection of 65kHz and 65kHz, its harmonic at 130kHz, and

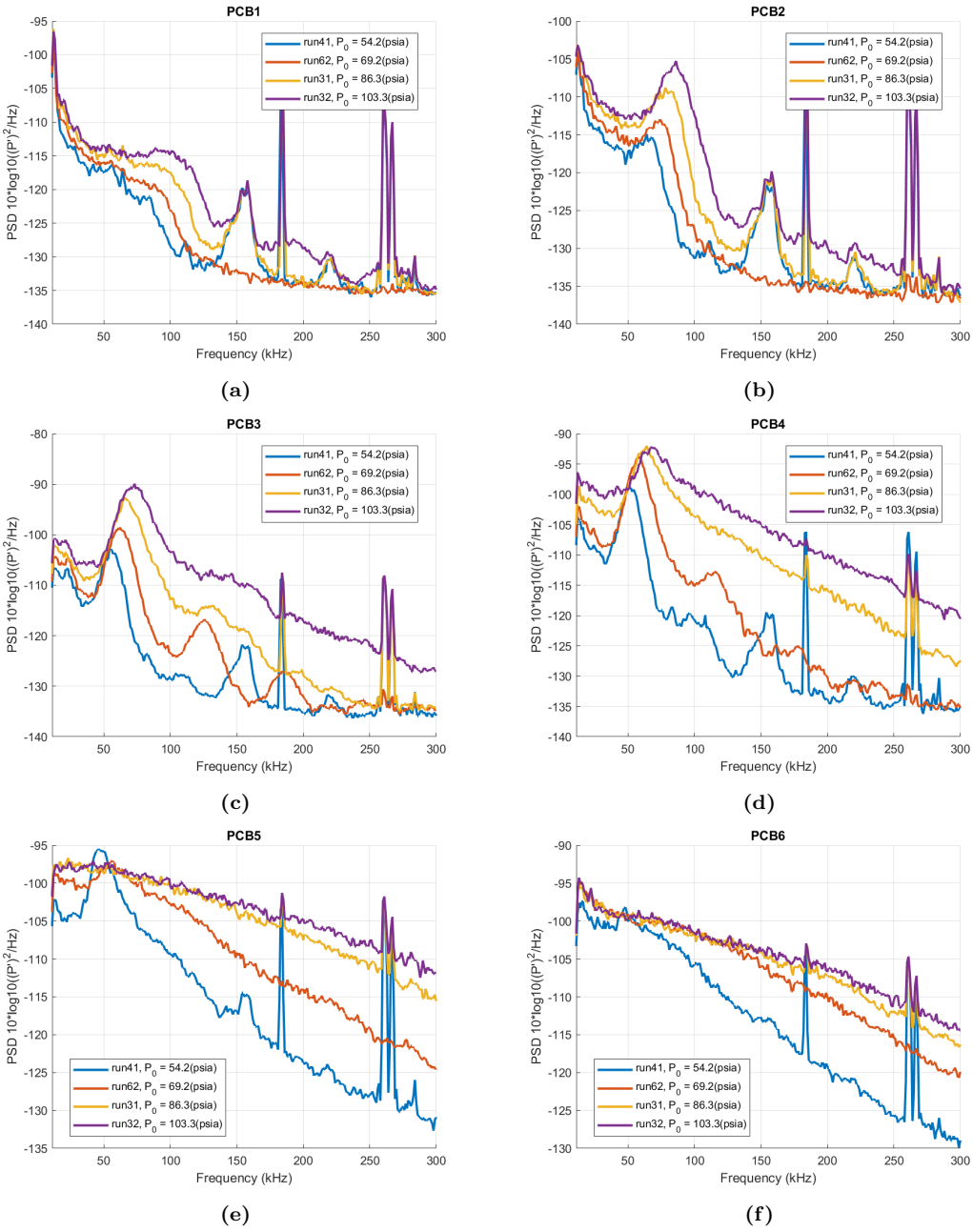


Figure 138. PSDs of each PCB sensor at various driver tube pressures over the 14 degree sharp ogive sampled during second quasi-steady periods (a) PCB 1 (b) PCB 2 (c) PCB 3 (d) PCB 4 (e) PCB 5 (f) PCB 6 (note: the ≈150kHz spike and other higher frequency spikes are electrical noise)

with the low frequency ∼15-20kHz band. This high level of bicoherence indicates that the 65kHz band and its harmonics are experiencing nonlinear effects at this sensor with possible interactions occuring with the lower frequency band as well.

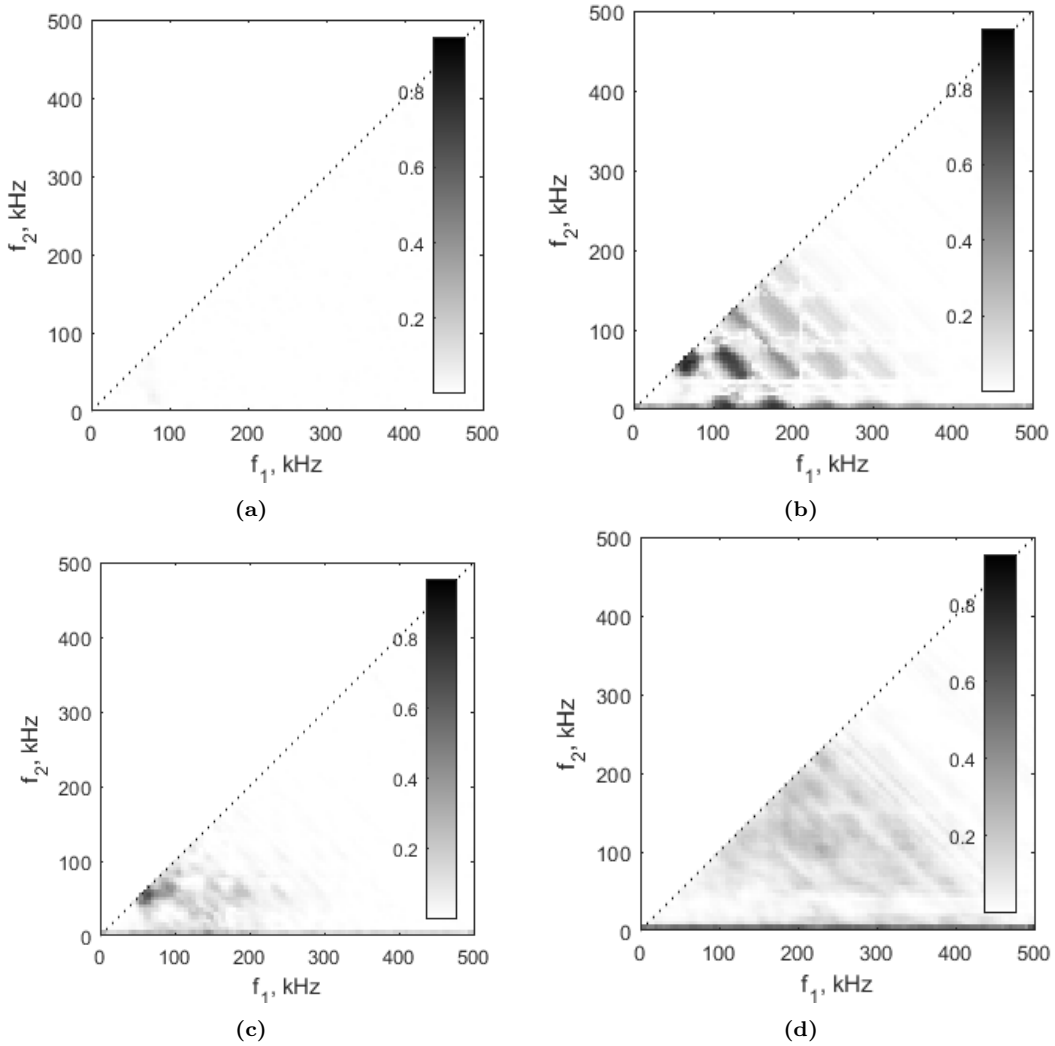


Figure 139. Bicoherence of the PCB traces for the 14 degree sharp ogive at a driver tube pressure of 100psia (a) PCB2 (b) PCB3 (c) PCB4 (d) PCB5 (note: the ≈150kHz spike and other higher frequency spikes are electrical noise)

Moving downstream to PCB 4 and 5, the bicoherence values broaden across the higher frequencies with no particular spike in bicoherence frequency. This broadening of the bicoherence values implies a dominance of nonlinear effects in the breakdown to turbulence for this run case.

Moving to the 28 degree sharp ogive and plotting each individual PCB sensor against driver tube pressure in Figure 140 reveals a similar behavior to the 14 degree sharp ogive, but with some distinct differences. First off, it is observed that the

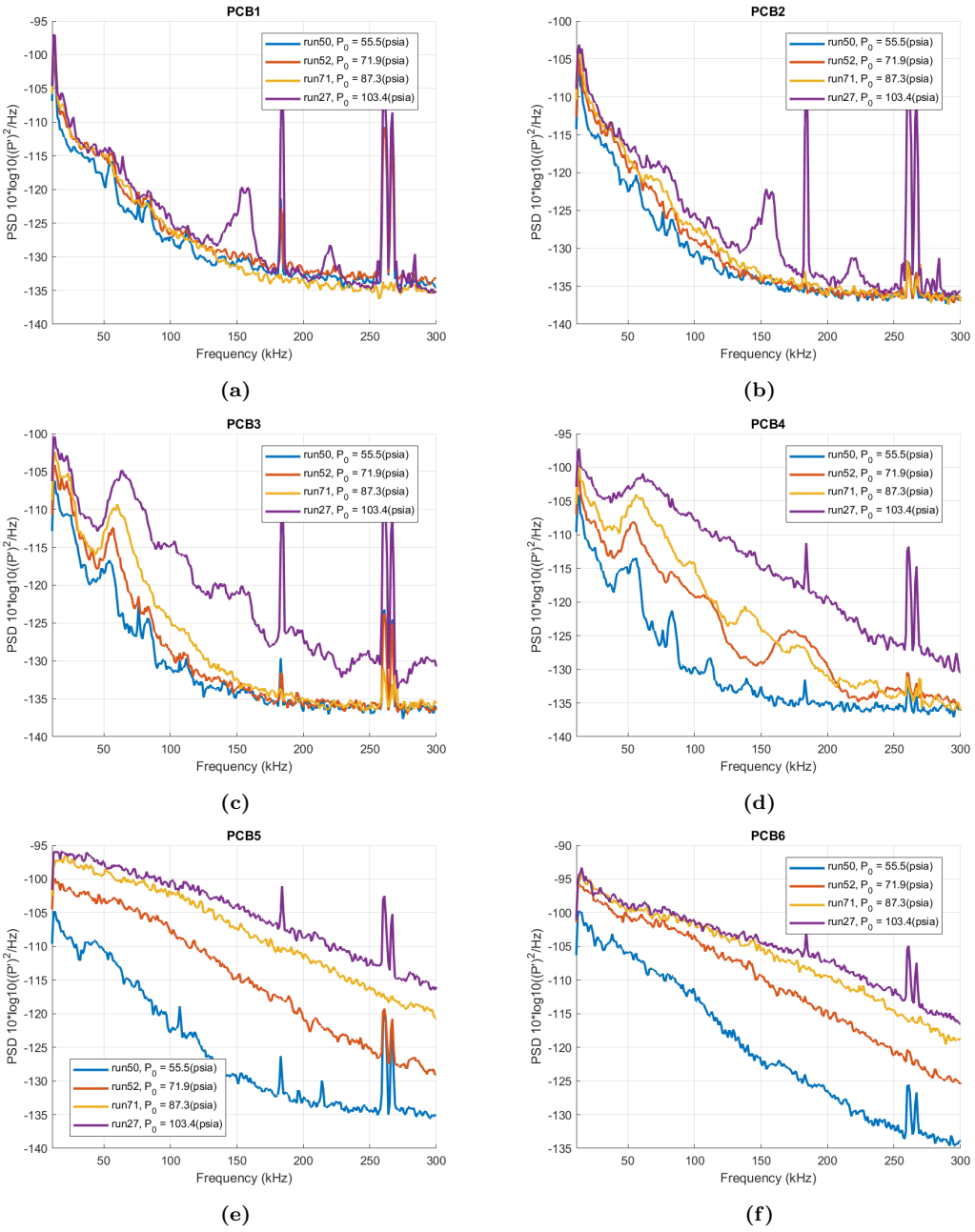


Figure 140. PSDs of each PCB sensor at various driver tube pressures over the 28 degree sharp ogive sampled during second quasi-steady periods (a) PCB 1 (b) PCB 2 (c) PCB 3 (d) PCB 4 (e) PCB 5 (f) PCB 6

first two sensors show little to no clear frequency peaks in their spectra. There is a possible peak at a 15-20kHz band, but the lack of PCB clarity at this frequency range leaves doubts as to whether this is truly a peak or sensor noise. By PCB sensor

3, the same modal instability peak at ∼60kHz as with the 14 degree sharp ogive is clearly observed. While this modal instability emerges at a more downstream sensor location than the 14 degree ogive, the instability appears to amplify and breakdown much more rapidly than the shallower angle ogive. PCB sensor 4 appears to show nonlinear interactions and by sensor 5, each run appears to either be transitional or fully turbulent.

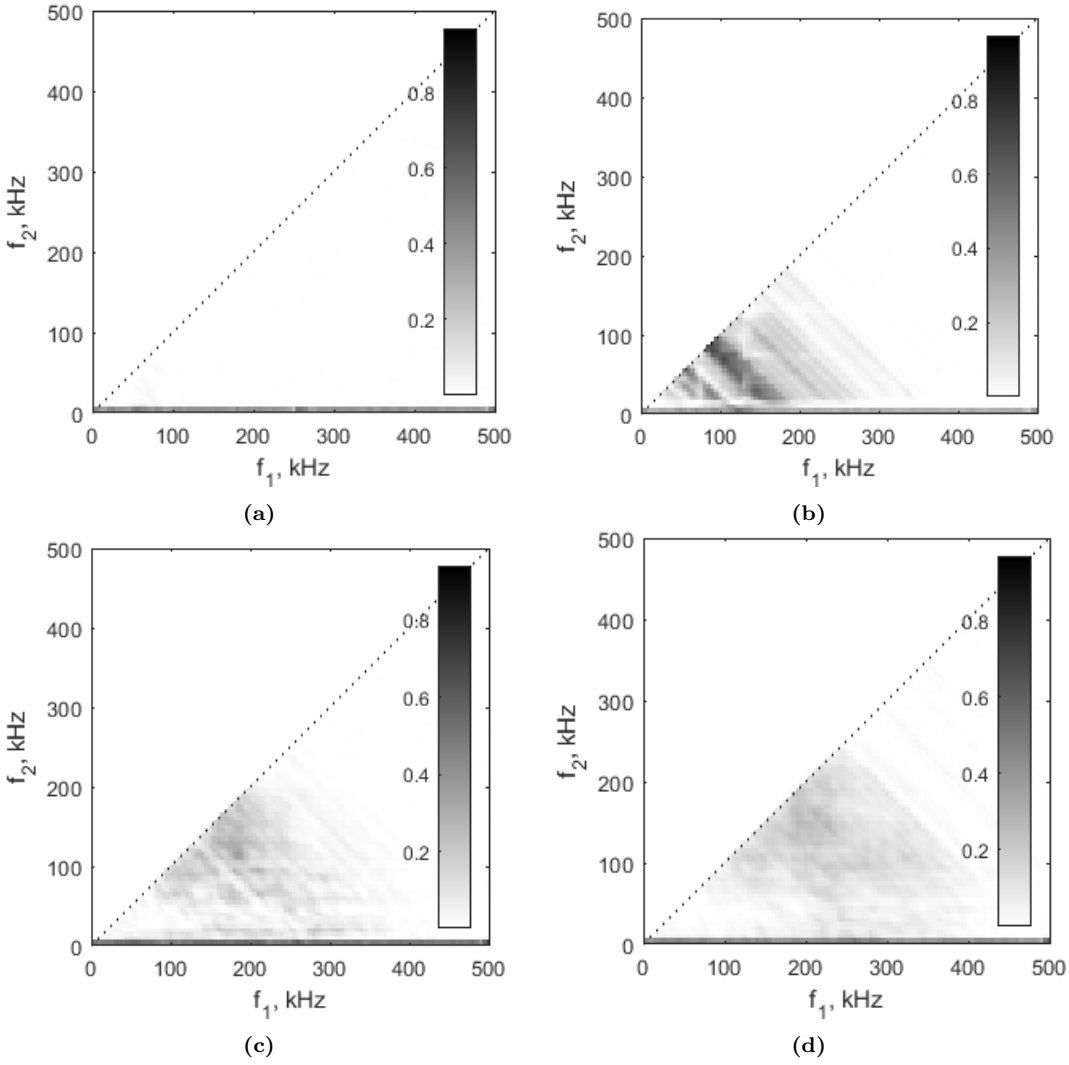


Figure 141. Bicoherence of the PCB traces for the 28 degree sharp ogive at a driver tube pressure of 100psia (a) PCB3 (b) PCB4 (c) PCB5 (d) PCB6

Another bicoherence analysis is performed for the 28 degree ogive PCB sensors to ensure the presence of nonlinear interactions. Figure 141 shows the results of the

bicoherence study for PCB sensors 3 through 6 of run 52 with a driver tube pressure of 100psia. PCB3 shows no sign of coherence, but by PCB4 there is a broad level of coherence around the 100kHz-100kHz intersection. This most likely indicates that the location of peak nonlinear interactions lies between the sensors and by PCB4 the instability is beginning to nonlinearly breakdown to turbulence. The presence of the nonlinear peak occuring prior to PCB4 would explain why PCB4 shows a strange harmonic response that appears warped when compared to the 14 degree ogive's harmonics.

For the 56 degree sharp ogive, Figure 142 shows the PSD results for each sensor of the model at a variety of run conditions. No frequencies are immediately evident in the first two sensors, but there is a slight spectral broadening around 50-60kHz. Moving downstream to the later sensors, a peak around 20kHz appears to emerge from the PCB signal filter. By PCB sensor 5, transition is occuring for the highest pressure settings in a seemingly broadband fashion and the 10kHz peak appears to strengthen until the 200psia driver tube pressure setting.

The blunt tips show non-modal transition behavior with nonlinear effects.

While the sharp ogives all exhibit what appears to be modal instabilities with nonlinear interactions, when spherical bluntness is added to the tips of the ogives, a clear shift in dominant instability mechanisms is observed in the frequency content from the PCB sensors. The blunted ogives all exhibit what appears to be non-modal transition behaviors with significant delay in transition for all of the run conditions used. Figures 143 through 148 show the PSD content for each sensor and run condition for the blunted ogive configurations.

For the 14 degree ogive with 1/4 base radius bluntness, the frequency spectra for

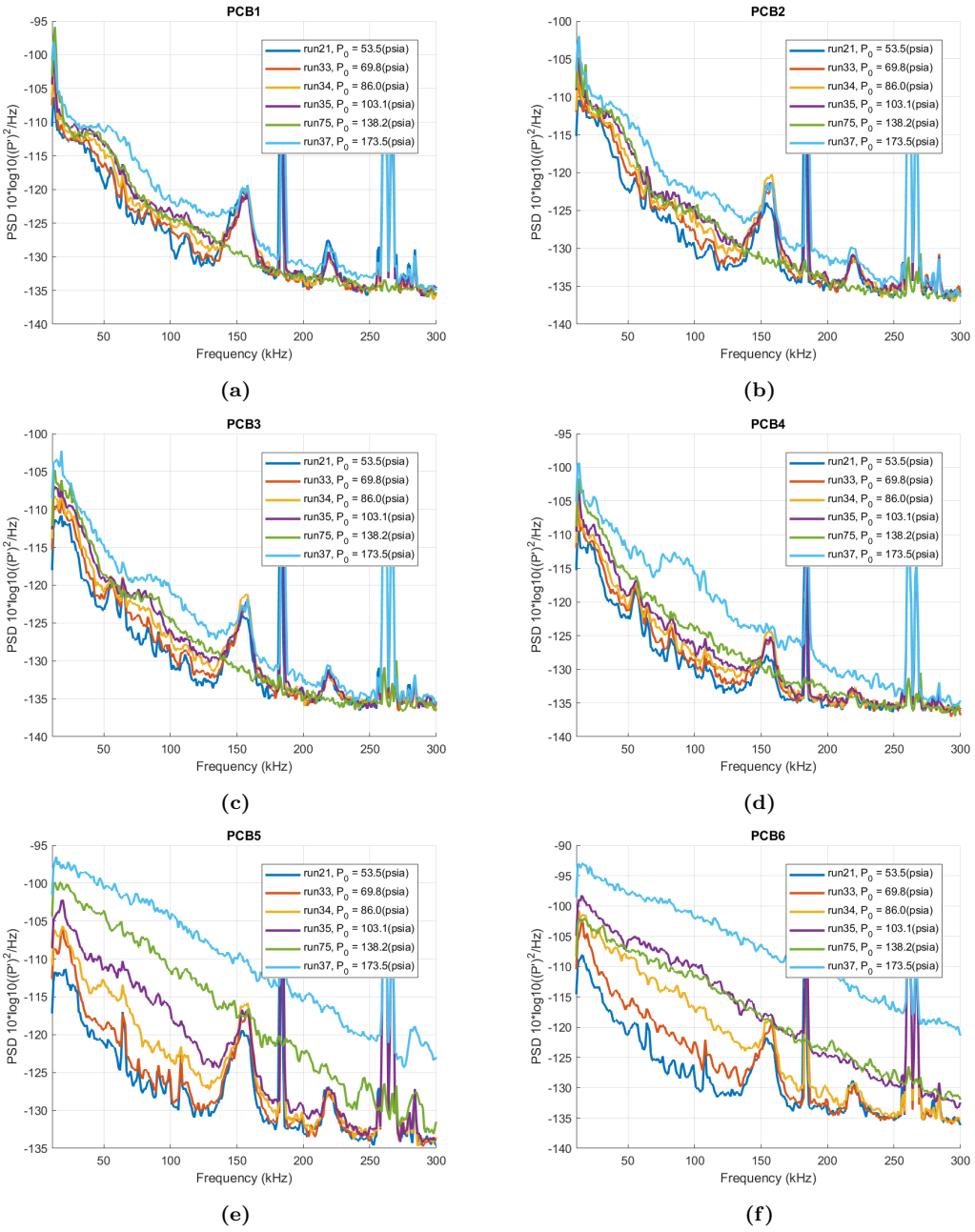


Figure 142. PSDs of each PCB sensor at various driver tube pressures over the 56 degree sharp ogive sampled during second quasi-steady periods (a) PCB 1 (b) PCB 2 (c) PCB 3 (d) PCB 4 (e) PCB 5 (f) PCB 6

the each PCB sensor at the various run conditions are shown in Figure 143. The clear delay in transition and suppression of any peak frequencies when compared to the 14 degree sharp ogive variant is immediately evident. The first sensor shows a mild

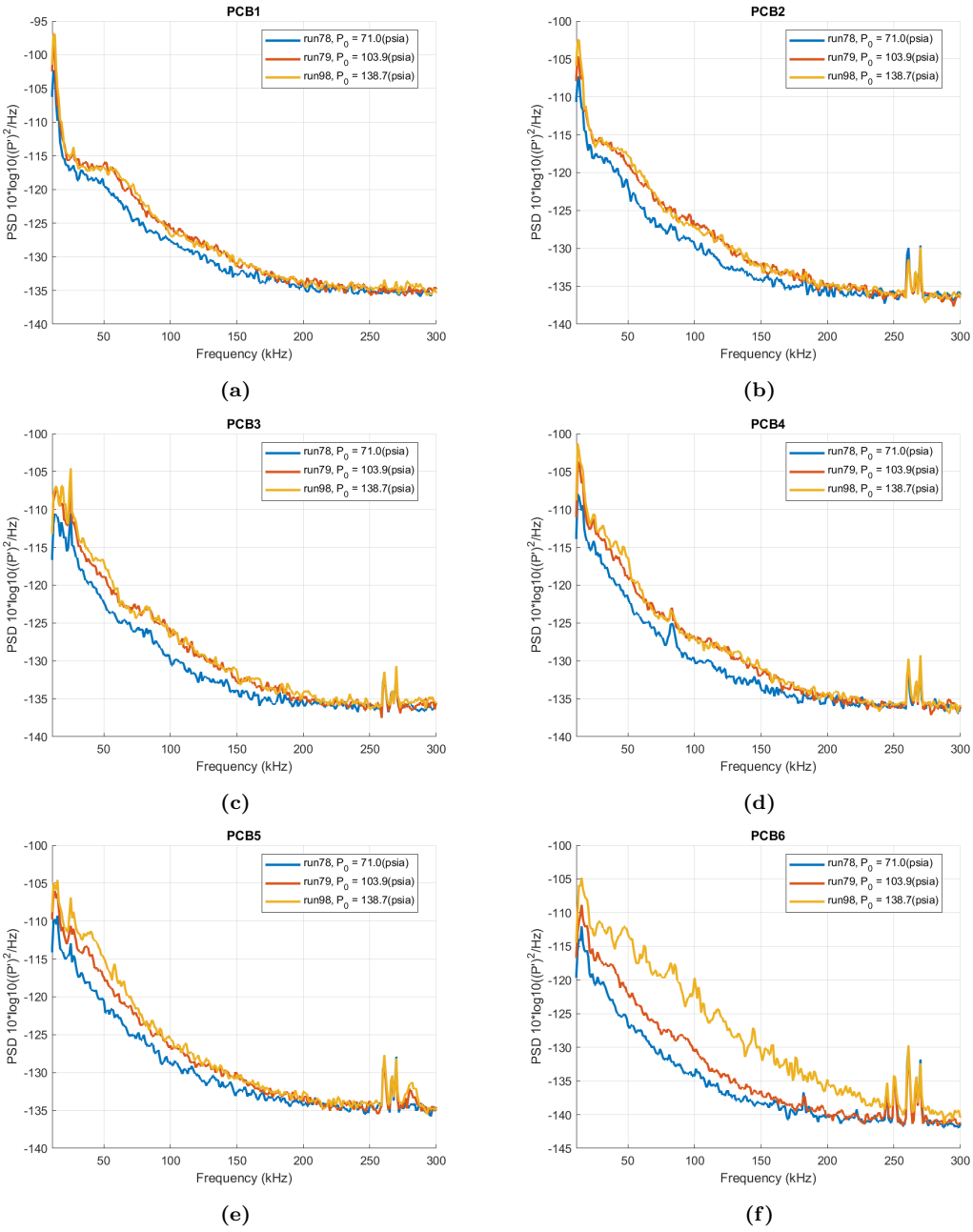


Figure 143. PCB PSD vs driver tube pressure over the 14 degree 1/4R blunted ogive sampled during second quasi-steady periods (a) PCB 1 (b) PCB 2 (c) PCB 3 (d) PCB 4 (e) PCB 5 (f) PCB 6

spectral broadening around 50kHz, but with further downstream distance the spectra appears almost entirely laminar for the following PCB sensors. It is only PCB sensor 6 at the highest pressure setting that shows and sign of transitional behavior. The

spectra's unevenness for this last sensor appears to show nonlinear behaviors and is in the midst of a transitional state.

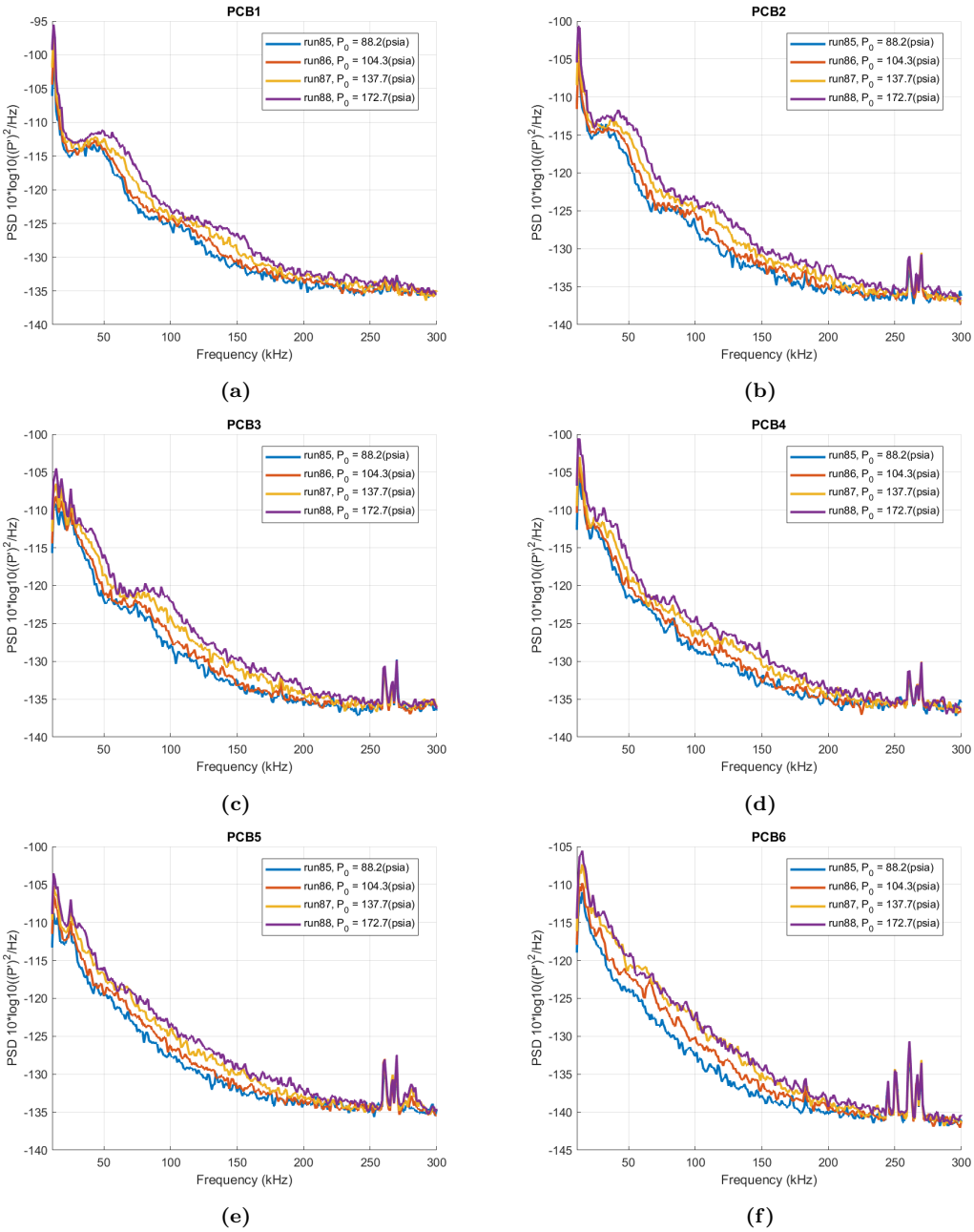


Figure 144. PCB PSD vs driver tube pressure over the 14 degree 1/2R blunted ogive sampled during second quasi-steady periods (a) PCB 1 (b) PCB 2 (c) PCB 3 (d) PCB 4 (e) PCB 5 (f) PCB 6

Further increasing the bluntness of the 14 degree ogive to 1/2 base radius and

plotting each PCB sensor at the various run conditions produces Figure 144. For this geometry, each run condition produced very consistent and almost identical frequency content. The first PCB spectra shows a broadening for all run conditions at ∼50kHz that appears to intensify in magnitude and drop in frequency by PCB sensor 2. By PCB sensor 3, the original peak appears to be washed in the sensor noise of the PCB and a second broadening appears around 100kHz. PCB sensors 4 and 5 show an almost entirely laminar frequency spectra with a peak around 25 kHz. PCB 6 also shows laminar frequency spectra, but the low frequency peak is no longer resolved.

Moving to the 28 degree ogive with 1/4 base radius bluntness and plotting the PCB spectra for various driver tube pressures is shown in Figure 145. The first three PCB sensors for this geometry show a very similar spectra to the 14 degree ogive with 1/4R bluntness with an overall laminar spectra with a mild broadening around 50kHz. Unlike the 14 degree 1/4R blunted variant however, this geometry shows a rapid progression to transition for the last three PCBs for the higher pressure settings. PCB sensor 5 at the 200psia driver tube pressure and PCB sensor 6 at the 100psia driver tube pressure both show signs of strong non-linear interactions in their spectra as apparent harmonic peaks form. This is an intriguing observation given that no clear modal instabilities are observed leading up to the nonlinear breakdown.

Performing a bicoherence analysis of at the 200psia driver tube pressure setting (run 83) for PCB sensors 4, 5, and 6 produces Figure 146. PCB 4 shows no sign of bicoherence, but by PCB sensor 5, a large amount of broadband bicoherence is observed. This production of high bicoherence in the signal is particularly interesting due to the lack of modal instability content prior to the appearance of nonlinear interactions. This could either be due to a rapid onset of a modal instability that forms and breaks down betwee the two sensors or it could indicate a nonlinear interaction with a nonmodal instability not bound to the boundary layer such as the entropy

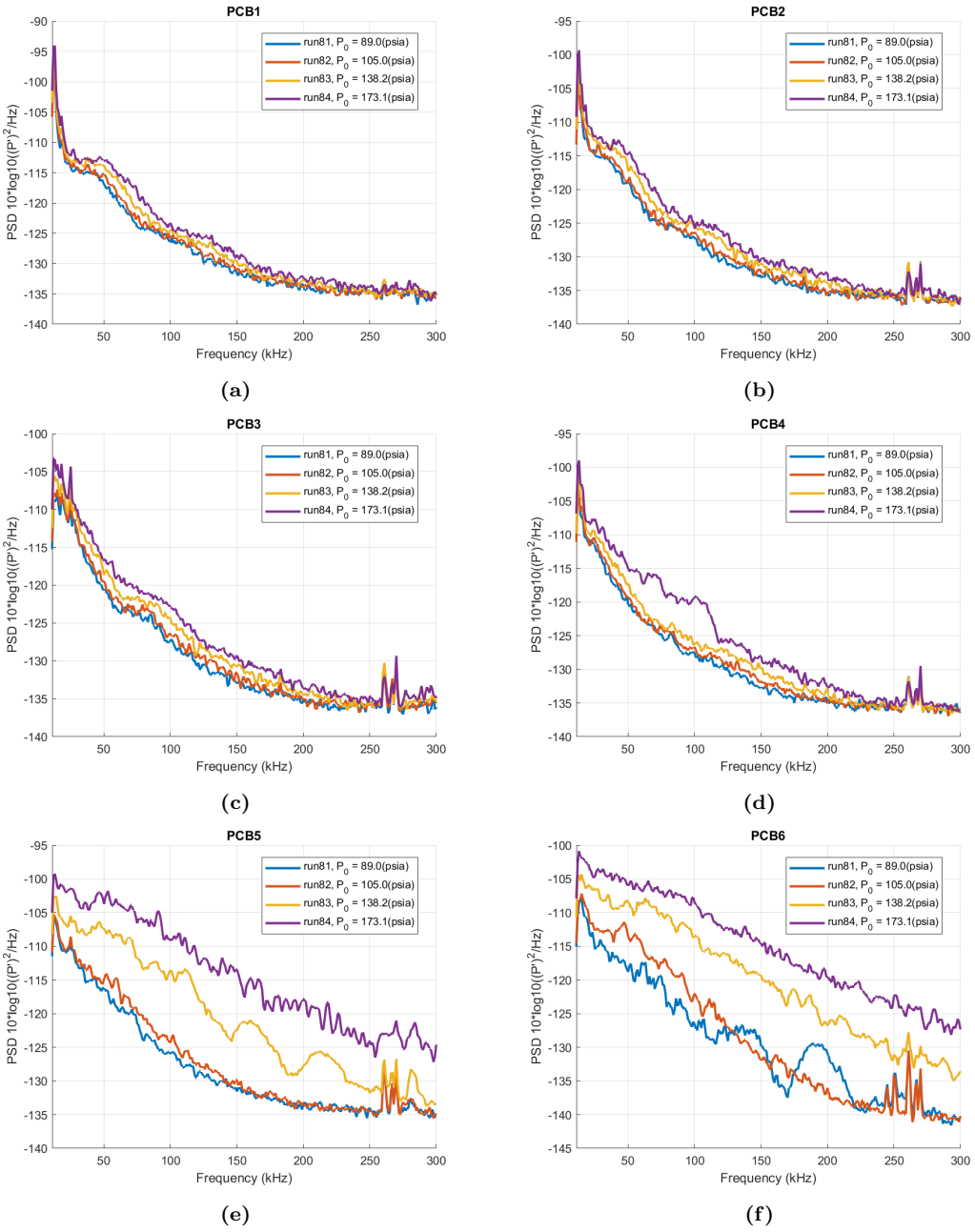


Figure 145. PCB PSD vs driver tube pressure over the 28 degree 1/4R blunted ogive sampled during second quasi-steady periods (a) PCB 1 (b) PCB 2 (c) PCB 3 (d) PCB 4 (e) PCB 5 (f) PCB 6

layer instabilities previously discussed in this study.

Increasing the 28 degree ogive bluntness to 1/2 base radius bluntness and plotting the PCB spectra produces Figure 147. Again, the first four PCB sensors show some

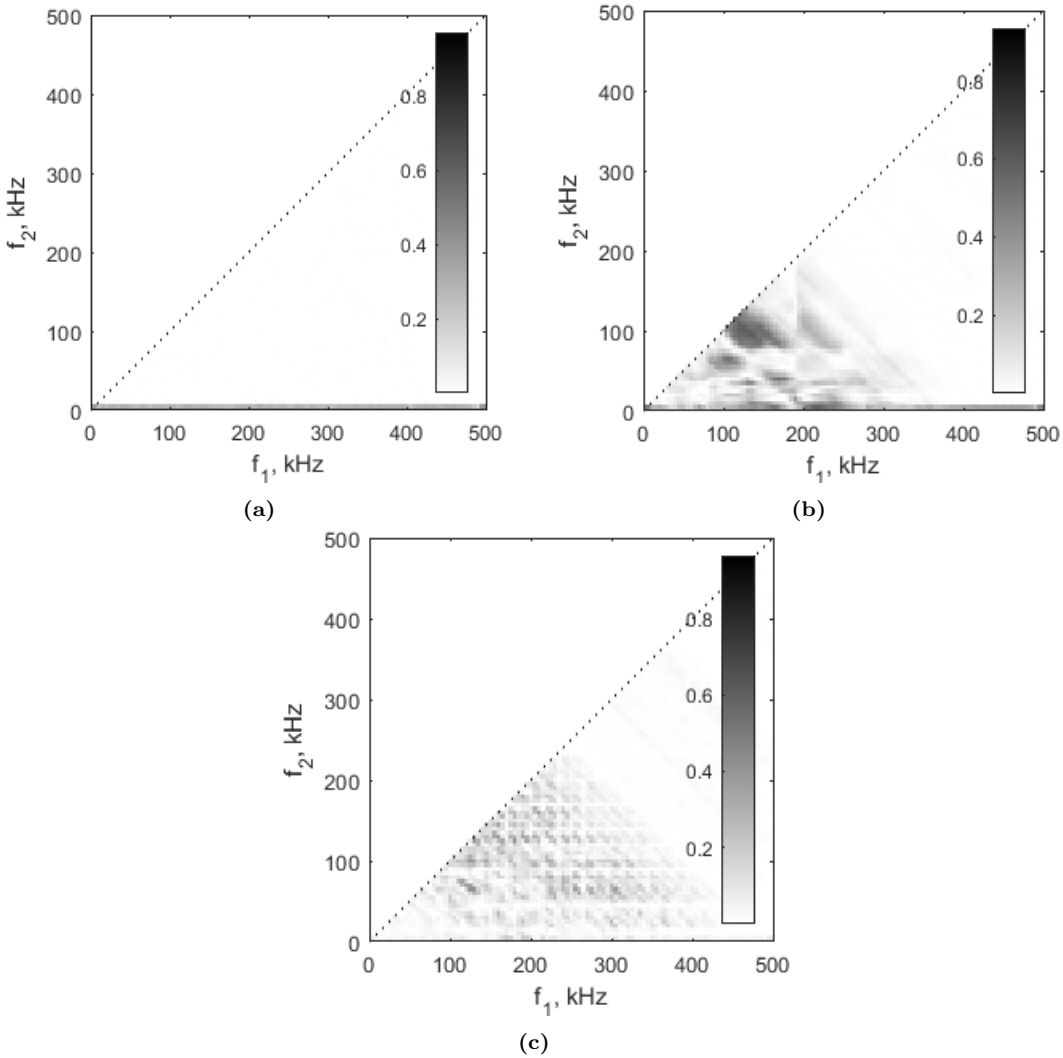


Figure 146. Bicoherence of the PCB traces for run 83 (a) PCB4 (b) PCB5 (c) PCB6

mild broadening of the spectra, but no clear modal instabilities are observed. PCB 5 shows the two highest pressure settings indicating the beginning of transition and by PCB 6 these two settings are showing transitional spectra with some possible nonlinear behavior.

Finally, the spectra of the PCBs over the spherically blunted tip variant are shown in Figure 148. From these spectra, it is clear that the transition onset over the model is dominated by an apparent non-modal instability that causes a broadband transition.

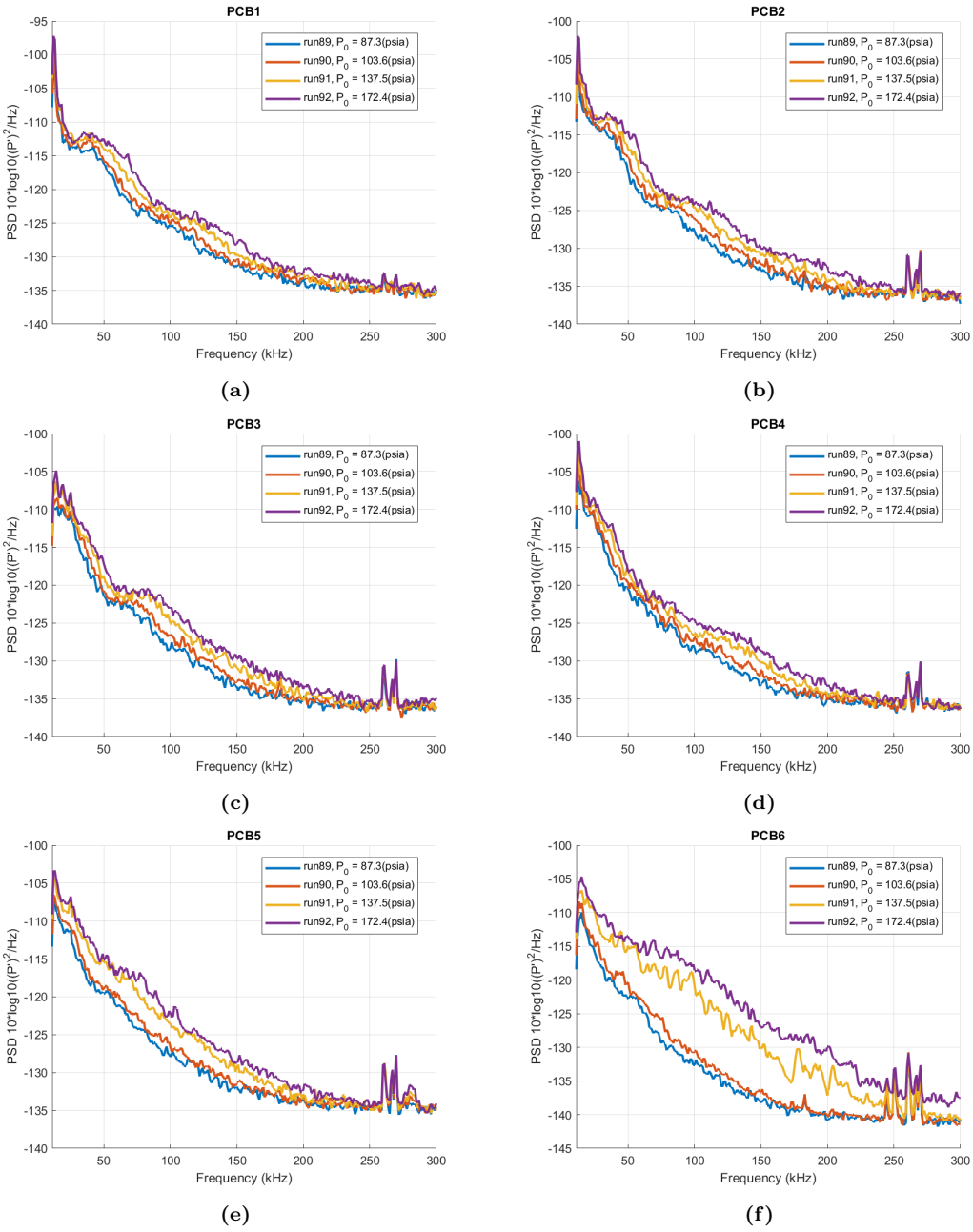


Figure 147. PCB PSD vs driver tube pressure over the 28 degree 1/2R blunted ogive sampled during second quasi-steady periods (a) PCB 1 (b) PCB 2 (c) PCB 3 (d) PCB 4 (e) PCB 5 (f) PCB 6

An apparent blunt tip transition reversal is observed.

In addition to the observations from the frequency spectra that the sharp and blunted ogive tips show signs of nonlinear breakdowns, trends in the transition be-

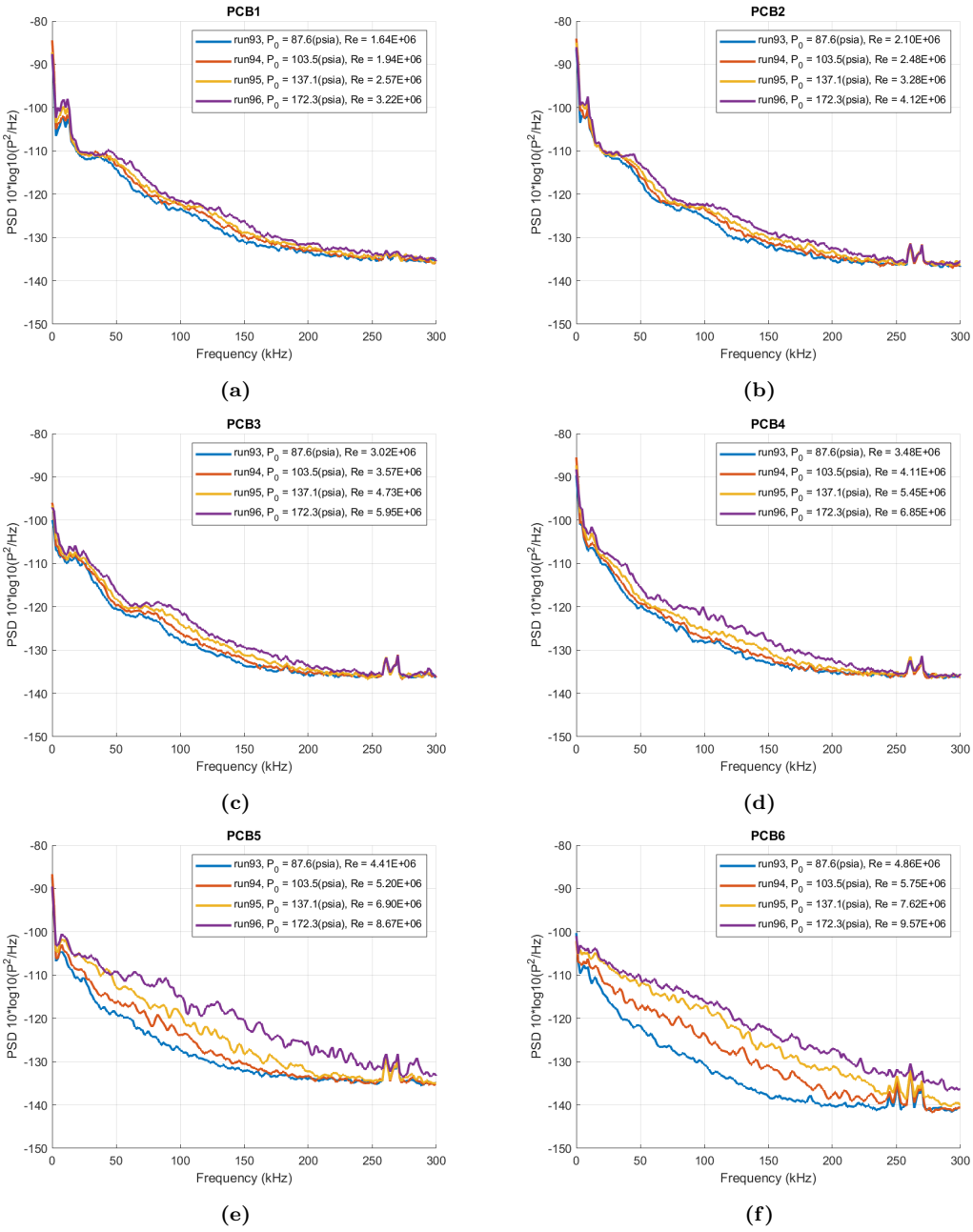


Figure 148. PCB PSD vs driver tube pressure over the spherically blunted tip sampled during second quasi-steady periods (a) PCB 1 (b) PCB 2 (c) PCB 3 (d) PCB 4 (e) PCB 5 (f) PCB 6

havior for the various tips can also be gleaned from the pressure sensor data sets. While surface mounted pressure sensors are an excellent measurement tool for capturing instability frequency and growth at discrete locations, they can also be used

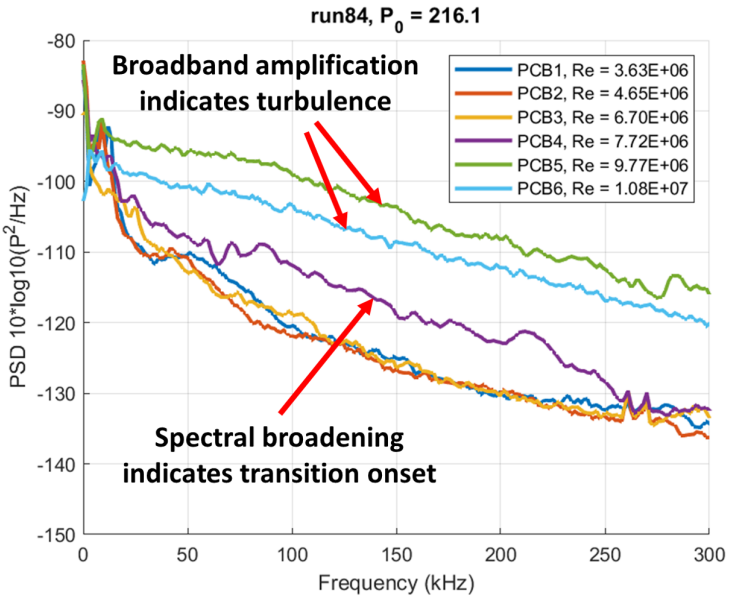


Figure 149. Example of transition onset and turbulence in the frequency domain

to estimate transition onset. This estimation of transition onset is determined as the first pressure sensor where the frequency spectra broadens and amplifies in a broadband manner with increasing downstream distance [84]. Spectral broadening and broadband amplification is a strong sign of turbulent spotting at the sensor location. Figure 149 provides an example of how the onset of transition and progression to turbulence appears in the frequency spectra.

With the definition of transition onset in the frequency domain defined, a study of transition trends was performed. Plotting the transition Reynolds number against the freestream unit Reynolds number for the 14, 28, and 56 degree sharp ogives results in Figure 150. A clear delay in transition Reynolds number is observed as the tip angle is increased (i.e. ogive radius is decreased) for the sharp ogives. This agrees with the trends in instability characteristics observed in Section 4.2.3 where increasing ogive angle showed an initial delay in the appearance of an instability in the boundary layer.

Moving from the sharp ogives to the blunt variants, it is observed that increasing

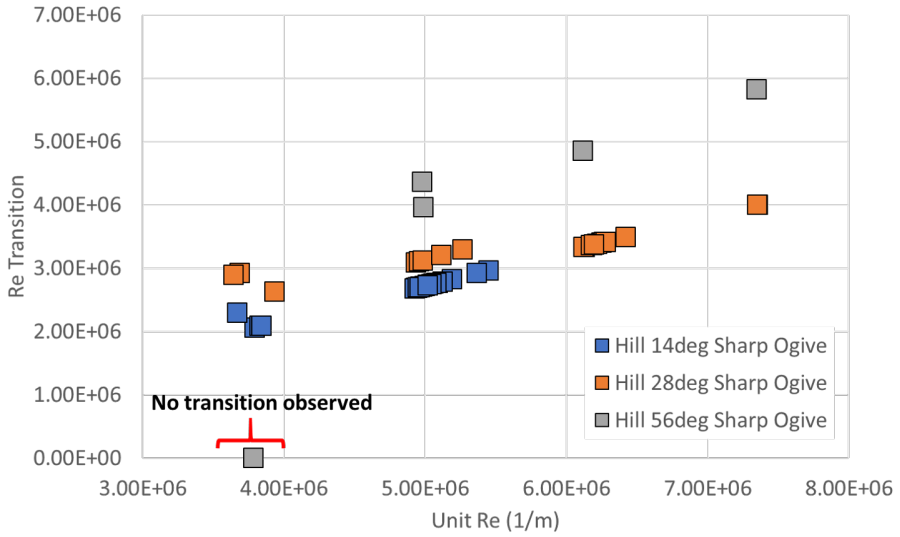


Figure 150. 14, 28, and 56 degree sharp ogives transition Reynolds number vs freestream unit Reynolds number

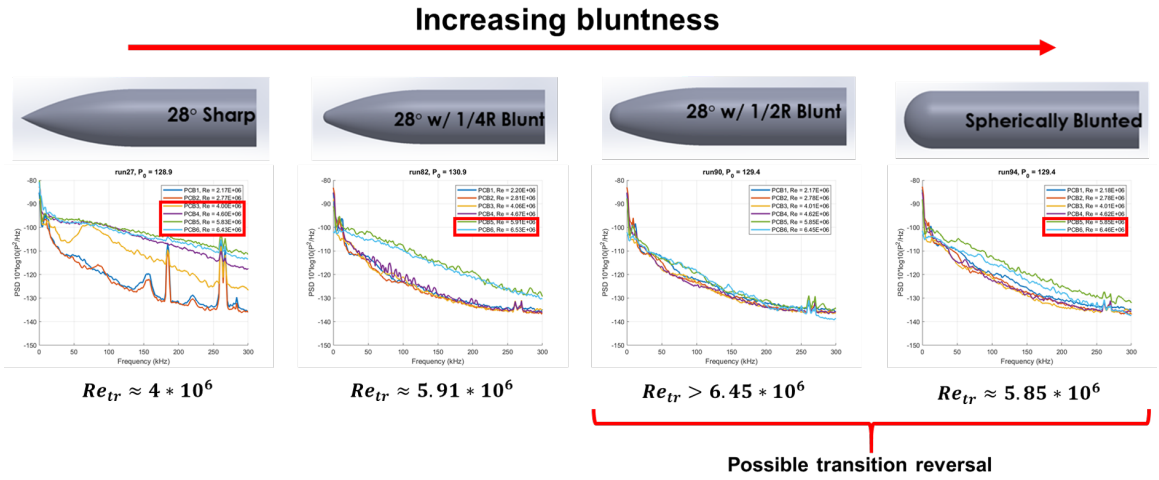
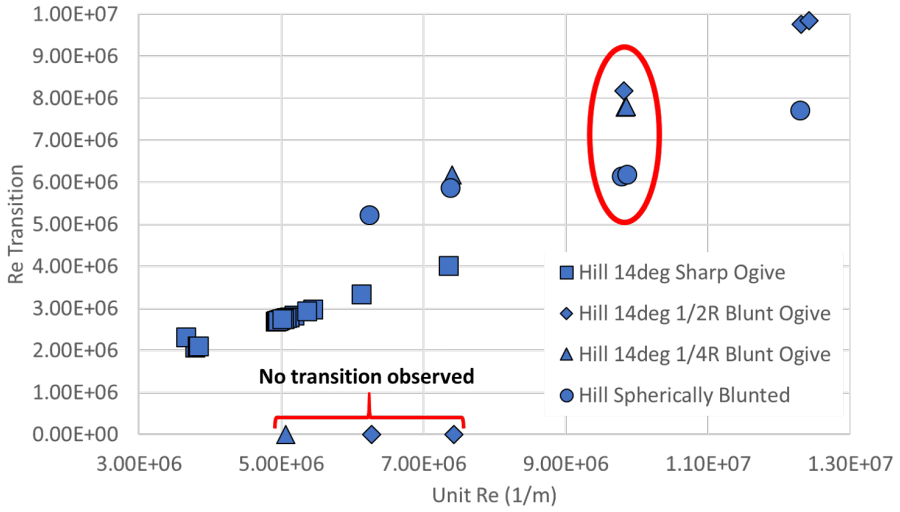


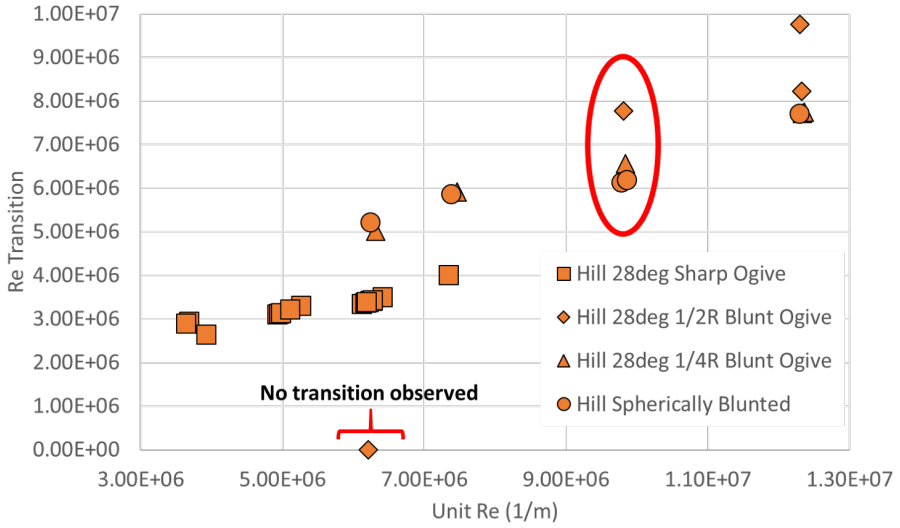
Figure 151. Example of apparent transition reversal observed in the frequency spectra

nose bluntness for a given ogive radius results in an initial delay in transition Reynolds number up to 1/2 radius bluntness. Further increasing the bluntness to the fully spherically blunted tip results in an apparent transition reversal. Figure 151 provides an example for the 28 degree ogive variants where this apparent transition reversal phenomenon occurs. It should be noted that both the 28 and 14 degree blunted ogive

variants show this trend of initial transition delay with increased tip bluntness and eventual reversal when the tip is fully blunted.



(a)



(b)

Figure 152. Transition Reynolds number vs freestream unit Reynolds number for the (a) 14 degree ogive variants (b) 28 degree ogive variants

Further evidence of the transition reversal behavior can be observed by plotting the transition Reynolds number trends for the sharp and blunt tips against the freestream unit Reynolds number as shown in Figure 152. While not every unit Reynolds number has data for every tip, the overall trend of initial transition delay and eventual reversal

is still evident. The circled data points at $\approx 1 * 10^6(1/m)$ are perhaps the clearest examples of this initial delay in transition from 1/4 radius to 1/2 radius bluntness and then a reversal in transition location as the bluntness is further increased to the fully blunted variant. This is perhaps the first instance of the transition reversal phenomenon being captured over this geometry. While transition to turbulence was not the primary focus of this study, the results shown here are extremely promising and open the door for further research to be performed in understanding why this behavior is occurring over this geometry for such drastically different tip geometries when compared to historical blunt cone transition reversal observations.

The entropy layer generated by the ogive curvature appears to be the dominant influence on transition for the blunt tip variants.

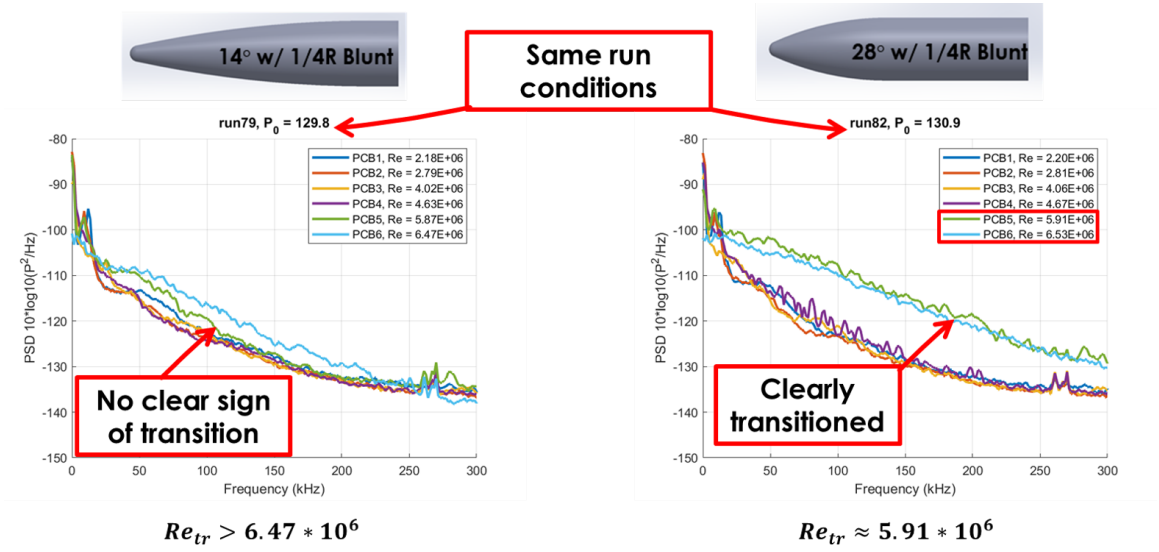


Figure 153. Example of earlier onset of transition over the 28 degree ogive curvature than the 14 degree ogive curvature variant for the same tip bluntness of 1/4 base radius

While the sharp tip ogives appear to show a consistent delay in transition with increased ogive angle (decreased ogive radius) as is shown in Figure 150, the blunt tip variants show a different behavior. As the example in Figure 153 depicts, for

any blunt ogive variant of a given nose bluntness radius, the 28 degree ogive contour always transitions at an earlier transition Reynolds number than the corresponding 14 degree ogive contour variant.

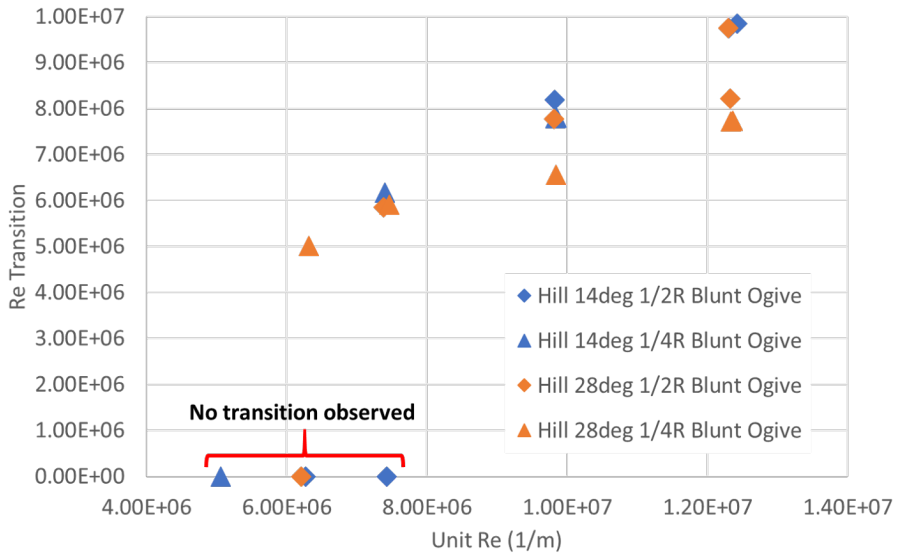


Figure 154. Transition Reynolds numbers of the blunted 14 and 28 degree ogives

The behavior of the blunted 28 degree ogive variants showing lower transition Reynolds numbers is re-emphasized in Figure 154. In this figure, the transition Reynolds numbers for the 14 and 28 degree blunt ogive variants are co-plotted to emphasize the consistent trend that is exemplified in Figure 153. The fact that the sharp tip variants and the blunt tip variants show inherently different transition behaviors as the ogive radius is changed indicates a possible shift in transition mechanisms from the sharp to blunt cases. This indication of a shift in instability and transition mechanisms agrees with the observations of changing instability structures previously discussed in this study.

The observation of the 28 degree ogive blunt tip variants showing earlier onset of transition than the 14 degree ogive blunt tip variants of equivalent tip bluntness points towards a transition mechanism most likely dominated by entropy layer effects

generated by the ogive curvature. It should also be noted that it appears as though these entropy layer effects from the different ogive curvatures dominate transition only for the blunted tips and not for the sharp tips due to the different observations between Figures 150 and 154. This is an unique observation because it suggests that the presence of tip bluntness is necessary for the ogive generated entropy layer effects to become dominant, but the entropy layer effects from the tip bluntness itself do not appear to dominate the transition behavior. It should be noted however that the amount of tip bluntness for a given ogive radius does affect the onset of transition, so there is most likely a complex interaction of entropy layer effects originating from the tip bluntness and those originating from the ogive curvature that are tied together to initiate the onset of transition.

A new curvature Reynolds number parameter appears to characterize the ogive-cylinder transition behavior.

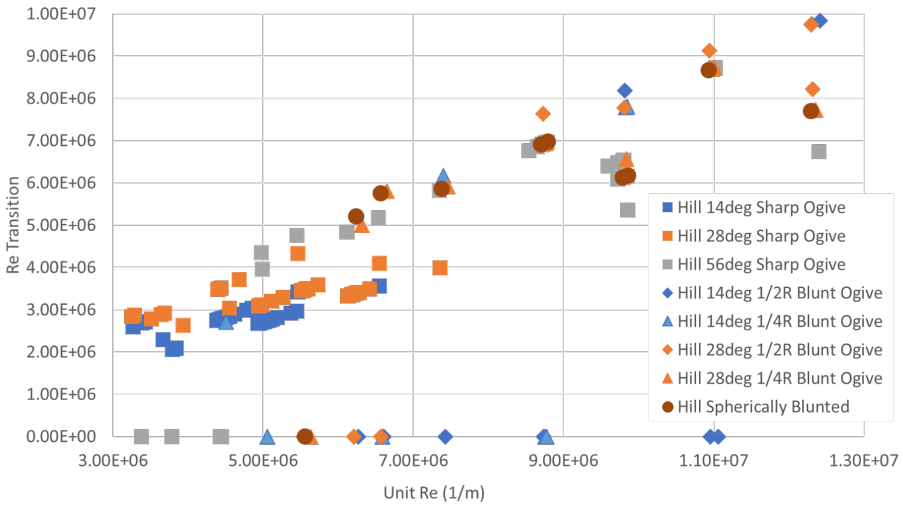


Figure 155. Transition Reynolds numbers for all ogive-cylinder variants tested

With the observations that blunt tip radius and the ogive radius are somehow tied together to influence the onset of transition over the ogive-cylinders, it is necessary

to explore possible non-dimensional parameters that can characterize the transition trends observed in an organized fashion. Taking the data from each run condition over each geometry and plotting the transition Reynolds number against the freestream unit Reynolds number results in Figure 155. It is observed that each model variant shows an overall upward trend in transition Reynolds number as the freestream unit Reynolds number is increased. This behavior is expected and agrees with historical transition trends for other geometries. Despite the overall upward trend in transition Reynolds number, it should be noted that the results show a large range of transition values at any given unit Reynolds number and this spread increases as the freestream unit Reynolds number is increased. This large range of transition values suggests that using a simple length factor such as the base radius or body length to non-dimensionalize the unit Reynolds number would not result in a collapse of the data sets to a single curve and thus there is another parameter which may better capture the transition effects over the ogive-cylinders.

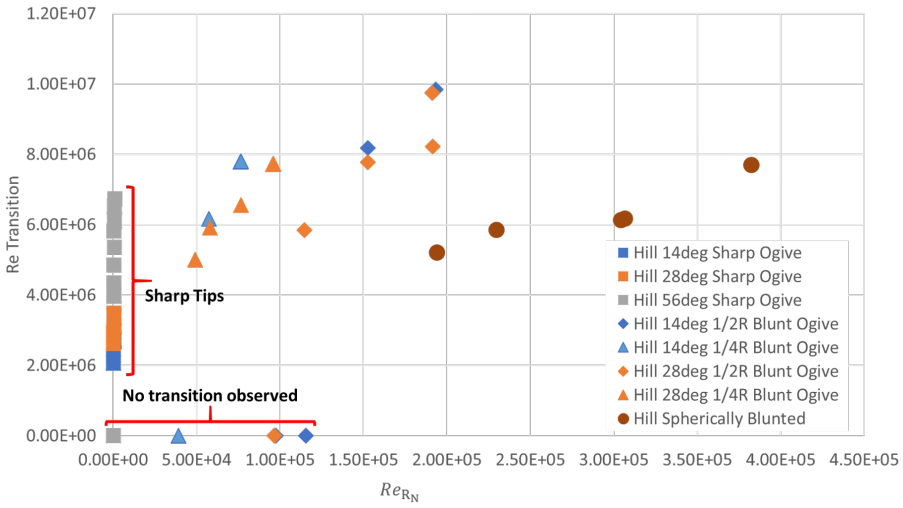


Figure 156. Transition Reynolds numbers versus nose radius Reynolds number for all ogive-cylinder variants tested

Blunt cone transition experiments, such as is shown in Figure 18, often use the blunt nose radius, R_N to non-dimensionalize the Reynolds number, Re_{R_N}. Plotting

the nose radius Reynolds number against transition Reynolds number for the conical geometries provides a clean and continuous curve that reveals the blunt cone transition reversal trend. Performing the same analysis for the ogive-cylinders used in this study results in Figure 156. It is observed that, while there are clear correlations and apparent linear trends for each nose bluntness radius, there is no direct relationship between each tip variant when using just the nose radius Reynolds number as the correlation parameter. It should also be noted that the use of the nose radius Reynolds number is ineffective at capturing any trends from the sharp tips where the tip radius is significantly less than the blunt tip variants.

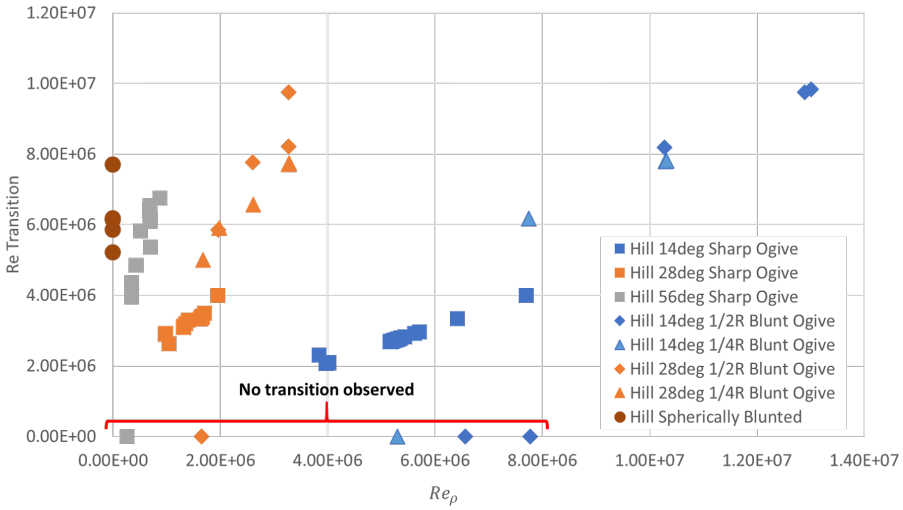


Figure 157. Transition Reynolds numbers versus ogive radius Reynolds number for all ogive-cylinder variants tested

With the recognition that the nose radius Reynolds number is insufficient to fully capture the transition trends for the ogive cylinders, a similar analysis was performed using the ogive radius, ρ, as the non-dimensionalization factor. This results in an ogive radius Reynolds number, Re_ρ, which can be plotted against transition Reynolds number as is shown in Figure 157. Again it is observed that, while there are clear correlations and apparent linear trends for sets of tips with the same ogive radius, there is no direct relationship between tips of different ogive radii. This again implies

that the transition characteristics over the ogive-cylinders are not simply the result of a single factor, such as nose or ogive radius, but are most likely the result of coupled effects.

With this in mind, a non-dimensionalization parameter is still desired that accurately captures the transition characteristics over the ogive-cylinders. If the transition characteristics over ogive-cylinders are being dominated by entropy layer effects, then perhaps a non-dimensionalization parameter tied to the entropy layer formation could provide some insight into the transition behavior.

Since the entropy layer is the result of shock curvature, a new Reynolds number parameter based on the degree of curvature of the shock is derived in an attempt to capture entropy layer effects. As discussed in Section 2.2.1, the shock curvature and contour generated by a hypersonic body closely matches the curvature and contour of the body's surface creating the shock. With this in mind, an estimation of the shock curvature for the ogive-cylinders can be estimated by using the curvature of the tip section.

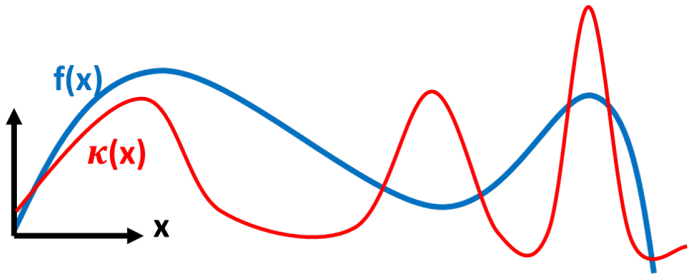


Figure 158. Generic diagram of curvature for a given curve

As is shown in Figure 158, for any given curve defined by a function $f(x)$, the curvature at any position along the length of that curve can be captured by a parameter known as curvature, $\kappa(x)$. Curvature is the magnitude of the rate of change of the unit tangent vector at point on a curve with respect to arc length of the curve, or in other words, is the measure of how quickly a curve changes direction at a given

point. The units of this parameter are technically $1/meter$, but can considered as $curvature/meter$ for practical application. The curvature of a line defined by $f(x)$ is found via equation 16 [85].

$$\kappa(x) = \frac{|f''(x)|}{[1 + (f'(x))^2]^{3/2}] } \tag{16}$$

If a curve has a constant radius along its length, the equation for curvature simplifies down to $\kappa = \frac{1}{R}$ where R is the radius of the curve. With the definition of curvature defined, the curvature of the nose sections for the ogive-cylinders can be found and used as the non-dimensionalization parameter moving forward. The spherically blunted portions of the blunted ogives have a constant spherical radius and the ogive sections of each tip have a constant ogive radius. This means that the blunted tip section and the ogive radius section each have their own distinct curvatures, $1/R_N$ and $1/\rho$ respectively, where R_N is the blunt section radius and ρ is the ogive radius. In order to determine the overall curvature of each tip, the curvatures from both the spherically blunted tip and the ogive radius are accounted for by "weighting" the contribution to tip curvature by the downstream length of each section and then summing the values together to achieve an overall "influence of curvature" for the tip. This summation can be written as $\frac{L_{R_N}}{R_N} + \frac{L_\rho}{\rho}$ where L_{R_N} is the length of the spherically blunted section of the tip and L_ρ is the length of the ogive section of the tip.

With the influence of curvature for the tip calculated, the value is then multiplied by the radius of the cylindrical body to provide units of meters. The body radius is used since it is constant between every tip variant and is the flow-normal direction along which the influence of curvature from the tip is impacting the flow. This dimensionalized influence of curvature is then multiplied by the freestream unit Reynolds number to result in a new, non-dimensional "curvature Reynolds number," Re_κ.

$$Re_\kappa = (unit\ Re) * (\frac{L_{R_N}}{R_N} + \frac{L_\rho}{\rho}) * R \tag{17}$$

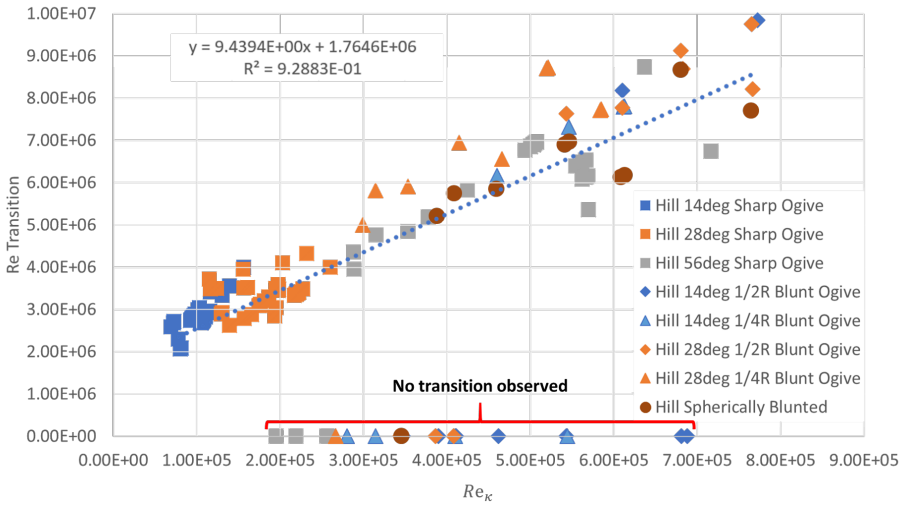


Figure 159. Curvature Reynolds number versus transition Reynolds number

Plotting the transition Reynolds number for each tip's curvature Reynolds number results in Figure 159. It appears that the new curvature Reynolds number effectively characterizes the general transition trends for each tip, regardless of tip bluntness or ogive radius. This suggests that compensating for both the blunt tip and ogive radius contributions in the Reynolds number parameter allows for the effects of the entropy layer on transition to more accurately be characterized. Applying a linear curve fit to this collapsed data set provides the approximation of $Re_{tr} \approx 9.44 * Re_\kappa + 1.76 * 10^6$. It should be noted that the derivation and use of Re_κ to collapse the transition results for this geometry is a preliminary attempt at better characterizing and capturing the physics dominating transition for this geometry, but more work is still to be completed to check this parameter against other similar geometries and in other testing facilities. Regardless of the work still to be completed, this parameter suggests that compensating for the curvature of the tip geometry could provide insights into predicting hypersonic blunt body transition location.

V. Conclusion

The problems surrounding hypersonic boundary layer transition have challenged the research community since the advent of hypersonic flight. Unlike the lower Mach number flow regimes, hypersonic flows have many complex characteristics that interact in a variety of ways to make studying the intricacies of the fluid flow at these velocities some of the most difficult undertakings in the fluid dynamics research. Many researchers have devoted their careers to the single goal of furthering humanity's understanding of hypersonic boundary layer transition. Despite the hypersonic instability research community dating back to the 1940s, there are still many unanswered questions and unexplained phenomenon surrounding the field.

One such unexplained behavior of hypersonic boundary layer transition and instabilities is the blunt cone transition reversal phenomenon. Many experiments have shown that nose bluntness greatly affects the driving mechanisms behind transition over hypersonic velocities, but the behavior of transition being initially delayed and then rapidly amplified as the nose bluntness is increased has left the community grasping for answers. A leading hypothesis to why this phenomenon occurs is that the behavior is closely tied to the entropy layer of the blunted geometries. In an attempt to further the community's understanding of nose geometry effects on downstream instabilities and transition with an emphases on possibly entropy layer effects, a one meter long ogive-cylinder model was design, built, and tested in the Air Force Research Lab (AFRL) Mach 6 Ludwieg tube.

Inspired by research on a cone-ogive-cylinder at Purdue in 2014, this study sought to use cutting-edge measurement techniques and a uniquely versatile geometry in a state-of-the art testing facility to expand the community's understanding of nose geometry effects on downstream ogive-cylinder boundary layer instabilities. Focused laser differential interferometry (FLDI), high speed Schlieren imaging, and two types

of high-frequency surface mounted pressure sensors were all used to measure passing instabilities. Eight different nose geometries were designed and tested in this study including three constant curvature ogives with tip half-angles of 14, 28, and 56 degrees, four blunted ogives designed from the 14 and 28 degree ogives with spherical bluntness radii of 1/4 and 1/2 the base radius of the cylinder, and a final fully spherically blunted tip. A variety of post-processing techniques were used to extract the structures and frequency content of the passing instabilities including Welch power spectral density estimates, spatial to temporal frequency analysis, image processing and enhancement, and bicoherence analysis. As a result of this effort, novel insights into the nature of instabilities over ogive-cylinders at Mach 6 were made.

5.1 Key Findings

The conclusion of this study leaves the reader with a few key findings.

5.1.1 The sharp ogive tips exhibit strong modal instabilities with nonlinear effects and breakdown.

The 14 and 28 degree sharp ogives produce boundary layers which exhibited strong modal instability behaviors. These modal instabilities were observed in the Schlieren, FLDI, and pressure sensor data and manifested as "rope-like" structures with frequencies typically around 60kHz. This frequency band exhibited classical modal instability behaviors. With increases in freestream Reynolds number, the modal instability showed an increase in frequency due to a thinner boundary layer. Also, for a given unit Reynolds number, an increase in downstream distance resulted in a drop in the instability's frequency due to the thicker boundary layer. This "tuning" effect of the boundary layer and the "rope-like" structures of the Schlieren images of the instability which have wavelengths approximately twice the boundary layer

thickness lead this author to conclude that a second Mack mode instability is driving this frequency band's presence.

This instability frequency band also experienced large amounts of nonlinear effects that manifested as harmonics in the spectra. The PCB pressure sensors show the 60kHz band creating strong first, second, and sometimes even third and fourth harmonics in the power spectral density plots for various run conditions. These harmonic nonlinear interactions appear to dominate transition for the 14 and 28 degree ogives.

5.1.2 A possible entropy layer instability is observed.

In addition to the clearly modal instability measured over the two shallow, sharp ogive tips, another lower frequency band was consistently observed for nearly every geometry in this study. This low frequency band was typically around 10-20kHz and saw little to no shift in frequency with increase in freestream unit Reynolds number or downstream progression. Due to these characteristics, it appears that this instability band is likely dominated by a non-modal instability not tied to the boundary layer. These factors lead this author to determine that this lower frequency band is likely an entropy layer instability.

From the Schlieren images, it was determined that the low frequency entropy layer instability band manifests itself with a unique structure. For geometries where the low frequency band was found within the boundary layer, an elongated, flat structure bound within the boundary layer with wavelengths approximately five times the boundary layer thickness were observed. This structure, while found within the boundary layer, is unlike any traditional modal instability structure this author has previously observed. The unique feature of this instability frequency band however is that it was not only observed within the boundary layer, but as the ogive angle

is increased to the 56 degree sharp ogive or if spherical bluntness is added to the tip, the band is clearly observed separate from the boundary layer between 3-5 times the boundary layer height. At this height, the 10-20kHz instability appears in the Schlieren as long, slanted waves that cross the window.

5.1.3 The blunted ogive tips exhibit non-modal transition with non-linear effects.

While the sharp ogives exhibited strong modal instability behaviors, when bluntness was added to the geometries, a significant shift in the primary instability mechanism was observed. Each blunted tip showed a significant delay in transition onset with no consistent or clear peak frequencies resolved in the spectra. As the freestream unit Reynolds number was increased to the point of transition onset, the power spectra showed broadband spectral broadening indicating non-modal transition onset. One of the blunted ogives however, did exhibit a different behavior. The 28 degree ogive contour with 1/4 base radius bluntness showed a strongly nonlinear breakdown before full turbulence was achieved. This behavior was only seen on this geometry, but it is possible that the nonlinear region over the body of the model for the geometries was very short and was simply missed by the sensors. Regardless, this behavior of nonlinear interactions in the presence of non-modal boundary layer transition behavior is unique and leaves more room for investigation. It is likely that the entropy layer instability observed in this study could be a driver for this nonlinear behavior.

5.1.4 An apparent transition reversal is observed over the blunted ogives.

Analysis of transition trends were gleaned from the pressure sensor results. One of the primary findings from this analysis was the presence of an apparent transition

reversal for the blunted ogives as the tip bluntness was increased from the 1/2 base radius variant to the fully blunted tip. This is perhaps the first time this behavior has been observed over this geometry and has significant implications for further works to be accomplished investigating this behavior in more depth.

5.1.5 A new curvature Reynolds number allows for characterization of the ogive-cylinder transition trends.

With the observation of unique transition trends for the various ogive tips, a new non-dimensional parameter was derived to characterize the transition trends. The traditional nose radius Reynolds number that is historically used to plot against transition Reynolds number for blunt cone transition reversal was shown to ineffectively capture all of the transition effects for the ogives used. The new non-dimensional parameter, referred to as the curvature Reynolds number, uses scaled degrees of curvature for the nose radius and ogive radius sections of each tip to determine an overall curvature factor. This new Reynolds number aims to capture the effects of the entropy layer on transition and was shown to effectively characterize the transition trend.

5.2 Recommendations and Future Work

With the conclusion of this study, a few recommendations and suggestions for future work are provided.

5.2.1 Expanded FLDI capabilities and characterization.

One of the original goals of this study was to accomplish non-intrusive density fluctuation measurements over the model using FLDI. While this was technically achieved, the large amount of time spent getting the system in working order and understanding how it functioned resulted in very few measurements being completed

at relevant heights above the boundary layer. It was also determined that the focal point separation distance for the FLDI setup was too small relative to the size and orientation of the waves passing over the ogive-cylinder. Future work should look to better characterize the effects of the FLDI focal point separation and orientation on the range of instability wavelengths it can effectively measure. Also, more sweeps at a greater range of heights above the model should be conducted in future studies to cross-verify the Schlieren observations. It is also the suggestion of this author to utilize multi-node FLDI in future work with this geometry to provide more off-body measurements for each run.

5.2.2 Angle of attack improvements.

For this study, great effort was put into achieving zero angle of attack and sideslip for each run. Despite this effort, there were complications with ensuring that the model was perfectly level each run due to a less than favorable angle adjustment method that required coarse adjustments and would sometimes overshoot the desired angle shift. For future works, an improvement on the angle of attack refinement and measurement methods for this model would be useful in ensuring less error is possibly introduced.

5.2.3 Transition characterization studies.

While not the original intent of this study, the results from the pressure sensors allowed for a preliminary transition study to be performed on the ogive-cylinders. The results from the transition analysis showed possible transition reversal effects and transition affected by entropy layer effects. Further work diving into the transition characteristics would be very useful in confirming the hypotheses and observations made in this study regarding the transition trends.

5.2.4 Continue to test the geometry.

The final recommendation is a call for others to continue this research and expand on the observations made. The limited timeline of this study resulted in many side studies and observations being cut short. Further investigations into the nature of the blunted ogive instabilities and the exact change in dominant mechanisms they introduce would be a fantastic starting point for future work. Use of new diagnostics and different facilities are recommended to ensure that the observations made in this facility are not unique and are replicable by other means.

Appendix A. Run Conditions

Table 11. Run conditions part 1

Run #	Desired Driver Pressure (psia)	Actual Driver Pressure (psia)	Vacuum Pressure (psia)	1st Period Stagnation Pressure (psia)	2nd Period Stagnation Pressure (psia)	Driver Temperature (Kelvin)	1st Period Stagnation Temperature (Kelvin)	2nd Period Stagnation Temperature (Kelvin)	1st Period Unit Reynolds Number (per meter)	2nd Period Unit Reynolds Number (per meter)	1st Period Unit Reynolds Number (per foot)	2nd Period Unit Reynolds Number (per foot)	Model	Measurements	FLDI height (mm)	FLDI position (m)
1-9	Initial runs used to familiarize with tunnel operations, no data gathered															
10	250	239.75	0.009	213.66	171.39	505.00	488.65	458.82	1.22E+07	1.09E+07	3.71E+06	3.31E+06	Oddo 7deg Cone	FLDI	0	0.2
11	250	240.68	0.009	214.40	171.90	505.00	488.59	458.70	1.22E+07	1.09E+07	3.73E+06	3.32E+06	Oddo 7deg Cone	FLDI	0	0.2
12	200	190.95	0.010	170.06	136.30	505.00	488.56	458.63	9.70E+06	8.64E+06	2.96E+06	2.63E+06	Oddo 7deg Cone	FLDI	0	0.2
13	100	99.98	0.010	89.09	71.35	505.00	488.64	458.60	5.08E+06	4.52E+06	1.55E+06	1.38E+06	Oddo 7deg Cone	FLDI	0	0.2
14	300	290.79	0.010	258.82	206.98	505.00	488.47	458.25	1.48E+07	1.31E+07	4.50E+06	4.00E+06	Oddo 7deg Cone	FLDI	0	0.2
15	200	191.20	0.009	170.30	136.51	505.00	488.57	458.65	9.72E+06	8.65E+06	2.96E+06	2.64E+06	Oddo 7deg Cone	FLDI	0	0.2
16	150	144.64	0.012	128.99	103.42	505.00	488.75	458.85	7.35E+06	6.55E+06	2.24E+06	2.00E+06	Oddo 7deg Cone	FLDI	0	0.2
17	100	96.34	0.011	85.84	68.71	505.00	488.62	458.51	4.90E+06	4.36E+06	1.49E+06	1.33E+06	Oddo 7deg Cone	FLDI	0	0.2
18	100	97.90	0.013	87.43	70.30	505.00	488.94	459.41	4.98E+06	4.44E+06	1.52E+06	1.35E+06	Hill 14deg Sharp Ogive	Schlieren, PCB, Kulite		
19	75	74.51	0.010	66.59	53.69	505.00	489.05	459.88	3.79E+06	3.39E+06	1.16E+06	1.03E+06	Hill 14deg Sharp Ogive	Schlieren, PCB, Kulite		
20	100	98.11	0.010	87.54	70.32	505.00	488.83	459.17	4.99E+06	4.45E+06	1.52E+06	1.36E+06	Hill 56deg Sharp Ogive	Schlieren, PCB, Kulite		
21	75	74.37	0.009	66.42	53.47	505.00	488.95	459.56	3.78E+06	3.38E+06	1.15E+06	1.03E+06	Hill 56deg Sharp Ogive	Schlieren, PCB, Kulite		
22	100	97.08	0.013	86.57	69.43	505.00	488.73	458.87	4.94E+06	4.40E+06	1.50E+06	1.34E+06	Hill 28deg Sharp Ogive	Schlieren, PCB, Kulite		
23	75	72.49	0.013	64.75	52.06	505.00	488.97	459.41	3.69E+06	3.29E+06	1.12E+06	1.00E+06	Hill 28deg Sharp Ogive	Schlieren, PCB, Kulite		
24	100	103.52	0.009	92.38	73.96	505.00	488.83	458.75	5.27E+06	4.69E+06	1.60E+06	1.43E+06	Hill 28deg Sharp Ogive	Schlieren, PCB, Kulite		
25	75	71.65	0.014	63.95	51.29	505.00	488.86	459.01	3.64E+06	3.25E+06	1.11E+06	9.90E+05	Hill 28deg Sharp Ogive	Schlieren, PCB, Kulite		
26	125	120.51	0.012	107.35	86.29	505.00	488.58	459.04	6.12E+06	5.46E+06	1.87E+06	1.66E+06	Hill 28deg Sharp Ogive	Schlieren, PCB, Kulite		
27	150	144.61	0.012	128.95	103.36	505.00	488.73	458.79	7.35E+06	6.55E+06	2.24E+06	2.00E+06	Hill 28deg Sharp Ogive	Schlieren, PCB, Kulite		
28	100	97.26	0.009	86.68	69.45	505.00	488.65	458.67	4.94E+06	4.40E+06	1.51E+06	1.34E+06	Hill 14deg Sharp Ogive	Schlieren, PCB, Kulite		
29	100	97.11	0.009	86.50	69.22	505.00	488.58	458.45	4.93E+06	4.39E+06	1.50E+06	1.34E+06	Hill 14deg Sharp Ogive	Schlieren, PCB, Kulite		
30	75	72.17	0.013	64.40	51.63	505.00	488.81	458.91	3.67E+06	3.27E+06	1.12E+06	9.96E+05	Hill 14deg Sharp Ogive	Schlieren, PCB, Kulite		
31	125	120.66	0.009	107.45	86.31	505.00	488.55	458.90	6.13E+06	5.47E+06	1.87E+06	1.67E+06	Hill 14deg Sharp Ogive	Schlieren, PCB, Kulite		
32	150	144.68	0.009	128.97	103.29	505.00	488.69	458.65	7.36E+06	6.55E+06	2.24E+06	2.00E+06	Hill 14deg Sharp Ogive	Schlieren, PCB, Kulite		
33	100	98.00	0.014	87.27	69.76	505.00	488.53	458.25	4.98E+06	4.43E+06	1.52E+06	1.35E+06	Hill 56deg Sharp Ogive	Schlieren, PCB, Kulite		
34	125	120.39	0.011	107.18	85.95	505.00	488.50	458.65	6.12E+06	5.45E+06	1.86E+06	1.66E+06	Hill 56deg Sharp Ogive	Schlieren, PCB, Kulite		
35	150	144.54	0.011	128.82	103.11	505.00	488.66	458.55	7.35E+06	6.54E+06	2.24E+06	1.99E+06	Hill 56deg Sharp Ogive	Schlieren, PCB, Kulite		
36	200	192.68	0.010	171.49	137.24	505.00	488.47	458.34	9.79E+06	8.71E+06	2.98E+06	2.65E+06	Hill 56deg Sharp Ogive	Schlieren, PCB, Kulite		
37	250	244.26	0.010	217.20	173.45	505.00	488.34	457.95	1.24E+07	1.10E+07	3.78E+06	3.36E+06	Hill 56deg Sharp Ogive	Schlieren, PCB, Kulite		
38	100	101.99	0.008	91.08	73.18	505.00	488.94	459.30	5.19E+06	4.63E+06	1.58E+06	1.41E+06	Hill 14deg Sharp Ogive	FLDI, PCB, Kulite	0	0.625856
39	75	75.34	0.009	67.22	54.14	505.00	488.82	459.49	3.83E+06	3.42E+06	1.17E+06	1.04E+06	Hill 14deg Sharp Ogive	FLDI, PCB, Kulite	0	0.625856
40	100	99.47	0.010	88.72	71.16	505.00	488.77	458.92	5.06E+06	4.51E+06	1.54E+06	1.37E+06	Hill 14deg Sharp Ogive	FLDI, PCB, Kulite	4	0.625856

Table 12. Run conditions part 2

Run #	Desired Driver Pressure (psia)	Actual Driver Pressure (psia)	Vacuum Pressure (psia)	1st Period Stagnation Pressure (psia)	2nd Period Stagnation Pressure (psia)	Driver Temperature (Kelvin)	1st Period Stagnation Temperature (Kelvin)	2nd Period Stagnation Temperature (Kelvin)	1st Period Unit Reynolds Number (per meter)	2nd Period Unit Reynolds Number (per meter)	1st Period Unit Reynolds Number (per foot)	2nd Period Unit Reynolds Number (per foot)	Model	Measurements	FLDI height (mm)	FLDI position (m)
41	75	75.57	0.014	67.39	54.24	505.00	488.74	459.34	3.84E+06	3.43E+06	1.17E+06	1.05E+06	Hill 14deg Sharp Ogive	FLDI, PCB, Kulite	4	0.625856
42	100	100.13	0.010	89.28	71.63	505.00	488.72	458.90	5.09E+06	4.54E+06	1.55E+06	1.38E+06	Hill 14deg Sharp Ogive	FLDI, PCB, Kulite	6	0.625856
43	100	107.17	0.010	95.64	76.61	505.00	488.84	458.81	5.45E+06	4.85E+06	1.66E+06	1.48E+06	Hill 14deg Sharp Ogive	FLDI, PCB, Kulite	8	0.625856
44	100	100.80	0.010	89.86	71.96	505.00	488.69	458.64	5.12E+06	4.56E+06	1.56E+06	1.39E+06	Hill 14deg Sharp Ogive	FLDI, PCB, Kulite	12	0.625856
45	100	105.54	0.010	94.19	75.48	505.00	488.84	458.87	5.37E+06	4.78E+06	1.64E+06	1.46E+06	Hill 14deg Sharp Ogive	FLDI, PCB, Kulite	4	0.625856
46	125	126.24	0.008	112.63	90.68	505.00	488.82	459.45	6.42E+06	5.73E+06	1.96E+06	1.75E+06	Hill 28deg Sharp Ogive	FLDI, PCB, Kulite	0	0.625856
47	125	122.85	0.011	109.61	88.20	505.00	488.81	459.39	6.25E+06	5.58E+06	1.90E+06	1.70E+06	Hill 28deg Sharp Ogive	FLDI, PCB, Kulite	4	0.625856
48	125	123.47	0.009	110.12	88.58	505.00	488.75	459.28	6.28E+06	5.60E+06	1.91E+06	1.71E+06	Hill 28deg Sharp Ogive	FLDI, PCB, Kulite	6	0.625856
49	100	97.57	0.010	86.97	69.74	505.00	488.68	458.80	4.96E+06	4.42E+06	1.51E+06	1.35E+06	Hill 28deg Sharp Ogive	FLDI, PCB, Kulite	6	0.625856
50	75	77.39	0.010	68.96	55.48	505.00	488.63	459.19	3.93E+06	3.51E+06	1.20E+06	1.07E+06	Hill 28deg Sharp Ogive	FLDI, PCB, Kulite	4	0.625856
51	100	98.07	0.013	87.42	70.04	505.00	488.68	458.69	4.99E+06	4.44E+06	1.52E+06	1.35E+06	Hill 28deg Sharp Ogive	FLDI, PCB, Kulite	4	0.625856
52	100	100.63	0.011	89.76	71.87	505.00	488.77	458.70	5.12E+06	4.55E+06	1.56E+06	1.39E+06	Hill 28deg Sharp Ogive	FLDI, PCB, Kulite	4	0.625856
53	200	188.90	0.001	168.17	134.58	505.00	488.50	458.37	9.60E+06	8.54E+06	2.92E+06	2.60E+06	Hill 56deg Sharp Ogive	FLDI, PCB, Kulite	4	0.625856
54	200	191.48	0.010	170.33	136.24	505.00	488.39	458.21	9.72E+06	8.65E+06	2.96E+06	2.64E+06	Hill 56deg Sharp Ogive	FLDI, PCB, Kulite	4	0.625856
55	200	192.65	0.009	171.53	137.33	505.00	488.53	458.45	9.79E+06	8.71E+06	2.98E+06	2.65E+06	Hill 56deg Sharp Ogive	FLDI, PCB, Kulite	4	0.625856
56	200	191.49	0.010	170.41	136.34	505.00	488.44	458.29	9.73E+06	8.65E+06	2.96E+06	2.64E+06	Hill 56deg Sharp Ogive	FLDI, PCB, Kulite	6	0.625856
57	200	193.08	0.012	171.81	137.51	505.00	488.44	458.33	9.81E+06	8.73E+06	2.99E+06	2.66E+06	Hill 56deg Sharp Ogive	FLDI, PCB, Kulite	8	0.625856
58	200	192.81	0.012	171.56	137.23	505.00	488.43	458.24	9.79E+06	8.71E+06	2.98E+06	2.66E+06	Hill 56deg Sharp Ogive	FLDI, PCB, Kulite	12	0.625856
59	100	98.85	0.012	87.96	70.22	505.00	488.45	458.00	5.02E+06	4.46E+06	1.53E+06	1.36E+06	Hill 14deg Sharp Ogive	FLDI, PCB, Kulite	4	0.625856
60	100	97.78	0.013	87.00	69.43	505.00	488.41	457.92	4.97E+06	4.41E+06	1.51E+06	1.34E+06	Hill 14deg Sharp Ogive	FLDI, PCB, Kulite	6	0.625856
61	100	97.06	0.015	86.35	68.89	505.00	488.40	457.89	4.93E+06	4.38E+06	1.50E+06	1.33E+06	Hill 14deg Sharp Ogive	FLDI, PCB, Kulite	2	0.625856
62	100	97.43	0.014	86.67	69.16	505.00	488.40	457.90	4.95E+06	4.40E+06	1.51E+06	1.34E+06	Hill 14deg Sharp Ogive	FLDI, PCB, Kulite	8	0.625856
63	100	99.87	0.008	89.18	71.69	505.00	488.93	459.37	5.08E+06	4.53E+06	1.55E+06	1.38E+06	Hill 14deg Sharp Ogive	FLDI, PCB, Kulite	0	0.54356
64	100	99.17	0.009	88.52	71.12	505.00	488.88	459.24	5.05E+06	4.50E+06	1.54E+06	1.37E+06	Hill 14deg Sharp Ogive	FLDI, PCB, Kulite	4	0.54356
65	100	98.25	0.009	87.68	70.42	505.00	488.85	459.17	5.00E+06	4.46E+06	1.52E+06	1.36E+06	Hill 14deg Sharp Ogive	FLDI, PCB, Kulite	6	0.54356
66	100	97.59	0.011	87.08	69.89	505.00	488.82	459.06	4.96E+06	4.42E+06	1.51E+06	1.35E+06	Hill 14deg Sharp Ogive	FLDI, PCB, Kulite	8	0.54356
67	100	98.69	0.011	88.03	70.63	505.00	488.77	458.95	5.02E+06	4.47E+06	1.53E+06	1.36E+06	Hill 14deg Sharp Ogive	FLDI, PCB, Kulite	12	0.54356
68	125	121.66	0.011	108.43	87.11	505.00	488.66	459.03	6.18E+06	5.51E+06	1.88E+06	1.68E+06	Hill 28deg Sharp Ogive	FLDI, PCB, Kulite	12	0.54356
69	125	123.28	0.010	109.91	88.37	505.00	488.71	459.18	6.27E+06	5.59E+06	1.91E+06	1.70E+06	Hill 28deg Sharp Ogive	FLDI, PCB, Kulite	8	0.54356
70	125	121.48	0.012	108.27	87.02	505.00	488.65	459.08	6.18E+06	5.51E+06	1.88E+06	1.68E+06	Hill 28deg Sharp Ogive	FLDI, PCB, Kulite	6	0.54356
71	125	121.91	0.011	108.63	87.27	505.00	488.63	459.00	6.20E+06	5.52E+06	1.89E+06	1.68E+06	Hill 28deg Sharp Ogive	FLDI, PCB, Kulite	4	0.54356
72	125	122.38	0.010	109.03	87.58	505.00	488.61	458.96	6.22E+06	5.55E+06	1.90E+06	1.69E+06	Hill 28deg Sharp Ogive	FLDI, PCB, Kulite	4	0.54356

Table 13. Run conditions part 3

Run #	Desired Driver Pressure (psia)	Actual Driver Pressure (psia)	Vacuum Pressure (psia)	1st Period Stagnation Pressure (psia)	2nd Period Stagnation Pressure (psia)	Driver Temperature (Kelvin)	1st Period Stagnation Temperature (Kelvin)	2nd Period Stagnation Temperature (Kelvin)	1st Period Unit Reynolds Number (per meter)	2nd Period Unit Reynolds Number (per meter)	1st Period Unit Reynolds Number (per foot)	2nd Period Unit Reynolds Number (per foot)	Model	Measurements	FLDI height (mm)	FLDI position (m)
73	125	123.56	0.011	110.06	88.30	505.00	488.58	458.78	6.28E+06	5.59E+06	1.91E+06	1.71E+06	Hill 28deg Sharp Ogive	FLDI, PCB, Kulite	2	0.54356
74	125	121.96	0.012	108.60	87.12	505.00	488.53	458.72	6.20E+06	5.52E+06	1.89E+06	1.68E+06	Hill 28deg Sharp Ogive	FLDI, PCB, Kulite	0	0.54356
75	200	193.03	0.008	172.10	138.23	505.00	488.71	459.05	9.81E+06	8.75E+06	2.99E+06	2.67E+06	Hill 56deg Sharp Ogive	FLDI, PCB, Kulite	0	0.54356
76	200	193.94	0.010	172.81	138.74	505.00	488.63	458.92	9.86E+06	8.79E+06	3.00E+06	2.68E+06	Hill 56deg Sharp Ogive	FLDI, PCB, Kulite	4	0.54356
77	200	193.75	0.010	172.64	138.48	505.00	488.63	458.79	9.85E+06	8.77E+06	3.00E+06	2.67E+06	Hill 56deg Sharp Ogive	FLDI, PCB, Kulite	6	0.54356
78	100	99.54	0.012	88.71	71.05	505.00	488.65	458.61	5.06E+06	4.50E+06	1.54E+06	1.37E+06	Hill 14deg 1/4R Blunt Ogive	PCB, Kulite		
79	150	145.60	0.013	129.77	103.92	505.00	488.66	458.61	7.40E+06	6.59E+06	2.26E+06	2.01E+06	Hill 14deg 1/4R Blunt Ogive	PCB, Kulite		
80	200	193.52	0.013	172.32	138.05	505.00	488.53	458.54	9.83E+06	8.75E+06	3.00E+06	2.67E+06	Hill 14deg 1/4R Blunt Ogive	PCB, Kulite		
81	125	124.22	0.009	110.74	89.01	505.00	488.70	459.13	6.32E+06	5.63E+06	1.92E+06	1.72E+06	Hill 28deg 1/4R Blunt Ogive	FLDI, PCB, Kulite	4	0.54356
82	150	146.72	0.011	130.87	104.97	505.00	488.77	458.92	7.46E+06	6.65E+06	2.27E+06	2.03E+06	Hill 28deg 1/4R Blunt Ogive	FLDI, PCB, Kulite	4	0.54356
83	200	193.61	0.012	172.42	138.20	505.00	488.55	458.63	9.84E+06	8.76E+06	3.00E+06	2.67E+06	Hill 28deg 1/4R Blunt Ogive	FLDI, PCB, Kulite	4	0.54356
84	250	242.70	0.013	216.09	173.09	505.00	488.52	458.51	1.23E+07	1.10E+07	3.76E+06	3.35E+06	Hill 28deg 1/4R Blunt Ogive	FLDI, PCB, Kulite	4	0.54356
85	125	123.30	0.012	109.86	88.24	505.00	488.62	458.96	6.27E+06	5.59E+06	1.91E+06	1.70E+06	Hill 14deg 1/2R Blunt Ogive	FLDI, PCB, Kulite	4	0.54356
86	150	146.06	0.012	130.21	104.30	505.00	488.70	458.68	7.43E+06	6.61E+06	2.26E+06	2.01E+06	Hill 14deg 1/2R Blunt Ogive	FLDI, PCB, Kulite	4	0.54356
87	200	193.24	0.012	172.03	137.70	505.00	488.50	458.40	9.82E+06	8.74E+06	2.99E+06	2.66E+06	Hill 14deg 1/2R Blunt Ogive	FLDI, PCB, Kulite	4	0.54356
88	250	242.31	0.012	215.65	172.65	505.00	488.46	458.39	1.23E+07	1.10E+07	3.75E+06	3.34E+06	Hill 14deg 1/2R Blunt Ogive	FLDI, PCB, Kulite	4	0.54356
89	125	122.25	0.013	108.85	87.29	505.00	488.52	458.66	6.21E+06	5.53E+06	1.89E+06	1.69E+06	Hill 28deg 1/2R Blunt Ogive	FLDI, PCB, Kulite	4	0.54356
90	150	145.17	0.012	129.37	103.55	505.00	488.65	458.54	7.38E+06	6.57E+06	2.25E+06	2.00E+06	Hill 28deg 1/2R Blunt Ogive	FLDI, PCB, Kulite	4	0.54356
91	200	193.14	0.012	171.87	137.54	505.00	488.44	458.31	9.81E+06	8.73E+06	2.99E+06	2.66E+06	Hill 28deg 1/2R Blunt Ogive	FLDI, PCB, Kulite	4	0.54356
92	250	242.22	0.013	215.51	172.44	505.00	488.42	458.28	1.23E+07	1.09E+07	3.75E+06	3.34E+06	Hill 28deg 1/2R Blunt Ogive	FLDI, PCB, Kulite	4	0.54356
93	125	122.92	0.012	109.40	87.65	505.00	488.45	458.48	6.24E+06	5.56E+06	1.90E+06	1.69E+06	Hill Spherically Blunted	FLDI, PCB, Kulite	4	0.54356
94	150	145.30	0.014	129.44	103.51	505.00	488.60	458.36	7.38E+06	6.57E+06	2.25E+06	2.00E+06	Hill Spherically Blunted	FLDI, PCB, Kulite	4	0.54356
95	200	192.76	0.012	171.50	137.13	505.00	488.42	458.19	9.79E+06	8.71E+06	2.98E+06	2.65E+06	Hill Spherically Blunted	FLDI, PCB, Kulite	4	0.54356
96	250	242.18	0.013	215.41	172.25	505.00	488.38	458.16	1.23E+07	1.09E+07	3.75E+06	3.33E+06	Hill Spherically Blunted	FLDI, PCB, Kulite	4	0.54356
97	200	194.02	0.011	173.00	138.95	505.00	488.72	459.05	9.86E+06	8.79E+06	3.01E+06	2.68E+06	Hill Spherically Blunted	Schlieren, PCB, Kulite		
98	200	193.69	0.011	172.68	138.66	505.00	488.70	459.01	9.85E+06	8.78E+06	3.00E+06	2.68E+06	Hill 14deg 1/4R Blunt Ogive	Schlieren, PCB, Kulite		
99	250	244.38	0.013	217.73	174.58	505.00	488.62	458.73	1.24E+07	1.11E+07	3.79E+06	3.37E+06	Hill 14deg 1/2R Blunt Ogive	Schlieren, PCB, Kulite		
100	250	243.18	0.010	216.67	173.72	505.00	488.62	458.73	1.24E+07	1.10E+07	3.77E+06	3.36E+06	Hill 28deg 1/4R Blunt Ogive	Schlieren, PCB, Kulite		
101	250	242.48	0.013	215.98	173.15	505.00	488.57	458.67	1.23E+07	1.10E+07	3.76E+06	3.34E+06	Hill 28deg 1/2R Blunt Ogive	Schlieren, PCB, Kulite		
102	150	149.34	0.010	133.29	107.05	505.00	488.86	459.18	7.60E+06	6.77E+06	2.32E+06	2.06E+06	Oddg 7deg Cone	FLDI	1	0.271018

Appendix B. FLDI Components

Table 14. FLDI components list

Component	Description	Supplier
"Excelsior One 532 Single Mode" diode pumped solid state continuous-wave laser	532 nm wavelength, 200 mW power	Spectra-Physics
"Excelsior CDRH" Power Supply	Power supply/controller	Spectra-Physics
Wollaston prism	2 arc minutes beam separation, 2 cm square	United Crystals (Port Washington, NY)
10mm focal length lens	(AC060-010-A-ML) Mounted Achromatic Doublet	Thorlabs
linear polarizer	LPVISB100-MP2	Thorlabs
photodetector	DET36A, Si Detector, 350-1100 nm	Thorlabs
amplifier (4 channels)	SR445A Fast Preamplifier DC-300MHz	Stanford Research Systems
1/2" absorptive ND filter, Optical Density 2.0 (1%)	NE513A	Thorlabs
1/2" absorptive ND filter, Optical Density 1.3 (5%)	NE520A	Thorlabs
300mm focal length lens	LA1256-A Ø2" N-BK7 Plano-Convex Lense	Thorlabs

Appendix C. Nose Geometry Equations

Table 15. Nose Geometry Equations

Geometry Number	Tip	Blunt - y eqn	Blunt - x1	Blunt - x2	Ogive - y eqn	Ogive - x1	Ogive - x2	Straight Length
SHARP TIPS								
1	14 deg ogive	N/A	N/A	N/A	(7479871186555493/4398046511104 - (x - 5616452816787275/562949953421312)^2)^(1/2) - 3519744042449077/87960930222080	0	9.9768	N/A
2	28 deg ogive	N/A	N/A	N/A	(7707105065807947/70368744177664 - (x - 5531778902306871/1125899906842624)^2)^(1/2) - 13004703727516267/1407374883553280	0	4.9132	5.0636
3	56 deg ogive	N/A	N/A	N/A	(8695104492017991/1125899906842624 - (x - 5187898892718237/2251799813685248)^2)^(1/2) - 8748204969139613/5629499534213120	0	2.3039	7.6729
1/4 R BLUNT TIPS								
4	14 deg ogive	sqrt(2401/25600 - (x - 190409217907105/14073 7488355328)^2)	1.0467	1.2884	(7479871186555493/4398046511104 - (x - 5616452816787275/562949953421312)^2)^(1/2) - 3519744042449077/87960930222080	1.2884	9.9768	1.0502
5	28 deg ogive	sqrt(2401/25600 - (x - 778489716502305/11258 99906842624)^2)	0.3852	0.5642	(7707105065807947/70368744177664 - (x - 5531778902306871/1125899906842624)^2)^(1/2) - 13004703727516267/1407374883553280	0.5642	4.9132	5.4533
1/2 R BLUNT TIPS								
6	14 deg ogive	sqrt(2401/6400 - (x - 3320035266829999/1125 899906842624)^2)	2.3363	2.8428	(7479871186555493/4398046511104 - (x - 5616452816787275/562949953421312)^2)^(1/2) - 3519744042449077/87960930222080	2.8428	9.9768	2.3419
7	28 deg ogive	sqrt(2401/6400 - (x - 3362980718054109/2251 799813685248)^2)	0.881	1.2809	(7707105065807947/70368744177664 - (x - 5531778902306871/1125899906842624)^2)^(1/2) - 13004703727516267/1407374883553280	1.2809	4.9132	5.9544
SPEHRICALLY BUNTED								
8	Blunt Sphere	sqrt(2401/1600 - (x - 5531778902306871/1125 899906842624)^2)	3.6883	4.9132	N/A	N/A	N/A	8.7672
DIMENSIONS ARE IN INCHES								

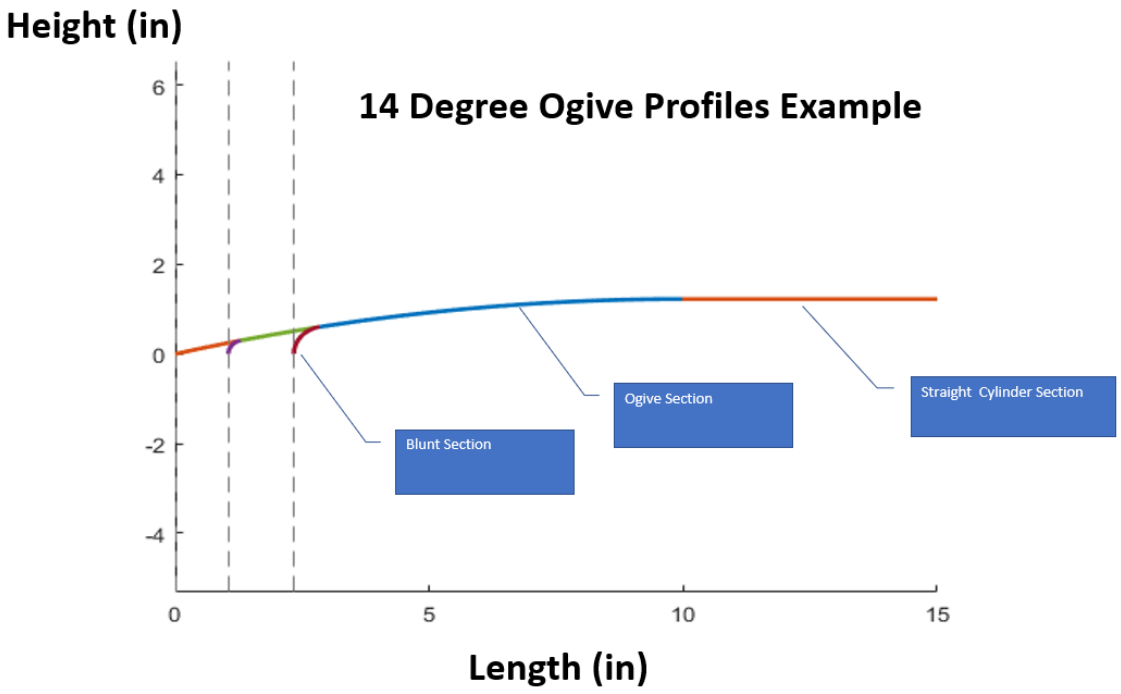


Figure 160. 14 degree sharp ogive nose example contours

Bibliography

1. Braslow, A. L., "Analysis of Boundary Layer Transition on X-15-2 Research Airplane," *NASA*, 1966.

2. Stetson, K., "Laminar boundary layer stability experiments on a cone at Mach 8. II- Blunt cone," *AlAA 22nd Aerospace Sciences Meeting*, 1984.

3. John D. Anderson, J., *Fundamentals of Aerodynamics*, McGraw-Hill, 2011.

4. Moretti, G. and Pandolfi, M., "Entropy Layers," *Polytechnic Institute of Brooklyn*, 1971.

5. Morkovin, M., Reshotko, E., and Herbert, T., "Transition in open flow systems - a reassesment," *Bull. Am. Phys. Soc.*, 1994.

6. White, F. A., *Viscous Fluid Flow*, McGraw-Hill, 1974.

7. Mack, L. M., "Boundary-Layer Linear Stability Theory," *AGARD Report*, 1984.

8. Fedorov, A., "Transition and Stability of High-Speed Boundary Layers," *Annual Review of Fluid Mechanics*, Vol. 43, 2011, pp. 79–95.

9. Stetson, K. F., "Comments on Hypersonic Boundary-Layer Transition," Air Force Research Lab, Wright-Patterson AFB OH, 1984-1990.

10. Knisely, C. and Zhong, X., "Significant Supersonic Modes and the Wall Temperature Effect in Hypersonic Boundary Layers," *AIAA*, Vol. 57, No. 4, 2019, pp. 1552–1566.

11. Casper, K., Beresh, S., Wagnild, R., Henfling, J., Spillers, R., and Pruett, B., "Simultaneous Pressure Measurements and High-Speed Schlieren Imaging of Disturbances in a Transitional Hypersonic Boundary Layer," *AIAA 43rd Fluid Dynamics Conference*, 2013.

12. Stetson, K., "Nosetip Bluntness Effects on Cone Frustrum Boundary Layer Transition in Hypersonic Flow," *AIAA 16th Fluid and Plasma Dynamics Conference*, 1983.

13. Marinaue, E., Moraru, G., Lewis, D., Norris, J., Lafferty, J., Wagnild, R., and Smith, J., "Mach 10 Boundary-Layer Transition Experiments on Sharp and Blunted Cones," *19th AIAA International Space Planes and Hypersonic Systems and Technologies Conference*, 2014.

14. Jewell, J. and Kimmel, R., "Boundary Layer Stability Analysis for Stetson's Mach 6 Blunt Cone Experiments," *54th AIAA Aerospace Sciences Meeting*, 2016.

15. Kennedy, R., Jagde, E., Laurence, S., Jewell, J., and Kimmel, R., "Visualizations of Hypersonic Boundary-Layer Transition on a Variable Bluntness Cone," *AIAA Aviation*, 2019.

16. Stetson, K., Thompson, E., Donaldson, J., and Siler, L., "Laminar Boundary Layer Stability Experiments on a Cone at Mach 8. Part I: Sharp Cone," *AIAA 16th Fluid and Plasmadynamics Conference*, 1983.

17. Kimmel, R. and Kendall, J., "Nonlinear Disturbances In a Hypersonic Laminar Boundary Layer," *AIAA 29th Aerospace Sciences Meeting*, 1991.

18. Jirsa, V. and Müller, V., "Cross-frequency coupling in real and virtual brain networks," *Frontiers in Computational Neuroscience*, Vol. 7, 2013, pp. 78.

19. Greenwood, R., *Measurements of entropy-layer instabilities over cone-ogive-cylinders at Mach 6*, Ph.D. thesis, Purdue University, 2014.

20. Kimmel, R., Borg, M., Jewell, J., Lam, K., Bowersox, R., Srinivasan, R., Fuchs, S., and Mooney, T., "AFRL Ludwieg Tube Initial Performance," *55th AIAA Aerospace Sciences Meeting*, 2017.

21. Labuda, D., *SCHLIEREN IMAGING AND FLOW ANALYSIS ON A CONE/FLARE MODEL IN THE AFRL MACH 6 LUDWIEG TUBE FACILITY*, Master's thesis, Air Force Institute of Technology, 2019.

22. Oddo, R., *High-Speed Schlieren Imaging of Second-Mode Disturbances in a Super-Cooled Hypersonic Boundary Layer*, Master's thesis, Air Force Institute of Technology, 2020.

23. "Kulite XCE-062 Product Specification Page," World Wide Web Page, Available at `https://kulite.com//assets/media/2018/01/XCE-062.pdf`.

24. "PCB 132B38 Product Specification Page," World Wide Web Page, Available at `https://www.pcb.com/contentstore/MktgContent/LinkedDocuments/Aerospace/AD-132B38_Lowres.pdf`.

25. Smeets, G., "Laser interferometer for high sensitivity measurements on transient phase objects," *IEEE Transactions on Aerospace and Electronic Systems*, Vol. AES-8, No. 2, 1972, pp. 186–190.

26. Rayleigh, L., "On the Stability or Instability of Certain Fluid Motions," *Scientific Papers*, Vol. 1, 1880, pp. 474–487.

27. Reynolds, O., "On the Dynamical Theory of Incompressible Viscous Fluids and the Determination of the Criterion," *Philosophical Transactions of the Royal Society of London. A*, Vol. 186, 1895, pp. 123–164.

28. Taylor, G. I., "Eddy motion in the atmosphere," *Philosphical Transactions of the Royal Society A*, Vol. 215, 1915, pp. 1–26.

29. Prandtl, L., "Bemerkungen über die Entstehung der Turbulenz," *ZAMM - Zeitschrift für Angewandte Mathematik und Mechanik*, Vol. 1, No. 6, 1921, pp. 431–436.

30. Tollmien, W., "Über die Entstehung der Turbulenz," *Nachrichten von der Gesellschaft der Wissenschaften zu Göttingen, Mathematisch-Physikalische Klasse*, 1929, pp. 21–44.

31. Tollmien, W., "General Instability Criterion of Laminar Velocity Distrobutions," *Nachrichten von der Gesellschaft der Wissenschaften zu Göttingen, Mathematisch-Physikalische Klasse*, Vol. 50, 1935, pp. 79–114.

32. Schlichting, H., "Zur Entstehung der Turbulenz bei der Plattenströmung," *Nachrichten von der Gesellschaft der Wissenschaften zu Göttingen, Mathematisch-Physikalische Klasse*, 1933, pp. 181–208.

33. Schlichting, H., "Berechnung der Anfachung kleiner Störungen bei der Plattenströmung," *ZAMM - Zeitschrift für Angewandte Mathematik und Mechanik*, Vol. 13, 1933, pp. 171–174.

34. Schlichting, H., "Amplitudenverteilung und Energiebilanz der kleinen Störungen bei der Plattengrenzschicht," *Nachrichten von der Gesellschaft der Wissenschaften zu Göttingen, Mathematisch-Physikalische Klasse*, Vol. 1, 1935, pp. 47–78.

35. Schlichting, H., "Über die theoretische Berechnung der kritischen Reynoldsschen Zahl einer Reibungsschicht in beschleunigter und verzögerter Strömung," *Jahrb. deut. Luftfahrtforsch*, Vol. 1, 1940, pp. 97.

36. Schubauer, G. B. and Skramstad, H. K., "Laminar Boundary-Layer Oscillations and Stability of Laminar Flow," *Journal of Aeronautical Sciences*, Vol. 14, No. 2, 1947, pp. 69–78.

37. Jaffe, Okamura, and Smith, "Determination of Spatial Amplification Factors and their Application to Predicting Transition," *AIAA Journal*, Vol. 8, 1970, pp. 301–307.

38. John D. Anderson, J., *Modern Compressible Flow*, McGraw-Hill, USA, 1982.

39. "Missile, Surface-to-Surface, V-2 (A-4)," Smithsonian National Air and Space Museum, Sat. 31 Aug 2019.
https://airandspace.si.edu/collection-objects/missile-surface-surface-v-2-4.

40. Shea, J., "Report of the Defense Science Board Task Force on the National Aerospace Plane (NASP)," 1988.

41. Kendall, J., "Wind tunnel experiments relating to supersonic and hypersonic boundary layer transition," *12th Aerospace Sciences Meeting*, 1974.

42. Demetriades, A., "Hypersonic viscous flow over a slender cone. III - Laminar instability and transition," *AIAA 7th Fluid and Plasma Dynamics Conference*, 1974.

43. Demetriades, A., "New Experiments on Hypersonic Boundary Layer Stability including wail lemperature Effects," *Proceedings of the Heat Transfer and Fluid Mechanics Institute*, 1978.

44. Stetson, K., "Comments on Hypersonic Boundary Layer Transition," *Wright Research and Development Center Report*, 1990.

45. Stetson, K. and Kimmel, R., "On the Breakdown of a Hypersonic Laminar Boundary Layer," *31st Aerospace Sciences Meeting and Exhibit*, 1993.

46. Stetson, K. and Kimmel, R., "On Hypersonic Boundary Layer Stability," *30th Aerospace Sciences Meeting and Exhibit*, 1992.

47. Stetson, K., "Effect of Bluntness and Angle of Attack on Boundary Layer Transition on Cones and Biconic Configurations," *17th Aerospace Sciences Meeting*, 1979.

48. Stetson, K., "Unsteady Transition Location," *AIAA Journal*, Vol. 27, No. 8, 1989, pp. 1135–1137.

49. Paredes, P., Choudhari, M., Jewell, J., Kimmel, R., Marineau, E., and Grossir, G., "Nose-Tip Bluntness Effects on Transiton at Hypersonic Speeds," *Journal of Spacecraft and Rockets*, Vol. 56, No. 2, 2019, pp. 369–387.

50. Herbert, T., "PARABOLIZED STABILITY EQUATIONS," *Annual Review of Fluid Mechanics*, Vol. 29, No. 1, 1997, pp. 245–283.

51. Nichols, J. and Candler, G., "Input-output analysis of complex hypersonic boundary layers," *AIAA Scitech 2019 Forum*, 2019.

52. John D. Anderson, J., "A Survey of Modern Research in Hypersonic Aerodynamics," *AIAA 17th Fluid Dynamics, Plasma Dynamics, and Lasers Conference*, 1984.

53. Newton, S. I., *Philosophiae Naturalis Principia Mathematica*, 1687.

54. John D. Anderson, J., *Hypersonic and High Temperaturee Gas Dynamics*, AIAA, Reston, Virginia, 2006.

55. Sakakeeny, J., Batista, A., and Kuehl, J., "How nose bluntness suppresses second-mode growth," *AlAA Aviation 2019 Forum*, 2019.

56. Chandrasekhar, S., *DHydrodynamic and Hydrodynamic Stability*, The International Series of Monographs on Physics, Oxford, 1961.

57. Rayleigh, L., "On the Stability of the Laminar Motion of an Inviscid Fluid," *Scientific Papers*, Vol. 6, 1913, pp. 197–204.

58. Lees, L. and Lin, C., "Investigation of the Stability of the Laminar Boundary Layer in a Compressible Fluid," *NACA Tech. Note No. 1115*, 1946.

59. Lees, L. and Reshotko, E., "Stability of the Compressible Laminar Boundary Layer," *Journal of Fluid Mechanics*, Vol. 12, 1962, pp. 555–590.

60. Chuvakhov, P. and Fedorov, A., "Spontaneous radiation of sound by instability of a highly cooled hypersonic boundary layer," *AIAA AVIATION Forum*, 2016.

61. Unnikrishnan, S. and Gaitonde, D., "Instability characteristics of cooled hypersonic boundary layers," *AIAA SciTech Forum*, 2020.

62. Evvard, J., "The Effects of Extreme Cooling on Boundary-Layer Transition at Supersonic Speeds," *American Physical Society Meeting*, 1957.

63. N Diaconis, J Jack, R. W., "Boundary-Layer Transition at Mach 3. 12 as Affected by Cooling and Nose Blunting," *NACA*, , No. 3928, 1957.

64. J Jack, R Wisniewski, N. D., "Effects of Extreme Surface Cooling on Boundary-Layer Transition," *NACA*, , No. 4094, 1957.

65. N Diaconis, J Jack, R. W., "Heat Transfer and Boundary-Layer Transition on Two Blunt Bodies at Mach Number 3. 12," *NACA*, , No. 4099, 1957.

66. Stetson, K. and Rushton, G., "A Shock Tunnel Investigation of the Effects of Nose Bluntness, Angle of Attack and Boundary Layer Cooling on Boudnary Layer Transition at a Mach number of 5.5," *AIAA 4th Aerospace Sciences Meeting*, , No. 66-495, 1966.

67. Rotta, N., "Effects of nose bluntness on the boundary layer characteristics of conical bodies at hypersonic speeds," *New York University Report NYUAA-66-66*, 1966.

68. Alba, C., Johnson, H., Bartkowicz, M., Candler, G., and Berger, K., "Boundary-layer stability calculations for the HIFiRE-1 transition experiment," *Journal of Spacecraft and Rockets*, Vol. 45, No. 6, 2008, pp. 1125–1133.

69. Jewell, J., Parziale, N., Leyva, I., and Shepherd, J., "Effects of Shock-Tube Cleanliness on Slender-Body Hypersonic Instability and Transition Studies at High Enthalpy," *AIAA Journal*, Vol. 55, No. 1, 2017, pp. 332–338.

70. Grossir, G., Pinna, F., Bonucci, G., Regert, T., Rambaud, P., and Chazot, O., "Hypersonic Boundary Layer Transition on a 7 Degree Half-Angle Cone at Mach 10," *7th AIAA Theoretical Fluid Mechanics Conference*, 2014.

71. Paredes, P., Choudhari, M., Li, F., Jewell, J., Kimmel, R., Marineau, E., and Grossir, G., "Nose-Tip Bluntness Effects on Transition at Hypersonic Speeds," *Journal of Spacecraft and Rockets*, Vol. 56, No. 2, 2019, pp. 369–387.

72. Mack, L., "Stability of Axisymmetric Boundary Layers on Sharp Cones at Hypersonic Mach Numbers," *AIAA 19th Fluid Dynamics, Plasma Dynamics and Lasers Conference*, 1987.

73. Stetson, K., "On Nonlinear Aspects of Hyperspnic Boundary-Layer Stability," *AIAA Journal*, Vol. 26, No. 7, 1988, pp. 883–885.

74. Zhu, Y., Zhang, C., Chen, X., Yuan, H., Wu, J., Chen, S., Lee, C., and el Hack, M. G., "Transition in Hypersonic Boundary Layers: Role of Dilatational Waves," *AIAA Journal*, Vol. 54, No. 10, 2016, pp. 3039–3049.

75. Kirk, L. and Candler, G., "Geometric Effects on the Amplification of First Mode Instability Waves," *AIAA 2013-0261*, 2013.

76. Zucrow, M. and Hoffman, J., *Gas Dynamics, Multidimensional Flow*, Vol. 2, Robert E. Krieger Publishing Company, 1984.

77. Friehmelt, H., Koppenwallner, G., and Müller-Eigner, R., "Calibration and First Results of a Redesigned Ludwieg Expansion Tube," *Theoretical and Computational Fluid Dynamics*, Vol. 21, 2007, pp. 81–98.

78. Robarge, T., "Laminar boundary-layer instabilities on hypersonic cones: Computations for becnhmark experiments," *35th AIAA Fluid Dynamics Conference and Exhibit*, 2005.

79. Demetriades, A., "Hypersonic viscous flow over a slender cone. III - Laminar instability and transition," *7th Fluid and Plasma Dynamics Conference*.

80. Gray, K., Chynoweth, B., Edelman, J., McKiernan, G., Wason, M., and Schneider, S., "Boundary-Layer Transition Measurements in the Boeing/AFOSR Mach-6 Quiet Tunnel," *55th AIAA Aerospace Sciences Meeting*, 2017.

81. Berridge, D., Casper, K., Rufer, S., Alba, C., Lewis, D., Beresh, S., and Schneider, S., "Measurements and Computations of Second-Mode Instability Waves in Three Hypersonic Wind Tunnels," *40th Fluid Dynamics Conference and Exhibit*, 2010.

82. Ceruzzi, A. and Cadou, C., "Simultaneous Velocity and Density Gradient Measurements using Two-Point Focused Laser Differential Interferometry," *AIAA Scitech Forum*, 2019.

83. Edelman, J., *Secondary instabilitiy of hypersonic stationary crossflow waves*, Ph.D. thesis, Purdue University, 2016.

84. Borg, M. and Kimmel, R., "Simultaneous Infrared and Pressure Measurements of Crossflow Instability Modes for HIFiRE-5," *AIAA SciTech 54th Aerospace Sciences Meeting*, 2016.

85. Stewart, J., *Calculus Concepts and Contexts 4th Edition*, Brooks/Cole CENGAGE Learning, 2010.

REPORT DOCUMENTATION PAGE

Form Approved
OMB No. 0704-0188

The public reporting burden for this collection of information is estimated to average 1 hour per response, including the time for reviewing instructions, searching existing data sources, gathering and maintaining the data needed, and completing and reviewing the collection of information. Send comments regarding this burden estimate or any other aspect of this collection of information, including suggestions for reducing the burden, to Department of Defense, Washington Headquarters Services, Directorate for Information Operations and Reports (0704-0188), 1215 Jefferson Davis Highway, Suite 1204, Arlington, VA 22202-4302. Respondents should be aware that notwithstanding any other provision of law, no person shall be subject to any penalty for failing to comply with a collection of information if it does not display a currently valid OMB control number.
PLEASE DO NOT RETURN YOUR FORM TO THE ABOVE ADDRESS.

1. REPORT DATE *(DD-MM-YYYY)*	2. REPORT TYPE	3. DATES COVERED *(From - To)*
03/26/2020	Master's Thesis	Sept 2018 - March 2020

4. TITLE AND SUBTITLE
Experimental Measurements of Hypersonic Instabilities over Ogive-Cylinders at Mach 6

5a. CONTRACT NUMBER

5b. GRANT NUMBER

5c. PROGRAM ELEMENT NUMBER

6. AUTHOR(S)
Hill, Jonathan L., 2nd Lt

5d. PROJECT NUMBER

5e. TASK NUMBER

5f. WORK UNIT NUMBER

7. PERFORMING ORGANIZATION NAME(S) AND ADDRESS(ES)
Air Force Institute of Technology
Graduate School of Engineering and Management (AFIT/EN)
2950 Hobson Way
Wright-Patterson AFB OH 45433-7765

8. PERFORMING ORGANIZATION REPORT NUMBER
AFIT-ENY-MS-20-M-265

9. SPONSORING/MONITORING AGENCY NAME(S) AND ADDRESS(ES)
Air Force Research Laboratory, Hypersonic Sciences Branch
Dr. Matt Borg
2145 5th Street, Building 24c
WPAFB, OH 45433
matthew.borg.3@us.af.mil

10. SPONSOR/MONITOR'S ACRONYM(S)
AFRL/RQH

11. SPONSOR/MONITOR'S REPORT NUMBER(S)

12. DISTRIBUTION/AVAILABILITY STATEMENT
Distribution Statement A. Approved for Public Release;Distribution Unlimited

13. SUPPLEMENTARY NOTES

14. ABSTRACT
Hypersonic boundary layer transition experiments were performed in the Air Force Research Lab (AFRL) Mach 6 Ludwieg tube over a meter long ogive-cylinder model with interchangeable nose tip angles and bluntnesses. Measurements of instabilities were captured via focused laser differential interferometry (FLDI), surface mounted pressure sensors, and high speed Schlieren imagery at nominal unit Reynolds numbers ranging from 4.0*10^6/m to 1.4*10^7/m. This study attempts to isolate the effects of increasing tip angle and spherical bluntness on instabilities measured downstream over the cylindrical body of the model.

15. SUBJECT TERMS
Hypersonic, Instability, Transition, Experimental, Wind Tunnel Testing, Ludwieg Tube, Focused Laser Differential Interferometry

16. SECURITY CLASSIFICATION OF:			17. LIMITATION OF ABSTRACT	18. NUMBER OF PAGES	19a. NAME OF RESPONSIBLE PERSON
a. REPORT	b. ABSTRACT	c. THIS PAGE			Lt Col Jeffrey Komives
					19b. TELEPHONE NUMBER *(Include area code)*
U	U	U	UU	257	(937) 255-6565 x4744 jeffrey.komives@afit.edu

INSTRUCTIONS FOR COMPLETING SF 298

1. REPORT DATE. Full publication date, including day, month, if available. Must cite at least the year and be Year 2000 compliant, e.g. 30-06-1998; xx-06-1998; xx-xx-1998.

2. REPORT TYPE. State the type of report, such as final, technical, interim, memorandum, master's thesis, progress, quarterly, research, special, group study, etc.

3. DATE COVERED. Indicate the time during which the work was performed and the report was written, e.g., Jun 1997 - Jun 1998; 1-10 Jun 1996; May - Nov 1998; Nov 1998.

4. TITLE. Enter title and subtitle with volume number and part number, if applicable. On classified documents, enter the title classification in parentheses.

5a. CONTRACT NUMBER. Enter all contract numbers as they appear in the report, e.g. F33315-86-C-5169.

5b. GRANT NUMBER. Enter all grant numbers as they appear in the report. e.g. AFOSR-82-1234.

5c. PROGRAM ELEMENT NUMBER. Enter all program element numbers as they appear in the report, e.g. 61101A.

5e. TASK NUMBER. Enter all task numbers as they appear in the report, e.g. 05; RF0330201; T4112.

5f. WORK UNIT NUMBER. Enter all work unit numbers as they appear in the report, e.g. 001; AFAPL30480105.

6. AUTHOR(S). Enter name(s) of person(s) responsible for writing the report, performing the research, or credited with the content of the report. The form of entry is the last name, first name, middle initial, and additional qualifiers separated by commas, e.g. Smith, Richard, J, Jr.

7. PERFORMING ORGANIZATION NAME(S) AND ADDRESS(ES). Self-explanatory.

8. PERFORMING ORGANIZATION REPORT NUMBER. Enter all unique alphanumeric report numbers assigned by the performing organization, e.g. BRL-1234; AFWL-TR-85-4017-Vol-21-PT-2.

9. SPONSORING/MONITORING AGENCY NAME(S) AND ADDRESS(ES). Enter the name and address of the organization(s) financially responsible for and monitoring the work.

10. SPONSOR/MONITOR'S ACRONYM(S). Enter, if available, e.g. BRL, ARDEC, NADC.

11. SPONSOR/MONITOR'S REPORT NUMBER(S). Enter report number as assigned by the sponsoring/ monitoring agency, if available, e.g. BRL-TR-829; -215.

12. DISTRIBUTION/AVAILABILITY STATEMENT. Use agency-mandated availability statements to indicate the public availability or distribution limitations of the report. If additional limitations/ restrictions or special markings are indicated, follow agency authorization procedures, e.g. RD/FRD, PROPIN, ITAR, etc. Include copyright information.

13. SUPPLEMENTARY NOTES. Enter information not included elsewhere such as: prepared in cooperation with; translation of; report supersedes; old edition number, etc.

14. ABSTRACT. A brief (approximately 200 words) factual summary of the most significant information.

15. SUBJECT TERMS. Key words or phrases identifying major concepts in the report.

16. SECURITY CLASSIFICATION. Enter security classification in accordance with security classification regulations, e.g. U, C, S, etc. If this form contains classified information, stamp classification level on the top and bottom of this page.

17. LIMITATION OF ABSTRACT. This block must be completed to assign a distribution limitation to the abstract. Enter UU (Unclassified Unlimited) or SAR (Same as Report). An entry in this block is necessary if the abstract is to be limited.